

EXPERIMENTAL INVESTIGATIONS OF
DISPERSIBILITY, STABILITY AND RHEOLOGICAL
BEHAVIOR OF AQUEOUS SUSPENSIONS OF
COLLOIDAL CLAYS

BY

SAMIM ALI

A THESIS SUBMITTED TO THE JAWAHARLAL NEHRU UNIVERSITY
FOR THE DEGREE OF DOCTOR OF PHILOSOPHY

DEPARTMENT OF SOFT CONDENSED MATTER

RAMAN RESEARCH INSTITUTE

BANGALORE 560 080

OCTOBER 2015

© Samim Ali, 2015.

Typeset in L^AT_EX 2_ε.

Certificate:

This is to certify that the thesis entitled “**Experimental investigations of dispersibility, stability and rheological behavior of aqueous suspensions of colloidal clays**” submitted by Samim Ali for the award of the degree of Doctor of Philosophy of Jawaharlal Nehru University is his original work. This has not been published or submitted to any other University for any other Degree or Diploma.

Prof. Ravi Subrahmanyam
(Director)
Raman Research Institute
Bangalore 560 080
India

Dr. Ranjini Bandyopadhyay
(Thesis Supervisor)

Declaration:

I hereby declare that the work reported in this thesis is entirely original. This thesis is composed independently by me at Raman Research Institute under the supervision of Dr. Ranjini Bandyopadhyay. I further declare that the subject matter presented in this thesis has not previously formed the basis for the award of any degree, diploma, membership, associateship, fellowship or any other similar title of any university or institution. I also declare that I have run it through **Turnitin** plagiarism detection software.

Dr. Ranjini Bandyopadhyay

Samim Ali

Soft Condensed Matter Group

Raman Research Institute

Bangalore 560 080

India

Acknowledgements

I would like to express my sincere gratitude to my supervisor and mentor, Ranjini Bandyopadhyay, for giving the opportunity to work with her. The completion of this thesis would not have been possible without her help, guidance, and support. I would also like to thank Dr. Pramod Pullarkat and Dr. Sadiq Rangwala for their positive disposition to be members of the advisory committee and their valuable advice and comments on this research work. I am grateful to Prof. Yogesh M. Joshi, IIT Kanpur, for illuminating discussions and active collaboration.

I would like to convey my sincere gratitude to Rajib Basak and Debasish Saha for helping me familiarize myself to various lab instruments during my initial months in the lab and getting me started with research at RRI. It has been a great pleasure to have regular discussions with Sanjay and Venketesh. I thank them for their help with sample preparation and measurements. My hearty thanks are also due to Jyothi for her help with the editing of the reference list and the cartoons presented in this thesis.

I thank Dr. Sanjib Sabhapandit and Dr. Abhishek Dhar for introducing me to the nonequilibrium statistical mechanics during my course work. I would also like to express my gratitude to Dr. V. Lakshminarayanan, Dr. V. A. Raghunathan, Dr. Arun Roy, Dr. Yashodhan Hatwalne for their encouragements, advice and for illuminating discussions on several occasions.

My sincere thanks also go to Mr. Ram, Mr. M. Mani, Mr. A. Dhason, Mr. Durai Chelvan for sharing their expertise during development of experimental setups and

for help with AFM and cryo-SEM imaging. I thank Mr. K. Radhakrishna for all his assistance with administrative works. I would also like to express my gratitude to Raja and Murali for extending their helping hands on countless occasions.

I would also like to take this opportunity to thank the director and all the people in various departments- administration, library, computer and networking, canteen, engineering-workshop, horticulture and cleaners in RRI for providing the basic support and friendly environment that were required for my research work.

I am lucky to have found many good friends in RRI. They have made my stay here really enjoyable through their love and affection. I thank all of them for being friends, for regular conversations on various topics and for their constructive criticism. I would always cherish the memory of times I spent with them.

Lastly, I express my deepest gratitude and love to my mother, my sister and my teacher, Mr. Gobordhan Sarkar, for their constant support and encouragement, without which I would not have come out of my village for higher studies.

Synopsis

Colloidal particles are abundant in nature and the suspensions of these submicron particles have become an important part of soft condensed matter research. The collective behavior of these systems is determined by the interactions that exist between the colloidal particles in their suspensions. These colloidal interactions can easily be manipulated by external means to achieve desired bulk properties.

This thesis work reports experimental studies of the dispersibility, stability and rheological behavior of aqueous suspensions of synthetic Laponite and natural Na-montmorillonite clays. The primary clay particle, known as platelet, has negative charges on its flat surfaces and pH dependent positive charges on its edge. In dry form, these platelets form stacks, known as tactoids, with positive counterions in the intercalated spaces. In aqueous suspensions, these tactoids exfoliate into single platelets with electric double layers on their surfaces. Due to screened repulsive interactions between the anisotropic electric double layers, the effective excluded volume is much higher than the geometrical volume of individual platelets. As a result, clay suspensions exhibit spontaneous phase transitions from freely flowing liquids to kinetically arrested, disordered glassy solids at particle volume fractions that lie far below the jamming transition concentration of hard spherical particles. The interaction force between two platelets is a function of the interparticle separation, mutual orientations and thickness of the electric double layers. Therefore, it is possible to tune the interactions

between the clay particles externally by controlling the particle and ionic concentrations in the dispersing medium and solution pH. Addition of appropriate amounts of salt leads to attractions between the screened electric double layers, which can result in the formation of volume-spanning network structures known as gels. Kinetically arrested phases, such as glasses and gels, are also characterized by their aging behavior, due to which the dynamics of clay particles slow down with time, leading to changes in their bulk properties. Besides their obvious importance in fundamental research, aqueous suspensions of these clay colloids find wide applications in the pharmaceutical, cosmetics, petroleum, coating, and food industries.

Chapter 1 of this thesis contains introductory material on colloids and colloidal interactions in suspensions. The formations of glass and gel phases in these systems are next described briefly. This is followed by a detailed description of the structures, swelling and exfoliation processes of Laponite and Na-montmorillonite in aqueous suspensions. Various phases that these clays exhibit at different particle and ionic concentrations are also presented in detail. A general description of several rheological models, including soft glassy rheology, is presented. The chapter concludes with a short discussion on the rheological behavior of clay suspensions.

Chapter 2 describes the various experimental methods used in this thesis work. The experimental techniques used here include rheological measurements, ultrasound attenuation spectroscopy, electroacoustics, atomic force microscopy and cryogenic scanning electron microscopy. Finally, a light-based, table-top setup for monitoring the stability of clay suspensions is described.

Chapter 3 describes the exfoliation kinetics of Laponite tactoids in an aqueous medium using ultrasound attenuation spectroscopy. The attenuation spectra measured in the frequency range 3 – 100 MHz are used to estimate bimodal size distributions of tactoids for different ages of clay suspensions in a concentration range where these suspensions show glassy behaviour. A theory of equivalent spherical diameter of colloidal discs under Stokes drag is used to estimate the average thicknesses of these

tactoids. This analysis shows that a substantial fraction of clay aggregates in suspension are tactoids that are composed of more than one platelet. This is understood in terms of the enhancement of intertactoid Coulomb repulsions during the exfoliation of clay aggregates with age of the suspension.

Chapter 4 describes the exfoliation behavior of Na-montmorillonite in aqueous suspensions below and above the jamming concentrations using ultrasound attenuation spectroscopy. It is seen, using a similar formalism developed in Chapter 3, that complete exfoliation is not achieved even below the glass transition concentration. Conductivity measurements in these suspensions are performed after varying the clay mineral concentration. The measurements indicate that the repulsive interactions may not be the sole factor for incomplete exfoliation of this clay. As the bulk concentration of the hydrated Na^+ counterions dissociated from the intra-tactoid spaces increases during exfoliation, the osmotic pressure difference between the bulk phase and the intra-tactoid space decreases with age. It is seen that this has a reverse effect on the exfoliation kinetics and leads to a reduction in the exfoliation rate at higher ages and clay concentration. This is verified by performing experiments after dispersing Na-montmorillonite in brine water. It is found that the presence of excess hydrated counterions in the bulk medium hinders the exfoliation process. The exfoliation of clay aggregates is also studied in a condition where counterions are added after dispersing the clay minerals in deionized water. It is found that the size of tactoids in this suspension increases before eventual saturation. This phenomenon is interpreted in terms of a process of tactoid reformation driven by the reverse osmotic pressure that is generated by the addition of counterions after dispersing clay. The influence of tactoid exfoliation on the suspension viscoelasticity and the stability of this natural clay is assessed using rheometry and electroacoustics.

Chapter 5 describes the salt-induced morphological changes in Na-montmorillonite gels and their macroscopic mechanical responses in oscillatory strain sweep experiments. When the salt concentration in the dispersing medium is increased systematically, viscoelasticity and yield stress of the suspensions exhibit a monotonic increase

upto a critical salt concentration before decreasing with the further addition of salt. This signifies a morphological change in the dispersion microstructures across the critical salt concentration. We directly visualize the microscopic structures of these kinetically arrested phases using cryogenic scanning electron microscopy. We observe the existence of honeycomb-like network morphologies for a wide range of salt concentrations. The transition of the gel morphology, dominated by overlapping coin (OC) and house of cards (HoC) associations of clay particles at low salt concentrations to a new network structure dominated by face-face coagulation of platelets, is observed across the critical salt concentration. Using electroacoustics, it is seen that these gels are highly stable under gravity over a wide salt concentration range even above the critical value of salt concentration.

Chapter 6 discusses the aggregation and stability behaviors of highly polydisperse and charge-anisotropic clay platelets of Na-montmorillonite in aqueous suspensions at a dilute concentration well below that required to achieve the glass transition. Using light transmission method and electroacoustics, it is seen that these platelets are not stable in salt-free aqueous suspensions in the dilute concentration regime and sediment under gravity with a particle concentration gradient along the sample height. The addition of salt to the clay suspension results in the formation of weak gels. By directly tracking the gel height with sample age using a light transmission method, it is further shown that the addition of salt after dispersing the clay mineral results in more stable gels even in very dilute suspensions. These weak gels are seen to exhibit transient collapse after a finite delay time, a phenomenon observed previously in depletion gels. The velocity of the collapse oscillates with age of the sample. However, the average velocity of collapse increases with sample age upto a peak value before decreasing at higher ages. With increasing salt concentration, the delay time for transient collapse decreases, while the peak value of the collapsing velocity increases. Using ultrasound attenuation spectroscopy, rheology and cryogenic scanning electron microscopy, we confirm that morphological changes of the gel network assembly, facilitated by thermal fluctuations, lead to the observed collapse phenomenon.

Chapter 7 describes the stress relaxation behavior of Laponite suspensions under applied step strains. Stress relaxation studies provide information about microscopic structures when the interactions between the constituent particles are known. In this study, the stress relaxation of clay suspensions are measured by varying particle and salt concentrations in suspension, sample idle time (time since preparation), suspension age and applied step strains. In the linear viscoelastic regime, all samples exhibit stress relaxation with a single-step decay which can be modeled using the Kohlrausch-Williams-Watt (KWW) function. The average relaxation times estimated from the KWW fits are seen to follow a power law increase with the age of the suspensions in this regime. On the other hand, under the application of nonlinear strains, a transition from single-step decay to two-step decay of stress is observed with age in the salt-free clay suspensions. The samples of varying ages are seen to exhibit power law decay of stress at short times. The extent of the power law fits is seen to increase with sample age upto a critical value of age. This critical value of age coincides with onset of the two-step decay process. It is further observed that the average relaxation time decreases with the increase in the applied step strains in the linear regime. On the contrary, the relaxation time increases with the increase in the strain in the nonlinear regime.

Chapter 8 presents the influence of the initial aggregate size distribution on the aging dynamics and rheology of Laponite clay suspensions. The initial size distributions of clay aggregates in concentrated suspensions are obtained by shear melting the clay samples of different idle times with varying flow rates of filtration using porous membranes of different pore sizes. The aging dynamics and jamming phase transitions of the resulting suspensions are studied using oscillatory rheological measurements. It is observed that the evolutions of the viscoelastic moduli with age after the filtration of samples become faster, with time for onset of arrested dynamics shifting to lower ages when the flow rate of filtration is increased and membrane pore size is decreased systematically. The viscoelastic moduli in the linear viscoelastic regime, yield strains and yield stresses determined from the oscillatory experiments exhibit monotonic increase with increase in the filtration rate and with the decrease in the membrane pore

sizes. These results indicate that a suspension with smaller aggregate sizes undergoes a faster rearrangement process facilitated by the thermal fluctuations, which results in the enhanced aging dynamics in the suspensions.

Chapter 9 summarizes the main results reported in this thesis and briefly discusses the scope for future work.

Publication List

Publications from this thesis:

1. Use of ultrasound attenuation spectroscopy to determine the size distribution of clay tactoids in aqueous suspensions, **Samim Ali** and Ranjini Bandyopadhyay, *Langmuir*, 2013, 29 (41), 12663 – 12669.
2. Evaluation of the exfoliation and stability of Na-montmorillonite in aqueous dispersion, **Samim Ali** and Ranjini Bandyopadhyay, *Applied Clay Science*, 2015, 114, 85 – 92.
3. Effect of electrolyte on the microstructure and yielding of aqueous dispersions of colloidal clay, **Samim Ali** and Ranjini Bandyopadhyay, *Soft Matter*, 2015, DOI:10.1039/c5sm01700a.
4. Aggregation and stability of anisotropic charged clay colloids in aqueous medium in the presence of salt, **Samim Ali** and Ranjini Bandyopadhyay, manuscript under review with *Faraday Discussions*.

5. Stress relaxation in aging clay suspensions in linear and nonlinear viscoelastic regimes, **Samim Ali**, Yogesh M. Joshi and Ranjini Bandyopadhyay, *manuscript in preparation*.

Contents

Acknowledgements	v
Synopsis	vii
Publication List	xiii
1 Introduction	5
1.1 Colloidal suspensions	5
1.2 Colloidal interactions	6
1.2.1 van der Waals interaction	6
1.2.2 Electric double layer interactions	7
1.2.3 DLVO interaction	9
1.3 Phases in colloidal suspensions	10
1.4 Rheological behavior of soft solid materials	14
1.5 Sedimentation of non-Brownian particles	17
1.6 Structure of a clay particle	21
1.7 Swelling and exfoliation of clays	23
1.8 Interactions and phase behavior of clay platelets in aqueous suspensions	24

1.9	Aging and rheological behaviors of clay suspensions	30
1.10	Thesis organization	34
	References	36
2	Experimental Techniques and Data Analysis	51
2.1	Introduction	51
2.2	Experimental techniques	52
2.2.1	Ultrasound attenuation spectroscopy: Theory and measurements	52
2.2.2	Experimental setups for stability characterization	57
2.2.3	Conductivity measurements	62
2.2.4	Atomic force microscopy (AFM)	64
2.2.5	Rheological measurements	66
2.2.6	SEM and Cryo-SEM techniques	74
2.2.7	Sample preparation for SEM measurements	77
2.2.8	Sample preparation for cryo-SEM measurements	78
	References	79
3	Dispersibility of clay in aqueous suspensions: Dependence on con-	
	centration and age	81
3.1	Introduction	81
3.2	Sample preparation and experimental methods	83
3.3	Results and discussion	85
3.4	Conclusions	97
	References	99

4 Exfoliation and stability of clay tactoids in aqueous suspensions: Dependence on ionic conditions	103
4.1 Introduction	103
4.2 Sample preparation	105
4.3 Results and discussion	105
4.4 Conclusions	123
References	125
5 Effect of electrolyte on the microstructure and yielding of aqueous suspensions of colloidal clay	129
5.1 Introduction	129
5.2 Sample preparation and experimental methods	131
5.3 Results and discussion	135
5.4 Conclusions	148
5.5 Analysis of cryo-SEM images using ImageJ software	149
References	151
6 Sedimentation kinetics of weak clay gels	155
6.1 Introduction	155
6.2 Sample preparation	157
6.3 Results and Discussion	158
6.3.1 Optical and rheological studies of sedimentation of dilute clay gels prepared at different ionic conditions	158
6.3.2 Electroacoustic studies of stability of concentrated clay gels prepared at different ionic conditions	171
6.4 Conclusions	172

References	175
7 Stress relaxation in clay suspensions in linear and nonlinear viscoelastic regimes	179
7.1 Introduction	179
7.2 Sample preparation	181
7.3 Experimental results and discussion	183
7.4 Conclusion	198
References	201
8 Influence of aggregate sizes on the aging behavior and viscoelasticity of clay suspensions	205
8.1 Introduction	205
8.2 Sample preparation	207
8.3 Experimental results and discussion	209
8.4 Conclusion	215
References	217
9 Summary and future directions	219

1

Introduction

1.1 Colloidal suspensions

A colloidal suspension is a multiphase system in which ‘small particles’ are dispersed in a continuous medium [1]. The sizes of these ‘small particles’ (colloidal particles) lie in the range 10 nm– 10 μm [2]. To be classified as a colloidal state, the dispersed particles have to be sufficiently small so that they are not affected by gravitational force, but large enough to be distinguishable from the molecules of the dispersing medium [1]. In general, both the dispersed particles and the continuous medium can be in gas, liquid or solid form [1, 3]. This generates a wide variety of colloidal suspensions in nature such as ink (solid in liquid), foam (gas in liquid), smoke (solid in gas), milk (liquid in liquid), ruby glass (solid in solid) [4–10]. Due to the submicron sizes of the colloidal particles, the ratio of the surface area to the volume per gram of a colloidal material is very large when compared to a bulk material. This is the origin of many of the interesting bulk properties of colloidal suspensions. The finer details of the chemical composition of the colloids are not important in this context. Colloidal

particles are sufficiently small such that their thermal fluctuations are very relevant. As a consequence of the random collisions by the background particles of the suspending medium (gas or liquid), colloidal particles undergo random movement known as Brownian motion which can be observed in experiments [11]. Usually, the thermal energy of these colloidal particle is of the order of few $k_B T$, where k_B is the Boltzmann constant and T is suspension temperature. Colloids find wide uses in the laboratory as a model systems to study various phases of matter such as glasses, gels and crystals [12–15]. Surface and shape modified colloidal particles can also be used as building blocks to design various hierarchical structures [15, 16]. Given the size range of colloidal particles (10nm-20 μ m), colloidal suspensions can be studied in the laboratory using various scattering and visualization techniques [17, 18].

1.2 Colloidal interactions

The nature of the colloidal interaction is very crucial for the microscopic organization and the stability of colloidal particles in their suspensions [19]. Depending on the nature of colloids and the suspending medium, various types of interactions may exist between colloidal particles. The most important interaction in the context of this thesis is the one that exists in suspensions of charged colloids with electric double layers on their surfaces. The interactions and stability of such colloids in electrolyte solutions are controlled by short range van der Waals attractions and the long range screened Coulomb repulsions [1, 20]. These two interactions are together described by the DLVO theory developed by Derjaguin, Landau, Verwey and Overbeek [21, 22].

1.2.1 van der Waals interaction

The van der Waals interaction acts between all atoms and molecules [23] and is attractive in nature. Usually two atoms having permanent dipole moments can attract

each other through dipole-dipole interactions [24]. However, such attractive interactions, known as London dispersion interactions, can also arise between two neutral atoms when transient dipole moments are induced by cooperative oscillation of electron clouds of two molecules at short distances [1, 25]. Total van der Waals attraction between two colloidal particles is the sum of all the pairwise London interactions that arise for all pairs of atoms in the two particles [26]. The effective range of this attraction can vary from 0.1 nm to 10 nm [27, 28]. The strength of this interaction depends on the dielectric properties of the colloidal particles and the liquid medium. For two parallel plates, which is an approximately correct description of the clay platelets investigated in this thesis, the van der Waals interaction energy is given as follows [29, 30]:

$$v_{vdW}(d) = -\frac{A}{48\pi} \left[\frac{1}{d^2} + \frac{1}{(d + \delta)^2} - \frac{2}{(d + \delta/2)^2} \right] \quad (1.1)$$

Here, d is the half distance between two plates, δ is thickness of the plates and A is a Hamaker constant which has a value of the order of 10^{-20} J ($5 - 25 k_B T$) [26].

1.2.2 Electric double layer interactions

Colloidal particles in suspension can acquire charges by several mechanisms such as surface adsorption of surfactants [31, 32], isomorphous substitution [33–35], and ionic exchange [36, 37]. The charged colloidal surfaces are surrounded by an equal amount of counterions to achieve electrical neutrality. However, due to thermal fluctuations, the counterions remain in a diffused state within a layer, which screens the charged surface. The concentration of these counterions decreases with the distance from the charged surface of the colloidal particles. This diffuse layer of counterions, together with the surface charges, form the electric double layer (EDL) [1]. The distribution of potential (ϕ) in the double layer is determined by the Poisson equation:

$$\nabla^2 \phi = -\frac{\rho}{\epsilon} \quad (1.2)$$

where ρ is the volume density of charge and ϵ is the dielectric permittivity of the dispersing medium.

In the diffuse charge layer, the number concentration n_i of the ions of the i^{th} species is given by the Boltzmann equation:

$$n_i = n_i^0 \exp(-z_i e \psi / k_B T) \quad (1.3)$$

where $\psi = \phi - \phi_0$ with ϕ_0 being the constant potential in the bulk solution, e is the electronic charge, z_i is the valency of i^{th} ion species and n_i^0 is the bulk concentration of i^{th} species.

Since, the volume density of charge is given by $\rho = \sum_i n_i z_i e$, Eqn. 1.2 and Eqn. 1.3 yield

$$\nabla^2 \psi = -\frac{1}{\epsilon} \sum_i e n_i^0 z_i \exp(-z_i e \psi / k_B T) \quad (1.4)$$

This equation is known as Poisson-Boltzmann equation and is the basis for understanding the electric double layer interactions. This equation can be solved after linearization using Debye-Huckel approximation which assumes that electrical energy is small compared to the thermal energy i.e. $|z_i e \psi| < k_B T$. However, Eqn. 1.4 can be exactly solved for a flat surface in the presence of symmetric electrolytes ($z_i = z_+ = z_- = z$). In this case, the Poisson-Boltzmann equation in one dimension with electrolyte concentration of n^0 is given by [1]:

$$\frac{d^2 \psi}{dx^2} = \frac{2n^0 z e}{\epsilon} \sinh\left(\frac{z e \psi}{k_B T}\right) \quad (1.5)$$

The solution of this equation at a distance $x = d$ from the charged surface is given by:

$$\psi = \frac{4k_B T}{z e \gamma} \exp[-\kappa(x - d)] \quad (1.6)$$

Here, $\gamma = \frac{\tanh(z e \psi_0)}{4k_B T}$ with $\psi_0 = \phi_s - \phi_0$ where ϕ_s is potential on the particle surface

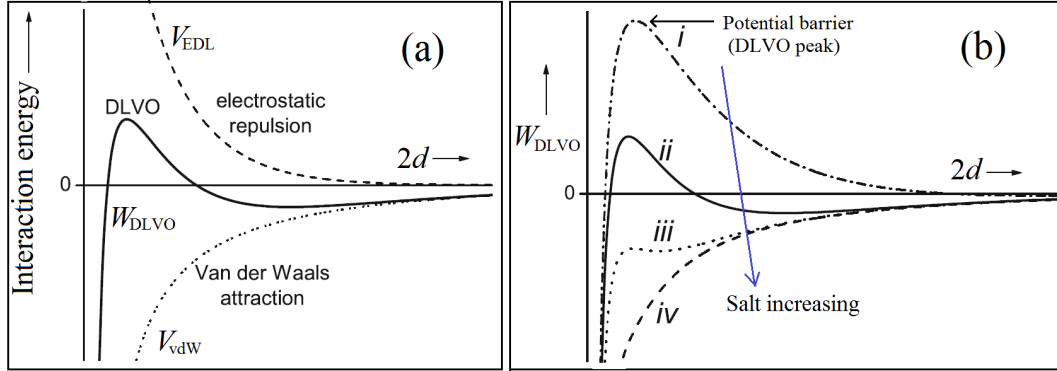


FIGURE 1.1: (a) Schematic plot of a typical electric double layer interaction, V_{EDL} (dashed line), the Van der Waals interactions, V_{vdW} (dotted line) and their sum, W_{DLVO} , the DLVO interaction potential (solid line) between two charged colloidal particles. (b) Plot of DLVO pair interactions between two charged colloidal particles in an electrolyte solution as a function of increasing salt concentrations (i→iv). The figure is adapted from [10]

and $\frac{1}{\kappa} = \left(\frac{\epsilon k_B T}{2e^2 n_0 z^2}\right)^{1/2}$ is known as Debye screening length which is a measure of the range of the electric potential of a charge screened colloidal particle. The magnitude of Debye screening length decreases with increasing counterion concentration in the medium.

The double layer interaction energy V_{EDL} between two charged plates separated by a distance $2d$ can be calculated using Eqn. 1.6 assuming a small double-layer overlap (i.e. $2d > 1/\kappa$) and is given by [1, 29]:

$$V_{EDL}(d) = \left(\frac{64n^0 k_B T \gamma^2}{\kappa}\right) \exp(-2\kappa d) \quad (1.7)$$

The electric double layer interaction is always repulsive which prevents the charged colloids from aggregation.

1.2.3 DLVO interaction

The DLVO interaction between two colloids is simply given by

$$W_{DLVO} = V_{vdW}(d) + V_{EDL}(d) \quad (1.8)$$

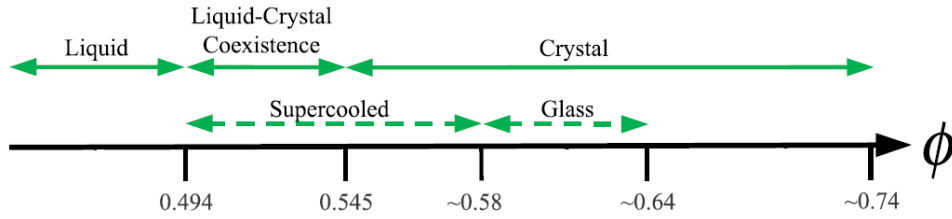


FIGURE 1.2: Phase diagram of nearly monodisperse hard sphere particles as a function of particle volume fraction, ϕ . Solid arrows indicate equilibrium states and dashed arrows indicate non-equilibrium states resulting from rapid quenching. This figure is reproduced from [2]

Here, $V_{vdW}(d)$ is the effective van der Waals attraction (Eqn. 1.1) and arises from the pair interactions between all the molecules/atoms present in the two colloidal particles. V_{EDL} is the repulsive interaction between the two screened colloidal particles. A schematic plot of V_{vdW} , V_{EDL} and W_{DLVO} as a function of the separation $2d$ between two colloids is shown in Fig. 1.1(a) by dotted, dashed and solid lines respectively. The DLVO potential exhibits a peak at a critical separation between two colloidal particles. Flocculation is prevented when the height of the DLVO peak is higher than the thermal energy of the colloids and is order of few $k_B T$. Addition of counterions (salt) reduces the repulsion between the colloidal particles and hence reduces the DLVO peak height (Fig. 1.1(b)). As a result, the colloidal particles approach each other. At some critical value of the salt, the particle surfaces get completely screened and the DLVO peak disappears completely. This leads to the aggregation of colloidal particles.

1.3 Phases in colloidal suspensions

A suspension of hard sphere colloidal particles is the simplest model system to understand the physics of the glass transition phenomenon [2, 38]. In a molecular glass transition process, a glass former such as glycerol and SiO_2 is quenched rapidly below its freezing point to avoid crystallization [39, 40]. The molecular glass transition is associated with a rapid increase in the relaxation time, viscosity and heat capacity near the glass transition temperature, T_g [39, 41–43]. At T_g , constituent particles in the system

undergo kinetic arrest within an extremely short duration and the viscosity of the system increases to the order of 10^{12} Pa.s, preventing study of the dynamics of the particles at the laboratory time scale. Such a difficulty can be overcome by mimicking the glass transition using colloidal suspensions [13]. The structures, dynamics and mechanical behavior of these systems can be studied using several experimental techniques such as light scattering, microscopy and rheology that are difficult to adapt to molecular glasses [18, 44–49]. The phase behavior of colloidal suspensions was first studied experimentally in hard sphere colloidal suspensions by Pusey and van Megan [50, 51]. The phase behavior in such suspensions is solely determined by excluded volume interactions between the nonpenetrating hard spheres [52]. Fig. 1.2 shows the phase diagram of nearly monodisperse (with small polydispersity of 8%) hard spheres as a function of volume fraction ϕ [2]. At equilibrium conditions, the suspension exhibits liquid state for $\phi < 0.494$, while it undergoes entropically driven liquid-crystalline transition at $\phi > 0.494$ (shown by solid arrow in Fig. 1.2)[50, 53]. However, when the system is quenched rapidly (or equivalently, particle volume fraction is increased rapidly), a supercooled phase arises for volume fractions $0.494 < \phi < \phi_g \approx 0.58$, whereas the suspension exhibit glassy phase between $\phi_g < \phi < \phi_{rcp} \approx 0.64$ (shown by dashed arrow in Fig. 1.2). Here, ϕ_{rcp} is the maximum volume fraction for randomly close packed spheres and its value depends on the polydispersity of the particles [54]. Above ϕ_{rcp} , the system exhibits domains of crystalline order. The packing volume fraction can be further increased upto the limit for hexagonal close packing at $\phi_{hcp} = 0.74$. The presence of polydispersity in the hard spheres shifts the boundaries between liquid and glass to slightly higher values [53, 55]. On the other hand, adding charges to the particles shifts the phase boundaries to substantially lower values [56–58]. For anisotropic particles, the volume fraction for the glass transition depends on the particle shape and polydispersity [19, 59–61]. However, depending on the volume fraction of particles, a suspension of anisotropic particles of regular shape can also exhibit other phases such as nematic or columnar phases [62, 63]. In case of colloidal particles with electric double layer on their surfaces, the effective excluded volume is much higher than the

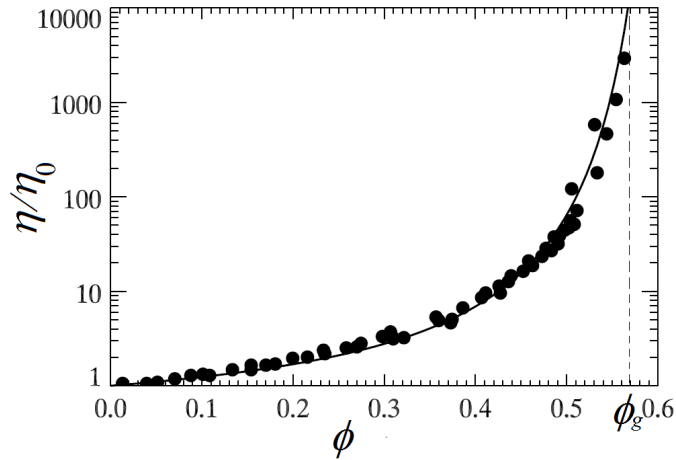


FIGURE 1.3: Normalized shear viscosity (η/η_0) as a function of volume fraction ϕ for a typical hard sphere colloidal suspension. Here, η_0 is the viscosity of the background medium. The vertical dashed line shows the position close to the glass transition volume fraction. This figure is reproduced from [2].

geometrical volume of the particles. As a result, the suspensions of these colloidal particles exhibit glass transition at particle concentrations below the values required for hard sphere particles [12, 46, 64–66].

In the glassy phase, a colloidal particle is arrested by its neighbors, a phenomenon often described as caging [40] and the dynamics of the particles slow down by several orders of magnitude [45]. As a result, the suspension viscosity increases drastically at the glass transition concentration, ϕ_g , as shown in Fig. 1.3. This behavior is reminiscent of the behavior of molecular glass formers which exhibit viscosities of the order of 10^{12} Pa.s at the glass transition temperature [39]. Both the molecular glasses and colloidal glasses, in principle, can be unjammed by applying sufficient load to them. Based on these generic features of the glass transition in complex systems including molecular glass formers, colloidal suspensions and granular matter, Liu and Nagel proposed a three dimensional jamming phase diagram as a function of temperature (T), load (σ) and inverse density (ϕ^{-1}) Fig. 1.4(a) [68]. This phase diagram suggests that jamming (glass transition) occurs when ϕ (number density of particles) is increased above a critical value. However, the critical value of density varies depending on the applied load (stress) and system temperature. This system can then be

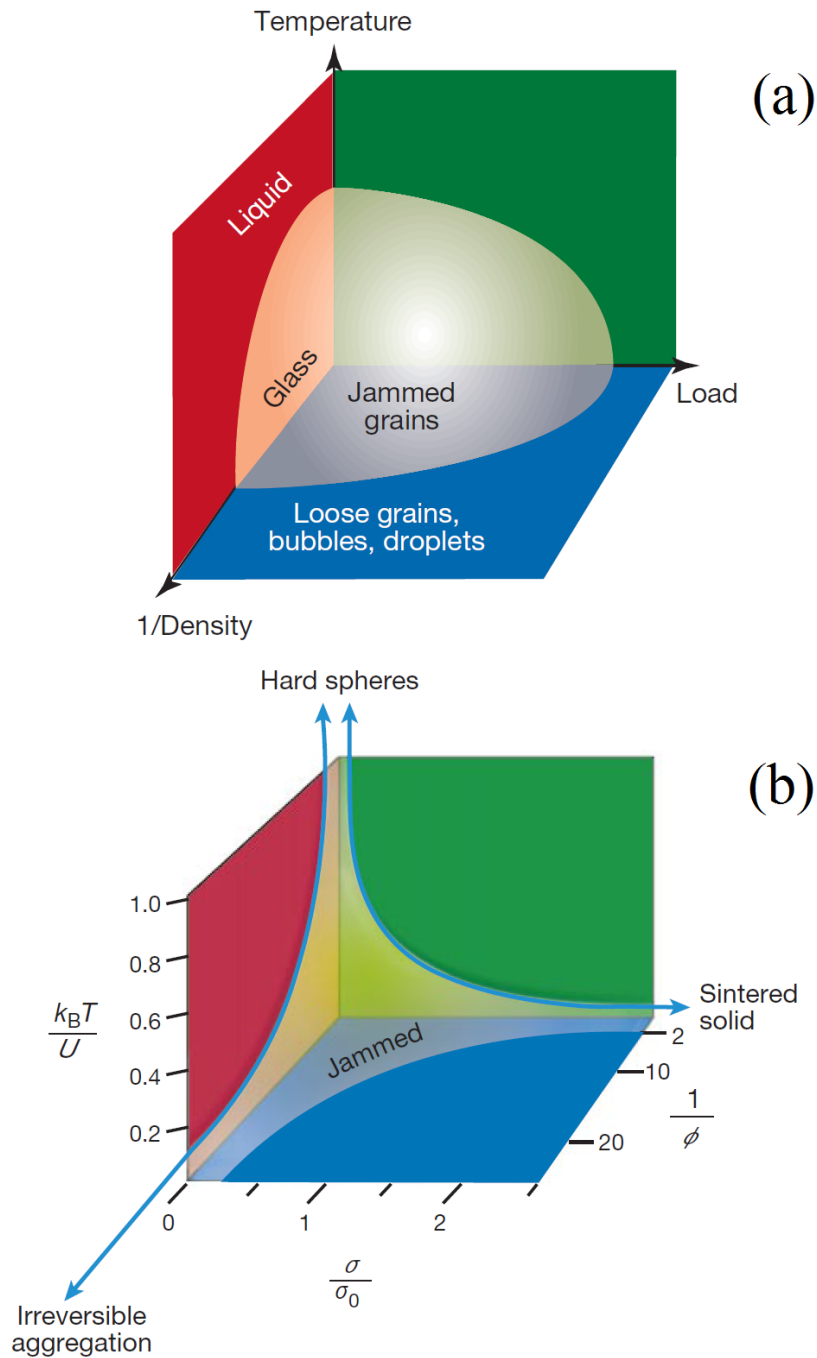


FIGURE 1.4: (a) Jamming phase diagram proposed by Liu and Nagel *et al.* plotted in the planes of inverse density ϕ^{-1} , temperature T and load σ . (b) Jamming phase diagram for attractive particles proposed by Trappe *et al.* in the planes of inverse density ϕ^{-1} , $k_B T/U$ and σ/σ_0 . [67]. Here, U is the attractive potential between two colloidal particles of diameter a and $\sigma_0 = k_B T/a^3$.

unjammed by applying sufficient load or by increasing temperature. The boundaries between the jammed and unjammed states is completely system dependent. At volume fractions below the glass transition concentration, the suspension of uncharged or completely screened colloidal particles can also exhibit kinetic arrest through gel transition mediated by attractive interactions [69]. A gel is a sample volume-spanning three dimensional network in which particles are connected by attractive bonds [70]. For such attractive particle systems, the jamming phase diagram was later modified by Trappe *et al.* [67] (Fig. 1.4(b)). In contrast to the phase diagram for hard spheres or repulsive particles, the phase boundaries of the latter have opposite curvature due to the attractive nature of the interparticle interactions. This phase diagram indicates that, apart from the applied load and density (concentration), the ratio of the thermal energy $k_B T$ and the attractive interaction U between particles is also important for jamming. In the limit of a very low stress (load), low attractive interactions and high concentration, the system exhibits glass like amorphous behavior. On the other hand, in the limit of strong attractive interactions at low stress and low concentrations, the system undergoes irreversible aggregation. In the intermediate state, the system exhibits fractal-like network structures [71]. The jamming phase diagrams discussed here include common features of the kinetic arrest process seen in most complex fluids. However, they fail to explain the shear induced jamming transition seen in cornstarch suspensions [72] or the age driven kinetic arrest seen in clay suspensions [73].

1.4 Rheological behavior of soft solid materials

Glasses and gels exhibit very interesting viscoelastic properties which can easily be tuned by controlling the interactions between colloidal particles. The elasticity in the glass originates due to the caging effect, while the attractive bonds between particles contribute to the elasticity in the gel phase [75–79]. The viscoelasticity of these soft solid materials, characterized by elastic modulus G' and viscous modulus G'' in an oscillatory rheological test, usually depends on applied frequency and strain (or stress)

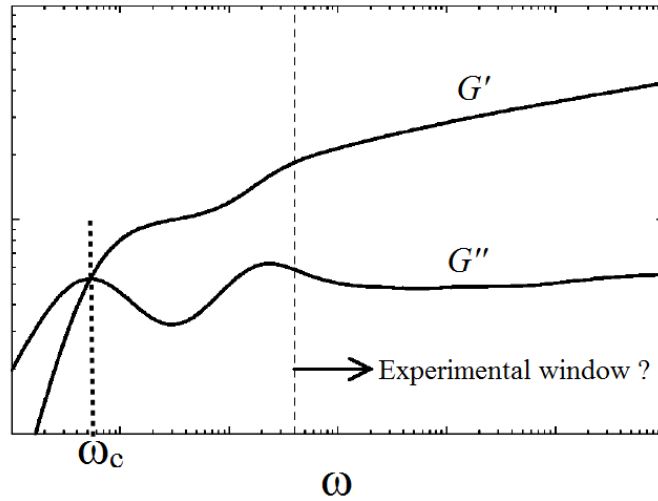


FIGURE 1.5: Sketch of frequency dependence of elastic modulus G' and viscous modulus G'' in the linear regime of a typical soft solid material. The vertical dotted line shows the position of the relaxation time ($= 1/\omega_c$) which usually lies much below the experimentally accessible measurement window. This figure is adapted from [74].

[80–82]. Fig. 1.5 shows the viscoelastic response of a typical soft solid material at varying frequencies of the applied oscillatory strain. At very low frequencies (long measurement time scale), the material exhibits liquid-like behavior ($G' < G''$) and both the moduli exhibit power law increase with frequency [81]. On the other hand, at very high frequency (very fast measurement time scale), the material exhibits solid-like behavior with $G' > G''$. The critical frequency $\omega = \omega_c$, at which $G' = G''$ defines the relaxation time ($\tau_0 = 1/\omega_c$) of the material.

It has been very difficult to describe the rheological behavior of complex fluids using a unified theory. However, many of the common features such as those shown in Fig. 1.5 have been successfully described by the soft glassy rheology (SGR) model proposed by Sollich *et al.* [83] based on Bouchaud's trap model [84]. According to this trap model, a particle find itself in trap formed by its neighbors. These traps are distributed with varying energy depths E in a metastable potential landscape. Particles in these traps formed by their neighbors undergo diffusive motion facilitated by thermal fluctuations such that the particles frequently collide with their neighbors. Bouchaud

assumed that the trapped particles can hop from one trap to another by thermal fluctuations when activation energy, $E \geq k_B T$. However, Sollich *et al.* argued that $k_B T$ is usually small compared to the typical trap depth E , which prevents hopping by thermal agitation [83]. The SGR model, instead, assumes that the hopping process is facilitated by long range interactions, in which rearrangement of particles in one region activates particles in other regions of the potential landscape. The SGR model describes such an activation process using a mean field temperature (or noise level) x . When a finite macroscopic strain γ is applied to the material, particles in traps experience local strains l which can have a distribution according to the local particle arrangement. In this situation, the activation energy reduces to $E - \frac{1}{2}kl^2$, where k is the local elastic constant. The local yielding occurs when $E \geq \frac{1}{2}kl_y^2$, where l_y is the local yield strain. Using the probability distribution of activation energy E proposed by Bouchaud's trap model for a mean field noise temperature x in the linear regime [84], the SGR model infers that when the system lies above the glass transition ($x > 1$), both G' and G'' vary with frequency as ω^{x-1} for $1 < x < 2$ in the limit of low frequencies (below a cutoff frequency ω_c). Below the glass transition regime ($x < 1$) and in the low frequency limit above ω_c , G' becomes almost independent of the frequency while G'' varies with frequency as ω^{x-1} [74].

Soft glassy materials exhibit two distinct regimes, linear and nonlinear, depending on the extent of the applied deformation. In the linear regime, the microstructures remain intact and the viscoelastic moduli (G' and G'') remain unchanged with the applied strain or stress. In the nonlinear regime, where the applied strain is above the yield strain value of the material, the constituent particles undergo irreversible rearrangements leading to the destruction of the microstructures and, consequently, the viscoelastic moduli become strongly dependent on the applied stress or strain. Many of the soft glassy materials exhibit common rheological features in the nonlinear regime. Storage modulus in this regime follows a power law decay of the form $G' \sim \gamma^{-2\nu_1}$ while the viscous modulus exhibits a peak before decreasing according to power law of the form $G'' \sim \gamma^{-\nu_2}$. SGR model predicts the power law decay of the viscous modulus

according to the form $G'' \sim \gamma^{x-2}$ in the limit $1 < x < 2$. However, this model cannot predict the behavior of the elastic modulus in the nonlinear regime. Miyazaki *et al.* proposed a qualitative description based on the mode coupling theory (MCT) [82]. It is assumed that the structural relaxation time of the complex system decreases under nonlinear strains following a relation: $1/\tau = 1/\tau_0 + K|\dot{\gamma}|^n$, where $\dot{\gamma}$ is the applied shear rate, K and n are constants, and τ_0 is the single relaxation time of the complex system following the Maxwell model [81]. This approximation results in the observation of a peak in viscous modulus at $\omega = 1/\tau$ and power law decay of the moduli at high strains in the nonlinear regime. For a material that can be described by the Maxwell model with a single relaxation time τ_0 , the ratio ν_1/ν_2 becomes equal to 2 [81].

Interestingly, the gelation process in a suspension of weakly aggregating colloidal particles exhibits remarkable similarity to the colloidal glass transition [67, 79]. Viscoelastic properties of many of the gel systems also show similar dependence on frequency and strain of deformation [85, 86, 181] This indicates the ubiquitous nature of the kinetic arrest and the SGR model, originally developed for glassy materials [88].

1.5 Sedimentation of non-Brownian particles

At low particle concentrations, colloids exhibit Brownian motion due to stochastic thermal fluctuations that arise from the background particles of the suspending medium. Stability of these colloidal particles under gravity depends on the competition between the diffusion time scale τ_d and the sedimentation time scale τ_s . The stability of a particle of size a and density ρ_c in a medium of density ρ_m is usually assessed by the dimensionless Peclet number P_e defined as follows [89]:

$$P_e = \frac{\tau_d}{\tau_s} = \frac{4\pi(\rho_c - \rho_m)ga^4}{3k_B T} \quad (1.9)$$

Thus, in a suspension for which $P_e \ll 1$, the diffusion of particles dominates, leading to a stable colloidal suspension [90]. On the other hand, a particle sediments

under gravity when $P_e > 1$. These particles are known as non-Brownian particles. A dilute suspension of non-Brownian particles undergoes sedimentation over time. Smoluchowski in 1906 pointed out that sedimentation equilibrium of these particles should follow the Barometric law for density of gases [91]. This law, when modified for non-Brownian particles takes the form [92]:

$$n_2 = n_1 e^{-\frac{4N_A}{3RT} [\pi a^3 \delta (h_2 - h_1) g]} \quad (1.10)$$

where n_1 and n_2 are the concentrations of particles at heights h_1 and h_2 respectively, a is the radius of particles, N_a is the Avogadro's number, R is the gas constant, δ is the density difference between the particle and the background fluid, and g is the gravitational acceleration.

Perrin used Eqn. 1.10 to directly determine the value of Avogadro's number, N_a , using suspensions of gamboge particles [93]. A sufficiently dilute solution of charged particles with electric double layers also exhibits a similar sedimentation profile [94]. However, when concentration of the particles is increased, the sedimentation profile deviates from Eqn. 1.10 and is found to satisfy this equation only within a short distance from the top surface of the suspension [92].

In the case of a single particle sedimenting in a fluid, the sedimentation velocity is given by Stokes relation: $v_s = \frac{2a^2 g \delta}{9\eta}$ [95]. For a multi-particle system with high Peclet number, P_e , long range hydrodynamic interactions between particles as well as back-flow of liquid in the sedimentation cell become very important [96–98]. Due to this reason, fluctuations in the sedimentation velocities were observed around their average values [97, 99]. The velocity fluctuations exhibit correlated regions in space in the form of swirls, the sizes of which strongly depend on the particle concentration and the size of the sedimentation cell [97, 100]. During sedimentation, various novel phenomena such as size segregation in polydisperse particles [101, 102] and nematic ordering in the sediment of anisotropic particles were also observed [103, 104].

We now discuss the sedimentation behavior of attractive particles in suspensions,

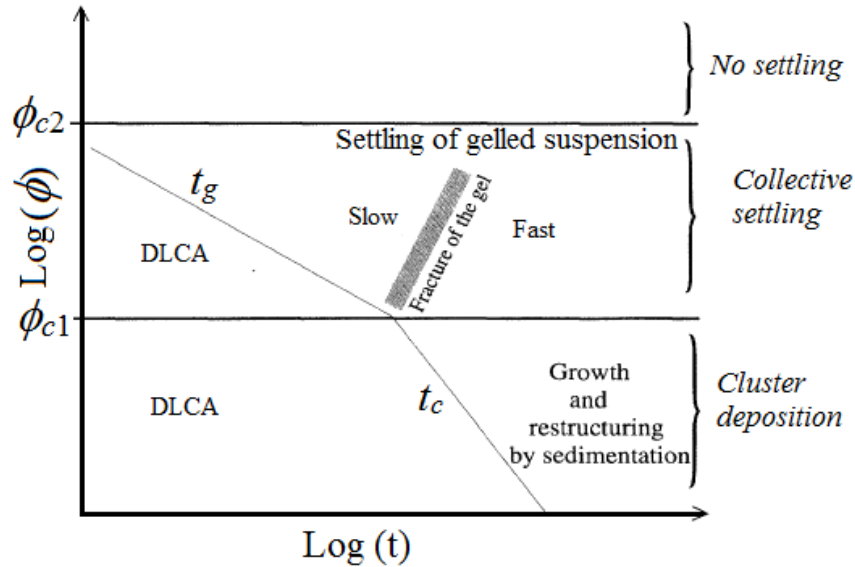


FIGURE 1.6: Sedimentation state diagram in the plane of volume fraction (ϕ) and age t of an aqueous suspension of calcium carbonate particles of average diameter 70 nm. t_g is the gelation time and t_c is the time-scale associated with cluster diffusion. This figure is reproduced from [105].

which is very relevant to the present thesis work. In the presence of attractive interactions, both the Brownian and non-Brownian particles exhibit interesting stability behaviors which depend on the particle concentrations and attractive strength [106]. Brownian particles in a suspension which were stable initially can sediment under gravity due to cluster formation [107–109]. Fig. 1.6 shows a stability state diagram in the plane of volume fraction ϕ and age t which is defined as the time since the loading of the sample in the sedimentation cell. This diagram describes the common stability behaviors of attractive particles in suspensions [105]. The coupling between aggregation and sedimentation leads to an interesting stability behavior of suspensions of attractive particles. The state diagram is divided into three regimes along the concentration (ϕ) axis as follows:

(1) Cluster regime ($\phi < \phi_{c1}$): At particle concentrations below a critical gelation concentration, ϕ_{c1} , particles exhibit diffusion limited cluster aggregation (DLCA) under the influence of attractive interactions [110]. The cluster sizes increase with increasing ϕ and t . The time scale, t_c , associated with cluster sedimentation process

decreases with decrease in cluster size. When $t < t_c$, the suspension exhibit DLCA without sedimentation. For $t > t_c$, clusters sediment under gravity and coagulate further during the sedimentation process [111].

(2) Slow and weak gelation regime ($\phi_{c1} < \phi < \phi_{c2}$): In this concentration regime, clusters rearrange with time to form a volume-spanning gel network with weak connectivity. The time scale, t_g , associated with the complete gel formation decreases with the increasing ϕ [105]. When $t < t_g$, the suspensions contain diffusing clusters. On the other hand, for $t > t_g$, weak gels are formed which collapse collectively under gravity with a clear liquid-water interface. Due to emergence of elasticity in the system after gelation, fractures in a sedimenting gel may also occur during the collapse process [112]. The rearrangements during the aging of weak colloidal gels can have dramatic consequence on their stability behaviors. Weakly aggregating colloidal gels can show delayed sedimentation. Such gels remain stable for a finite delay time before showing transient collapse under gravity. This phenomenon has been widely studied in polymer-mediated depletion gels during the last two decades [113–117]. However, the origin of such behavior is still poorly understood. It is argued that colloidal particles undergo rearrangements facilitated by thermal fluctuations with age. This process leads to the gradual formation of a gel with heavier network strands. The gel then starts collapsing when its local yield stresses are overcome by the gravitation stresses [115, 118, 119].

(3) Fast and strong gelation regime ($\phi > \phi_{c2}$): Particles form a volume spanning network with strong connectivity immediately after sample preparation. These gels do not sediment as the local yield stresses of the gel are always higher than the gravitational stresses [120].

For this thesis work, we have used shape and charge anisotropic colloidal clays such as Laponite and Na-montmorillonite. In aqueous suspensions, the clay particles bear anisotropic electrical double layers (EDLs) on their surfaces. Aqueous suspensions of these clay particles are excellent model systems to understand the phase and

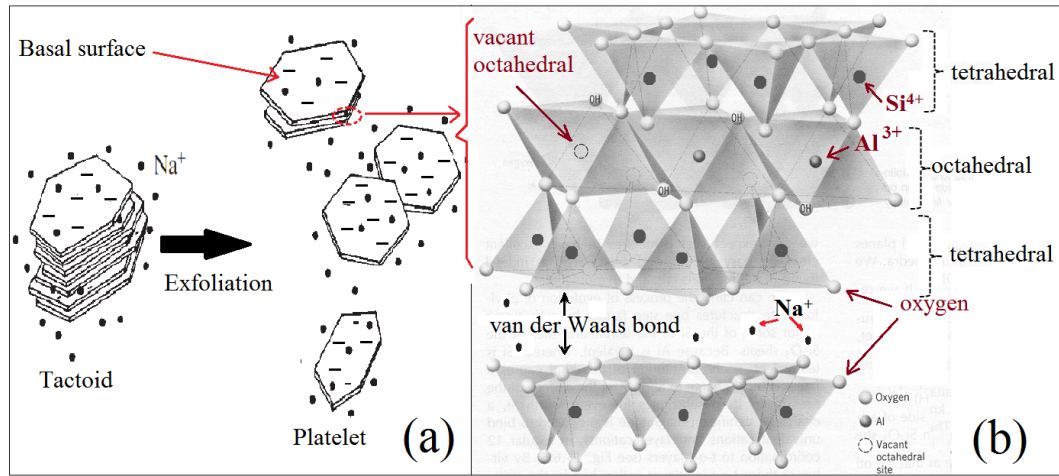


FIGURE 1.7: (a) Schematic diagram of Na-montmorillonite tactoid exfoliation in an aqueous medium. This figure is adapted from [34]. (b) Schematic diagram showing a 2:1 crystalline structure of Na-montmorillonite platelet. The figure is adapted from [128].

rheological behaviors of suspensions of charged anisotropic particles [121, 122]. Besides their use for fundamental studies, aqueous suspensions of clay minerals have diverse technological applications such as in oil-bore drilling [123], cosmetics and personal products, in health and food products as stabilizers [124–126], and in non-drip paints [127] due to their spontaneous aging, yielding and shear thinning properties. The structures of these clay particles, and the complex phases and rheological behaviors of their aqueous suspensions are described briefly in the following sections.

1.6 Structure of a clay particle

Clay minerals are excellent model systems to study the phase behavior of anisotropic, charged colloidal particles [46, 76, 129–135]. Clay minerals, or ‘clays’ in short, belong to the phyllosilicate group having ‘leafy’ or layered structures (Fig. 1.7)(a). There is a great diversity in the structures and compositions of naturally available clays. Clay minerals such as kaolinite, illite, bidellite, mica and saponite are naturally available in abundance in nature [136]. The two particular clays we have used as model systems in this thesis work are Na-montmorillonite and Laponite. Na-montmorillonite

is a naturally available clay mineral extracted from volcanic ash while Laponite is a synthetic designer clay. These clays are also known as smectites and are characterized by 2:1 phyllosilicate structures. A unit phyllosilicate layer, known as a platelet, consists of an aluminum octahedral (AlO_6) sheet sandwiched between two tetrahedral silica (SiO_6) sheets (Fig. 1.7)(b). The oxide anions at the apices of the tetrahedral subunits are directed inward where they are surrounded by the interior aluminum atoms, thereby forming the octahedral subunits of the octahedral layers. The bonding between the interior oxide anions and the cations in both the tetrahedral and the octahedral layers link the sub-layers together forming a unit layer with thickness of approximately 0.96 nm. The lateral size of the Na-montmorillonite unit layer (platelet) may vary from a few tens of nanometers to several micrometers and displays the unique sheet/lamellar structure characteristic of clay samples [137, 138]. These platelets carry permanent negative charges on their surfaces (known as basal planes) due to the isomorphous substitution of some of the Al ions in the octahedral layer by Mg and Fe ions. The idealized formula of this mineral when Al ions are replaced by Mg ions is $\text{Na}_x^+[(\text{Al}_{2-x}\text{Mg}_x)\text{Si}_4\text{O}_{10}(\text{OH})\cdot n\text{H}_2\text{O}]^-$ [136]. Natural clays have both octahedral and tetrahedral substitution and this plays a vital role in unit layer interactions, orientation and swelling. The heterogeneity of the basal surface charge distribution on clay sheets due to random isomorphous substitution results in very complex arrangements of sheets in its dry form as well as in aqueous suspension. The total negative charge on these surfaces is compensated by exchangeable sodium counterions localized in the interlamellar spaces between two successive sheets. The van der Waals interactions between unit layers lead to a disordered stacking of the sheets containing counterions and adsorbed layers of water molecules from the ambient environment. One monolayer of water molecules in the intercalated space corresponds to a c-spacing of 1.25 nm. These stacks of clay sheets are known as tactoids and occur in different shapes and sizes. In dry powder form, these tactoids associate to form large aggregates or granules. Laponite displays crystalline structures that are very similar to those in Na-montmorillonite with the exception that there are Li ions in the octahedral position in

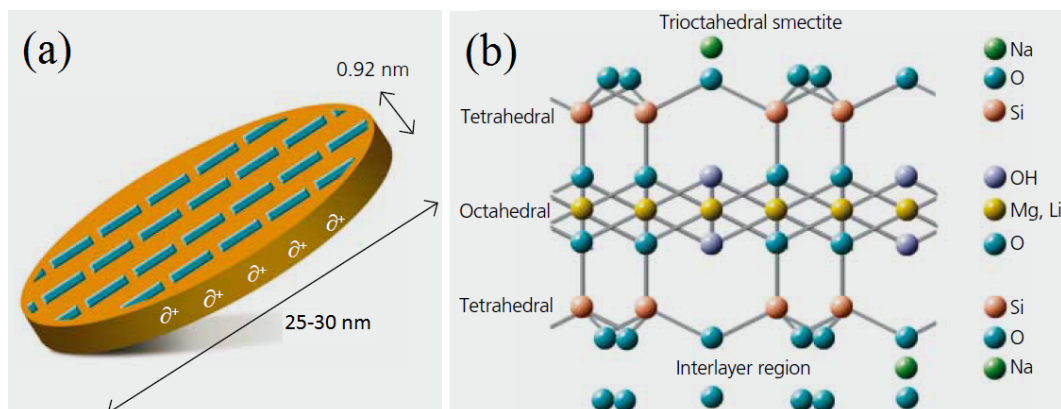


FIGURE 1.8: (a) A single Laponite platelet (b) Schematic diagram showing a 2:1 crystalline structure of Laponite platelet. The figure is adapted from [126].

its unit layer structures as shown in Fig. 1.8(b). Mg ions replace some of the Li ions isomorphically leading to negative charges on the basal surfaces [139]. The structural formula of Laponite clay is $\text{Na}^{+0.7}[\text{Si}_8\text{Mg}_{5.5}\text{Li}_{0.3}\text{O}_{20}(\text{OH})_4]^{-0.7}$ [126]. In contrast to the Na-montmorillonite platelets which are flexible, very irregular and polydisperse in their sizes and shapes, the Laponite platelets are rigid, have very regular circular disc shape and are almost monodisperse (sizes between 25 – 30 nm) [140].

1.7 Swelling and exfoliation of clays

When dry clay granules are added in water, the clay tactoids swell and exfoliate due to the absorption of water in the intercalated spaces. Two main mechanisms are found to be responsible for the tactoid swelling process, namely, crystalline swelling and osmotic swelling [141]. In the process of crystalline swelling, water molecules hydrate the Na^+ counterions as well as silicate layers. The affinity of water molecules to the negatively charged silicate sites is higher than its affinity to the counterions. As a result, water molecules get adsorbed layer by layer on the silicate basal surfaces, thereby increasing the interlayer distance. This process is very fast. The next step involves the hydration of Na^+ counterions by the excess water molecules inside the intercalated space. This leads to high osmotic pressures of the hydrated counterions which diffuse

out of the clay tactoids. This makes the negative basal surfaces repel each other, leading to further separation. The distance between the platelets further increases when the repulsive force between the negatively charged basal surfaces overcomes the interlayer van der Waals attraction. This results in the exfoliation of tactoids into smaller entities [136, 142–144]. Since the hydration of counterions and their subsequent release from the tactoid is diffusion limited, the process of osmotic swelling and the subsequent exfoliation is slower than crystalline swelling and depends on the lateral size of the clay tactoids. Due to the wider lateral sizes of Na-montmorillonite tactoids, their exfoliation process is slower than that for Laponite tactoids.

1.8 Interactions and phase behavior of clay platelets in aqueous suspensions

The knowledge of interactions between the anisotropic clay platelets in aqueous suspensions is very important in understanding their phase transitions and rheological behaviors. As described earlier, a clay platelet has dissimilar charges on their surfaces and edges. At natural pH value (nearly 10 for Laponite and 7-9 for Na-montmorillonite), the edges of a platelet have weak positive charges [139, 145]. Spillover of the negative potential onto the edges is an important aspect of clay platelets. The extent of the spillover depends on the basal surface area. In case of the Na-montmorillonite platelets which have wide lateral size (~ 450 nm), the spillover leads to an effective negative potential on the edges [146]. In contrast, the extent of spillover in the case of a Laponite platelet is negligible due to its much smaller lateral size (~ 30 nm). The addition of salt to the dispersing medium leads to the screening of the negative charges on the basal surfaces of clay particles, which, in turn, decreases the spillover effect substantially. Furthermore, a decrease in the pH below the natural pH value increases the number of positive edge charges. This, in turn, leads to an effective positive potential on the edges.

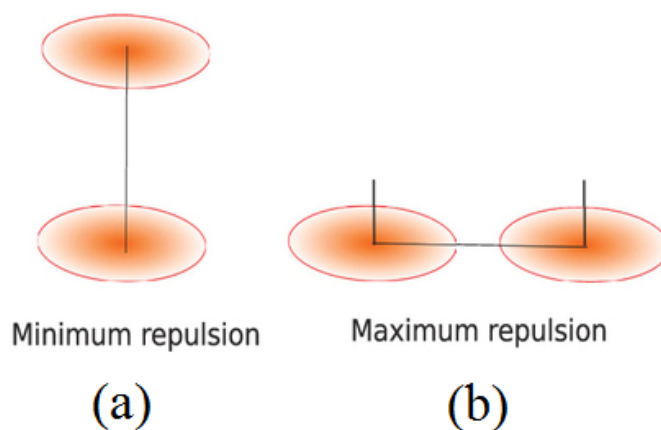


FIGURE 1.9: Two interacting parallel charged platelets in (a) stacked and (b) coplanar configurations correspond to minimum and maximum repulsion, respectively, for an equal center to center distance. The figure is adapted from [147].

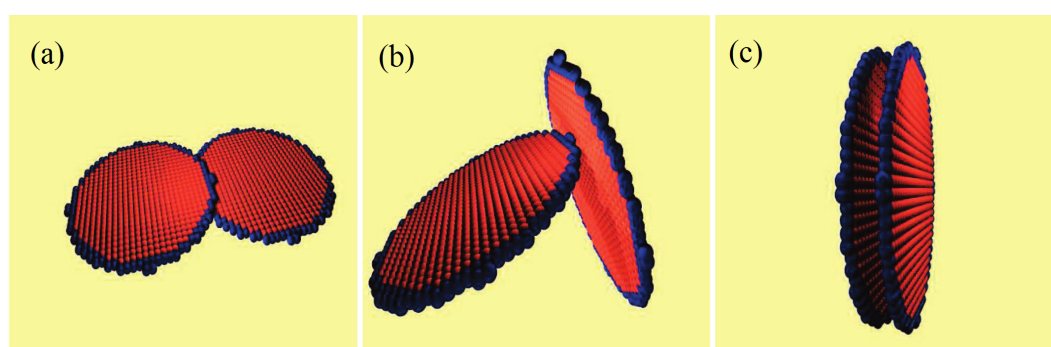


FIGURE 1.10: Associations of two clay platelets with negatively charged faces (indicated by red) and positively charged edges (indicated by blue). (a) Overlapping coins (OC) configuration (b) House of cards configuration (HoC) (c) Face-face stack. The figure is adapted from [148].

Before discussing the collective behavior of clay platelets in suspension, it is very important to understand the interactions and associations (configurations) which minimize the potentials energy between two clay particles at different ionic concentrations and pH values in the medium. Unlike charged spherical colloids, the interaction potential between two clay platelets depends on their mutual orientations and the nature of the edge charges [149]. Many theoretical and simulation studies have been performed to find the equilibrium configuration between two platelets by considering an anisotropic interaction between them for different conditions of surface and edge charges [121, 147, 148, 150]. When the surfaces and the edges have negative potentials, the stack configuration (Fig. 1.9 (a)) is favored when compared to the coplanar configuration (Fig. 1.9 (b)) for an equal center to center distance [147]. The clay particles can make attractive bonds when the edges have positive potential at low pH and in the presence of salt. Different configurations for attractive bond formation are possible depending on the degree of screening of the basal negative charges under the condition of equal density of charges on the edges and basal surfaces [148]. The overlapping coin (OC) configuration is found to be favorable for low screening of the basal negative charges by low concentrations of salt which slightly exposes the positive edges [148]. In the OC configuration, the positive edge of a platelet attaches to the negative basal surface near the edge of another platelet in a parallel fashion (Fig. 1.10(a)). At intermediate salt concentrations, where negative charges are screened further, the house of cards (HoC) configuration is most favorable. In this configuration, the positive edge of a platelet attaches attractively to the central negative part of the basal surface of another platelet (Fig. 1.10(b)). At very high salt concentrations, the basal negative charges get completely screened. The van der Waals attraction dominates in this situation, resulting in face-face stack formation (Fig. 1.10(c)). Such transitions between different configurations occur smoothly with increasing salt concentration.

In a suspension with many clay particles, pure OC, HoC or stack configurations are not observed. However, one of these configurations dominates depending on the clay and salt concentrations [151]. In the last few decades, aqueous suspensions of

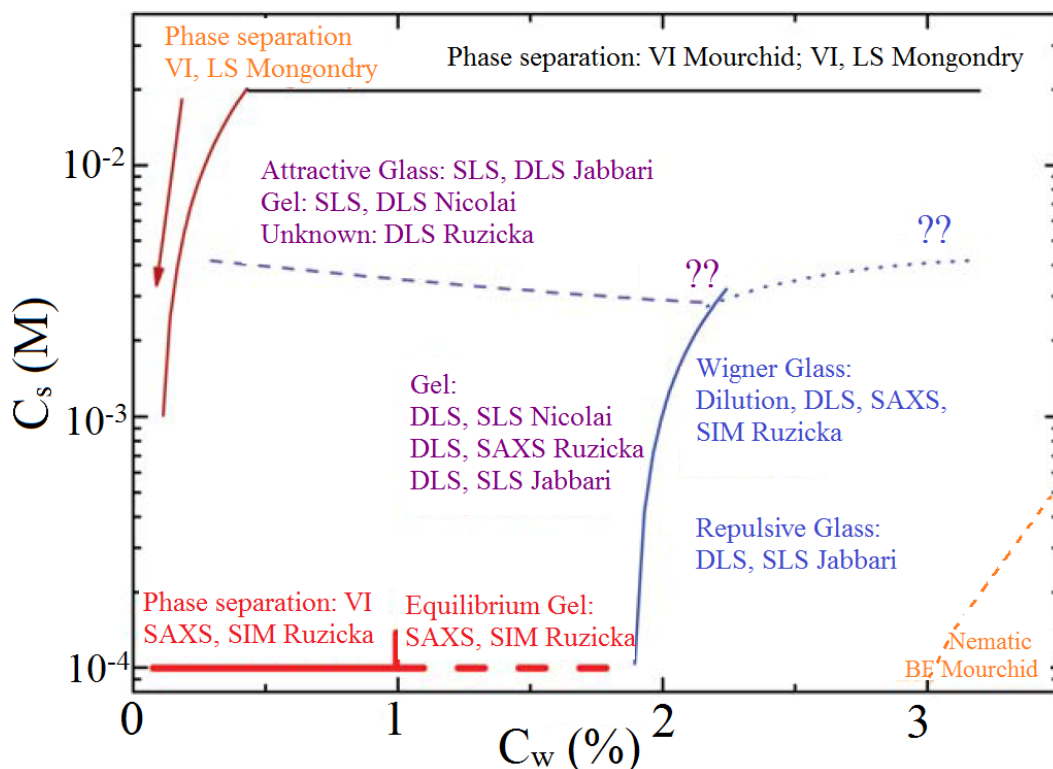


FIGURE 1.11: Phase diagram of Laponite suspensions proposed in a recent review article by Ruzicka *et al.* [131] with data from several previous studies obtained using different methods for large waiting times. In the figure, VI, LS, SLS, DLS, SAXS and SIM refer to visual inspection, light scattering, static light scattering, dynamic light scattering, small angle X-ray scattering and numerical simulations respectively. Details of the other references mentioned in the figure can be found in [131].

Laponite and Na-montmorillonite have been studied in great detail and various phases such as gels, glasses and nematic phase have been reported in the literature [14, 30, 46, 104, 129, 131, 135, 142, 147, 152–156]. In the gel phase, clay particles form a volume spanning network through attractive bond formation between particles. In the glass phase, clay particles remain self-suspended and are stabilized by screened Coulomb repulsions [129].

Recently, Ruzicka *et al.* presented a revised phase diagram (Fig. 1.11) for Laponite clay suspensions in a study that was based on previously reported results [131]. The phase diagram reports the behavior of Laponite suspensions for large waiting times after sample preparation. Initial studies by Ruzicka and coworkers using dynamic light scattering (DLS), small angle X-ray scattering (SAXS), simulations and dilution

methods show that salt-free Laponite suspensions have gel-like morphology for concentration $C_w < 1.8$ wt% and repulsive glass-like or a Wigner glass structure stabilized by repulsions between particles at higher concentrations [157–159]. Further investigations by Ruzicka and coworkers show that salt-free Laponite suspensions of concentrations $C_w \leq 1$ wt% phase separate into clay-rich and clay-poor phases when observed for several years, while suspensions with concentrations $1 \text{ wt}\% < C_w < 1.8 \text{ wt}\%$ give rise to formation of equilibrium gels which remain stable for long times [160].

At higher concentrations $C_w > 1.8$ wt%, repulsions between the clay platelets become significant due to the decrease in the interparticle distances. There is a widespread debate in the literature on whether the platelets remain stabilized by repulsive interactions (repulsive glass) or they reorient with time to form attractive bonds (gel) in this concentration regime [130]. Dilution experiments on seven days old 3 wt% salt-free Laponite suspensions by Ruzicka *et al.* [159] and dynamical investigations using DLS in freshly prepared Laponite suspensions with concentrations in the range 2–3.5% w/v by Saha *et al.* [30] indicate that the influence of edge-face attractive interactions cannot be ignored even at higher clay concentrations. Very recent observations by Ruzicka *et al.* indicate that a repulsive glass phase can exhibit a slow transition to an attractive glass phase in which particles forms aggregates such as disconnected house of card structures [161]. At the highest concentrations explored, formation of a nematic phase is reported in the literature by birefringence studies [162, 163].

Addition of salt to clay suspensions induces attractions between the clay particles. When salt concentration C_s is increased to a value above 1 mM, Laponite suspensions of low concentrations ($C_w < 0.3$ wt%) undergo phase separation with time, while suspensions with higher concentrations form gels [122]. At salt concentration above 20 mM, Laponite suspensions exhibit phase separation [162, 164]. The suspension behavior for $C_s > 3$ mM and $C_w > 2$ wt% is not yet clearly known [131].

Depending on the source, natural Na-montmorillonites have different particle size distributions, surface charge densities and points of zero charge for the positive edges [165]. Due to this reason, the ranges of clay and salt concentrations for the formation

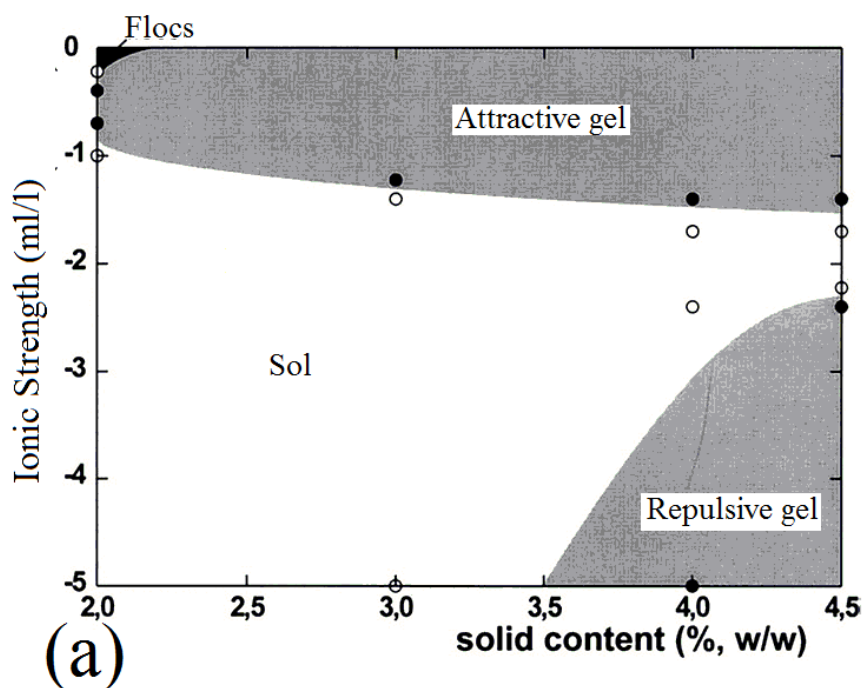


FIGURE 1.12: Phase diagram of Wyoming Na-montmorillonite proposed by Abend and Lagaly [135].

of glass and gel phases in aqueous suspensions vary for Na-montmorillonite obtained from different sources [166]. Fig. 1.12 shows a typical phase diagram of Wyoming Na-montmorillonite proposed by Abend and Lagaly [135], which is qualitatively very similar to the Laponite phase diagram. Some differences arise due to the strong spillover effect of the basal negative potential onto the edge of the platelet [146]. At extremely low ionic strengths (10^{-5} ml/l, no added salt), the clay suspension exists in a sol state upto a clay concentration of 3.5% w/w. Above this, the Na-montmorillonite suspensions exhibit a repulsive gel (Wigner glass) phase stabilized by the repulsive interactions between clay particles. Addition of salt at clay concentrations above 3.5% w/w reduces the interparticle repulsions, resulting in a transition to the sol phase. Such re-entrant behavior can be clearly seen in Fig. 1.12 upto ionic strengths of 0.05 ml/l for a clay concentration of 4.5% w/w. Above ionic strength of 0.1 ml/l, an attractive gel is observed for all clay concentrations. There are several studies showing that Na-montmorillonite platelets undergo nematic ordering in the absence of the salt

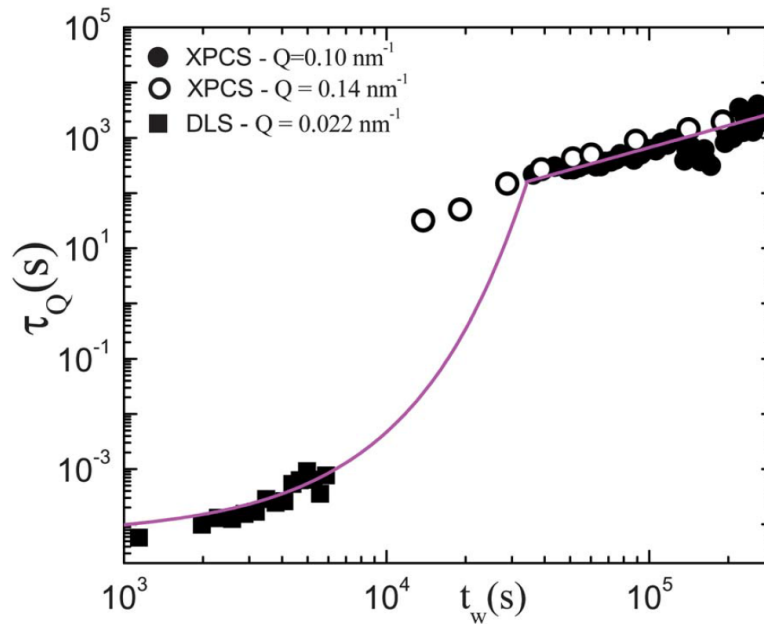


FIGURE 1.13: Evolution of the relaxation time (τ_Q) with age (t_w) of an aqueous Laponite suspension at a concentration of 3.0 wt% measured by dynamic light scattering (DLS) at $Q=0.022 \text{ nm}^{-1}$ (full squares) and X-ray photon correlation spectroscopy (XPCS) at $Q=0.10 \text{ nm}^{-1}$ (full circles). The data obtained using XPCS by Bandyopadhyay *et al.* [64] at the same concentration is also plotted (empty circles). The relaxation times exhibit exponential and power law behaviors with t_w at small and large t_w , respectively. The figure is reproduced from [168].

[104, 154, 167] and at even lower concentrations in the presence of hydrodynamic flow [155] in suspensions in the concentration range of 2 – 3.5% w/w. It should be noted again that the exact concentration range of such behavior strongly depends on the particle sizes and their surface charges [154]. It is argued that such nematic ordering possibly arises due to the presence of negative potentials on the edges of clay platelets, which favors face-face ordering of clay particles (Fig. 1.9) [147].

1.9 Aging and rheological behaviors of clay suspensions

When a clay suspension, initially in a liquid like-state, approaches a glass or a gel phase, the dynamics of the particles slow down with time leading to an increase in its

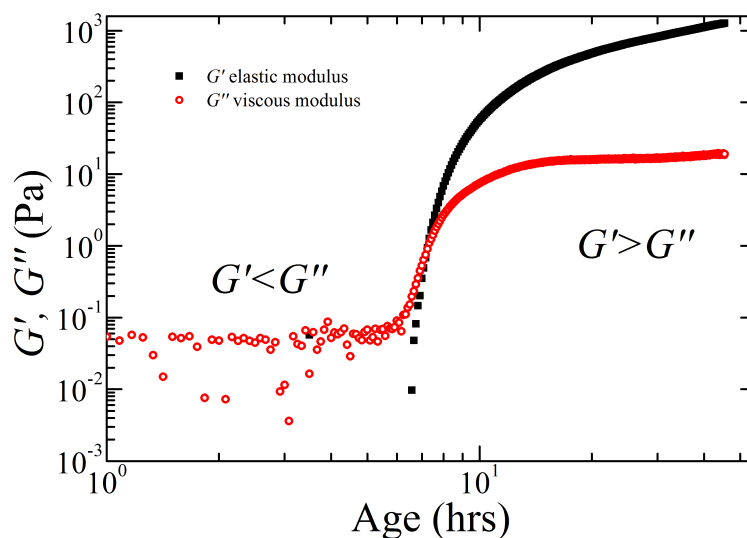


FIGURE 1.14: Evolution of elastic modulus G' and viscous modulus G'' with age of a 3% w/v Laponite clay suspension.

relaxation time. This process is known as physical aging and progresses even in the arrested state. Aging in these systems occurs by the spatially and temporally correlated local rearrangements of particles that can overcome local energy barriers, with the system exploring progressively deeper energy wells in phase space [64, 168–172]. Fig. 1.13 shows the variation of average relaxation time τ_Q with age t_w of Laponite suspensions of concentration 3% w/w [168]. Initially, τ_Q grows almost exponentially with age. At higher ages, the dynamics slow down further and the τ_Q typically shows a power law behavior with t_w [64]. It is believed that the particles trapped in metastable states slowly rearrange to reach the local minima of the complex potential landscape that exist in a concentrated clay suspension [75]. Particles are trapped in cages formed by their neighbors and the rearrangement process occurs through cage diffusion which gives rise to cooperative rearrangement processes over large spatial extents [75]. Saha *et al.* recently established that the inverse of age, t_w , of a clay suspension is equivalent to the temperature, T , of a supercooled liquid that can be quenched to a glassy phase by rapidly decreasing T [46]. This analogy is extremely useful in understanding the glass transition process in supercooled liquids using clay suspension as a model system [30, 173, 174].

Aqueous suspensions of clays exhibit interesting rheological behaviors including thixotropy, yielding, shear thinning and viscoelasticity under different applied stress-strain conditions [135, 175–177]. The aging process, which arises from a combination of the tactoid exfoliation process and the modification of the Debye layers with time due to the diffusion of the exposed Na^+ counterions, has a strong effect on the rheological behavior of the clay suspension [176, 178]. This leads to increase in the viscoelastic moduli with age of a freshly prepared clay suspension as can be seen for 3% w/v Laponite suspension in Fig. 1.14. The clay suspension initially exhibits liquid-like behavior ($G' < G''$). Both the moduli increase with time after an initial quiescent period and show a crossover with further increase of suspension age. The point of crossover defines the apparent transition time to a kinetically arrested phase. Similarly, all other rheological properties of clays such as thixotropy, stress relaxation, creep and shear thinning behaviors become strongly age and shear history dependent [179]. On the application of stresses above a yield value, the elastic and viscous moduli of these soft solids decrease and the suspensions eventually flow like fluids. Once the applied stress is removed, the suspension gradually recovers its jammed state [49, 180].

Kinetically arrested phases of aqueous clay suspensions exhibit soft glassy rheology (Fig. 1.15 (a)) typically observed in colloidal glasses and gels [83]. Fig. 1.15 (a) shows that the elastic modulus G' of the suspension is almost frequency independent and is much larger than the viscous modulus G'' . On the contrary, the G'' values are weakly dependent on the applied shearing frequencies. Fig. 1.15 (b) shows the typical response of a kinetically arrested clay sample under varying amplitudes γ of an oscillatory strain at a constant applied frequency. The range of γ , where the mechanical moduli show constant values, is defined as the linear viscoelastic (LVE) regime. In this regime, G' is much higher than G'' . The LVE regime is followed by a yielding regime above a yield strain γ_y . For $\gamma > \gamma_y$, G' decreases monotonically while G'' shows a peak at γ_p before decreasing monotonically due to the destruction of the sample's microstructures under high strains. The peak almost coincides with the crossover point between G' and G'' after which the suspension goes to a liquid-like state under high

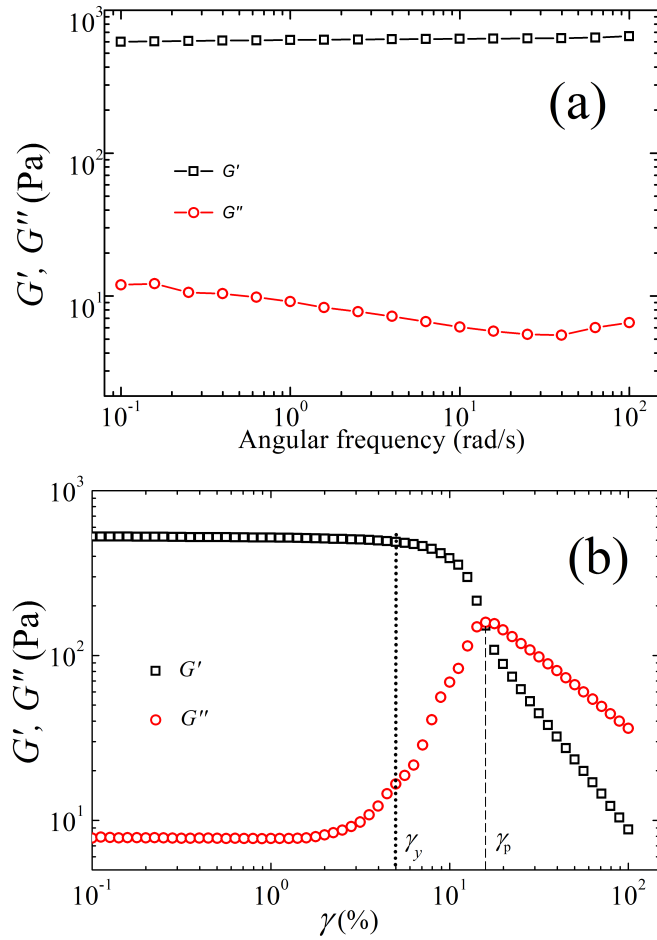


FIGURE 1.15: (a) Variation of elastic modulus G' and loss modulus G'' with applied oscillatory frequency at strain amplitude $\gamma = 0.1\%$. (b) G' and G'' as a function of amplitude γ of an oscillatory strain. The vertical dotted and dashed lines indicate the position of yield strain γ_y and position of γ_p respectively. The position of γ_y is determined following the method described in [181].

strains. Above the crossover point, both moduli decrease following power laws under high applied strains. For the clay suspensions studied here, the different kinetically arrested phases such as glasses and gels exhibit qualitatively similar rheological behavior in their linear regime. It is therefore not easy to distinguish between these two phases using linear rheology [178].

1.10 Thesis organization

The rest of thesis is organized as follows.

The experimental methods and the relevant theory used in this thesis work are briefly described in Chapter 2.

Chapter 3 describes the influence of intertactoid repulsions on the exfoliation kinetics of clay tactoids in aqueous suspensions of the model clay Laponite using ultrasound attenuation spectroscopy (UAS). The presence of incompletely exfoliated tactoids are identified using the Jenning-Parslow relation for the equivalent spherical diameter in a concentration regime where Laponite suspensions exhibit the glass transition.

Chapter 4 reports the existence of incompletely exfoliated clay tactoids in Na-montmorillonite suspensions in a concentration regime below the glass transition concentration using UAS. Further studies of Na-montmorillonite suspensions prepared at different ionic conditions using rheological and conductivity measurements, and electroacoustics confirm the influence of the reverse osmotic pressure of hydrated counterions on the exfoliation process.

In Chapter 5, we establish the link between the nonmonotonic rheological behavior with the underlying microscopic structures of Na-montmorillonite gels at different salt concentrations using rheological methods and cryogenic scanning electron microscopy (cryo-SEM). We show the existence of honeycomb-like network morphologies for a wide range of salt concentrations. The transition of the gel morphology, dominated by overlapping coin (OC) and house of cards (HoC) associations of clay platelets at low salt concentrations, to a new network structure dominated by face-face coagulation

of platelets, is observed across the critical salt concentration. We further assess the stability of these gels under gravity using electroacoustics.

Chapter 6 focuses on the gravitational stability of clay suspensions prepared at different ionic conditions using light transmission, electroacoustics and UAS methods. Transient collapse behavior of clay gels reported in this chapter is further investigated using the rheological method and direct visualization of the underlying microstructures using cryo-SEM.

Chapter 7 deals with the stress relaxation behavior in clay suspensions in their glass and gel phases at varying idle times and sample ages. A transition from a single-step stress relaxation to a two-step relaxation with age of the clay suspension under nonlinear step strains is reported in this chapter.

In Chapter 8, we describe the influence of the initial aggregate size distributions on the aging dynamics of shear-melted clay suspensions. Different aggregate sizes in suspensions are obtained by filtering samples with different flow rates through porous membranes of varying pore sizes. Faster aging dynamics in suspensions with smaller aggregate sizes are observed using rheological measurements.

In chapter 9, a summary of the original results presented in this thesis and the scope of future research is presented.

References

- [1] R. J. Hunter, *Foundations of Colloid Science*, Clarendon Press, Oxford, 1995, vol. I.
- [2] G. L. Hunter and E. R. Weeks, *Reports on Progress in Physics*, 2012, **75**, 066501.
- [3] J. Lyklema, *Fundamentals in Colloid and Interface Science*, Elsevier: Amsterdam, Netherlands, 1991, vol. 1.
- [4] W. B. Russel, D. A. Saville and W. R. Schowalter, *Colloidal dispersions*, Cambridge university press, 1992.
- [5] E. Dickinson and D. J. McClements, *Advances in food colloids*, Springer Science & Business Media, 1995.
- [6] A. R. Hemsley, M. E. Collinson, W. L. Kovach, B. Vincent and T. Williams, *Philosophical Transactions: Biological Sciences*, 1994, **345**, pp. 163–173.
- [7] H. Booij and H. Bungenberg de Jong, in *Biocolloids and their Interactions*, Springer Vienna, 1956, vol. 1 / 2, pp. 3–7.
- [8] O. Kruglova, P.-J. Demeyer, K. Zhong, Y. Zhou and K. Clays, *Soft Matter*, 2013, **9**, 9072–9087.

-
- [9] D. Genovese, J. Lozano and M. A. Rao, *Journal of Food Science*, 2007, **72**, R11–R20.
- [10] H. N. Lekkerkerker and R. Tuinier, *Colloids and the depletion interaction*, Springer, 2011, vol. 833.
- [11] G. E. Uhlenbeck and L. S. Ornstein, *Physical Review*, 1930, **36**, 823.
- [12] H. Tanaka, J. Meunier and D. Bonn, *Physical Review E*, 2004, **69**, 031404.
- [13] L. Berthier, G. Biroli, J.-P. Bouchaud, L. Cipelletti, D. El Masri, D. L'Hôte, F. Ladieu and M. Pierno, *Science*, 2005, **310**, 1797–1800.
- [14] D. van der Beek, P. B. Radstake, A. V. Petukhov and H. N. W. Lekkerkerker, *Langmuir*, 2007, **23**, 11343–11346.
- [15] S. C. Glotzer and M. J. Solomon, *Nature Materials*, 2007, **6**, 557 – 562.
- [16] Y. Wang, Y. Wang, D. R. Breed, V. N. Manoharan, L. Feng, A. D. Hollingsworth, M. Weck and D. J. Pine, *Nature*, 2012, **491**, 51–55.
- [17] P. Varadan, and M. J. Solomon, *Langmuir*, 2003, **19**, 509–512.
- [18] E. R. Weeks, J. C. Crocker, A. C. Levitt, A. Schofield and D. A. Weitz, *Science*, 2000, **287**, 627–631.
- [19] M. J. Solomon and P. T. Spicer, *Soft Matter*, 2010, **6**, 1391–1400.
- [20] P. C. Hiemenz and R. Rajagopalan, *Principles of Colloid and Surface Chemistry, revised and expanded*, CRC press, 1997, vol. 14.
- [21] B. V. Derjaguin and L. Landau, *Acta Physicochimica USSR*, 1941, **14**, 633–662.
- [22] E. Verwey and J. Overbeek, *Theory of Stability of Lyophobic Colloids*, Elsevier: Amsterdam, Netherlands, 1948.
- [23] A. Stone, *The theory of intermolecular forces*, Oxford University Press, 2013.

- [24] D. J. Griffiths, *Introduction to electrodynamics*, Prentice-Hall, 1999.
- [25] F. London, *Transactions of the Faraday Society*, 1937, **33**, 8b–26.
- [26] H. Hamaker, *Physica*, 1937, **4**, 1058–1072.
- [27] M. W. Cole, D. Velegol, H.-Y. Kim and A. A. Lucas, *Molecular Simulation*, 2009, **35**, 849–866.
- [28] J. Israelachvili, V. Degiorgio and M. Corti, *Proceedings of the International School of Physics ÔEnrico FermiÕ (Societa Italiana di Fisica), North-Holland, Amsterdam*, 1985, 24.
- [29] H. van Olphen, *John Wiley and Sons Inc.: New York*, 1977, **53**, 230–230.
- [30] D. Saha, R. Bandyopadhyay and Y. M. Joshi, *Langmuir*, 2015, **31**, 3012–3020.
- [31] E. M. Lee and L. K. Koopal, *Journal of Colloid and Interface Science*, 1996, **177**, 478 – 489.
- [32] K. Marinova, R. Alargova, N. Denkov, O. Velev, D. Petsev, I. Ivanov and R. Borwankar, *Langmuir*, 1996, **12**, 2045–2051.
- [33] G. Sposito, N. T. Skipper, R. Sutton, S.-h. Park, A. K. Soper and J. A. Greathouse, *Proceedings of the National Academy of Sciences*, 1999, **96**, 3358–3364.
- [34] G. Lagaly and S. Ziesmer, *Advances in Colloid and Interface Science*, 2003, **100-102**, 105 – 128.
- [35] X. Yin, V. Gupta, H. Du, X. Wang and J. D. Miller, *Advances in colloid and interface science*, 2012, **179**, 43–50.
- [36] L. H. Allen and E. Matijevic, *Journal of Colloid and Interface Science*, 1970, **33**, 420–429.

- [37] C. A. Bunton, F. Nome, F. H. Quina and L. S. Romsted, *Accounts of chemical research*, 1991, **24**, 357–364.
- [38] Dauchot, Olivier and Bertin, Eric, *European Physical Journal E*, 2014, **37**, 31.
- [39] C. A. Angell, *Science*, 1995, **267**, 1924–1935.
- [40] P. G. Debenedetti and F. H. Stillinger, *Nature*, 2001, **410**, 259–267.
- [41] M. D. Ediger, *Annual review of physical chemistry*, 2000, **51**, 99–128.
- [42] V. Novikov and A. Sokolov, *Nature*, 2004, **431**, 961–963.
- [43] M. Ediger and P. Harrowell, *The Journal of chemical physics*, 2012, **137**, 080901.
- [44] P. Pusey and R. Tough, in *Dynamic light scattering*, Springer, 1985, pp. 85–179.
- [45] E. R. Weeks and D. Weitz, *Chemical physics*, 2002, **284**, 361–367.
- [46] D. Saha, Y. M. Joshi and R. Bandyopadhyay, *Soft Matter*, 2014, **10**, 3292–3300.
- [47] S. Gokhale, K. H. Nagamanasa, R. Ganapathy and A. Sood, *Nature communications*, 2014, **5**, 4685(1)–4685(7).
- [48] A. M. Puertas and T. Voigtmann, *Journal of Physics: Condensed Matter*, 2014, **26**, 243101.
- [49] Y. M. Joshi, *Annual review of chemical and biomolecular engineering*, 2014, **5**, 181–202.
- [50] P. Pusey and W. Van Megen, *Nature*, 1986, **320**, 340–342.
- [51] P. N. Pusey and W. van Megen, *Physical Review Letters*, 1987, **59**, 2083–2086.
- [52] J. D. Bernal, *Proceedings of the Royal Society of London. Series A, Mathematical and Physical Sciences*, 1964, 299–322.

-
- [53] P. Pusey, E. Zaccarelli, C. Valeriani, E. Sanz, W. C. Poon and M. E. Cates, *Philosophical Transactions of the Royal Society of London A: Mathematical, Physical and Engineering Sciences*, 2009, **367**, 4993–5011.
- [54] T. T. M. Torquato S and P. G. Debenedetti, *Physical Review Letters*, 2000, **84**, 2064–2067.
- [55] M. Fasolo and P. Sollich, *Physical Review Letters*, 2003, **91**, 068301.
- [56] J. Hernández-Guzmán and E. R. Weeks, *Proceedings of the National Academy of Sciences*, 2009, **106**, 15198–15202.
- [57] A.-P. Hynninen and M. Dijkstra, *Physical Review E*, 2003, **68**, 021407.
- [58] W. Härtl, *Current opinion in colloid & interface science*, 2001, **6**, 479–483.
- [59] T. M. Truskett, S. Torquato, S. Sastry, P. G. Debenedetti and F. H. Stillinger, *Physical Review E*, 1998, **58**, 3083–3088.
- [60] E. Brown, H. Zhang, N. A. Forman, B. W. Maynor, D. E. Betts, J. M. DeSimone and H. M. Jaeger, *Physical Review E*, 2011, **84**, 031408.
- [61] M. Dijkstra, *Advances in Chemical Physics*, *Advances in Chemical Physics*, 2014, **156**, 35.
- [62] J. A. C. Veerman and D. Frenkel, *Physical Review A*, 1992, **45**, 5632–5648.
- [63] M. Marechal, A. Cuetos, B. Martinez-Haya and M. Dijkstra, *The Journal of Chemical Physics*, 2011, **134**, –.
- [64] R. Bandyopadhyay, D. Liang, H. Yardimci, D. A. Sessoms, M. A. Borthwick, S. G. J. Mochrie, J. L. Harden and R. L. Leheny, *Physical Review Letters*, 2004, **93**, 228302.
- [65] K. Kang and J. K. G. Dhont, *Physical Review Letters*, 2013, **110**, 015901.

-
- [66] M. Delhorme, B. Jönsson and C. Labbez, *RSC Advances*, 2014, **4**, 34793–34800.
- [67] V. Trappe, V. Prasad, L. Cipelletti, P. Segre and D. Weitz, *Nature*, 2001, **411**, 772–775.
- [68] A. J. Liu and S. R. Nagel, *Nature*, 1998, **396**, 21–22.
- [69] W.-H. Shih, W. Y. Shih, S.-I. Kim, J. Liu and I. A. Aksay, *Physical Review A*, 1990, **42**, 4772–4779.
- [70] L. Cipelletti, S. Manley, R. C. Ball and D. A. Weitz, *Physical Review Letters*, 2000, **84**, 2275–2278.
- [71] D. Weitz and M. Oliveria, *Physical Review Letters*, 1984, **52**, 1433.
- [72] A. Fall, N. Huang, F. Bertrand, G. Ovarlez and D. Bonn, *Physical Review Letters*, 2008, **100**, 018301.
- [73] B. Abou, D. Bonn and J. Meunier, *Physical Review E*, 2001, **64**, 021510.
- [74] P. Sollich, *Physical Review E*, 1998, **58**, 738–759.
- [75] D. Bonn, H. Tanaka, G. Wegdam, H. Kellay and J. Meunier, *EPL (Europhysics Letters)*, 1999, **45**, 52.
- [76] Y. M. Joshi, *The Journal of Chemical Physics*, 2007, **127**, 081102(1)–081102(5).
- [77] R. C. Kramb and C. F. Zukoski, *Journal of Physics: Condensed Matter*, 2011, **23**, 035102.
- [78] E. Zaccarelli and W. C. K. Poon, *Proceedings of the National Academy of Sciences*, 2009, **106**, 15203–15208.
- [79] P. N. Segrè, V. Prasad, A. B. Schofield and D. A. Weitz, *Physical Review Letters*, 2001, **86**, 6042–6045.

-
- [80] R. G. Larson, *The structure and rheology of complex fluids*, Oxford University Press, Oxford, 1999.
- [81] C. W. Macosko and R. G. Larson, *Rheology: principles, measurements, and applications*, VCH New York, 1994.
- [82] K. Miyazaki, H. M. Wyss, D. A. Weitz and D. R. Reichman, *EPL (Europhysics Letters)*, 2006, **75**, 915–921.
- [83] P. Sollich, F. Lequeux, P. Hébraud and M. E. Cates, *Physical Review Letters*, 1997, **78**, 2020–2023.
- [84] J.-P. Bouchaud, *Journal de Physique I*, 1992, **2**, 1705–1713.
- [85] H. Walls, S. B. Caines, A. M. Sanchez and S. A. Khan, *Journal of Rheology (1978-present)*, 2003, **47**, 847–868.
- [86] J. R. Stokes and W. J. Frith, *Soft Matter*, 2008, **4**, 1133–1140.
- [181] M. Laurati, S. U. Egelhaaf and G. Petekidis, *Journal of Rheology (1978-present)*, 2011, **55**, 673–706.
- [88] G. Yin and M. J. Solomon, *Journal of Rheology (1978-present)*, 2008, **52**, 785–800.
- [89] S. Ramaswamy, *Advances in Physics*, 2001, **50**, 297–341.
- [90] J. Padding and A. Louis, *Physical Review Letters*, 2004, **93**, 220601.
- [91] M. Von Smoluchowski, *Annalen der physik*, 1906, **326**, 756–780.
- [92] F. Laird, *The Journal of Physical Chemistry*, 1927, **31**, 1034–1049.
- [93] J. Perrin, *Annals of Chemistry and Physics*, 1851, **18(8)**, .
- [94] E. F. Burton, *The physical properties of colloidal solutions*, Longmans, Green, 1921.

-
- [95] G. G. Stokes, *Trans. Cambridge Philos. Soc.*, 1851, **9**, year.
- [96] A. J. Ladd, *Physical Review Letters*, 1996, **76**, 1392.
- [97] P. N. Segrè, E. Herbolzheimer and P. M. Chaikin, *Physical Review Letters*, 1997, **79**, 2574–2577.
- [98] J. T. Padding and A. A. Louis, *Physical Review E*, 2008, **77**, 011402.
- [99] P. Snabre, B. Pouligny, C. Metayer and F. Nadal, *Rheologica Acta*, 2009, **48**, 855–870.
- [100] S.-Y. Tee, P. J. Mucha, L. Cipolletti, S. Manley, M. P. Brenner, P. N. Segre and D. A. Weitz, *Physical Review Letters*, 2002, **89**, 054501.
- [101] C. G. Serrano, J. J. McDermott and D. Velegol, *Nature materials*, 2011, **10**, 716–721.
- [102] M. Kohl and M. Schmiedeberg, *Soft matter*, 2014, **10**, 4340–4347.
- [103] M. Leocmach, C. P. Royall and H. Tanaka, *EPL (Europhysics Letters)*, 2010, **89**, 38006.
- [104] E. Paineau, A. Philippe, K. Antonova, I. Bihannic, P. Davidson, I. Dozov, J. Gabriel, M. Imperor-Clerc, P. Levitz, F. Meneau and L. Michot, *Liquid Crystals Reviews*, 2013, **1**, 110–126.
- [105] C. Allain, M. Cloitre and M. Wafra, *Physical Review Letters*, 1995, **74**, 1478–1481.
- [106] A. Moncho-Jordá, A. Louis and J. Padding, *Physical Review Letters*, 2010, **104**, 068301.
- [107] J. S. Abel, G. C. Stangle, C. H. Schilling and I. A. Aksay, *Journal of materials research*, 1994, **9**, 451–461.

-
- [108] J. K. Whitmer and E. Luijten, *The Journal of chemical physics*, 2011, **134**, 034510.
- [109] A. Moncho-Jordá, A. Louis and J. Padding, *The Journal of chemical physics*, 2012, **136**, 064517.
- [110] P. Meakin, *Physical Review Letters*, 1983, **51**, 1119.
- [111] H. Wu, M. Lattuada, P. Sandkühler, J. Sefcik and M. Morbidelli, *Langmuir*, 2003, **19**, 10710–10718.
- [112] A. A. Potanin and W. B. Russel, *Physical Review E*, 1996, **53**, 3702–3709.
- [113] W. Poon, J. Selfe, M. Robertson, S. Ilett, A. Pirie and P. Pusey, *Journal de Physique II*, 1993, **3**, 1075–1086.
- [114] W. C. Poon, L. Starrs, S. Meeker, A. Moussaid, R. M. Evans, P. Pusey and M. Robins, *Faraday Discussions*, 1999, **112**, 143–154.
- [115] S. Manley, J. M. Skotheim, L. Mahadevan and D. A. Weitz, *Physical Review Letters*, 2005, **94**, 218302.
- [116] S. W. Kamp and M. L. Kilfoil, *Soft Matter*, 2009, **5**, 2438–2447.
- [117] R. Buscall, T. H. Choudhury, M. A. Faers, J. W. Goodwin, P. A. Luckham and S. J. Partridge., *Soft Matter*, 2009, **5**, 1345–1349.
- [118] M. L. Kilfoil, E. E. Pashkovski, J. A. Masters and D. A. Weitz, *Philosophical Transactions of the Royal Society of London A: Mathematical, Physical and Engineering Sciences*, 2003, **361**, 753–766.
- [119] P. Bartlett, L. J. Teece and M. A. Faers, *Physical Review E*, 2012, **85**, 021404.
- [120] T. Tanaka, *Physical Review Letters*, 1978, **40**, 820.
- [121] E. Trizac, L. Bocquet, R. Agra, J.-J. Weis and M. Aubouy, *Journal of Physics: Condensed Matter*, 2002, **14**, 9339.

-
- [122] P. Mongondry, J. F. Tassin and T. Nicolai, *Journal of Colloid and Interface Science*, 2005, **283**, 397 – 405.
- [123] R. Anderson, I. Ratcliffe, H. Greenwell, P. Williams, S. Cliffe and P. Coveney, *Earth-Science Reviews*, 2010, **98**, 201 – 216.
- [124] J. Wang, F. Yang, J. Tan, G. Liu, J. Xu and D. Sun, *Langmuir*, 2010, **26**, 5397–5404.
- [125] C. Viseras, C. Aguzzi, P. Cerezo and A. Lopez-Galindo, *Applied Clay Science*, 2007, **36**, 37 – 50.
- [126] *Datasheet of Laponite*, Byk additives and instruments technical report, (Last accessed on 04th May 2015).
- [127] H. H. Murray, *Applied Clay Science*, 2000, **17**, 207 – 221.
- [128] *Nanocor Inc. Technical data sheet*, Nanocor Inc. Technical data sheet G-105, (Last accessed on 22nd February 2015).
- [129] D. Bonn, H. Kellay, H. Tanaka, G. Wegdam and J. Meunier, *Langmuir*, 1999, **15**, 7534–7536.
- [130] S. Jabbari-Farouji, H. Tanaka, G. H. Wegdam and D. Bonn, *Physical Review E*, 2008, **78**, 061405.
- [131] B. Ruzicka and E. Zaccarelli, *Soft Matter*, 2011, **7**, 1268–1286.
- [132] M. S. Zbik, D. J. Williams, Y.-F. Song and C.-C. Wang, *Journal of Colloid and Interface Science*, 2014, **435**, 119 – 127.
- [133] P. F. Luckham and S. Rossi, *Advances in Colloid and Interface Science*, 1999, **82**, 43 – 92.
- [134] B. Benazzouz and A. Zaoui, *Physica B: Condensed Matter*, 2012, **407**, 2462–2470.

- [135] S. Abend and G. Lagaly, *Applied Clay Science*, 2000, **16**, 201 – 227.
- [136] F. Bergaya and G. Lagaly, in *Handbook of Clay Science*, ed. F. Bergaya and G. Lagaly, Elsevier, 2013, vol. 5, pp. 1 – 19.
- [137] H. V. Olphen, *Journal of Colloid Science*, 1962, **17**, 660 – 667.
- [138] Y. Zheng and A. Zaoui, *Solid State Ionics*, 2011, **203**, 80 – 85.
- [139] S. L. Tawari, D. L. Koch and C. Cohen, *Journal of Colloid and Interface Science*, 2001, **240**, 54 – 66.
- [140] M. Kroon, G. H. Wegdam and R. Sprik, *Physical Review E*, 1996, **54**, 6541–6550.
- [141] D. A. Laird, *Applied Clay Science*, 2006, **34**, 74 – 87.
- [142] J. D. F. Ramsay, S. W. Swanton and J. Bunce, *Journal of Chemical Society, Faraday Transactions*, 1990, **86**, 3919–3926.
- [143] S. Ali and R. Bandyopadhyay, *Langmuir*, 2013, **29**, 12663–12669.
- [144] S. Ali and R. Bandyopadhyay, *Applied Clay Science*, 2015, **114**, 85–92.
- [145] M. Kosmulski, *Journal of Colloid and Interface Science*, 2009, **337**, 439–448.
- [146] R. Secor and C. Radke, *Journal of Colloid and Interface Science*, 1985, **103**, 237 – 244.
- [147] S. Jabbari-Farouji, J.-J. Weis, P. Davidson, P. Levitz and E. Trizac, *Scientific reports*, 2013, **3**, 1–6.
- [148] B. Jonsson, C. Labbez and B. Cabane, *Langmuir*, 2008, **24**, 11406–11413.
- [149] R. Agra, E. Trizac and L. Boucquet, *European Physical Journal E*, 2004, **15**, 345–357.

- [150] S. Jabbari-Farouji, J.-J. Weis, P. Davidson, P. Levitz and E. Trizac, *The Journal of Chemical Physics*, 2014, **141**, 224510.
- [151] M. Delhorme, B. Jonsson and C. Labbez, *Soft Matter*, 2012, **8**, 9691–9704.
- [152] J. M. Saunders, J. W. Goodwin, R. M. Richardson and B. Vincent, *The Journal of Physical Chemistry B*, 1999, **103**, 9211–9218.
- [153] I. Bihannic, L. J. Michot, B. S. Lartiges, D. Vantelon, J. Labille, F. Thomas, J. Susini, M. Salome and B. Fayard, *Langmuir*, 2001, **17**, 4144–4147.
- [154] L. J. Michot, I. Bihannic, K. Porsch, S. Maddi, C. Baravian, J. Mougel and P. Levitz, *Langmuir*, 2004, **20**, 10829–10837.
- [155] L. J. Michot, I. Bihannic, S. Maddi, C. Baravian, P. Levitz and P. Davidson, *Langmuir*, 2008, **24**, 3127–3139.
- [156] R. K. Pujala and H. B. Bohidar, *Soft Matter*, 2012, **8**, 6120–6127.
- [157] B. Ruzicka, L. Zulian and G. Ruocco, *Physical Review Letters*, 2004, **93**, 258301.
- [158] B. Ruzicka, L. Zulian, R. Angelini, M. Sztucki, A. Moussaïd and G. Ruocco, *Physical Review E*, 2008, **77**, 020402.
- [159] B. Ruzicka, L. Zulian, E. Zaccarelli, R. Angelini, M. Sztucki, A. Moussaïd and G. Ruocco, *Physical Review Letters*, 2010, **104**, 085701.
- [160] B. Ruzicka, E. Zaccarelli, L. Zulian, R. Angelini, M. Sztucki, A. Moussaïd, T. Narayanan and F. Sciortino, *Nature Materials*, 2011, **10**, 56 – 60.
- [161] R. Angelini, E. Zaccarelli, F. A. de Melo Marques, M. Sztucki, A. Fluerasu, G. Ruocco and B. Ruzicka, *Nature communications*, 2014, **5**, 1–7.
- [162] A. Mourchid, E. Lecolier, H. Van Damme and P. Levitz, *Langmuir*, 1998, **14**, 4718–4723.

-
- [163] B. Lemaire, P. Panine, J. Gabriel and P. Davidson, *EPL (Europhysics Letters)*, 2002, **59**, 55.
- [164] A. Shalkevich, A. Stradner, S. K. Bhat, F. Muller and P. Schurtenberger, *Langmuir*, 2007, **23**, 3570–3580.
- [165] E. Paineau, I. Bihannic, C. Baravian, A.-M. Philippe, P. Davidson, P. Levitz, S. S. Funari, C. Rochas and L. J. Michot, *Langmuir*, 2011, **27**, 5562–5573.
- [166] L. Bailey, H. N. W. Lekkerkerker and G. C. Maitland, *Soft Matter*, 2015, **11**, 222–236.
- [167] J.-C. P. Gabriel, C. Sanchez, and P. Davidson, *The Journal of Physical Chemistry*, 1996, **100**, 11139–11143.
- [168] R. Angelini, L. Zulian, A. Fluerasu, A. Madsen, G. Ruocco and B. Ruzicka, *Soft Matter*, 2013, **9**, 10955–10959.
- [169] H. Tanaka, S. Jabbari-Farouji, J. Meunier and D. Bonn, *Physical Review E*, 2005, **71**, 021402.
- [170] A. S. Negi and C. O. Osuji, *Journal of Rheology (1978-present)*, 2010, **54**, 943–958.
- [171] V. Tudisca, M. A. Ricci, R. Angelini and B. Ruzicka, *RSC Advances*, 2012, **2**, 11111–11116.
- [172] S. Jabbari-Farouji, R. Zargar, G. H. Wegdam and D. Bonn, *Soft Matter*, 2012, **8**, 5507–5512.
- [173] D. Saha, Y. M. Joshi and R. Bandyopadhyay, *arXiv preprint arXiv:1508.05758*, 2015.
- [174] D. Saha, Y. M. Joshi and R. Bandyopadhyay, *arXiv preprint arXiv:1506.02971*, 2015.

- [175] F. Pignon, A. Magnin and J.-M. Piau, *Journal of Rheology (1978-present)*, 1998, **42**, 1349–1373.
- [176] P. Coussot, H. Tabuteau, X. Chateau, L. Tocquer and G. Ovarlez, *Journal of Rheology (1978-present)*, 2006, **50**, 975–994.
- [177] U. Brandenburg and G. Lagaly, *Applied Clay Science*, 1988, **3**, 263 – 279.
- [178] A. Shahin and Y. M. Joshi, *Langmuir*, 2012, **28**, 15674–15686.
- [179] B. Baldewa and Y. M. Joshi, *Soft Matter*, 2012, **8**, 789–796.
- [180] D. Bonn, S. Tanase, B. Abou, H. Tanaka and J. Meunier, *Physical Review Letters*, 2002, **89**, 015701.
- [181] M. Laurati, S. U. Egelhaaf and G. Petekidis, *Journal of Rheology (1978-present)*, 2011, **55**, 673–706.

2

Experimental Techniques and Data

Analysis

2.1 Introduction

This chapter discusses the different experimental methods that are used in this thesis to study colloidal suspensions both at microscopic and macroscopic levels. Ultrasound attenuation spectroscopy (UAS) and electroacoustics are used to study the exfoliation (dispersibility) behavior of clay tactoids in aqueous suspensions. The influence of exfoliation and ionic concentration in the dispersing medium on the stability of the clay suspensions are characterized using table-top experimental setups developed using light based and electroacoustic methods. The rheological characterization of clay suspensions is done using a commercially available rheometer. Atomic force microscopy (AFM) and scanning electron microscopy (SEM) are used to investigate the microscopic structures of suspensions at different clay and salt concentrations.

2.2 Experimental techniques

2.2.1 Ultrasound attenuation spectroscopy: Theory and measurements

Ultrasound attenuation spectroscopy (UAS) is an excellent tool to study soft matter systems due to its applicability even for a concentrated, highly structured and opaque medium. A very low power ultrasound is used so that it does not affect the internal structures of the samples. The tool is already used extensively for characterizing biomedical materials such as bone, tissue, blood [1]. The relevant theoretical and experimental aspects of this method are described below.

The attenuation of ultrasound in a colloidal suspension can occur due to a combination of viscous, thermal, scattering, intrinsic, structural, and electrokinetic interactions. The attenuation coefficient α can be written as a sum of the different loss mechanisms, $\alpha = \alpha_v + \alpha_{th} + \alpha_{sc} + \alpha_{int}$, where α_v , α_{th} , α_{sc} and α_{int} are the contributions of the viscous, thermal, scattering and intrinsic mechanisms, respectively. Depending on the nature and concentration of the colloidal particles under study, it may be possible to separate the different loss mechanisms in the ultrasound frequency domain. The wavelength of ultrasound in water changes from 1 mm to 15 μm when the ultrasound frequency changes from 1 MHz to 100 MHz. The scattering loss is negligible when the wavelength range of ultrasound is much larger than the sizes of the particles. The contributions from thermal, structural and electrokinetic losses are also typically negligible for colloids having high particle density contrasts and rigidities. The expression for the complex wave number k of ultrasound propagation derived from the coupled phase model [2, 3] that considers only viscous loss in the long wavelength limit ($ka \ll 1$), can be written as: [4]

$$\frac{k^2 M^*}{\omega^2 \rho_s} = \frac{1 - \frac{\rho_p}{\rho_s} \sum_{i=1}^N \frac{\phi_i}{1 - (9j\rho_m \Omega_i / 4s_i^2 \rho_p)}}{1 + \left(\frac{\rho_s}{\rho_p} - 2\right) \sum_{i=1}^N \frac{\phi_i}{1 - (9j\rho_m \Omega_i / 4s_i^2 \rho_p)}} \quad (2.1)$$

where

$$s_i^2 = \frac{a_i^2 \omega \rho_m}{2\eta_m} \quad (2.2)$$

$$\rho_s = \rho_p \phi + \rho_m (1 - \phi) \quad (2.3)$$

and

$$M^* = \frac{\rho_p \rho_m c_p^2 c_m^2}{\phi \rho_p c_p^2 + (1 - \phi) \rho_m c_m^2} \quad (2.4)$$

Here, ω is the angular frequency of the ultrasound waves, M^* is the stress modulus, ρ_p is the density of the particle, ρ_m is the density of the medium, ρ_s is the density of the suspension, c_m and c_p are the velocities of ultrasound in liquid and solid media respectively, ϕ_i is the volume fraction of the i th species of the particulate phase, ϕ is the total volume fraction of the particulate phase, a_i is the diameter of a particle of the i th species, η_m is the shear viscosity of the medium and Ω_i is the drag coefficient of a particle of size a_i . The hydrodynamic interactions between the particles is calculated using the Happel cell model [5]. The attenuation coefficient α_v and the sound speed c through the suspension can then be calculated from the following relations:

$$\alpha_v = -Im(k) \quad (2.5)$$

$$c = \frac{\omega}{Re(k)} \quad (2.6)$$

It is to be noted that α_v is closely related to the size distributions of the colloidal particles in the suspension medium.

In a typical experiment, if the incident ultrasound intensity is I_0 and the attenuated intensity after passing through a sample of length x is I_x , then Beer-Lambert law gives

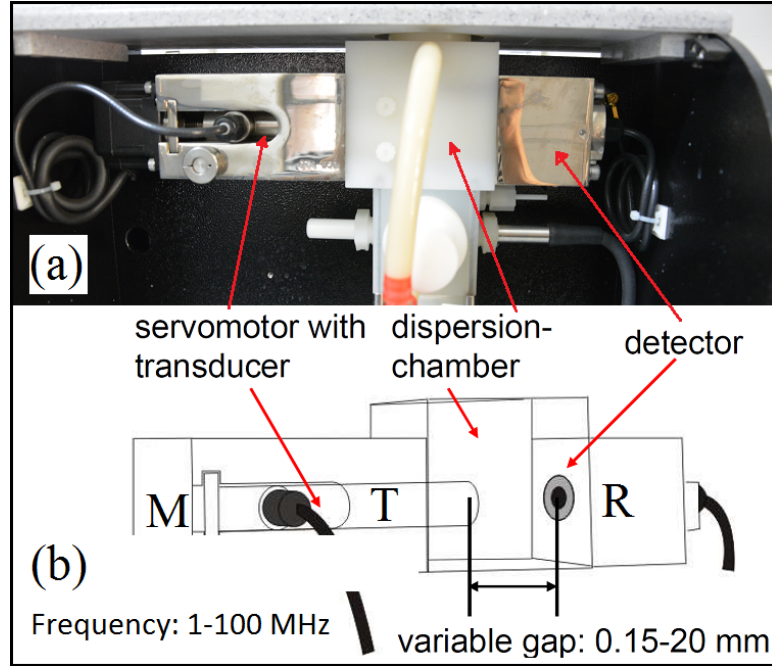


FIGURE 2.1: (a) The different components of the ultrasound attenuation measuring unit of DT1200. (b) A schematic of the DT1200 adapted from the manual of DT1200, Dispersion Technology, Inc. [6].

an expression for the attenuation coefficient α of the medium [5]:

$$\alpha_v = \frac{10}{x} \log \frac{I_0}{I_x} \quad (2.7)$$

Here, α_v is usually expressed in $\text{dB} \cdot \text{cm}^{-1} \cdot \text{MHz}^{-1}$ and depends on the acoustic frequency ω .

For this thesis work, the attenuation spectra and ultrasound speed are measured using a DT-1200 ultrasound spectrometer from Dispersion Technology Inc (Fig. 2.1). Details of this spectrometer can be found in [7]. For each attenuation measurement, 130 ml of a suspension is loaded in a cell containing two identical piezoelectric transducers separated by a sample gap. The sample gap can be varied in the range 0.15-20 mm using a stepper motor (M in Fig. 2.1(b)) having translational precision of a few micrometers. The transmitting transducer (T in Fig. 2.1(b)) that is attached to the stepper motor converts input electrical signals into ultrasound tone bursts of different intensities and frequencies. The ultrasound pulse that is generated propagates through the

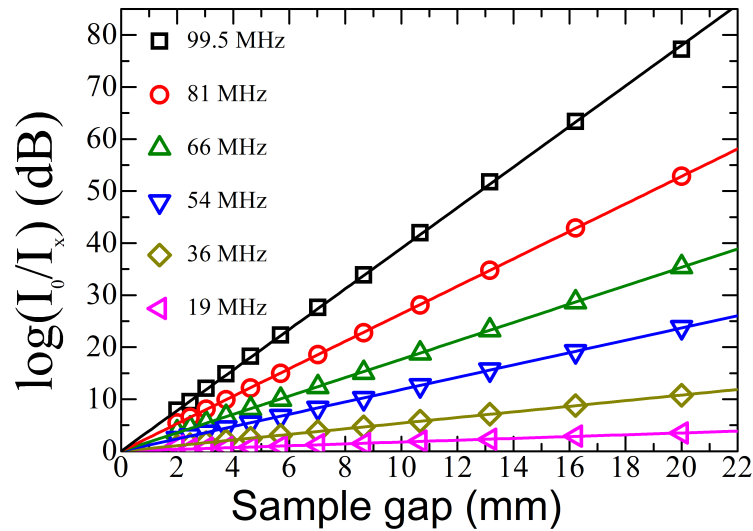


FIGURE 2.2: Colloidal attenuation of acoustic energy in a suspension of 10% w/v Silica Ludox TM50 is plotted versus gap between the ultrasound transducers (i.e. different sample thicknesses) for several frequencies. The solid straight lines are fits to the Beer-Lambert law (Eqn. 2.7).

suspension and interacts with the colloidal particles and the liquid medium. This interaction decreases the ultrasound intensity, with the predominant loss mechanisms being the viscous loss of the colloids and the intrinsic loss of water. The intensity amplitude of the pulse, received by the detecting transducer (R in Fig. 2.1(b)), is converted back into an electric pulse for comparing with the initial input pulse. For each frequency, the signal processor receives data for a minimum of 800 pulses to achieve a signal-to-noise ratio of at least 40 dB. The intrinsic loss contribution from the dispersing medium is subtracted from the total intensity loss to estimate the attenuation arising from the colloids alone. The sound pulses used here are of low power (10 mW) and are not expected to destroy the microscopic structures of the suspensions. The sound speed c is obtained by measuring the time delay between the emitted and received pulses. The samples can be continuously pumped through the measuring cell to prevent sedimentation. Prior to these experiments, the sample cell is calibrated for acoustic diffraction using Milli-Q water.

Fig. 2.2 shows the measured colloidal attenuation for varying sample lengths x

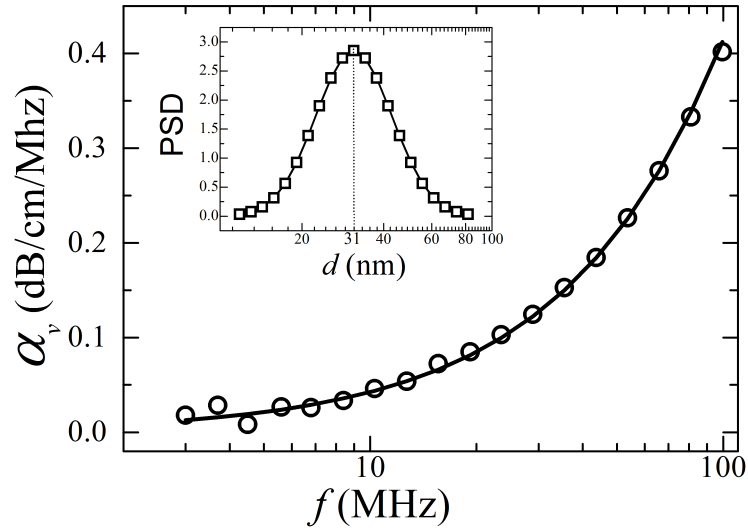


FIGURE 2.3: The attenuation spectrum (circles) for an aqueous suspension of 10% w/v Silica Ludox TM50 measured in a frequency range 3-99.5 MHz at 25 °C. The solid line is a theoretical fit to Eqn. 2.1 considering a unimodal size distribution. The unimodal particle size distribution (PSD) obtained from this theoretical fit is plotted in the inset. The supplied values at 25 °C are: $\rho_m = 0.997$ g/cc, $\eta_m = 0.89$ mPas, $\rho_p = 2.2$ g/cc, $c_p = 6000$ m/s.

in an aqueous suspension of 10% w/v Silica Ludox TM50 (Sigma Aldrich) at different applied ultrasound frequencies measured at 25 °C. The value of the attenuation coefficient α_v at a particular frequency can be calculated by fitting the colloidal attenuation data to the Beer-Lambert law (Eqn. 2.7). The measurements of α_v at various frequencies give an attenuation spectrum as shown in Fig. 2.3 for the 10% w/v Silica Ludox TM50 suspension. This spectrum can be fitted with the theoretical prediction (Eqn. 2.1) using the supplied values of ρ_m , η_m , ρ_p , c_p and ϕ to find the particle size distribution (PSD).

An analysis algorithm developed by the manufacturer and based on the theory described earlier is used to determine the PSD from the acquired attenuation spectrum. The algorithm, assuming unimodal or bimodal distributions, runs a global search in the size range from 1 nm to 1 mm for the PSD that best fits the data. For a unimodal (lognormal) distribution, the median and the standard deviation of the particle sizes are the fitting parameters. For a bimodal PSD, essentially a sum of two lognormal PSDs, the algorithm adjusts four parameters: the two median values (d_1 and d_2) of the lower

and higher modes, their standard deviations (assumed to be of the same magnitude σ for both modes) and the relative volume fraction (ϕ_2) of particles in the higher mode. During the search process, the algorithm calculates the theoretical attenuation values for each PSD using Eqn. 2.1 and Eqn. 2.6 and fits the experimental attenuation spectrum by minimizing the fitting error. The searching algorithm stops when the fitting error saturates to the lowest value. The inset of Fig. 2.3 shows the unimodal PSD estimated from the measured attenuation spectrum using the method described above. The median value of this distribution, $d_1 = 31$ nm, is very close to the standard spherical size of 32 nm of Ludox TM50 procured from Sigma Aldrich. Table 2.1 list the supplied values of the parameters used to calculate theoretical attenuation from Eqn. 2.1 – Eqn. 2.6.

Parameter name	Notation	Value
Density of Ludox TM50	ρ_p	2.2 g/cc
Density of Laponite	ρ_p	2.53 g/cc
Density of Na-montmorillonite	ρ_p	2.6 g/cc
Sound speed in solid media	c_p	6000 m/s
Density of water	ρ_m	0.997 g/cc
Viscosity of water	η_m	0.89 mPas

Table 2.1: Supplied values of the parameters at 25 °C used for the PSD calculations using Eqn. 2.1 – Eqn. 2.6.

2.2.2 Experimental setups for stability characterization

Two different table-top setups using diffused light and ultrasound are developed to monitor the stability of colloidal suspensions under gravity. The electroacoustic setup using ultrasound is used to measure the extent of gel collapse with a resolution of a few tens of micrometers.

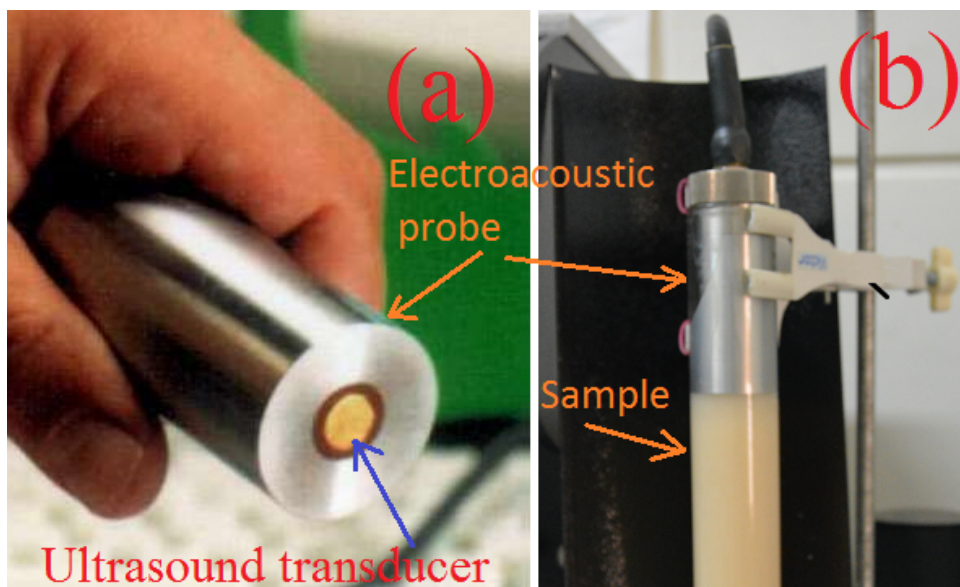


FIGURE 2.4: (a) Electroacoustic probe from Dispersion Technology used for the sedimentation study. (b) Snapshot of the sedimentation setup.

A. Electroacoustic based experimental setup

Electroacoustic measurements are used to indirectly monitor the stability of clay samples at higher clay concentrations. This methods described below have several advantages over light based techniques. The lensing effect of the liquid meniscus at the sample-air interface gives rise to indeterminacy in the position calculation in light-based measurements. Furthermore, the resolution of displacement measurement is higher in the electroacoustics method.

When a charged colloidal particle immersed in a fluid is subject to oscillatory motion using longitudinal ultrasound waves, the electric double layer (EDL) around the particle oscillates. This gives rise to a small oscillating dipole moment [8], with the dynamical relaxation time of the EDL being less than the period of oscillation of the ultrasound. In the suspension, the induced dynamic dipole moments from all the particles add up to generate an electric field which, in turn, induces a current known as the colloid vibration current (I_{CVI}) in the receiving transducer circuit placed in the suspension. If the suspension contains ions from a salt, the probe simultaneously detects an ionic vibration current (I_{IVI}) which arises due to the relative motion between the two

ion species in the ultrasound field. In this case, the electroacoustic response, known as total vibration current (I_{TVI}), is the vector sum of I_{CVI} and I_{IVI} . In the present study, a specially designed electroacoustic probe is used to measure the magnitudes and phases of I_{CVI} and I_{TVI} in a sedimentation setup (Fig. 2.4). The details of the probe can be found in [7]. The front flat surface of the cylindrical shaped probe is placed in contact with the top surface of the sample column (Fig. 2.4). The probe launches plane ultrasound waves of frequency 3 MHz along the height of the sample. The electric field generated in the sample is sensed by the metal part of the probe and finally converted to a current using an electronic circuit. The strength and phase of the I_{CVI} signal depend on the concentration and size of the suspended colloidal particles in the path of the ultrasound that is emitted from the flat surface of the probe. When charged particles in the suspension move away from the probe/sample contact surface, the magnitude of the electroacoustic signal decreases, making this technique very effective for monitoring the sedimentation of particles in an opaque suspension. Using this setup, a displacement as small as $250 \mu\text{m}$ of the sedimenting front of a collapsing gel can be measured precisely by measuring oscillations of I_{TVI} values [9]. The I_{CVI} phase is calibrated to 180° for negatively charged colloids using a 10% w/v suspension of Ludox TM50 silica particles.

Key features	Specifications
Image type	Monochromatic
Image sensor	Sony ICx285AL
Resolution	1392×1040
Minimum exposure time	$1 \mu\text{s}$
Pixel Size	$6.45 \times 6.45 \mu\text{m}^2$
Digitization rate	12 bit@20 MHz
Readout Noise	7e-rms at 20 MHz
Cooling	Thermoelectric, 0°C
Frame readout	96ms/frame

Table 2.2: Specifications of CCD camera.

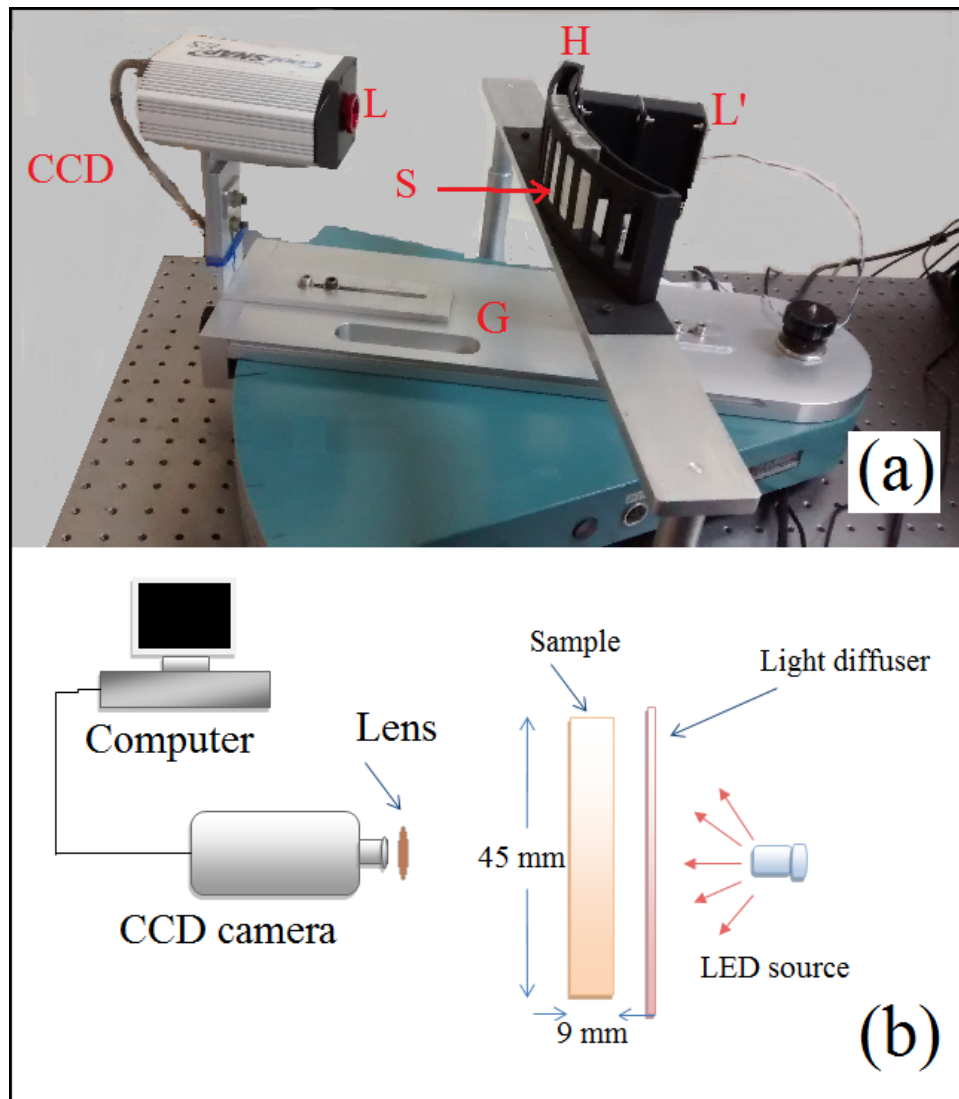


FIGURE 2.5: (a) Snapshot of the light based experimental setup used for the sedimentation study. The main components of this setup are – a light source (L'), sample cuvettes (S), cuvette holder (H), goniometer (G), CCD camera and lens assembly (L). (b) Schematic diagram of the experimental setup.

B. Light based experimental setup

A homemade light based experimental setup, shown in Fig. 2.5 (a), is used to monitor the sedimentation of clay suspensions. A schematic diagram of this setup is shown in Fig. 2.5 (b). A linear light source made from red LEDs (midband wavelength=633 nm) is housed within a rectangular box (L') containing two layers of light shaping diffusers procured from Luminix™. This arrangement produces a homogeneous and diffused light source which is used to illuminate the samples. The intensity of the diffused light is controlled by changing the current to the LEDs. Rectangular glass cuvettes (S) of inner dimensions 10 mm (w) × 9 mm (d) × 48 mm (h) are used to hold the clay suspensions. The cuvettes are then housed in a cuvette-holder (H) fixed to the goniometer (G) arm. Cuvettes containing samples of height $h_0 = 45$ mm are sealed using a silicone sealant to prevent evaporation of water. The temperature of the sample is kept constant at 25 ± 0.2 °C. The diffused light is incident perpendicularly to the cuvette wall. The light transmitted through the sample is collected using a CCD camera (Photometrics CoolSnap ES, Roper Scientific Inc.) and a lens (L). Specifications of the CCD camera is given in Table 2.2. The intensity of the incident light is adjusted so that the transmitted intensity detected by the CCD camera remains below the saturation level of the CCD sensor. The CCD images are finally analyzed using Winview and Matlab softwares. The transmitted intensity I_{tr} at each pixel of the CCD image is measured in terms of the grey value. To eliminate the spatial inhomogeneity of the incident light, the value of I_{tr} at each pixel of the CCD image is normalized by the background intensity of light that passes through clear water.

A CCD snapshot of sedimenting particles in a 20% w/v aqueous cornstarch suspension at observation time $t_s = 15$ min after loading the sample is shown in the inset of Fig. 2.6. Cornstarch particles are denser than water (density difference=1.5 g/cc) and have particle sizes in the range 3 – 25 μm . As a result, the particles sediment under gravity, leading to a distinct interface between clear water (the supernatant) and the sedimenting particles. The average intensity distribution of the transmitted light along the height of the sample is plotted in Fig. 2.6. Such plots are useful in locating the

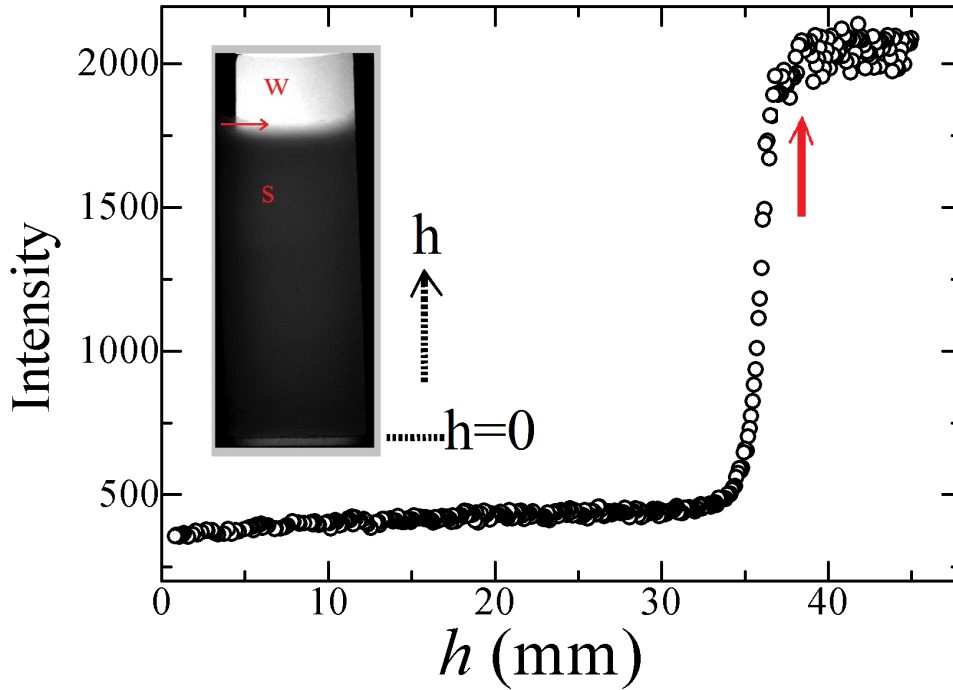


FIGURE 2.6: Average transmitted intensity I_{tr} is plotted as a function of vertical distance h of a sedimenting suspension of 20% w/v cornstarch at observation time $t_s = 15$ min. Here $h = 0$ is at the bottom of the sample column and $t_s = 0$ is defined as the time at which stirring of the suspension in the cuvette is stopped. The corresponding CCD image of the sample is shown in the inset. The solid arrows indicate the position of the interface between clear supernatant (W) and the particles (S).

position of the supernatant-particle interface.

2.2.3 Conductivity measurements

Conductivity measurements of charged colloidal suspensions is very useful in estimating the concentration of the counterions present in the bulk phase of the suspensions. The conductivity of colloidal suspensions depends on the concentration, valence and mobility of the counterions at a particular temperature. However, the contribution of the colloidal particles to the bulk conductivity is usually negligible due to their small mobility [10]. The conductivity, K , is measured using the following simple formula:

$$K = \kappa G \quad (2.8)$$

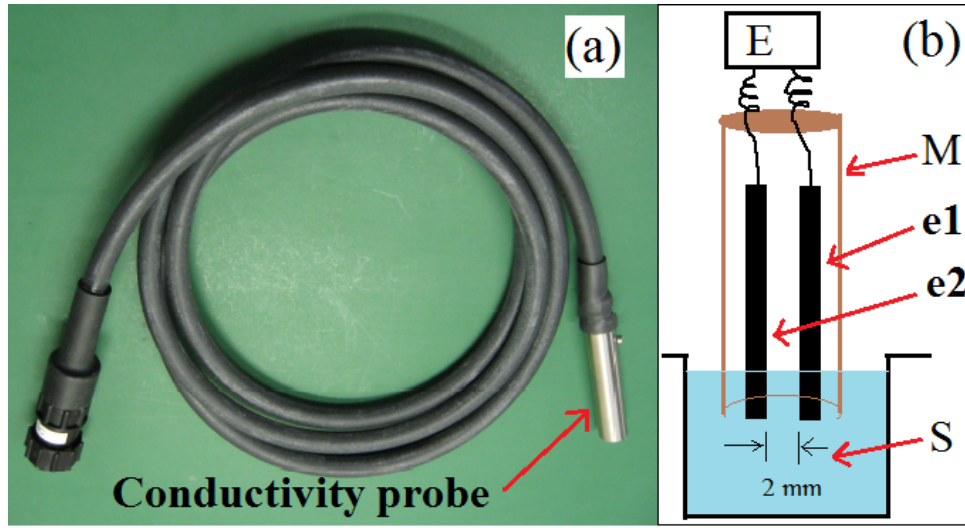


FIGURE 2.7: (a) A snapshot of the DT1200 conductivity probe. (b) The schematic diagram of the conductivity probe which consists of two parallel metal electrodes $e1$ and $e2$ operated by an electronics assembly (E). The electrodes are enclosed inside a metal body (M). The ends of the electrodes are immersed in a sample (S). Figure (a) is reproduced from [6].

Here,

$$\text{Cell constant, } \kappa = \frac{l}{a} \quad (2.9)$$

and

$$\text{Conductance, } G = \frac{I}{V} \quad (2.10)$$

where l is the distance between the electrodes, a is the effective area of the electrodes and I is the current between the electrodes for applied voltage difference of V . The calibration of the conductivity cell usually involves measuring the cell constant (κ) using a standard solution of known conductivity.

To measure the conductivity K , a probe (Fig. 2.7)(a) attached to the DT-1200 instrument from Dispersion Technology Inc. is used [6]. The probe consists of two parallel cylindrical metal electrodes insulated from each other and separated by a distance of 2 mm, housed inside another metal cylinder (Fig. 2.7)(b). During each measurement, the instrument applies a sinusoidal voltage (V) with frequency 3 MHz across the

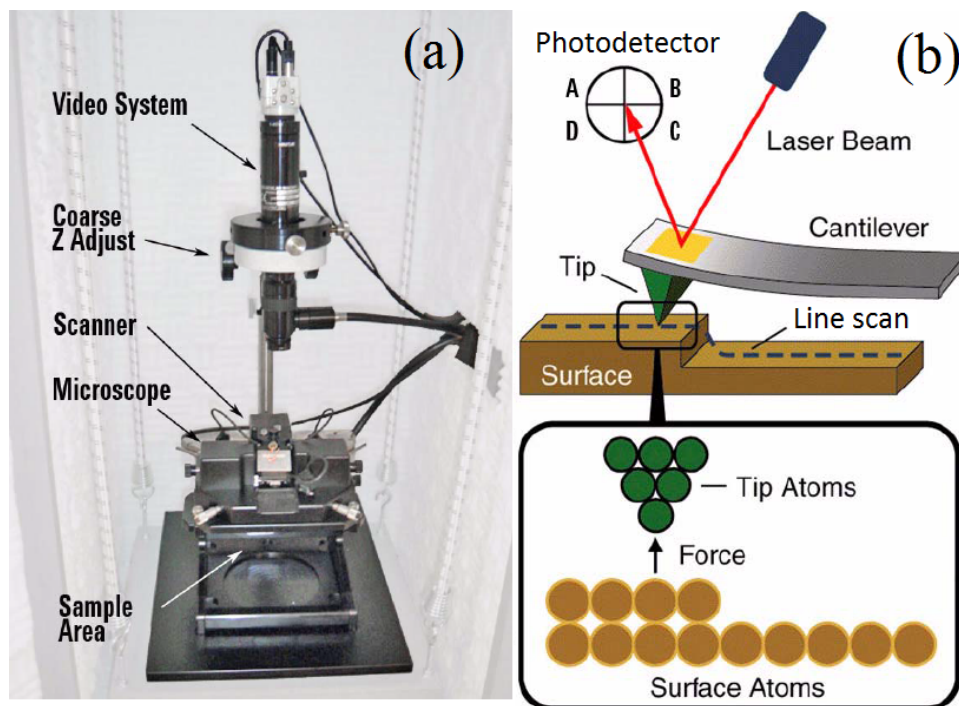


FIGURE 2.8: (a) Snapshot of PicoPlus 5500 scanning probe microscope. (b) Schematic diagram of the basic components of an atomic force microscopy. The figures are reproduced from [11].

electrodes and measures the sinusoidal current (I) that flows through the sample. The conductivity measured using this oscillatory applied voltage is not affected by electrode polarization effects. The probe used here is calibrated using 0.01 M KCl solution which has a conductivity of $1411 \mu\text{S}$ at 25°C .

2.2.4 Atomic force microscopy (AFM)

For atomic force microscope (AFM) imaging, we have used a high resolution PicoPlus scanning probe microscope from Molecular Imaging Company (Fig. 2.8(a)). This microscope can resolve surface topography of the order of angstroms in lateral dimension and of the order of few picometers in the vertical dimension [11]. As shown in Fig. 2.8(b), a sharp tip containing a few molecules at the end of a cantilever is brought in contact with the surface of a sample. The probe tip interacts with the surface, with the cantilever bending forward or backward depending on the nature of the interaction

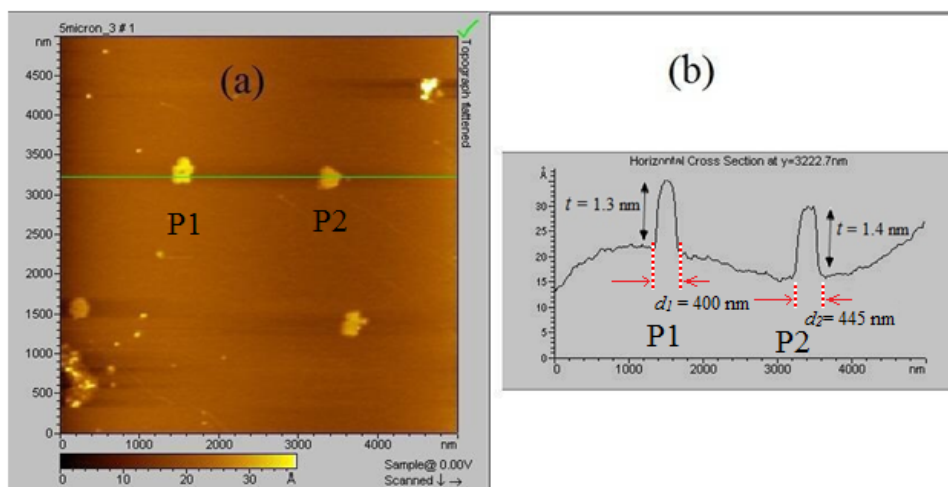


FIGURE 2.9: (a) Representative AFM micrograph containing Na-montmorillonite clay platelets scanned in tapping mode using PicoPlus 5500 scanning probe microscope. (b) Height distribution along the green line in figure (a). This distribution is used to calculate the thicknesses ($t_1 = 1.3$ nm and $t_2 = 1.4$ nm) and lateral sizes ($d_1 = 400$ nm and $d_2 = 445$ nm) along the selected green line on the platelets P1 and P2 indicated in figure (a).

[12]. To measure the vertical displacement of the cantilever, a laser spot is reflected from the cantilever free end onto a photosensitive quadrant diode. The tip deflection is measured in terms of the voltage differences between the different parts of the quadrant diodes.

The AFM can be operated in tapping mode or contact mode. In the tapping mode, an oscillating tip is brought in proximity with the surface of the samples. The van der Waals attraction between the tip and the closest atoms on the sample surface induces a shift in the resonant frequency of the cantilever. The images can be taken by keeping a constant frequency shift and allowing the amplitude of the oscillation to vary using a feedback loop during line scanning. In this mode, the tip-sample interactions are very small, resulting in good vertical resolution. In contact mode, the cantilever tip is brought in contact with the surface of the sample. The cantilever deflection is kept constant by applying an external force using a feedback loop during scanning. The variations in the applied forces give the surface topography.

Sample preparation method for AFM imaging: For the AFM studies reported in this thesis, a drop of $10 \mu\text{l}$ sample is deposited on a freshly cleaved mica surface (area

of 1 cm²) and allowed to dry in a closed petri dish under ambient conditions. In the tapping mode, a cantilever of dimension 225 $\mu\text{m} \times 38 \mu\text{m} \times 7 \mu\text{m}$ with a tip height of 10 μm , oscillates at its resonant frequency, which, in air, has a value 146 – 236 kHz. In the contact mode, a cantilever of dimension 450 $\mu\text{m} \times 50 \mu\text{m} \times 2 \mu\text{m}$ with a tip height of 10 μm is used. Data acquisition and size analysis are done using PicoScan 5.3.3 software supplied by Molecular Imaging Company.

Fig. 2.9(a) shows a representative AFM micrograph of Na-montmorillonite platelets scanned in tapping mode. It is seen in this micrograph that the Na-montmorillonite platelets (light yellow patches in the figure) are very irregular in their shape and sizes. Fig. 2.9(b) shows the height distribution along the green line drawn in Fig. 2.9(a). This distribution can be used to calculate the thicknesses and lateral sizes of particles as shown by arrows in Fig. 2.9(b). The thicknesses ($t_1 = 1.3 \text{ nm}$ and $t_2 = 1.4 \text{ nm}$) and lateral sizes ($d_1 = 400 \text{ nm}$ and $d_2 = 445 \text{ nm}$) are calculated for platelets P1 and P2 indicated in Fig. 2.9(a).

2.2.5 Rheological measurements

The rheological measurements reported in this thesis are performed using a stress controlled Rheometer (MCR 501) (Fig. 2.10(a)) with a CC17 measuring geometry from Anton Paar. In the stress controlled mode, the rheometer applies a known shear stress to the material under study and measures the resultant strain. The instrument can also be used to control strain or shear rate through a feedback mechanism. This computer controlled rheometer can be operated in both oscillatory and rotational modes such that various important rheological quantities such as viscosity, storage and loss moduli can be measured directly. Data acquisition is done using the Rheoplus–V3.4 software developed by Anton Paar. A schematic diagram of the main components of the rheometer is shown in Fig. 2.10(b). For a rheological measurement, a measuring head is attached to a synchronous motor contained in the rheometer head. The shaft inside the motor is supported by an air bearing to give it a friction free environment. For this, a high steady pressure (3 bars) is maintained in the head by supplying dust-free and moisture-free

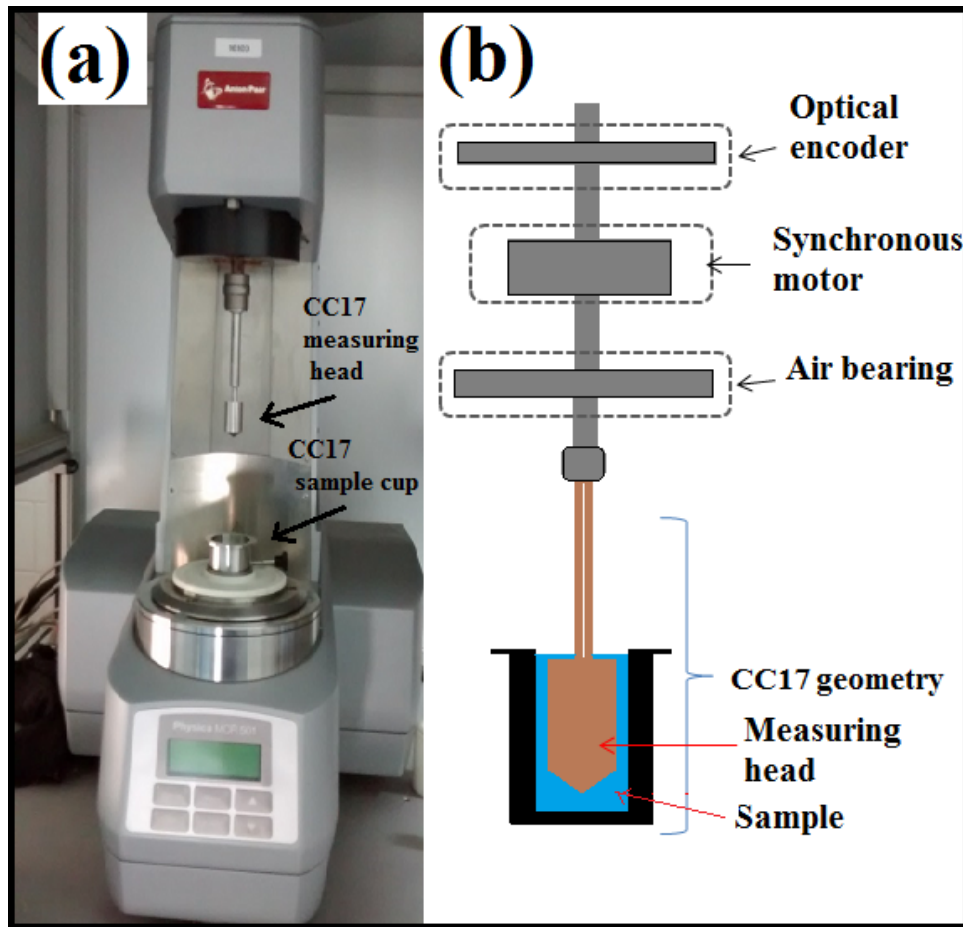


FIGURE 2.10: (a) The Anton Paar MCR 501 rheometer (b) A schematic diagram of the main components of a Anton Paar MCR 501 rheometer with CC17 measuring geometry. The figure (b) is adapted from [13].

compressed air using a compressor. During measurement, the motor of the rheometer applies a torque on the measuring rod, while a high-resolution optoelectronic encoder detects the resulting deflection angles and rotational speeds. Due to the use of the air bearing, torques as small as 2 nN.m, with a resolution of 0.01 nN.m, can be measured using this rheometer. A water-circulating unit (Viscotherm VT2) is used to control the temperature of the sample in the measuring geometry in the range between 5 °C and 80 °C with a temperature stability of ± 0.1 °C.

The measuring geometry CC17 consists of a co-axially arranged cylindrical cup and a rotating cylindrical measuring head (Fig. 2.10(b)). The geometry has a gap length of 0.71 mm and an effective length of 24.99 mm. A test fluid of volume 4.7

ml is kept in the annulus between the cylinder surfaces. Stress and strain induced in the sample are measured in terms of the torque (M) and deflection angle (θ) by the rheometer. This data is converted to strain (γ), stress (σ), and shear rate ($\dot{\gamma}$) for the CC17 geometry using the following relations:

$$\gamma = \frac{1}{10} \cdot \frac{1 + \delta^2}{\delta^2 - 1} \cdot \theta \quad (2.11)$$

$$\sigma = \frac{1 + \delta^2}{\delta^2 \cdot r_i^2} \cdot \frac{M}{4000 \cdot \pi L C_L} \quad (2.12)$$

$$\dot{\gamma} = \frac{\pi \cdot n}{30} \cdot \frac{1 + \delta^2}{\delta^2 - 1} \quad (2.13)$$

$$\delta = \frac{r_e}{r_i} \quad (2.14)$$

where, r_i = radius of the measuring head, r_e = inner radius of the measuring cup, L is the gap length, $C_L = 1.10$ is the correction factor and n is the rotational speed [13].

This rheometer, equipped with the CC17 geometry, is capable of measuring shear strains (γ) above 1.23×10^{-5} , shear stresses (σ) in the range between 771.345×10^{-6} Pa and 17740.935 Pa and shear rates ($\dot{\gamma}$) from $1.283 \times 10^{-7} \text{ s}^{-1}$ to $3.849 \times 10^3 \text{ s}^{-1}$.

Applications of the rheometer

Various measurement protocols can be designed to characterize samples using this rheometer. It has two basic modes of operation, viz. oscillatory and rotational. In an oscillatory rheological measurement, a sinusoidal perturbation (strain or stress) is usually applied on a test sample and the response of the sample is measured in terms of the resultant stress or strain. For example, if an oscillatory shear strain γ of amplitude γ_0 is applied to the sample and is given by [14]:

$$\gamma(\omega) = \gamma_0 \sin(\omega t) \quad (2.15)$$

then, for small strain amplitudes, the out-of-phase stress response σ of the sample is given by:

$$\sigma(\omega) = \sigma_0 \sin(\omega t + \phi) \quad (2.16)$$

Here, σ_0 is a shear stress amplitude and ϕ is the phase lag. The value of ϕ is zero for purely elastic materials and 90° for purely viscous materials. The viscoelastic moduli, that is the elastic modulus G' and viscous modulus G'' , can be calculated as follows:

$$G' = \frac{\sigma_0}{\gamma_0} \cos(\delta) \quad (2.17)$$

$$G'' = \frac{\sigma_0}{\gamma_0} \sin(\delta) \quad (2.18)$$

The absolute value of the complex modulus can be calculated as [14]:

$$|G^*| = \sqrt{G'^2 + G''^2} \quad (2.19)$$

The ratio of these two mechanical moduli is called loss factor and is defined as $\tan(\delta) = G''(\omega)/G'(\omega)$.

For this thesis work, the following three oscillatory measurements have been used.

A. Time sweep oscillatory tests: In this test, viscoelastic moduli are measured following application of an oscillatory strain of a constant amplitude γ_0 and a constant frequency ω to an aging sample with varying times of observation. Usually, a very small value of γ_0 in the linear viscoelastic regime is selected so that the applied strain does not destroy the sample microstructure. A similar experiment can be performed by applying an oscillatory stress instead of strain. Such experiments help to monitor the time evolution of the viscoelastic moduli of aging or reactive samples. Fig. 2.11 shows the evolution of G' (\square) and G'' (\circ) with time t_w of an aging 3.5% w/v Laponite suspension after preparation.

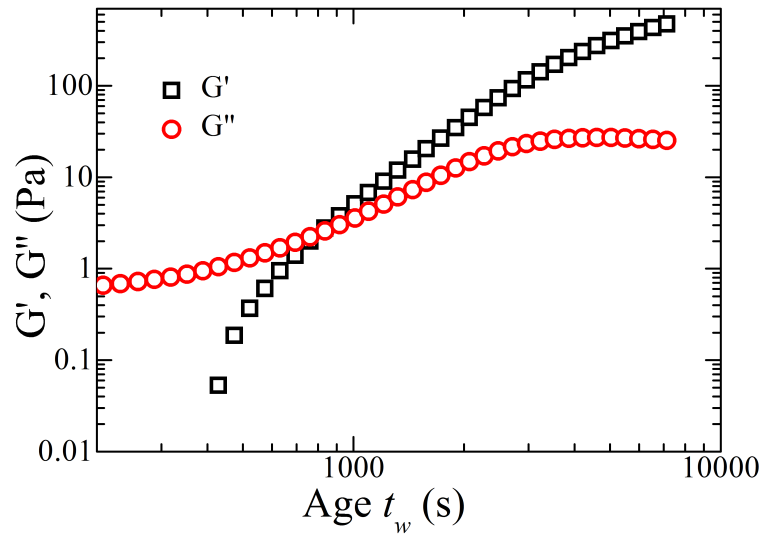


FIGURE 2.11: Evolution of the elastic modulus G' (\square) and viscous modulus G'' (\circ) with age (time since preparation) t_w of a 3.5% w/v aqueous suspensions of Laponite. Here, $t_w = 0$ is defined as the time at which stirring of the sample is stopped. To monitor the aging of this suspension, an oscillatory strain of amplitude 0.1% and angular frequency of 6 rad/s is applied to the sample.

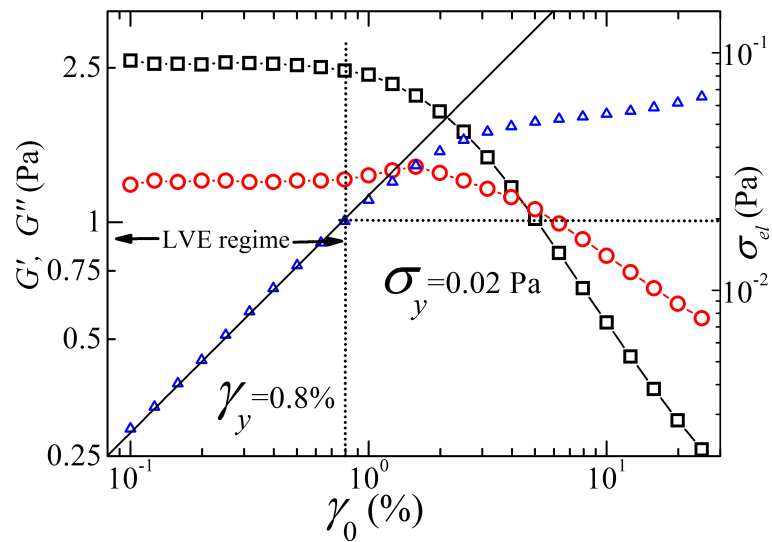


FIGURE 2.12: Variation of elastic modulus G' (\square), viscous modulus G'' (\circ) and elastic stress σ_{el} (Δ) with strain amplitude γ_0 at an angular frequency of 1 rad/s for a 71% w/w aqueous suspensions of silicon dioxide. The solid line is the linear fit to the σ_{el} vs γ_0 data. The vertical and horizontal dotted lines show the position of the yield strain $\gamma_y = 0.8\%$ and yield stress $\sigma_y = 0.02$ Pa.

B. Strain amplitude sweep: In an amplitude sweep test, viscoelastic moduli are measured by varying the value of γ_0 of the applied oscillatory strain at a constant ω . This test is usually performed to find the extent of linearity of viscoelastic materials. Fig. 2.12 shows the variation of the elastic modulus G' (\square) and viscous modulus G'' (\circ) with strain amplitude γ_0 at an angular frequency of 1 rad/s for a 71% w/w aqueous suspensions of silicon dioxide. The range of the amplitudes of the applied strain γ_0 , where the mechanical moduli show constant values, is defined as the linear viscoelastic (LVE) regime. The LVE regime is followed by a yielding regime above a critical value of the applied strains, known as yield strain γ_y (shown by a vertical dotted line in Fig. 2.12). For $\gamma_0 > \gamma_y$, G' decreases monotonically while G'' shows a weak peak before decreasing monotonically due to destruction of the sample's microstructures under high strains.

To determine the yield strain γ_y accurately, we follow the method described by Laurati *et al.* [15]. In this method, the elastic stress $\sigma_{el} = G'\gamma_0$ (Δ in Fig. 2.12) is plotted versus γ_0 , which helps to separate the contribution of the viscous stress from the total stress. At low γ_0 values, the elastic stress vs strain data is fitted to $\sigma_{el} = G'\gamma_0$. The value of γ_y is defined at which the measured value of σ_{el} starts deviating more than 3% from the theoretically calculated value. In the case of the 71% w/w silicon dioxide paste, a yield strain $\gamma_y = 0.8\%$ and yield stress $\sigma_y = 0.02$ Pa are calculated.

C. Frequency sweep: In a frequency sweep measurement, the amplitude of the applied oscillatory strain γ_0 is kept constant, the frequency, ω , of the oscillatory strain varies with time and the corresponding viscoelastic moduli are measured. Such measurements are generally performed in the LVE regime of materials. Fig. 2.13 shows the plots of G' (\square) and G'' (\circ) for a worm-like micellar solution prepared by adding 400 mM sodium salicylate (NaSal) to 100 mM cetyl trimethylammonium bromide (CTAB), where the amplitude of strain is kept constant at 0.5%. It can be seen that both the moduli are strongly dependent on the frequency of the applied strain, with $G'' > G'$ indicating liquid-like behavior for $\omega < \omega_c$. The system exhibits solid-like behavior with $G' > G''$ for $\omega > \omega_c$. The magnitude of ω_c can be used to estimate the

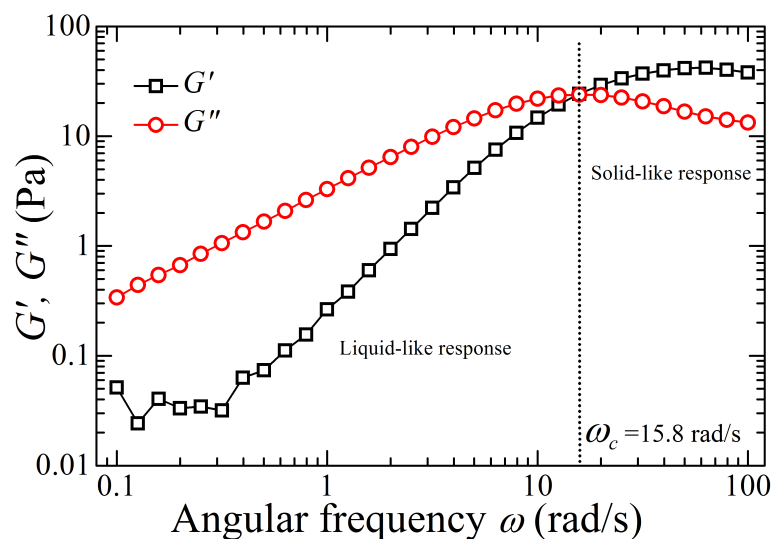


FIGURE 2.13: Variation of elastic modulus G' (\square) and viscous modulus G'' (\circ) with angular frequency (ω) at an applied strain of 0.5% for a worm-like micellar solution prepared by adding 400 mM sodium salicylate (NaSal) to 100 mM CTAB. The vertical dotted line indicates the position of critical frequency $\omega_c = 15.8$ rad/s.

relaxation time of the viscoelastic system.

Rotational experiments

In a rotational experiment, a unidirectional shear strain, stress or shear rate is applied to the sample to estimate its flow behavior by measuring the shear stress, strain response (σ) or viscosity (η). Such experiments are often used to investigate shear thinning, shear thickening, shear banding, creep and stress relaxation behaviors of soft solid materials. The rotational experiments that are relevant to this thesis are discussed below:

A. Flow curves and viscosity measurements: Such measurements are useful to estimate viscosities and yields stresses of test samples. The flow curve is measured by controlling shear rate $\dot{\gamma}$ (CSR mode) or stress σ (CSS mode) and measuring the response in terms of σ or $\dot{\gamma}$ respectively. Fig. 2.14 shows the flow behavior and the corresponding viscosity plot of glycerol. The viscosity of glycerol is independent of applied shear rate ($\dot{\gamma}$), thereby revealing Newtonian liquid behavior. Fig. 2.15 shows

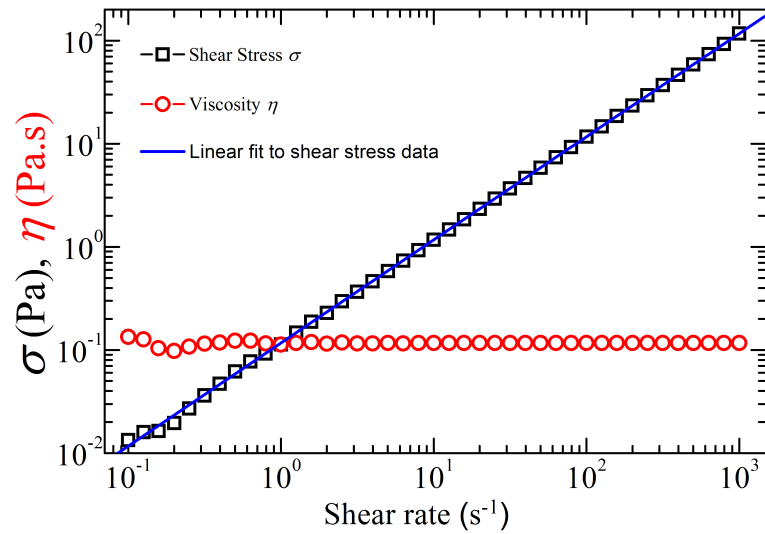


FIGURE 2.14: Plot of shear stress σ (\square) and the viscosity η (\circ) as a function of applied shear rate in glycerol at a temperature 25°C . The solid line is the linear fit with zero intercept to the shear stress data obtained in the applied shear rate regime. Viscosity remains constant at $0.11\text{ Pa}\cdot\text{s}$ in this regime, confirming the Newtonian flow behavior of glycerol.

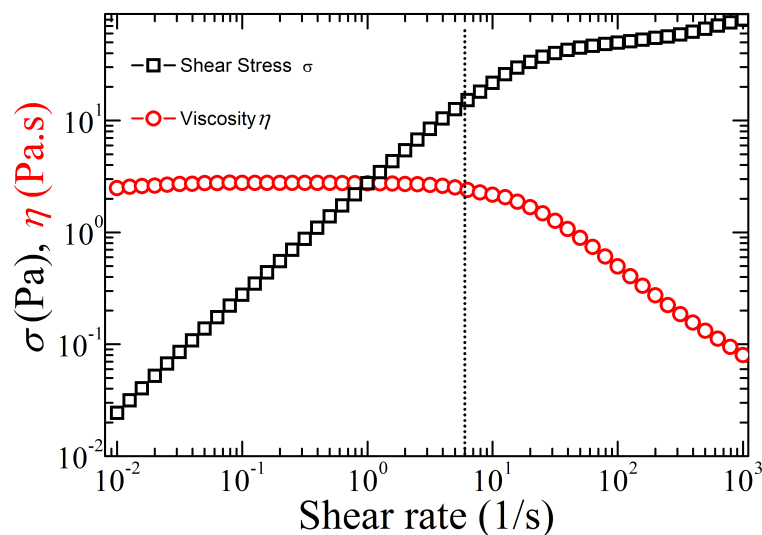


FIGURE 2.15: Plot of shear stress, σ (\square) and corresponding viscosity, η (\circ) as a function of applied shear rate in a worm-like micellar solution prepared by adding 400 mM sodium salicylate (NaSal) to 100 mM CTAB at temperature 25°C . The vertical dotted line indicates the position of the critical shear rate $\dot{\gamma}_c$ above which the solution begins to exhibit shear thinning behavior. The position of the $\dot{\gamma}_c$ is determined from the point of inflection where viscosity deviates from the plateau behavior.

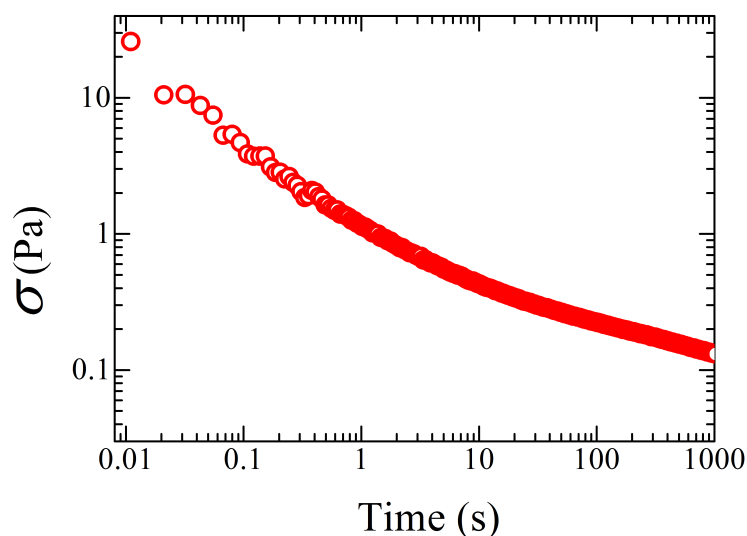


FIGURE 2.16: Stress relaxation with time under a constant strain of amplitude $\gamma = 1\%$ in a crosslinked PDMS prepared by mixing Sylgard PDMS samples base with Sylgard curing agent at a volume ratio of 80:1.

the flow behavior of a worm-like micellar solution prepared by adding 400 mM sodium salicylate (NaSal) to 100 mM CTAB at temperature 25°C . The viscosity of the sample decreases at high shear rate values, reflecting a shear thinning behavior of the worm-like micellar solution.

B. Stress relaxation: In a stress relaxation experiment, a step strain γ is applied to the sample and the time evolution of induced stress σ is measured. The relaxation modulus at time t is defined as, $G(t) = \sigma(t)/\gamma$ [14]. Fig. 2.16 shows stress relaxation behavior of crosslinked polydimethylsiloxane (PDMS) when it is subjected to a step strain of 1%. The induced stress relaxes with time due to the slow rearrangement of the constituent particles under the deformation field.

2.2.6 SEM and Cryo-SEM techniques

Scanning electron microscopy (SEM) is a powerful technique to observe a sample's microstructures down to a few nanometers [18]. Over the last decades, the technique has been widely used to investigate the microstructures of biological samples, polymer

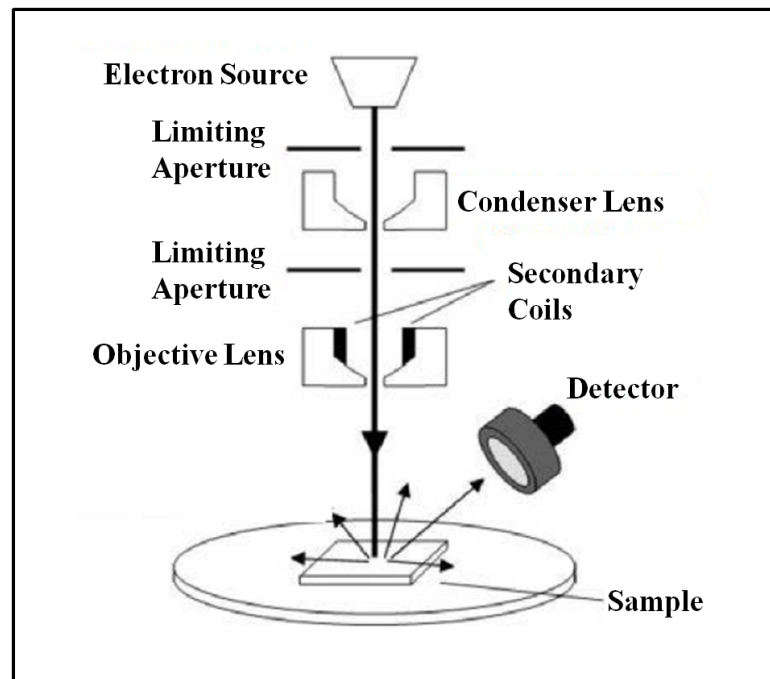


FIGURE 2.17: Schematic diagram of a scanning electron microscopy (SEM) setup. The figure is reproduced from [16].

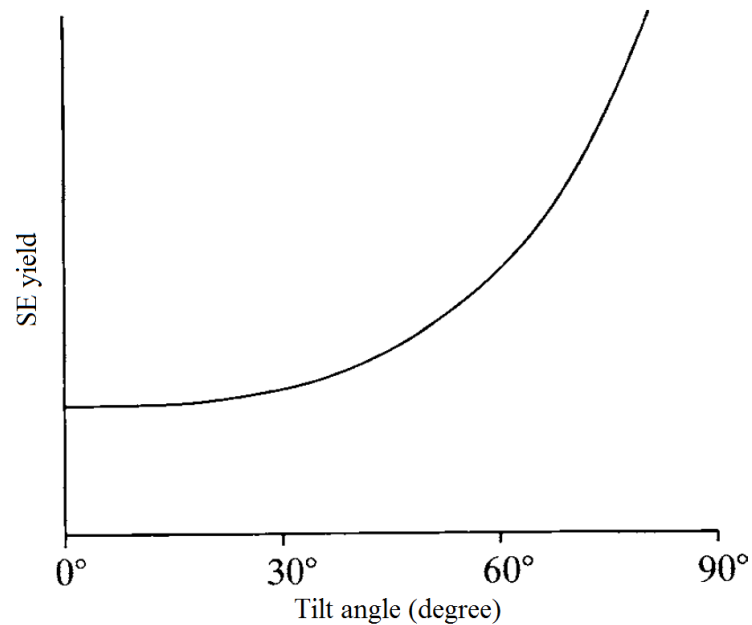


FIGURE 2.18: The variation of secondary-electron yield (SE-yield) with the angle of tilt of the sample surface relative to the incident beam. This figure is reproduced from [17].

blends, hydrogels, colloidal suspensions and micellar solutions [19–23]. Usually, a dried sample deposited on a conducting plate such as an indium tin oxide (ITO) plate or a cryo-fractured sample coated with a thin metal layer is irradiated with a high power electron beam. The image of the microstructure is recovered from the secondary electrons emitted or the electrons back-scattered from the sample.

A field effect scanning electron microscopy (ULTRA-PLUS FESEM) from Carl Zeiss is used for this thesis work. Fig. 2.17 shows a schematic diagram of the main components of a typical SEM setup. It consists of an electron column, a scanning system, a detector, a vacuum system and a display unit [16]. The electron column comprises an electron gun and two or more electromagnetic lenses. The electron gun produces a collimated beam of electrons of diameter $\sim 50 \mu\text{m}$ using a combination of a tungsten filament, a grid kept at a suitable negative potential and cathode coils. The free electrons generated from the filament are accelerated to energies in the range 1-100 keV. A set of electromagnetic lenses, each consisting of a copper coil carrying a direct current, surrounded by an iron shroud, focuses an electron beam down to 1 nm onto the surface of the specimen [16]. Each surface point of the specimen that is struck by accelerated electrons emits backscattered electrons (BSE) and secondary electrons (SE). BSEs are in fact a part of the incident electrons which enters the specimen and recoils from the atoms of the sample. On the other hand, the secondary electrons are ejected from the sample's atoms that are struck by the incident beam and the backscattered electrons. The secondary electrons are distinguishable from the BSEs owing to their much lower energies which is of the order of few electron volts [17].

In this work, secondary electrons are detected to obtain topographical images of microstructures of samples. Secondary electrons are ejected from the region very close to the sample's surface. The yield of the secondary electron increases with decreasing angle between the direct incident beam and the specimen surface (Fig. 2.18) [17]. The topographical information therefore contained in the spatial variation of the SE-yield value of a specimen surface. SE electrons are collected by an electron detector placed near the sample. The topographical information is obtained by sweeping the

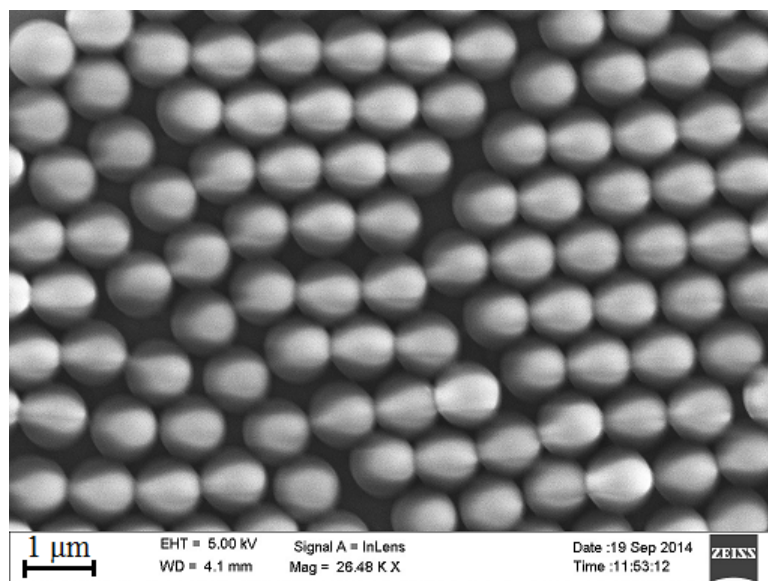


FIGURE 2.19: SEM image of polystyrene spheres obtained using a field effect scanning electron microscope (FESEM) from Carl Zeiss at an electron beam strength of 5 KeV. The average diameter measured is 996 ± 20 nm, which is very close the average diameter (1000 ± 100) quoted by the manufacturer (Bangs Laboratories, Inc.).

electron beam across the specimen in a raster while the output of an electron detector is amplified and displayed on the screen of a synchronously scanned visual display unit such as a computer monitor [16]. The electron imaging in this work is performed using a electron beam of strength in the range of 2 – 5 KeV.

2.2.7 Sample preparation for SEM measurements

Glass plates coated with indium tin oxide (ITO) are used to scan dried samples. The ITO surface is made hydrophilic by keeping the glass plate in a solution of H_2O_2 , NH_3OH and water in the ratio 1:3:7 at a temperature of 80°C for 5 hours. The glass plate is subsequently washed with deionised water and dried. A drop of $10\ \mu\text{L}$ of 1% w/v sample is spread on the hydrophilized ITO-glass plate and dried very fast (within 10 seconds) in an oven at a temperature of 200°C to avoid coagulation of colloidal particles. Data acquisition and size measurements are carried out using SmartSEM (Carl Zeiss) and ImageJ softwares respectively. Fig. 2.19 shows an SEM-micrograph

of standard polystyrene spheres procured from Bangs Laboratories, Inc. The average diameter measured on the micrograph is 996 ± 25 nm which is very closed to the value 1000 ± 100 nm specified by the supplier.

2.2.8 Sample preparation for cryo-SEM measurements

In this method, the sample under study is vitrified quickly using liquid nitrogen and is fractured before imaging. This method helps in preserving the internal microstructures of the sample. For our work, the samples are loaded in capillary tubes (procured from Hampton Research, USA) of bore size 1 mm using a syringe. The ends of the capillaries are then quickly sealed. A home made sample holder is used for holding the sample capillaries. The samples are vitrified using liquid nitrogen slush of temperature -207°C . The vitrified samples are then transferred in vacuum condition to a cryotransfer system (PP3000T from Quorum Technologies) kept at temperature -150°C . The samples are next fractured using an in-built knife and subsequently sublimated for 10-20 min depending on the nature of the sample at temperature -90°C . Finally, a thin layer (1 nm) of platinum is deposited on the surface of sample at temperature -150°C for the purpose of imaging. The samples are then transferred under vacuum onto the cold stage of FESEM.

References

- [1] A. P. Sarvazyan, O. V. Rudenko and W. L. Nyborg, *Ultrasound in medicine & biology*, 2010, **36**, 1379–1394.
- [2] R. L. Gibson and M. N. Toksoz, *The Journal of the Acoustical Society of America*, 1989, **85**, 1925–1934.
- [3] A. H. Harker and J. A. G. Temple, *Journal of Physics D: Applied Physics*, 1988, **21**, 1576.
- [4] A. S. Dukhin and P. J. Goetz, *Langmuir*, 1996, **12**, 4987–4997.
- [5] J. Happel, *AIChE Journal*, 1958, **4**, 197–201.
- [6] *User's Guide: DT1200*, Dispersion Technology Inc. (<http://www.dispersion.com>), 2012.
- [7] A. S. Dukhin and P. J. Goetz, *Characterization of Liquids, Nano- and Microparticulates, and Porous Bodies using Ultrasound*, Elsevier: New York, 2010.
- [8] B. J. Marlow, D. Fairhurst and H. P. Pendse, *Langmuir*, 1988, **4**, 611–626.
- [9] A. Dukhin and V. Shilov, *Journal of Colloid and Interface Science*, 2010, **346**, 248 – 253.

-
- [10] S. S. Dukhin and B. V. Derjaguin, *Electrokinetic phenomena, in: E. Matijevic (Ed.), Surface and Colloid Science*, Wiley, New York, NY, 1974.
- [11] *User's Guide: Agilent Technologies 5500 Scanning Probe Microscope*, 2008.
- [12] P. Eaton, and P. West, *Atomic Force Microscopy*, Oxford University Press, Oxford, 2010.
- [13] *User's Guide: MCR 501*, Anton Paar, www.antonpaar.com, 2013.
- [14] C. W. Macosko and R. G. Larson, *Rheology: principles, measurements, and applications*, VCH New York, 1994.
- [15] M. Laurati, S. U. Egelhaaf and G. Petekidis, *Journal of Rheology (1978-present)*, 2011, **55**, 673–706.
- [16] *User's Guide: ULTRA-PLUS FESEM*, Carl Zeiss, www.zeiss.com, 2013.
- [17] S. J. B. Reed, *Electron microprobe analysis and scanning electron microscopy in geology*, Cambridge University Press, 2005.
- [18] R. Egerton, *Physical principles of electron microscopy: an introduction to TEM, SEM, and AEM*, Springer Science & Business Media, 2006.
- [19] J. Bastacky, C. Wodley, R. LaBrie and C. Backhus, *Scanning*, 1987, **9**, 219–225.
- [20] S. L. Erlandsen, C. Ottenwaelter, C. Frethem and Y. Chen, *BioTechniques*, 2001, **31**, 300–305.
- [21] H. M. Wyss, M. Hütter, M. Müller, L. P. Meier and L. J. Gauckler, *Journal of colloid and interface science*, 2002, **248**, 340–346.
- [22] R. P. Apkarian, E. R. Wright, V. A. Seredyuk, S. Eustis, L. A. Lyon, V. P. Conticello and F. M. Menger, *Microscopy and Microanalysis*, 2003, **9**, 286–295.
- [23] R. Basak and R. Bandyopadhyay, *Langmuir*, 2013, **29**, 4350–4356.

3

Dispersibility of clay in aqueous suspensions: Dependence on concentration and age

3.1 Introduction

Laponite suspensions with concentration above 2% w/v undergo a spontaneous phase transition with time from a liquid-like state to a repulsion-dominated glassy phase through the physical aging process [1]. Aging in these systems occurs by the spatially and temporally correlated local rearrangements of particles that can overcome local energy barriers, with the system exploring progressively deeper energy wells in phase space [2]. It is also believed that a major factor contributing to the time-varying dynamics of freshly prepared aqueous Laponite suspensions is the swelling and subsequent

breakup of large Laponite clusters into smaller entities [3]. However, in most of the experimental studies undertaken previously, clusters of clay particles were assumed to exfoliate into individual platelets when dispersed in water. Several earlier studies also show that clay particles can exist as rigid aggregates, known as tactoids, that consist of more than one platelet oriented parallelly [4]. Many experimental methods e.g. atomic force microscopy (AFM), transmission electron microscopy (TEM), cryogenic scanning electron microscopy (Cryo-SEM), small angle X-ray scattering (SAXS), small angle neutron scattering (SANS), dynamic light scattering (DLS) and transient electrically induced birefringence (TEB) have been employed to characterize the tactoid sizes of clays in aqueous suspensions at different concentrations and under varying experimental conditions [5–10]. However, a systematic study of the particle size distribution (PSD) in aqueous clay suspensions and its dependence on clay volume fraction and suspension age is still lacking. Indeed, DLS has been used intensively for particle sizing, but its application is limited to very dilute suspensions where the single scattering mechanism and the Stokes-Einstein relation are valid. Several DLS studies show the onset of a sol-glass transition with increase in concentration and age of the clay suspensions [11–14]. Intensity auto-correlation data obtained in DLS experiments is typically analyzed in terms of a fast (τ_1) and a slow relaxation time (τ_2) [15]. However, it is very difficult to acquire PSD information from τ_1 and τ_2 in the glassy phase as the Stokes-Einstein relation is not valid for soft glasses.

The aim of this chapter is to investigate suspensions of Laponite clay in aqueous suspensions of different ages using ultrasound attenuation spectroscopy (UAS). As described in Chapter 2, the UAS technique offers a unique possibility of estimating PSDs for soft solid systems and can be used to analyze non-transparent and even highly structured systems. At the same time, it is a non-destructive technique that uses very low intensity ultrasound. The measurement does not, therefore, affect the sample micro-structures and yields an accurate estimate of average particle sizes and PSDs. Over the last two decades, this technique has been applied in different particulate systems of quartz, rutile, latex, alumina particles and also in emulsions [16]. In

this work, we measure ultrasound attenuation spectra to estimate PSDs of clay tactoids in Laponite suspensions in a concentrations range (1.5% – 4% w/v) where the suspensions spontaneously show liquid to soft solid transitions with increasing age. We have verified the results obtained with Laponite by performing similar experiments on Na-montmorillonite clay suspensions at low concentrations. The average platelet sizes estimated for Na-montmorillonite suspensions are then compared with scanning electron microscopy (SEM) data.

3.2 Sample preparation and experimental methods

Two different smectite clays: Laponite and Na-montmorillonite are investigated in this study. Laponite of RD grade (mass density 2.53 g/cc) is purchased from Southern Clay Products and Na-montmorillonite (mass density 2.60 g/cc) is procured from Nanocor Inc. The structural information of these clay minerals is provided in detail in Chapter 1 (Section 1.6). These clay minerals are highly hygroscopic and absorb water from the atmosphere into their interlayer spaces. The amount of absorbed water depends on the relative humidity of the atmosphere. To ensure good reproducibility of the sample composition, the clay mineral powder is heated in an oven at a temperature of 120°C for 24 hours to remove absorbed moisture before it is dispersed in highly deionized Milli-Q water under vigorous stirring conditions. The powder is added very slowly and in very small amounts to avoid the formation of large aggregates, following which the suspension is stirred vigorously for 45 minutes using an IKA Turrex drive to ensure a homogeneous distribution of the aggregates. The Na-montmorillonite suspension is stirred for 152 hours to avoid sedimentation before using for UAS and SEM measurements.

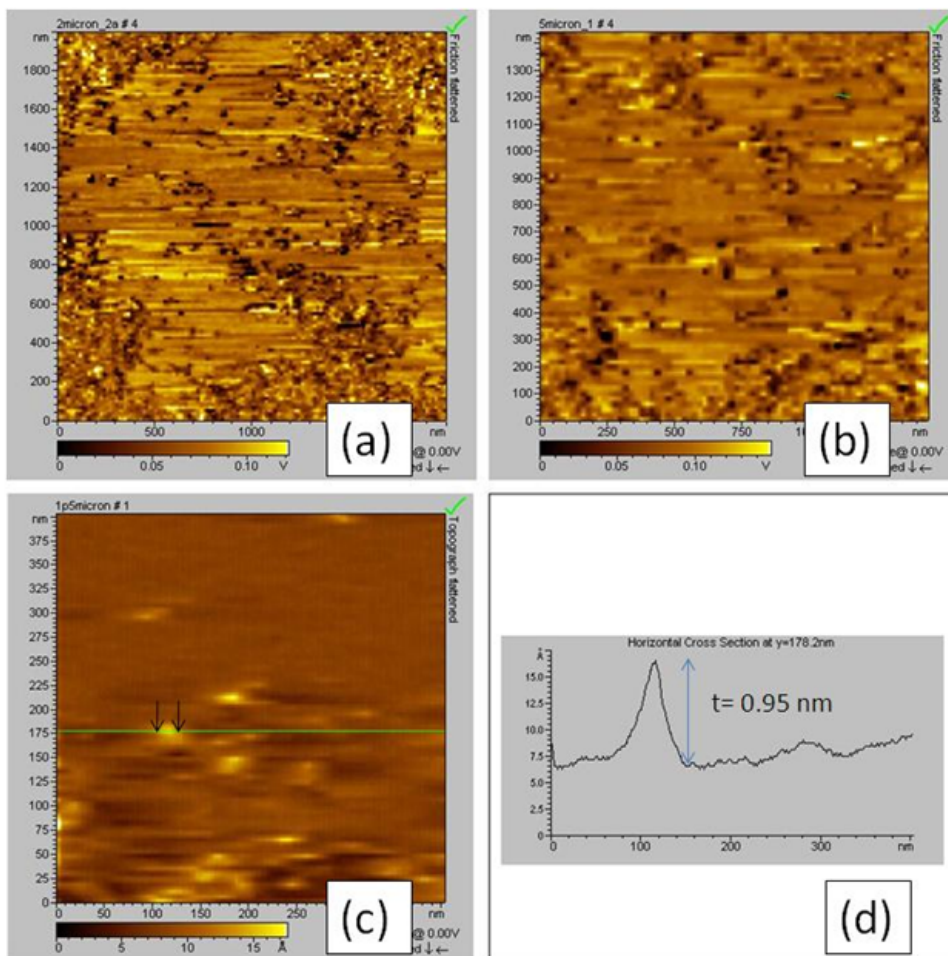


FIGURE 3.1: Representative AFM images of Laponite tactoids scanned in contact mode with different sized windows. Figures (a) and (b) correspond to the friction flattened images used for lateral size measurement. Figure (c) is a representative topographical image which is used to measure platelet thickness as shown in (d).

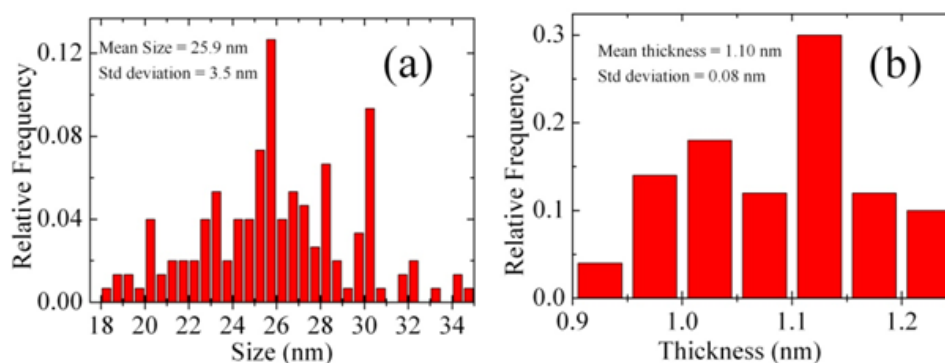


FIGURE 3.2: (a) Diameter distribution, estimated from 150 Laponite platelets selected in AFM micrographs. (b) The thickness distribution estimated for 30 isolated Laponite platelets selected carefully from AFM micrographs. The mean diameter d is the range of 22.4 – 29.4 nm and thickness $t = 1.10 \pm 0.08$ nm.

3.3 Results and discussion

We first measure the diameters and thickness of Laponite platelets using an atomic force microscope (AFM) in contact mode. A concentration of 0.05% w/v Laponite clay suspension, stirred for a week, is dried quickly at 150 °C on freshly cleaved mica sheets for imaging purpose. Details of the method for imaging using AFM and size measurements can be found in Chapter 2 (Section 2.2.4). Fig. 3.1 (a) and (b) show the friction flattened representative images of Laponite platelets obtained using an AFM in contact mode. The lateral size distribution of the platelets from these micrographs for 150 platelets is shown in Fig. 3.2(a). An average diameter, $d = 25.9$ nm, is measured from this distribution. The thicknesses of clay platelets are measured using topographical images as shown in Figs. 3.1 (c) and (d). An average platelet thickness of $t = 1.1 \pm 0.08$ nm is obtained from the distribution shown in Fig. 3.2(b). The values thus obtained from the AFM micrographs are very close to the platelet diameter (25 – 30) nm and thickness (1 nm) previously reported in the literature [11, 17].

Particle size distributions of Laponite particles in aqueous suspensions of different clay concentrations and sample ages are next estimated by measuring the attenuation spectra (attenuation coefficient α_v vs frequency ω) and sound speed using a DT-1200 acoustic spectrometer from Dispersion Technology Inc. The details of the ultrasound

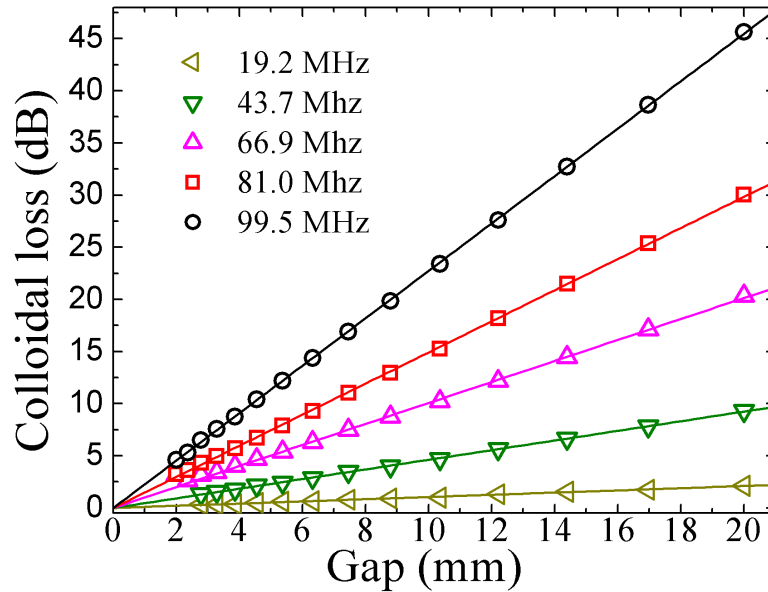


FIGURE 3.3: Colloidal loss ($\log \frac{I_0}{I_x}$) of ultrasound in a 3 % w/v Laponite suspension of age, $t_w = 6$ hours, plotted versus length of gap between transducers, at frequencies 19.2 MHz (\leftarrow), 43.7 MHz (∇), 66.9 MHz (\triangle), 81.0 MHz (\square) and 99.5 MHz (\circ). The solid straight lines are linear fits that show the validity of Beer-Lambert law (Eqn. 2.7 of Chapter 2). The gap between the two transducers is varied using a micrometer-precision step motor.

attenuation spectroscopy and the relevant theory are described in Chapter 2 (Section 2.2.1). All experiments are performed at 25 °C. We have tested the Beer Lambert law (Eqn. 2.7 of Chapter 2) in the Laponite suspensions for the calculation of the attenuation spectrum (Eqns. 2.1 – 2.6 of Chapter 2). Fig. 3.3 shows the colloidal loss ($\frac{I_0}{I_x}$) of a 3% w/v Laponite suspension with varying sample lengths (x) in the range 2 – 20 mm for different ultrasound frequencies. Here, I_0 is the incident intensity of ultrasound launched into the sample by a transmitting transducer and I_x is the attenuated intensity measured by a detecting transducer after the ultrasound passes through a sample of length x . It is seen from the fits to the data that the Beer-Lambert law (Eqn. 2.7 of Chapter 2) is valid for all the samples. To monitor the exfoliation state (the dispersibility) of clay tactoids, attenuation spectra are measured for different ages, t_w , of the clay suspensions by varying the ultrasound frequency in the range 10 to 99.5 MHz with a fixed sample length of 20 mm. Here, $t_w = 0$ is defined as the time at which the stirring

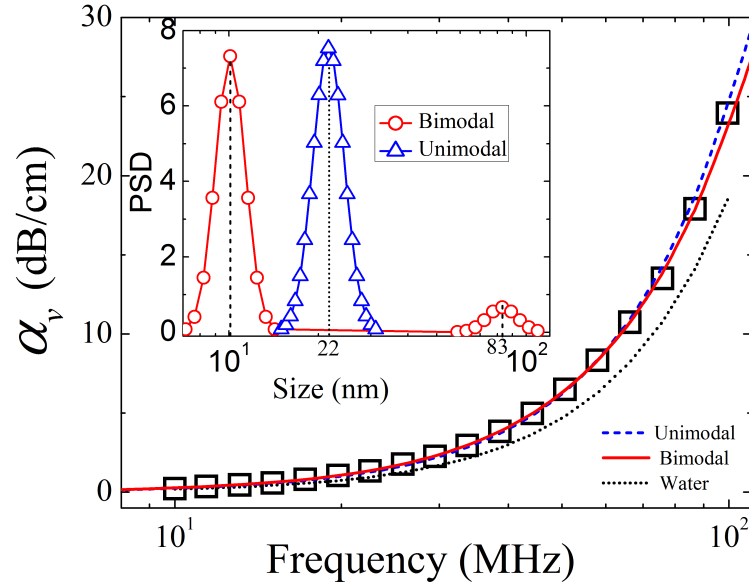


FIGURE 3.4: The attenuation spectrum (\square) for a 3% w/v Laponite suspension at $t_w = 6$ hours. The dashed and solid lines are theoretical fits considering unimodal and bimodal size distributions, respectively. The dotted line corresponds to the intrinsic attenuation in pure water. The inset shows the unimodal (\triangle) and bimodal (\circ) particle size distributions (PSDs) obtained from the theoretical fits to the attenuation spectrum.

of the sample is stopped. The sample is kept undisturbed during the whole experimental time to prevent destruction of the jammed structures that form as the suspension ages. The values of the parameters that have been used in Eqs. 2.1 – 2.6 to estimate theoretical prediction of attenuation are listed in Table 2.1.

Fig. 3.4 shows the measured attenuation spectrum (\square) for a 3% w/v Laponite suspension of age $t_w = 6$ hours. The dashed and solid lines are the theoretical fits for unimodal and bimodal PSDs respectively, estimated using a fitting algorithm and Eqs. 2.1 – 2.6 of Chapter 2. The unimodal fitting is obtained by adjusting median size (d_u) and standard deviation of the particle size distribution. On the other hand, the bimodal PSD, essentially a sum of two unimodal PSDs, is obtained by adjusting four parameters: the two median values (d_1 and d_2) of the lower and higher modes, their standard deviations (assumed to be of the same magnitude for both modes) and the relative volume fraction (ϕ_2) of particles in the higher mode. The fitting errors thus obtained are 3.6% for the unimodal distribution and 1.3% for the bimodal distribution. The PSDs

estimated from the two fits are plotted in the inset of Fig. 3.4 and can be seen to differ substantially.

As a clay platelet is anisotropic, the viscous loss is dependent on its orientation relative to the sound propagation direction. A disc moving edgewise causes greater viscous loss than a disc moving broadside [18, 19]. The theory for ultrasound attenuation (Eqns. 2.1 – 2.6 in Chapter 2), which is used to estimate sizes, considers the dispersed particles as spheres. The theoretical fits to the experimental data therefore yield an equivalent spherical diameter (ESD) d_s which can be related to the platelet dimension using the Jennings-Parslow relation for anisotropic particle under Stokes drag [20]:

$$d_s = d \left[\frac{3 \arctan \sqrt{\left(\frac{d}{t}\right)^2 - 1}}{2 \sqrt{\left(\frac{d}{t}\right)^2 - 1}} \right]^{\frac{1}{2}} \quad (3.1)$$

Here, d and t are the diameter and thickness of the disc. This equation can be solved graphically by rearranging as follows:

$$y_1(d) = y_2(d) \quad (3.2)$$

where $y_1(d) = \arctan \sqrt{\left(\frac{d}{t}\right)^2 - 1}$ and $y_2(d) = \frac{2}{3} \cdot \frac{d_s^2}{d^2} \cdot \sqrt{\left(\frac{d}{t}\right)^2 - 1}$. When $y_1(d)$ and $y_2(d)$ are plotted against d , the solution for the thickness t and disc diameter d corresponds to the intersection of the functions $y_1(d)$ and $y_2(d)$ for the supplied values of d_s (such as in Fig. 3.5).

The inset of Fig. 3.4 shows that the unimodal fit (Δ) to the attenuation curve has a median particle size value of 22 nm. We can estimate the thickness t of a tactoid from d_s by using Eqn. 3.2. Considering a one-dimensional stack of platelets, the optimum graphical solution of Eqn. 3.2 (shown in Fig. 3.5) gives a disc diameter d of 25 – 30 nm with a thickness $t = 9 \pm 1$ nm. As the thickness of a single platelet is 1 nm, this indicates that the majority of the tactoids in suspension are composed of 9 platelets. On the other hand, the bimodal fit (\circ in Fig. 3.4) gives two median values: $d_1 = 10$ nm for the lower mode and $d_2 = 83$ nm for the higher mode, with the relative concentration

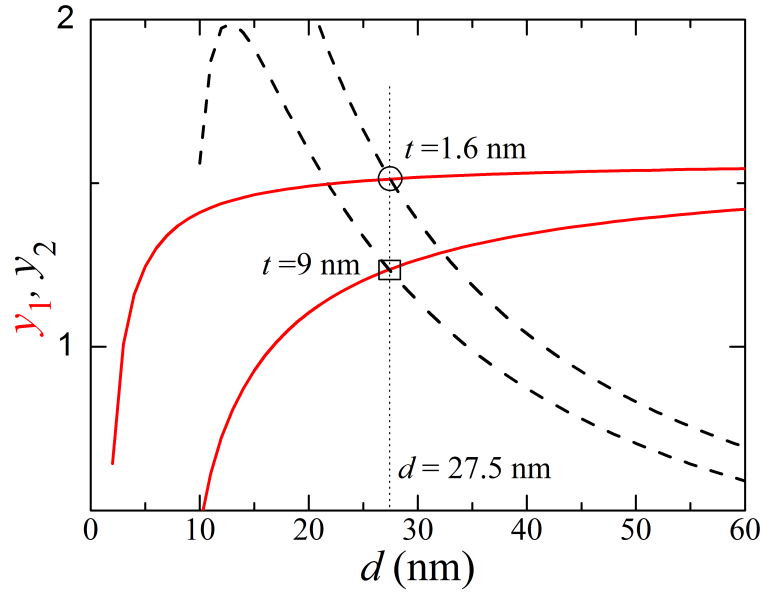


FIGURE 3.5: The graphical solutions of Eqn. 3.2 for different ESDs. The solution for the median size ($d_s = d_u = 22$ nm) obtained in the unimodal fit corresponds to a disc of diameter 25 – 30 nm when its thicknesses is $t = 9$ nm (indicated by a square). For the bimodal fit, a median size $d_1 = 10$ nm is obtained for the lower mode. This corresponds to a disc thickness of $t = 1.6$ nm (indicated by a circle). Here, $y_1 = \arctan \sqrt{(\frac{d}{t})^2 - 1}$ is plotted using solid lines and $y_2 = \frac{2}{3} \cdot \frac{d_s^2}{d^2} \cdot \sqrt{(\frac{d}{t})^2 - 1}$ is plotted using dashed lines.

ϕ_2 for the higher mode being around 10%. From the graphical solution of Eqn. 3.1 (shown in Fig. 3.5), $d_s = 10$ nm, corresponding to the lower mode of the bimodal fit, implies a thickness $t = 1.6 \pm 0.15$ nm for a disc diameter d of 25 – 30 nm. The bimodal assumption is therefore reasonable and confirms earlier reports that claimed the existence of very small Laponite tactoids in suspension [5–8]. The spread in the lower mode of the bimodal PSD indicates a size polydispersity and implies that tactoids with more than one platelet are also present in suspension.

The contribution to the higher mode of the bimodal distribution (inset of Fig. 3.4), with a median value (d_2) of 80 nm, is believed to be from larger aggregates and from a very small number of unavoidable bubbles. We should point out here that there is a fair possibility of the incomplete disintegration of some of the clay clusters in the aqueous medium [21]. The presence of small fractions of larger aggregates has also been shown in some previous studies, e.g. in electro-optical experiments with 0.01 wt% Laponite

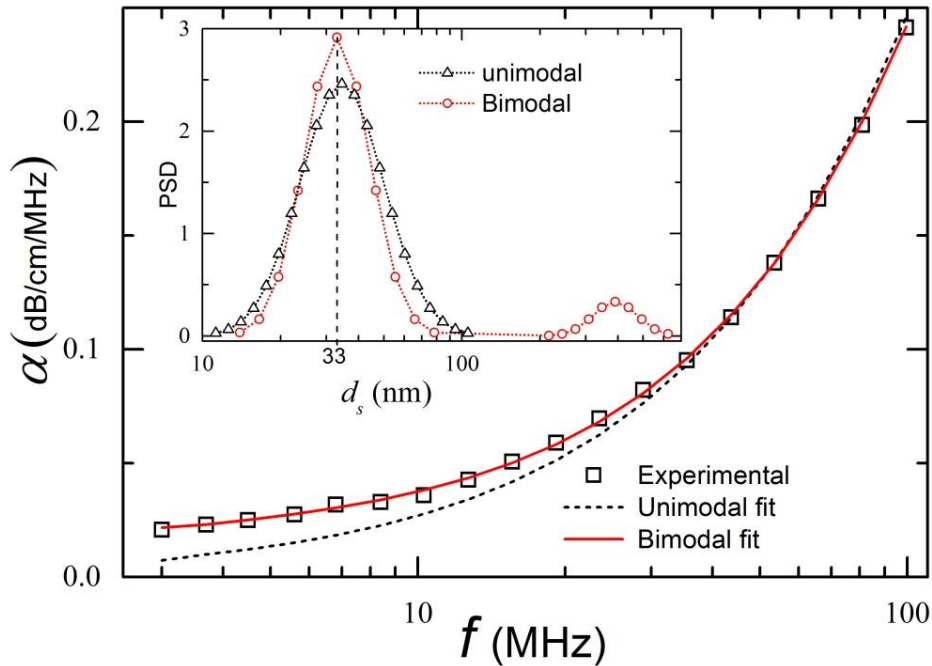


FIGURE 3.6: Attenuation spectrum (\square) measured in 1% w/v Na-montmorillonite suspension immediately after stirring for 152 hours. The dashed and solid lines are unimodal and bimodal fits to the attenuation spectrum respectively. Inset shows the unimodal PSD (Δ) and the bimodal PSD (\circ) estimated from the unimodal and bimodal fits to the attenuation spectrum.

suspensions [22]. We therefore believe that modeling the aggregate size distribution with a bimodal function is a better choice than the unimodal function, as the former can efficiently separate the contribution of the big aggregates.

Ultrasound attenuation measurements have also been performed in aqueous suspensions of another anisotropic colloidal clay, Na-montmorillonite, to verify the techniques already described. Compared to Laponite, Na-montmorillonite clay particles are more polydisperse in size and have irregular edge boundaries [23]. Fig. 3.6 shows the attenuation spectrum and the aggregate size distribution measured for 1% w/v Na-montmorillonite suspension immediately after stirring for 152 hours. It is seen in this figure that the unimodal approximation (dashed line) does not fit the attenuation spectrum properly (fitting error=18%), especially in the low frequency regime. On the other hand, the bimodal approximation (solid line) fits the attenuation loss data very well with fitting error of 2.4%. Inset shows the unimodal PSD (Δ) and the bimodal PSD (\circ) estimated from the unimodal and bimodal fits to the attenuation spectrum.

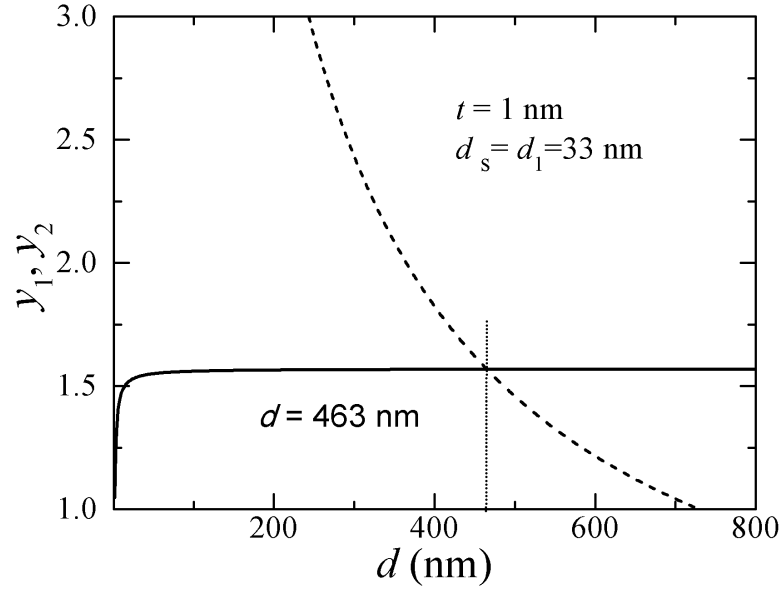


FIGURE 3.7: The graphical solution of Eqn. 3.2 for a median size $d_1 = d_s = 33$ nm. This corresponds to a platelet thickness of $t = 1$ nm for the Na-montmorillonite platelet and a disc diameter of $d = 463$ nm (indicated by a vertical dotted line). Here, $y_1 = \arctan \sqrt{(\frac{d}{t})^2 - 1}$ is plotted using the solid line and $y_2 = \frac{2}{3} \cdot \frac{d_s^2}{d^2} \cdot \sqrt{(\frac{d}{t})^2 - 1}$ is plotted using the dashed line.

The unimodal PSD has a median size of $d_u = 37$ nm, while the bimodal PSD has $d_1 = 33$ nm, $d_2 = 280$ nm and $\phi_2 = 11\%$. As the clay concentration is very low and the sample is stirred vigorously for several days, we can assume that a substantial part of clay aggregates are exfoliated into single platelets. We calculate diameter $d = 463$ nm using the graphical methods described earlier (Fig. 3.7) by considering a platelet thickness of $t = 1$ nm and the ESD, $d_1 = 33$ nm for the lower mode of bimodal size distribution. To verify the platelet diameter thus obtained, we have directly visualized the Na-montmorillonite platelets using scanning electron microscope (SEM). The details of the sample preparation, SEM imaging and size measurements are given in Chapter 2 (Sections 2.2.6 and 2.2.7). A representative SEM micrograph containing Na-montmorillonite platelets is shown in the inset of Fig. 3.8. Lateral size distribution of Na-montmorillonite platelet measured from the SEM micrographs is plotted in Fig. 3.8. The distribution gives a average lateral size of 425 nm which is close to the value (463 nm) obtained using the ultrasound measurements discussed above. The

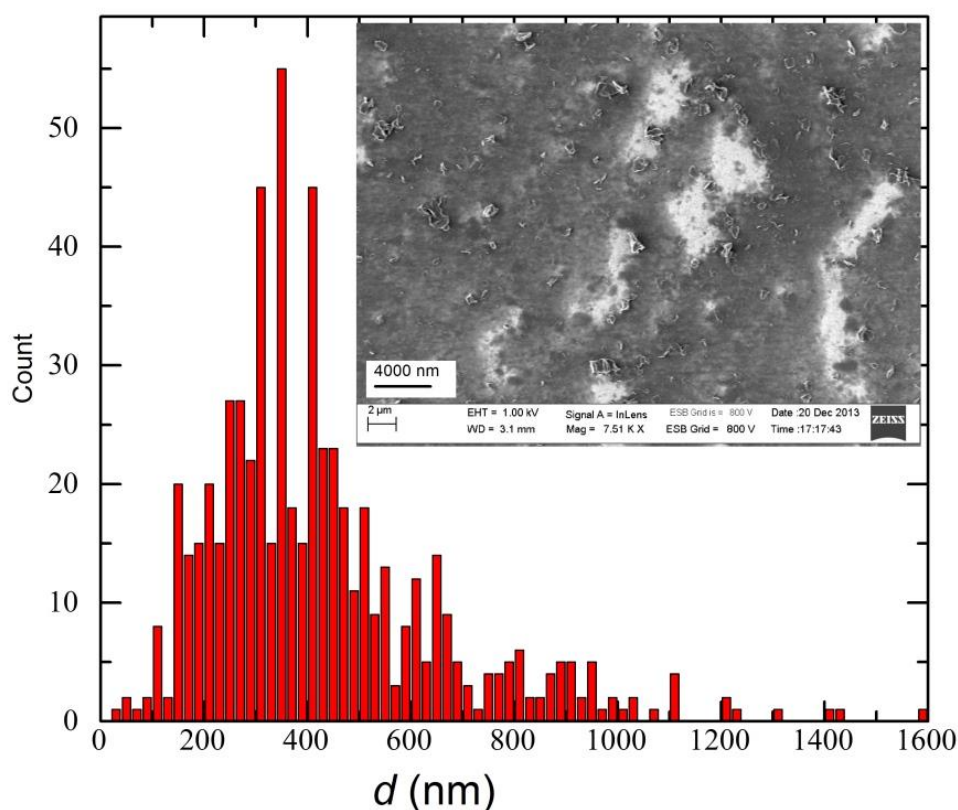


FIGURE 3.8: Lateral size distribution of Na-montmorillonite layers measured using SEM. Calculation of distribution is done with 600 single layers identified on SEM micrographs. The average diameter calculated from the distribution is 425 nm. Inset shows typical SEM micrographs containing Na-montmorillonite layers.

median size of the higher mode of the bimodal PSD fit, d_2 , corresponds to aggregates of several tactoids that exist in suspension because of the incomplete disintegration of the clay powder. These results confirm the feasibility of using ultrasound attenuation spectroscopy in the study of aging aqueous clay suspensions.

In powder form, Laponite clay comprises big clusters of tactoids. Upon dispersing in water, most of the clusters hydrate and disintegrate into smaller entities. The disintegration of the big tactoids happens due to the absorption of water in the successive monolayers, which, in turn, hydrates the sodium ions between each pair of platelets. The osmotic pressure of the hydrated sodium ions pushes the platelets apart in a process that leads to the absorption of more water layers. Finally, the screened Coulombic

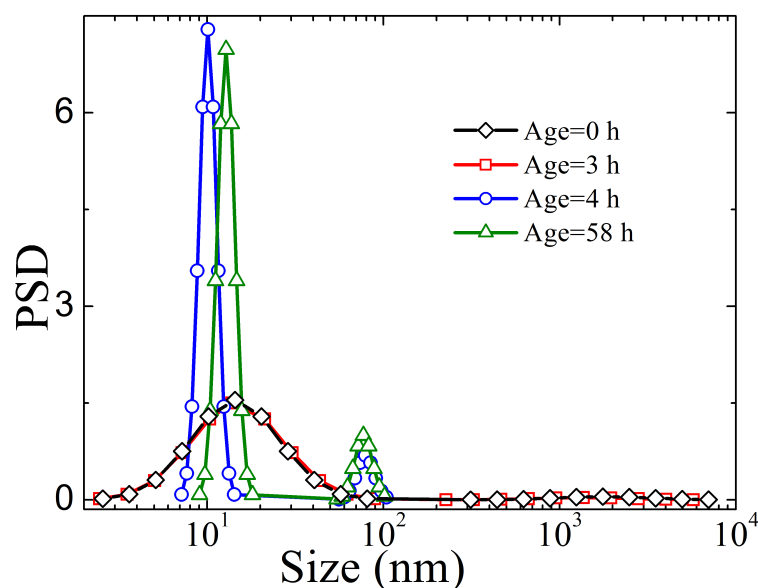


FIGURE 3.9: Bimodal size distributions of aggregates in 3% w/v Laponite suspension of $t_w = 0$ hour (\diamond), 3 hours (\square), 4 hours (\circ) and 58 hours (\triangle).

repulsions that develop between the platelets overcome the intra-platelet van der Waals attractions, resulting in tactoid exfoliation into smaller entities. As a new smaller tactoid is produced, the hydrated sodium ions distribute around the exposed negatively charged surfaces forming diffused layers that extend into the bulk water phase. The effective volume of each particle increases several times due to the presence of these electrical double layers.

It should be noted here that the fragmentation of clay particle is very fast during the initial stages of the stirring process. As the breakup process results in a build-up of strong inter-tactoid repulsions, the subsequent fragmentation becomes slower with time. The evolution of PSDs with t_w after the preparation of a 3% w/v Laponite suspensions is shown in Fig. 3.9. All the PSDs here are obtained from fits to bimodal distributions. For $t_w \leq 3$ hours, the distributions (data points are denoted by \diamond and \square in Fig. 3.9) show the presence of some big aggregates ($\phi_2 = 4\%$) that measure a few micrometers, while the rest of the aggregates are distributed around a median size d_1 of 14.6 nm but with a wide spread in sizes. We estimate the tactoid thickness of 3.5 nm from this median size in the lower mode by employing graphical solutions of Eqn. 3.1

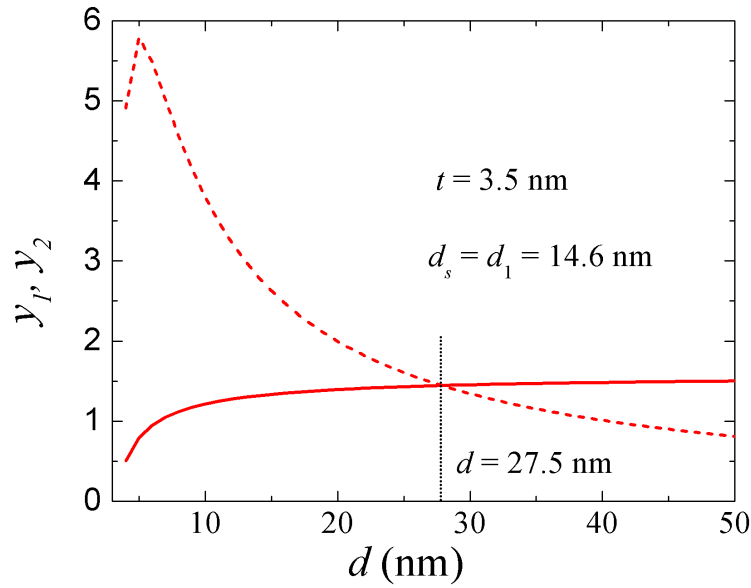


FIGURE 3.10: The graphical solution of Eqn. 3.2 for a median size $d_1 = d_s = 14.6$ nm. This corresponds to a tactoid thickness of $t = 3.5$ nm and a disc diameter of $d = 27.5$ nm (indicated by a vertical dotted line). Here, $y_1 = \arctan \sqrt{\left(\frac{d}{t}\right)^2 - 1}$ is plotted using a solid line and $y_2 = \frac{2}{3} \cdot \frac{d_s^2}{d^2} \cdot \sqrt{\left(\frac{d}{t}\right)^2 - 1}$ is plotted using a dashed line.

as shown in Fig. 3.10. This suggests that the lower mode is populated by tactoids composed of three to four platelets. However, as indicated by the broad distributions of the lower modes of the PSDs, tactoids with more than four platelets could also be present. At higher ages, most of the bigger aggregates are fragmented into smaller aggregates and there is the clear emergence of a higher mode of median size $d_2 = 80$ nm and $\phi_2 = 9\%$. The remaining tactoids have median size d_1 of 10 nm at $t_w = 4$ hours (\circ in Fig. 3.9). At this stage, the lower mode shows a very narrow distribution of sizes and most of the tactoids are composed of one to two tactoids as estimated before. As the sample ages, the size d_1 in the lower mode increases very slowly. This can be seen from the distribution at $t_w = 58$ hours (Δ). Since the re-coagulation of clay platelets are prevented due to strong repulsions, the increase in particle sizes could be due to the slow absorption of one or two layers of water by the tactoids comprising more than one platelet. The complete exfoliation of most of these swollen tactoids are prevented as the inter-tactoid repulsions are much stronger than the intra-tactoid repulsions. A slow

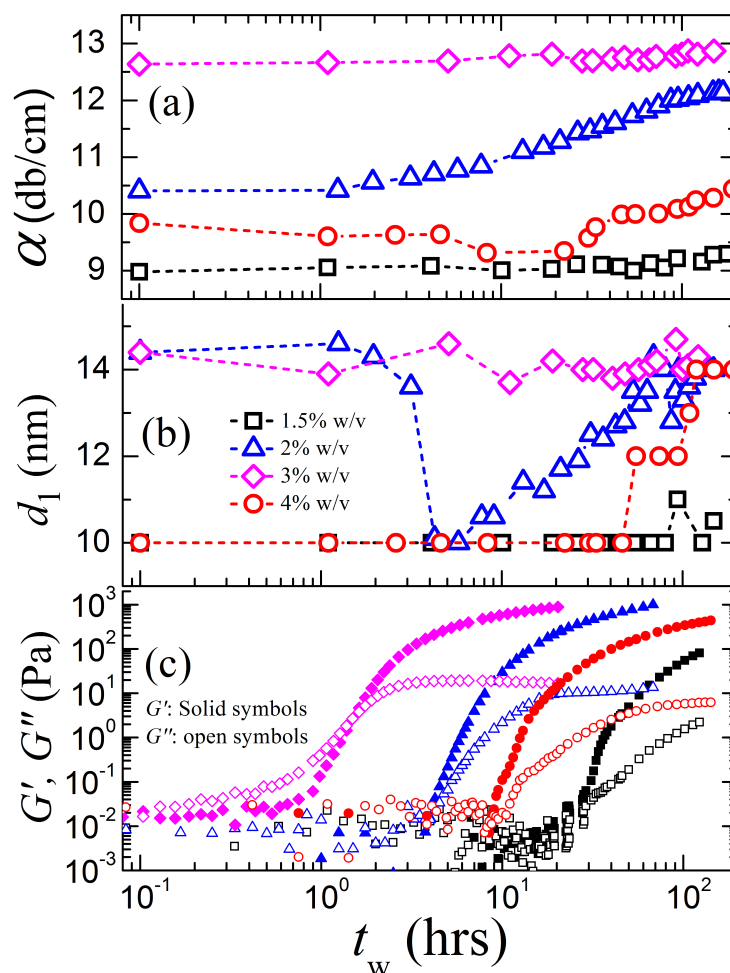


FIGURE 3.11: Evolutions of (a) the attenuation coefficient α_v at an ultrasound frequency of 66.3 MHz, (b) the median sizes d_1 and (c) the elastic moduli G' (solid symbols) and the viscous moduli G'' (open symbols) with age t_w for 1.5% w/v (\square), 2% w/v (\circ), 3% w/v (\triangle) and 4% w/v (\diamond) Laponite suspensions. For rheological measurements, oscillatory shear strains of amplitude $\gamma_0 = 0.5\%$ at an angular frequency of $\omega = 1$ rad/s were applied. Details of the experimental method for the rheological measurements can be found in Chapter 2 (Section 2.2.5).

growth of the inter-tactoid repulsions has been indicated in a previous study using X-ray photon correlation spectroscopy [24]. Such an increase in the repulsive force with suspension age explains the ergodic to non-ergodic transition observed frequently in experiments on Laponite suspensions of concentrations above 2% w/v [1]. The slow exfoliation of tactoids after sample preparation releases intercalated Na^+ ions into the bulk water. This contributes to an increase in suspension conductivity with age of the clay suspension and has been observed in a previous study [24, 25].

To find the dependence of exfoliation state (the dispersibility) on the clay concentration in the suspensions, we have repeated the acoustic measurements described above for Laponite suspensions of three other concentrations: 1.5%, 2% and 4% w/v. The major contribution to ultrasound attenuation is consistently seen to arise from the particles in the lower modes of the distributions. The evolutions of the attenuation coefficients α_v at a frequency of 66.3 MHz and the lower median size d_1 with t_w for all the four different concentrations are shown in Fig. 3.11(a) and Fig. 3.11(b), respectively. Even at other applied frequencies in the range 10 – 99.5 MHz, the trends reported below for α_v are repeated [26]. Due to the slow exfoliation and the swelling of the tactoids described earlier, the attenuation for the 3% w/v suspension (Δ) increases slowly over time and shows an approximately 16% increase before finally saturating. The 2% w/v sample (\circ) shows an increase in attenuation coefficient α_v and the lower mode of median size d_1 at a much later age when compared to the 3% w/v sample. The other two samples of concentrations 1.5% w/v (\square) and 4% w/v (\diamond) do not show any substantial change in α_v , with d_1 values remaining nearly constant at 10 nm and 14.6 nm, respectively. As the free volume in the 1.5% w/v suspension is quite large, most of the clusters break down to single platelets during the stirring period and a steady state is reached easily. This explains the constant values of α_v and d_1 for the 1.5% w/v suspension. On the other hand, the clusters in the 4% w/v suspension disintegrate into tactoids composed of two to three platelets during stirring, following which the suspension rapidly undergoes kinetic arrest due to the highly repulsive interactions between the tactoids. In this case, the inter-tactoid repulsions, which are much higher than the intra-tactoid repulsions, prevents further swelling and disintegration. This is clearly observed in Fig. 3.11(a) and Fig. 3.11(b). The enhancement of the inter-tactoid repulsions as a result of the exfoliation of the tactoids is confirmed qualitatively with the age-dependent viscoelastic responses of the Laponite suspensions. The evolutions of elastic modulus G' (solid symbols) and viscous modulus G'' (empty symbols) with t_w in freshly prepared Laponite suspensions of different clay concentrations are shown in Fig. 3.11(c). Soon after preparation, the 4% w/v Laponite suspension (\diamond) begins to

show a predominantly elastic response which indicates a jammed state. With aging, both the moduli increase rapidly by several decades due to microscopic rearrangements and the sample finally exhibits a predominantly elastic response. The 3% w/v suspension (Δ) starts exhibiting viscoelastic response at an age where the median size of particles drops to a minimum value (Fig. 3.11(b) and Fig. 3.11(c)). The origin of the enhanced mechanical moduli in the 1.5 % w/v Laponite suspension (\square) exhibited at very large ages cannot be related to the repulsion-induced jamming behavior as there is no change in tactoid sizes (\square in Fig. 3.11(b)). It has been well known that a Laponite platelet contains weak positive charges on its rim [27, 28]. The enhanced G' and G'' in the 1.5% w/v suspension can be attributed to the formation of gels due to the presence of face-rim attractive interactions between the suspended Laponite particles [1].

3.4 Conclusions

In this chapter, the exfoliation process of highly anisotropic particles of Laponite clay in aqueous suspensions is studied using ultrasound attenuation spectroscopy (UAS). As the aggregate sizes are smaller than the acoustic wavelength used, the calculated theoretical loss fits well to the experimental data considering only the visco-inertial interactions. The PSDs are extracted by modeling the data using bimodal distributions. The number of platelets per tactoid is estimated using an ESD formula proposed in the literature [20] and presented in Eqn. 3.1. The validity of using bimodal distribution and the ESD formula is verified using suspensions of Na-montmorillonite platelets. Our analysis confirms the presence of tactoids that consist of more than one platelet in Laponite suspensions of concentrations between 1.5% and 4% w/v. The viscous attenuation for concentrations below 1.5% w/v is very small and becomes comparable to the noise of measurement of the intrinsic attenuation. This results in difficulty in the analysis. Some earlier studies using SAXS, DLS, and AFM have demonstrated the presence of tactoids comprising more than one platelet in aqueous Laponite suspensions of concentrations less than 1.5% w/v [5–8]. A transient electrically induced birefringence

(TEB) study on Laponite RD suspensions has also indicated an increase in the average tactoid size with volume fraction of clay particles in the concentration range 0.1–0.8% w/v [9]. However, at very low concentration (0.025% w/v was studied in [10]), aggregates are found to quickly disperse into individual discs. The data from these previous studies, along with the results obtained from the ultrasound spectroscopy experiments reported here, indicate that the tactoid size distributions in aqueous suspensions of clay depend on the concentration of clay particles. The time evolution of PSDs in a 3% w/v Laponite suspension indicates that the polydispersity of tactoid sizes decreases substantially with age. The age evolution of the ultrasound attenuation coefficient α_v (and hence the PSDs) for different clay concentrations indicates a major role of electrostatic interactions in the tactoid exfoliation process. During the aggregate suspension process, when the inter-tactoid repulsions becomes comparable to the intra-tactoid repulsions, further exfoliation of the tactoids into smaller entities becomes very slow. We believe that this is the main reason behind the incomplete disintegration of clay clusters in the concentration range studied here. The present study therefore justifies our claim that UAS is a useful technique to elucidate the PSDs of colloidal suspensions whose concentrations lie in a range where other techniques like DLS or AFM often fail.

References

- [1] B. Ruzicka and E. Zaccarelli, *Soft Matter*, 2011, **7**, 1268–1286.
- [2] S. Jabbari-Farouji, R. Zargar, G. H. Wegdam and D. Bonn, *Soft Matter*, 2012, **8**, 5507–5512.
- [3] Y. M. Joshi, *The Journal of Chemical Physics*, 2007, **127**, 081102(1)–081102 (5).
- [4] W. B. Kleijn and J. D. Oster, *Clays and Clay Minerals*, 1982, **30**, 383.
- [5] D. W. Thompson and J. T. Butterworth, *Journal of Colloid and Interface Science*, 1992, **151**, 236 – 243.
- [6] J. M. Saunders, J. W. Goodwin, R. M. Richardson and B. Vincent, *The Journal of Physical Chemistry B*, 1999, **103**, 9211–9218.
- [7] L. Rosta and H. von Gunten, *Journal of Colloid and Interface Science*, 1990, **134**, 397 – 406.
- [8] E. Balnois, S. Durand-Vida and P. Levitz, *Langmuir*, 2003, **19**, 6633–6637.
- [9] A. Bakk, J. O. Fossum, G. J. da Silva, H. M. Adland, A. Mikkelsen and A. Elgsaeter, *Physical Review E*, 2002, **65**, 021407.
- [10] T. Nicolai*, and S. Cocard, *Langmuir*, 2000, **16**, 8189–8193.

-
- [11] M. Kroon, G. H. Wegdam and R. Sprik, *Physical Review E*, 1996, **54**, 6541–6550.
- [12] D. Bonn, H. Tanaka, G. Wegdam, H. Kellay and J. Meunier, *EPL (Europhysics Letters)*, 1999, **45**, 52.
- [13] B. Ruzicka, L. Zulian and G. Ruocco, *Physical Review Letters*, 2004, **93**, 258301.
- [14] S. Jabbari-Farouji, G. H. Wegdam and D. Bonn, *Physical Review E*, 2012, **86**, 041401.
- [15] B. Abou, D. Bonn and J. Meunier, *Physical Review E*, 2001, **64**, 021510.
- [16] A. S. Dukhin and P. J. Goetz, *Characterization of Liquids, Nano- and Microparticulates, and Porous Bodies using Ultrasound*, Elsevier: New York, 2010.
- [17] R. Avery and J. Ramsay, *Journal of Colloid and Interface Science*, 1986, **109**, 448 – 454.
- [18] A. S. Ahuja and W. R. Hende, *The Journal of the Acoustical Society of America*, 1978, **63**, 1074–1080.
- [19] F. Babick and A. Richter, *The Journal of the Acoustical Society of America*, 2006, **119**, 1441–1448.
- [20] B. R. Jennings and K. Parslow, *Proceedings of the Royal Society of London. A. Mathematical and Physical Sciences*, 1988, **419**, 137–149.
- [21] D. Bonn, H. Kellay, H. Tanaka, G. Wegdam and J. Meunier, *Langmuir*, 1999, **15**, 7534–7536.
- [22] A. M. Zhivkov and S. P. Stoylov, *Colloids and Surfaces A: Physicochemical and Engineering Aspects*, 2002, **209**, 315 – 318.
- [23] A. Cadene, S. Durand-Vidal, P. Turq and J. Brendle, *Journal of Colloid and Interface Science*, 2005, **285**, 719 – 730.

- [24] R. Bandyopadhyay, D. Liang, H. Yardimci, D. A. Sessoms, M. A. Borthwick, S. G. J. Mochrie, J. L. Harden and R. L. Leheny, *Physical Review Letters*, 2004, **93**, 228302.
- [25] A. Shahin and Y. M. Joshi, *Langmuir*, 2012, **28**, 15674–15686.
- [26] S. Ali, *Unpublished*.
- [27] B. Ruzicka, E. Zaccarelli, L. Zulian, R. Angelini, M. Sztucki, A. Moussaid, T. Narayanan and F. Sciortino, *Nature Materials*, 2011, **10**, 56 – 60.
- [28] S. L. Tawari, D. L. Koch and C. Cohen, *Journal of Colloid and Interface Science*, 2001, **240**, 54 – 66.

4

Exfoliation and stability of clay tactoids in aqueous suspensions: Dependence on ionic conditions

4.1 Introduction

In aqueous suspension, the powdered minerals of the natural clay Na-montmorillonite swell due to the absorption of water and exfoliate into smaller entities, known as tactoids, with electric double layers on their surfaces. The exfoliation rate of such tactoids in a synthetic Laponite clay suspension is seen to be greatly reduced at the jamming transition (Chapter 3). This results in the existence of tactoids that are composed of more than one platelet in the concentration regime where the suspensions usually show glassy behavior due to screened Coulomb repulsions.

Clay exfoliation involves the hydration of intercalated Na^+ counterions during the crystalline swelling of tactoids and the subsequent release of counterions into the bulk medium through the process of diffusion [1–3]. The diffusion of counterions strongly depends on the osmotic pressure difference between the intertactoid space and the bulk medium, and also on the affinity of the basal surface to the counterions. When a tactoid exfoliates into smaller entities, the hydrated counterions redistribute around the clay particle immediately to reach an electrostatic equilibrium. The presence of the counterions in the bulk medium further reduces the osmotic pressure difference between the intratactoid and intertactoid spaces. This may have a reverse effect on the subsequent tactoid exfoliation process, especially in the high concentration regime. This fact has never been tested experimentally in the literature.

There have been several experimental, theoretical and simulation studies to address the swelling mechanism of 2:1 layered clay minerals [4–14]. These studies have been very significant in understanding the different kinds of swelling mechanisms, namely, crystalline and osmotic swelling, *etc.* However, it is also crucial to understand the effects of inter-tactoid repulsion and counterion concentration on the exfoliation state and on the stability of the suspensions under gravity.

The understanding of the exfoliation kinetics and stability of Na-montmorillonite in suspension is very important due to their wide use as fillers in polymer-clay nanocomposites [15–17], as absorbents for the treatment of contaminated water and radio-active waste [18–20], as thickeners in paints and drilling fluids [21], as an emulsifying agent that results in high stability against coalescence [22], as an adsorber of RNA and DNA molecules [23, 24], as an active green catalyst [25] and in bio-sensing applications [26, 27].

In this chapter, we monitor the evolution of the size distribution of Na-montmorillonite tactoids/aggregates with suspension age for different clay mineral concentrations and counterion conditions by employing ultrasound attenuation spectroscopy (UAS). The effect of different ionic conditions on tactoid exfoliation and its subsequent influence on the stability and viscoelasticity of Na-montmorillonite gels in the low clay mineral

concentration regime (below the glass transition concentration) are further investigated using electroacoustic spectroscopy and rheometry.

4.2 Sample preparation

Two different clays, Laponite and Na-montmorillonite, are used for the present work. The structural information of these clays is provided in detail in Chapter 1 (Section 1.6). The clay mineral powder is heated in an oven at a temperature of 120°C for 24 hours to remove absorbed moisture before it is dispersed in highly deionized Milli-Q water under vigorous stirring conditions. The preparation of Laponite suspensions are described in Chapter 3. After dispersing Na-montmorillonite powder in Milli-Q water, the mixture is next stirred vigorously for three hours using a magnetic stirrer to ensure a homogeneous distribution of the aggregates. The age $t_w = 0$ is defined as the time at which the stirring of the sample is stopped. The Na-montmorillonite samples with added NaCl salt are prepared following two different protocols. In the first protocol, a NaCl salt solution (brine) of the required molarity is prepared and then Na-montmorillonite powder is added to the brine and stirred for 3 hours. These samples are designated as SBC (Salt added Before Clay mineral). In the second protocol, the required amount of salt is added to an aqueous suspension of Na-montmorillonite of different ages. These samples are designated as SAC (Salt added After Clay mineral). These mixtures are stirred for thirty minutes after the addition of salt to ensure homogenization. All samples are kept under vacuum conditions (pressure of 160 mmHg for two minutes) to remove trapped air bubbles from the suspensions.

4.3 Results and discussion

Tactoid size distribution of Na-montmorillonite is estimated by measuring the attenuation spectrum (attenuation coefficient α_v vs frequency ω) and sound speed using a DT-1200 acoustic spectrometer from Dispersion Technology Inc. [28]. Details of the

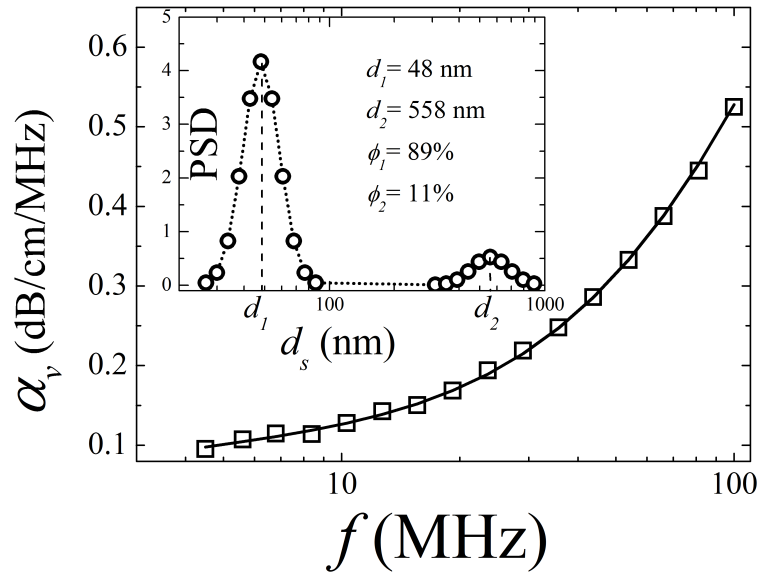


FIGURE 4.1: Attenuation spectrum measured for a $\phi_w = 4\%$ w/v Na-montmorillonite suspension at age $t_w = 45$ hours. The solid line is the bimodal fit to the experimental data. The inset shows the bimodal PSD estimated by theoretical fitting. The dotted lines in the inset are guides to the eye.

experimental setup and the measurement methods are provided in Chapter 2. The attenuation spectra are measured for different ages, t_w , and particle concentrations, ϕ_w , of Na-montmorillonite suspensions by varying the ultrasound frequency in logarithmic steps in the range 3 to 99.5 MHz and for 12 different sample gaps ranging from 5 mm to 20 mm. The samples are continuously pumped through the cell to prevent sedimentation. Prior to these experiments, the sample cell is calibrated for acoustic diffraction using Milli-Q water. All the experiments reported here are performed at 25 °C.

For the clay suspensions studied here, the unimodal approximation does not fit the attenuation spectrum properly, especially in the low frequency regime (Fig. 3.6 of Chapter 3). We therefore estimate bimodal particle size distributions (PSDs) from the measured attenuation spectra using a combination of theory and an analysis algorithm detailed in Chapter 2 (Section 2.2.1). The validity of the bimodal size distribution has already been established in the context of suspensions of both Laponite and Na-montmorillonite in Chapter 3 [29]. A representative attenuation spectrum and estimated bimodal PSD using Eqns. 2.1 – 2.7 of Chapter 2 is shown in Fig. 4.1 for a

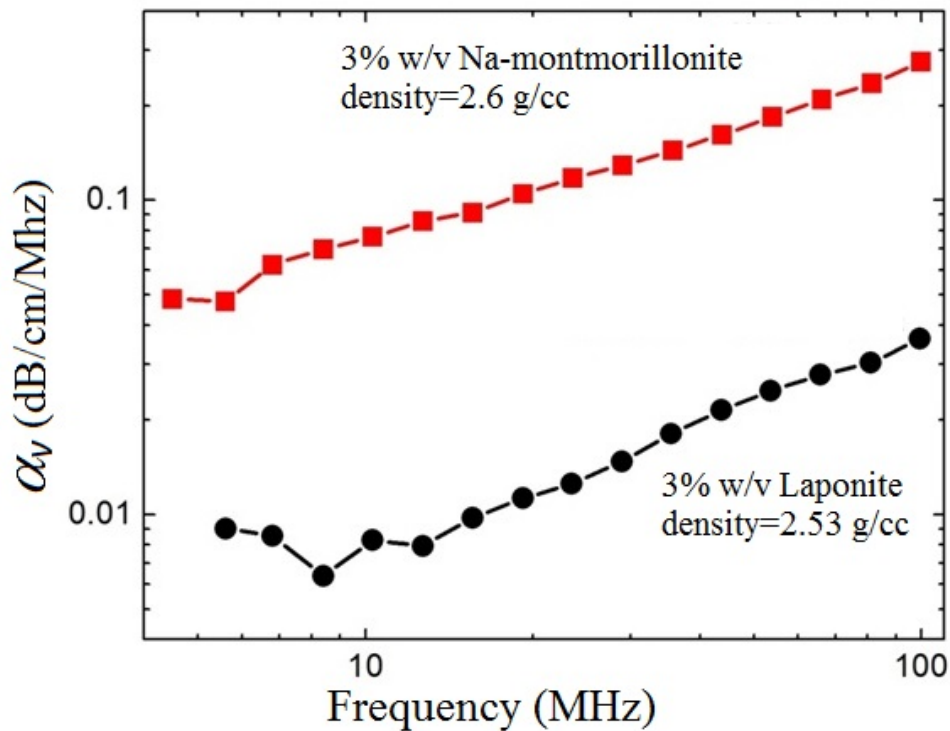


FIGURE 4.2: Ultrasound attenuation spectra measured for 3% w/v Na-montmorillonite (■) and 3% w/v Laponite (●) suspensions at age $t_w = 24$ hours.

4% w/v Na-montmorillonite suspension at $t_w = 45$ hours. The bimodal PSD for this sample is characterized by lower median size of $d_1 = 48$ nm and higher median size $d_2 = 558$ nm with a relative volume fraction $\phi_2 = 11\%$ of particles in the higher mode. The values of the parameters that have been used in Eqns. 2.1 – 2.6 to estimate PSDs are listed in Table 2.1 of Chapter 2.

The coefficient of viscous attenuation, α_v , decreases with decreasing particle size for an identical concentrations of particles. This has been reported in the literature, for example, in a 10% w/v colloidal suspension of silica particles (Ludox) of sizes 11 nm - 31 nm [28]. We also verify this behavior for suspensions of Laponite and Na-montmorillonite particles, both of which have the same average thickness of 1 nm and average diameters of 30 nm and 425 nm, respectively (Fig. 4.2). The densities of these two clay minerals are very close (2.53 g/cc and 2.61 g/cc). However, the attenuation in 3% w/v Na-montmorillonite suspensions (■ in Fig. 4.2) is much higher than that observed in the 3% w/v Laponite suspensions (● in Fig. 4.2) due to the higher

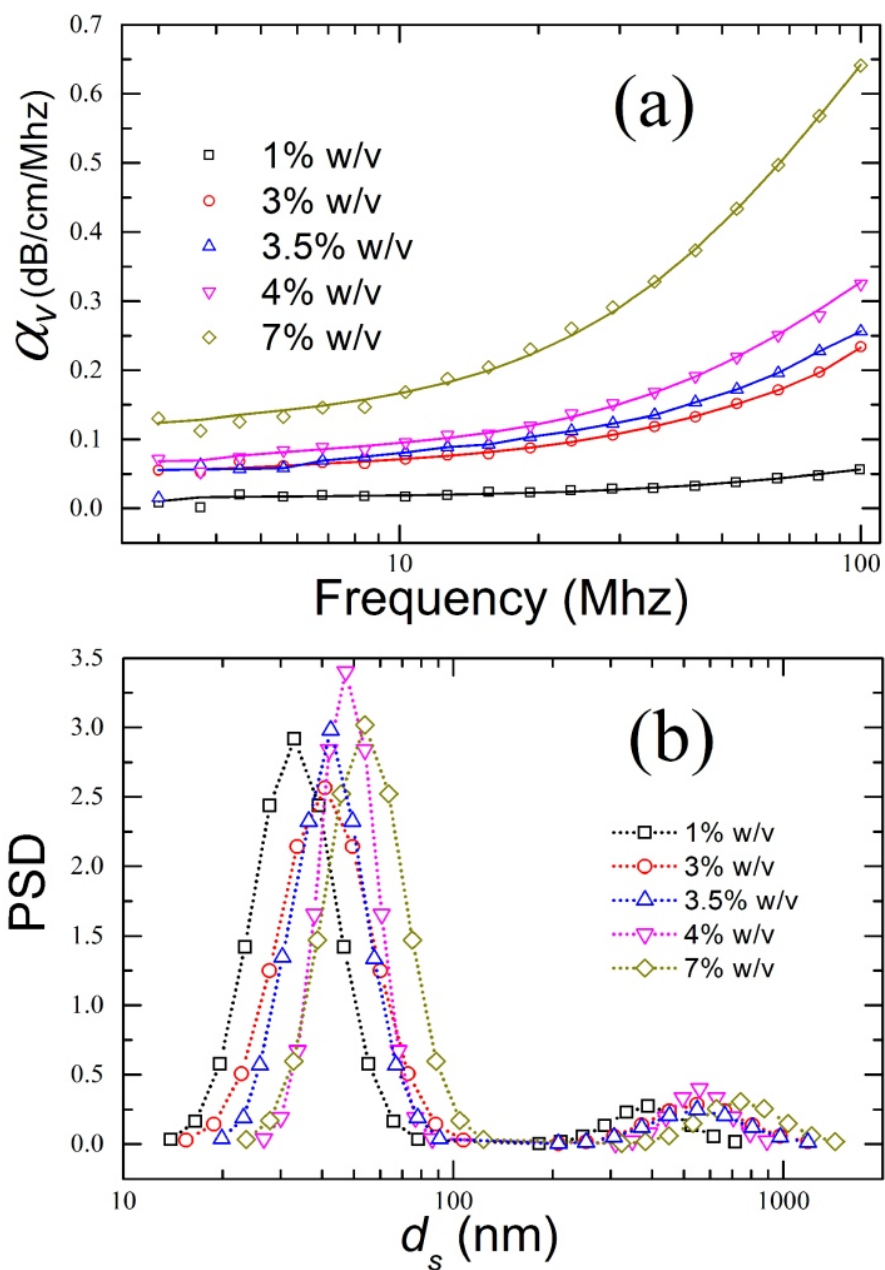


FIGURE 4.3: (a) Ultrasound attenuation spectra and (b) estimated bimodal particle size distributions (PSDs) measured in 1% w/v (\square), 3% w/v (\circ), 3.5% w/v (\triangle), 4% w/v (∇) and 7% w/v (\diamond) suspensions of Na-montmorillonite of age $t_w = 166$ hours. The solid lines in (a) correspond to the bimodal fits to the experimental data.

lateral size of the Na-montmorillonite particles. Under an acoustic field, the motion of the bigger particle is associated with a higher phase lag. This results in the observed higher values of α_v in the viscous attenuation regime.

We use the changes in the values of α_v to monitor the exfoliation kinetics of Na-montmorillonite tactoids in aging suspensions of different concentrations characterized by different t_w values. Fig. 4.3 (a) shows the attenuation spectra measured for suspensions of age $t_w = 166$ hours and Na-montmorillonite concentrations ϕ_w in the range 1 – 7% w/v. It is seen that α_v increases monotonically with increasing clay concentration in the entire ultrasound frequency range (3 – 99.5 MHz) investigated here. The bimodal size distributions of clay particles in the suspensions estimated from these attenuation spectra are shown in Fig. 4.3 (b). These distributions clearly show that both the median sizes (d_1 and d_2) increase monotonically with increasing ϕ_w . This indicates that the degree of exfoliation of clay tactoids decreases with increasing ϕ_w .

To understand the kinetics of the exfoliation process with time, the evolutions of the normalized attenuation coefficients α_{vw} ($= \alpha_v/\phi_w$) with t_w , at a typical ultrasound frequency $f = 53.6$ MHz, for ϕ_w values in the range 1 – 7% w/v, are shown in Fig. 4.4(a). It indicates two different ϕ_w -dependent regimes of tactoid exfoliation. For $\phi_w < 4\%$ w/v (\square , \circ and \triangle in Fig. 4.4(a) correspond to $\phi_w = 1, 3$ and 3.5% w/v respectively), α_{vw} decreases rapidly and reaches stationary values. The rate of decay of α_{vw} in these samples increases with decreasing ϕ_w . This indicates faster exfoliation of mineral layers from tactoids in samples with lower ϕ_w . In contrast, for $\phi_w \geq 4\%$ w/v (∇ and \diamond in Fig. 4.4(a) correspond to $\phi_w = 4$ and 7% w/v respectively), no significant changes in α_{vw} are observed except at the initial ages after sample preparation. The plateau value of α_{vw} increases with increase in ϕ_w , indicating that the exfoliation mechanism slows down with the increase in ϕ_w .

A clearer picture of the exfoliation state is obtained when particle sizes are estimated for suspensions with different clay concentrations and ages. For the sake of simplicity, only the d_1 value, which approximately accounts for 90% of the clay mineral content, is plotted in Fig. 4.4(b) against sample ages. After decreasing initially,

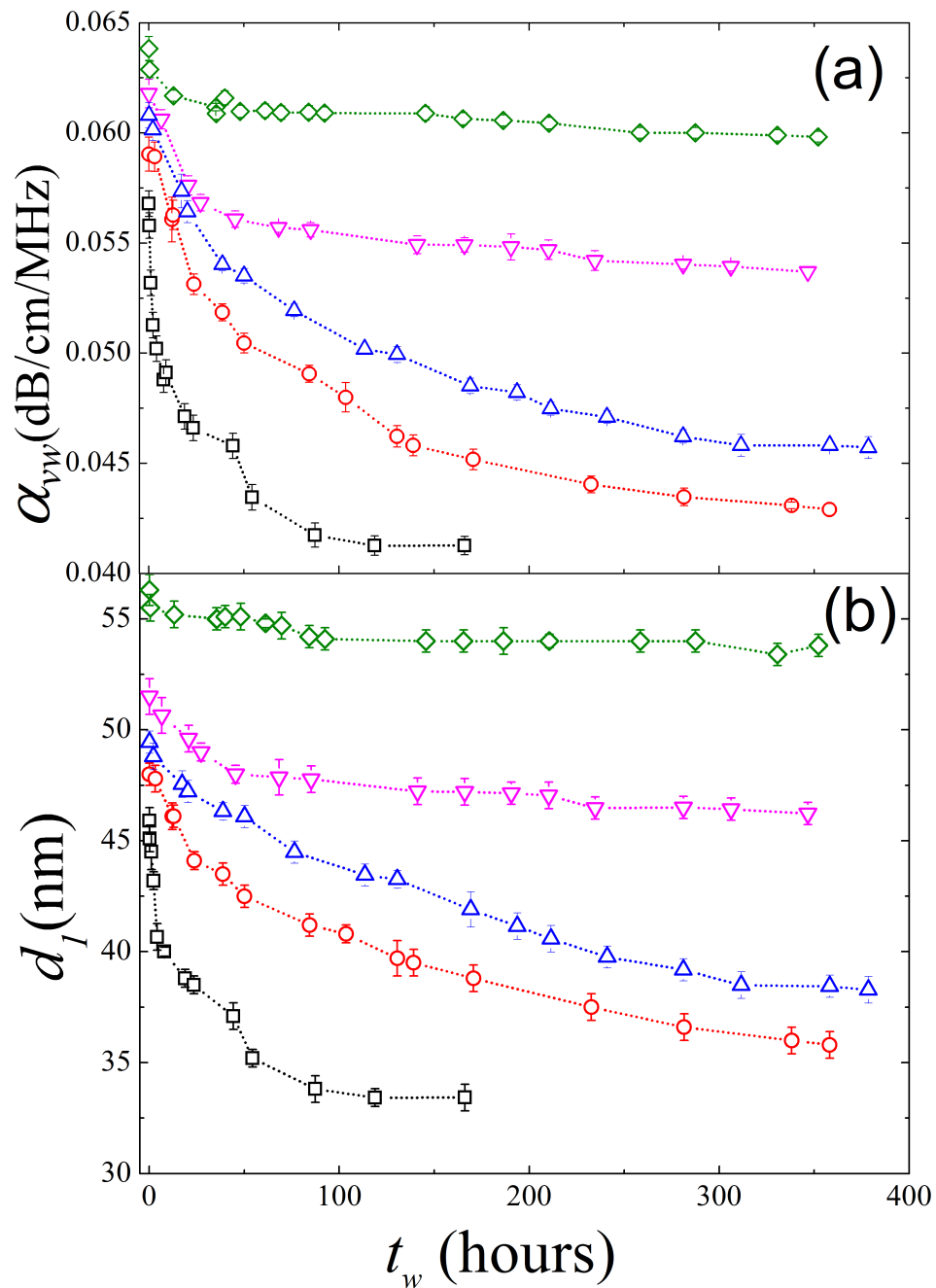


FIGURE 4.4: Evolutions of (a) the specific attenuation coefficient α_{vw} ($=\alpha_v/\phi_w$) at an ultrasound frequency of 53.6 MHz and (b) the lower median size d_1 with age t_w for 1% w/v (\square), 3% w/v (\circ), 3.5% w/v (\triangle), 4% w/v (∇) and 7% w/v (\diamond) Na-montmorillonite suspensions. The dotted lines are guides to the eye.

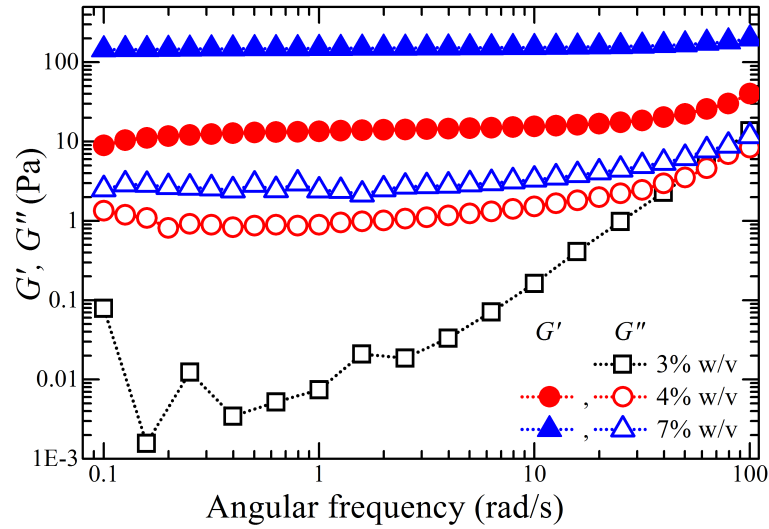


FIGURE 4.5: Frequency dependence of storage modulus G' (solid symbols) and loss modulus G'' (empty symbols) of Na-montmorillonite suspensions at $\phi_w = 3\%$ w/v (\square), 4% w/v (\circ) and 7% w/v (\triangle) at age $t_w = 24$ hours. An oscillatory shear strain amplitude of 0.5% was applied in these experiments. The samples are pre-sheared using a large oscillatory stress (60 Pa at an angular frequency ω of 10 rad/s) for one minute to achieve a reproducible starting point for all experiments. After inducing shear-melting by this process, all samples are left undisturbed to evolve for 3 hours before performing the frequency sweep experiments. The details of the rheometer used can be found in Section 2.2.5 of Chapter 2.

no significant change in d_1 values is seen for the two samples with $\phi_w = 4\%$ w/v and 7% w/v at $t_w \geq 24$ hours (denoted by ∇ and \diamond in Fig. 4.4(b)). We have investigated the viscoelastic properties of these suspensions at $t_w = 24$ hours using frequency sweep measurements that are performed by varying the angular frequency from 0.1 rad/s to 100 rad/s at a very small strain amplitude of 0.2% (Fig. 4.5). Interestingly, we find that $\phi_w = 4\%$ w/v lies close to the glass transition concentration ϕ_j and the soft glassy response of this sample can be observed from the frequency sweep data (\circ in Fig. 4.5). It is seen in this figure that for the samples with $\phi_w = 4\%$ w/v and 7% w/v, the elastic moduli G' of the suspensions are almost frequency independent and much larger than the corresponding viscous moduli G'' . It is also noted in this regime that the measured G'' values are weakly dependent on the applied shearing frequencies. These are typical signatures of soft glassy rheology [30]. The suspension with Na-montmorillonite concentration of 3% w/v (i.e. $\phi_w < \phi_j$) does not show any elastic response, with G''

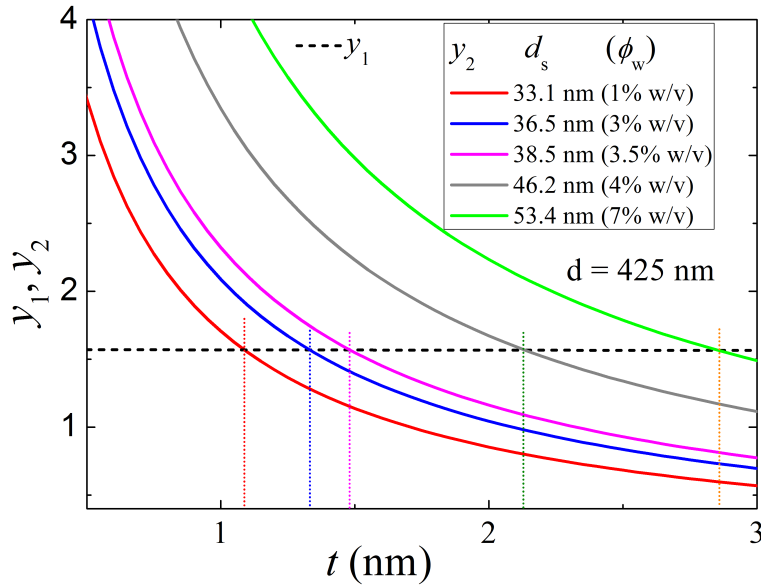


FIGURE 4.6: The graphical solutions of Eqn. 3.1 of Chapter 3 for different ESDs $d_s = d_1$ at $t_w = 320$ hours obtained for clay concentrations $\phi_w = 1\%$ w/v (red), 3% w/v (blue), 3.5% w/v (magenta), 4% w/v (gray) and 7% w/v (green). An average lateral size of $d = 425$ nm is used for the calculations. Here, $y_1 = \arctan \sqrt{(\frac{d}{t})^2 - 1}$ is plotted using dashed line and $y_2 = \frac{2}{3} \cdot \frac{d_s^2}{d^2} \cdot \sqrt{(\frac{d}{t})^2 - 1}$ is plotted using solid lines. The thicknesses calculated here for different ϕ_w is plotted in Fig. 4.7.

(□ in Fig. 4.5) showing an almost power law dependence that is typical of a liquid-like sample and not of a soft glass.

We have reported the exfoliation behavior of synthetic Laponite suspensions in Chapter 3. In this chapter, we argued that the strong intertactoid repulsive interactions at the jamming concentration ϕ_j restricts the complete exfoliation of the remaining tactoids in Laponite suspensions. Interestingly, it is seen in the present study that even when the sample concentration is less than ϕ_j ($=4\%$ w/v) the values of α_{vw} and d_1 measured for 3% w/v and 3.5% w/v (denoted by ○ and △ in Fig. 4.4) reach plateaus at higher ages, at values that are much higher than those for 1% w/v sample (□ in Fig. 4.4). We next extract the average thickness t of Na-montmorillonite tactoid from the measured values of the equivalent spherical diameters ($d_s = d_1$) of the lower mode, d_1 , using the formalism developed in Chapter 3 based on the Jennings–Parslow relation (Eqn. 2.1 of Chapter 2) [29, 31]. The average lateral size of $d = 425$ nm measured

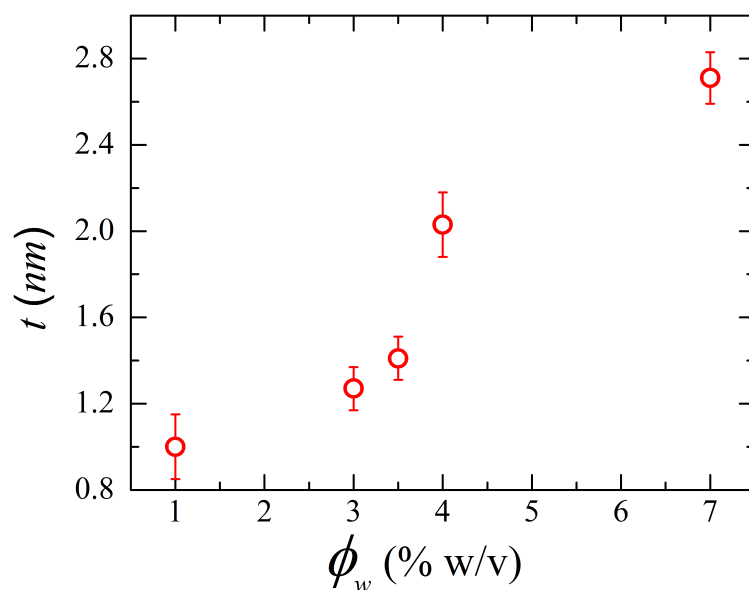


FIGURE 4.7: Variation of Na-montmorillonite tactoid thicknesses estimated from the equivalent spherical sizes d_1 at $t_w = 320$ hours using Jennings-Parslow relation (Eqn. 3.1 of Chapter 3). The average diameter of 425 nm for the tactoids is measured using field effect scanning electron microscopy (FESEM) as shown in Fig. 3.8 of Chapter 3.

using SEM (Fig. 3.8 of Chapter 3) is used in Eqn. 3.2 of Chapter 3 to calculate t by employing graphical methods (Fig. 4.6). The average thickness t of tactoids calculated is seen to increase with Na-montmorillonite concentration even below $\phi_w = 4\%$ w/v (Fig. 4.7). This clearly indicates that complete exfoliation of the tactoids is not accomplished below the jamming transition ϕ_j and that, in addition to repulsive interactions, there is the possibility of other dominant physicochemical factors that can influence tactoid exfoliation.

The conductivity of Na-montmorillonite suspensions is next measured using a high frequency ac electric field. Details of the conductivity measurement method can be found in Chapter 2 (Section 2.2.3). The contribution to the conductivity K comes from the hydrated Na^+ counterions that are dissociated during the exfoliation of the tactoids in the aqueous suspension. Fig. 4.8 shows a decrease in the normalized conductivity $\sigma_w (=K/\phi_w)$ with ϕ_w at age $t_w = 320$ hours. For complete exfoliation, the value of σ_w is expected to remain constant with changes in ϕ_w . This observation verifies our previous result, reported in Fig. 4.4 and Fig. 4.7, that the degree of exfoliation (or the

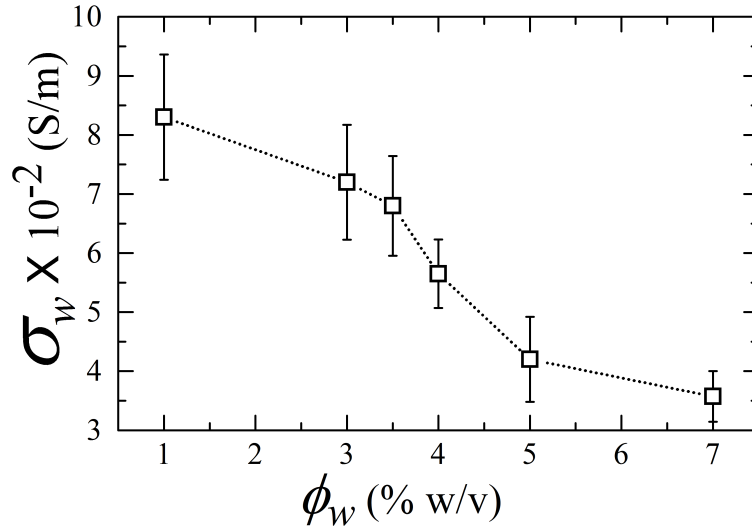


FIGURE 4.8: Normalized conductivity $\sigma_w (= K/\phi_w)$ measured for different concentrations ϕ_w of Na-montmorillonite suspensions of age $t_w = 320$ hours.

dispersibility) decreases at higher concentrations of clay mineral.

It has been mentioned earlier that the observed slowdown in the exfoliation kinetics above ϕ_j can be attributed at least partially to the large repulsive inter-particle interactions. It is also to be noted that as the exfoliation process progresses, the concentration of the dissociated Na^+ ions increases. As a consequence, the osmotic pressure difference between the intra-tactoid regime and the bulk water medium decreases, which is also expected to contribute to the observed slowdown of the exfoliation kinetics in the samples of $\phi_w = 3\%$ w/v and 3.5% w/v reported earlier (\circ and \triangle in Fig. 4.4). To investigate the effects of the Na^+ counterions present in the bulk medium on the exfoliation kinetics of tactoids, the counterion concentration is increased by adding salt (NaCl) in the suspension. A suspension is prepared by adding 3% w/v Na-montmorillonite powder in a 30 mM brine solution (NaCl in water). Fig. 4.9 compares the attenuation spectrum of this SBC (Salt added Before Clay mineral) sample (\circ) with that of a 3% w/v suspension without any added salt (\square) at $t_w = 24$ hours. The higher attenuation in the SBC sample with added salt indicates a smaller degree of exfoliation in this sample and is evident from the estimated PSDs plotted in the inset of Fig. 4.9. This verifies that the presence of counterions in bulk water can slow down the tactoid exfoliation

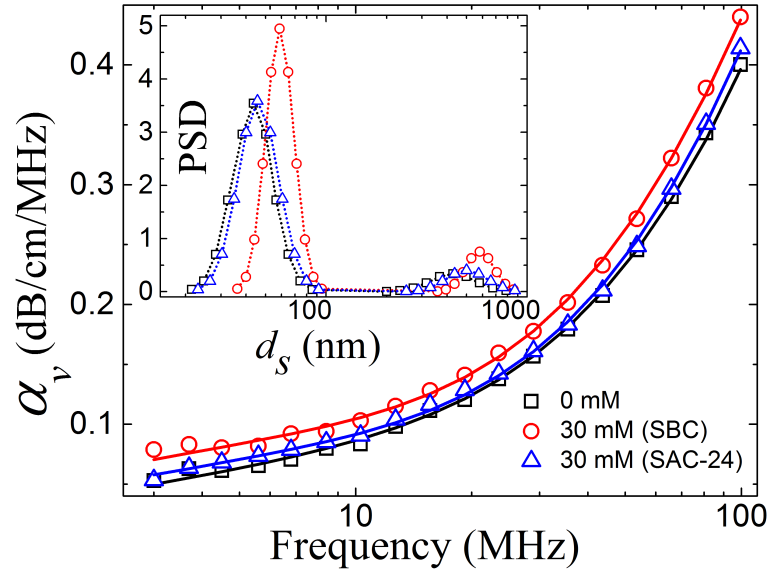


FIGURE 4.9: Ultrasound attenuation spectra measured at $t_w = 24$ hours in 3% w/v Na-montmorillonite suspensions with 0 mM NaCl (\square), a 3% w/v Na-montmorillonite suspension prepared in a 30 mM brine solution (\circ), and when 30 mM NaCl is added 24 hours after dispersing 3% w/v Na-montmorillonite (\triangle). The solid lines are bimodal fits to the experimental data. The inset shows the estimated PSDs for the three different cases. The dotted lines in the inset are guides to the eye.

process by reducing the osmotic pressure of counterions between bulk water and the inter-tactoid spaces.

We monitor the evolution of the tactoid size distributions of the sample with externally added salt at different sample ages t_w and then compare with the data obtained for sample without added salt. Fig. 4.10 shows the evolution of PSDs for 3% w/v Na-montmorillonite SBC sample with 30 mM salt for three typical ages. The PSDs of this sample shift to lower average sizes, indicating the gradual exfoliation with age. To understand the exfoliation kinetics of the tactoids in the presence of salt, the age-dependences of attenuation coefficients α_v measured at a typical ultrasound frequency $f = 53.6$ MHz and the corresponding lower median values d_1 are plotted in Fig. 4.11. In the suspension with 3% w/v Na-montmorillonite (\square in Fig. 4.11), the values of α_v and d_1 decrease with t_w due to the slow exfoliation of the tactoids. It can be seen from these data that the breakup process becomes extremely slow after $t_w = 250$ hours. For the SBC sample in which Na-montmorillonite powder is added to a premixed brine

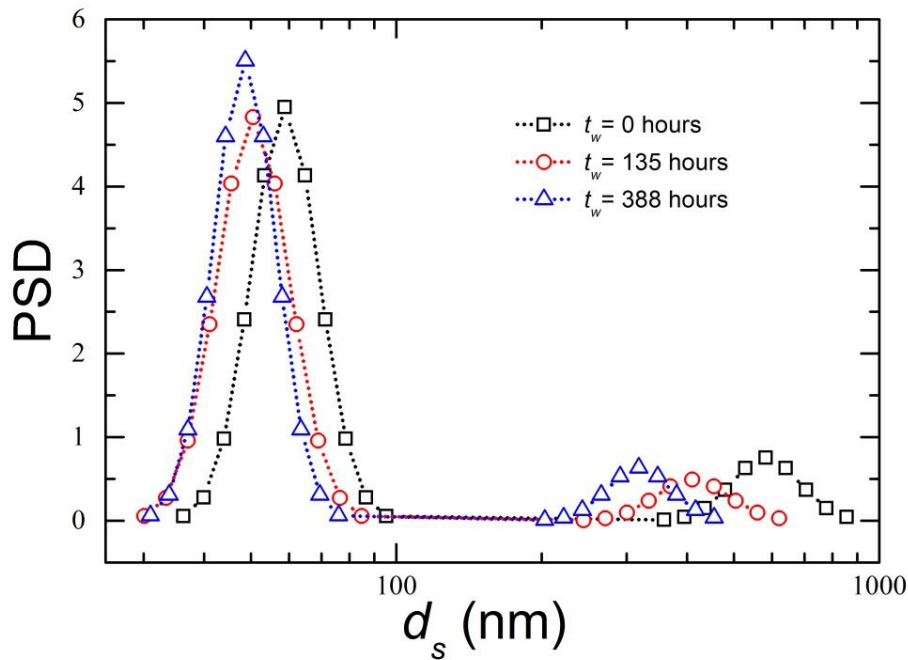


FIGURE 4.10: PSDs at some representative ages, $t_w = 0$ hour (\square), 135 hours (\circ) and 388 hours (\triangle) of 3% w/v Na-montmorillonite suspension prepared by adding the clay mineral in 30 mM brine solution. This sample is designated as SBC (Salt added Before dispersing Clay mineral).

solution (\circ in Fig. 4.11), the values of α_v and d_1 decrease at the initial ages and then almost saturate after $t_w = 100$ hours. However, the d_1 value for this sample is always higher than the 3% w/v sample without any added salt (\square Fig. 4.11). The presence of excess counterions in the aqueous phase of the SBC sample is expected to cause a decrease in the osmotic pressure difference between the intra-tactoid space and the bulk medium, which slows down the diffusion of the intercalated Na^+ counterions. On the one hand, the addition of counterions reduces the inter-tactoid repulsions by directly screening the exposed surface charges of the tactoids. On the other hand, it simultaneously suppresses the intra-tactoid repulsions by reducing the osmotic pressure difference, thereby resulting in a significant slowing down in the exfoliation process in the SBC sample.

It is also interesting to investigate the exfoliation state of Na-montmorillonite samples at different ionic conditions, for example, where counterions (NaCl) are added after dispersing the clay mineral powder in deionized water. For this, the attenuation

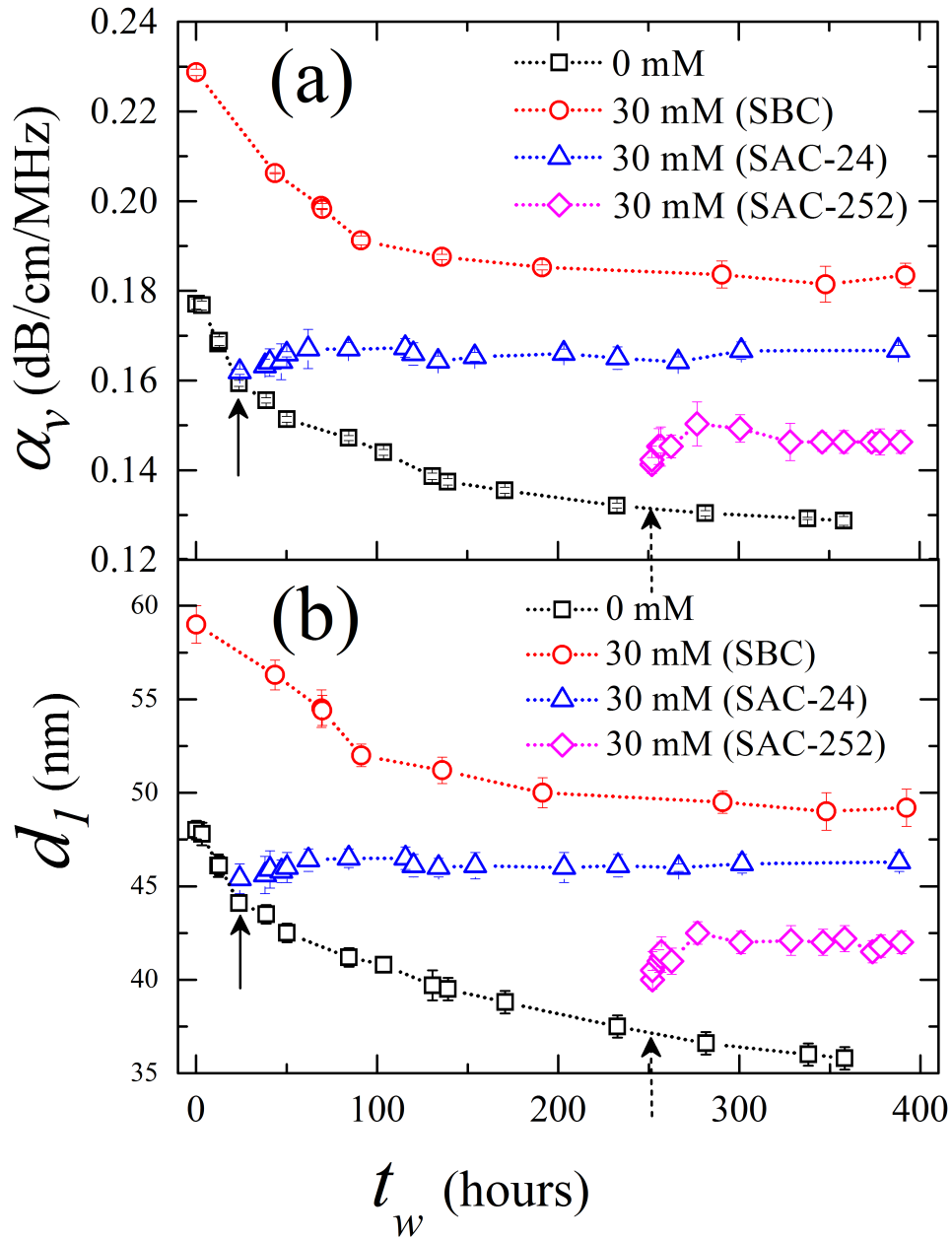


FIGURE 4.11: Evolution of (a) attenuation coefficient α_γ at ultrasound frequency $f = 53.6$ MHz with age t_w of a 3% w/v Na-montmorillonite suspensions with 0 mM salt (\square), a 3% w/v Na-montmorillonite suspension prepared in a 30 mM brine solution (\circ), 30 mM salt added after dispersing 3% w/v Na-montmorillonite at $t_w = 24$ hours (indicated by a solid arrow; \triangle) and 30mM salt added after dispersing the clay mineral at age $t_w = 252$ hours (\diamond ; indicated by a dashed arrow).

spectrum is measured for a suspension, designated as SAC-24, in which 30 mM salt is added to an already dispersed 3% w/v Na-montmorillonite suspension of age $t_w = 24$ hours (Δ in Fig. 4.9). It is seen in the inset of Fig. 4.9 that the average particle size in the SAC-24 sample increases slightly when compared to the sample with no added salt, but is much smaller than that in the SBC sample even though both the SAC and the SBC samples contain identical concentrations of Na-montmorillonite and added salt. Clearly, a sample with no salt is expected to undergo significant exfoliation at $t_w = 24$ hours. Thus, for the SAC-24 sample, the addition of salt in the bulk medium at $t_w = 24$ hours is expected to cause a redistribution of the native Na^+ ions that are dissociated from the tactoids. Some of the Na^+ ions can get attracted to the electrically negative surfaces of the silicate layers in an attempt to acquire electrostatic equilibrium. This can, in addition to flocculation, result in a deswelling process, in which some of the clay mineral layers may reorganize into a tactoid structure [32]. The subsequent t_w dependences of α_v at frequency $f = 53.6$ MHz and the corresponding d_1 values for the SAC-24 sample are plotted in Fig. 4.11(a) and Fig. 4.11(b) respectively (data denoted by Δ s). Both α_v and d_1 increase slowly upto $t_w = 62$ hours, before they reach plateau values where further exfoliation stops. A similar experiment is performed by adding 30mM salt to an already dispersed 3% w/v aqueous Na-montmorillonite suspension of age $t_w = 252$ hours. This sample is designated by SAC-252. The subsequent evolutions of α_v and d_1 with t_w for this sample are shown by \diamond in Fig. 4.11(a) and Fig. 4.11(b) respectively. In this case, both α_v and d_1 increase upto $t_w = 277$ hours before they reach plateau values. This behavior again supports our previous argument that the addition of salt in an already dispersed Na-montmorillonite suspension encourages the formation of tactoids under the influence of reverse osmotic pressure. Most importantly, it is also simultaneously seen, throughout the range of t_w accessed here, that the values of α_v and d_1 for both the SAC samples (having identical compositions) (Δ and \diamond in Fig. 4.11) are always lower when compared with the SBC sample (\circ in Fig. 4.11) prepared in a premixed brine solution. The degree of exfoliation in the SBC sample is therefore always lower than in the SAC samples. Na-montmorillonite tactoids in the 3% w/v

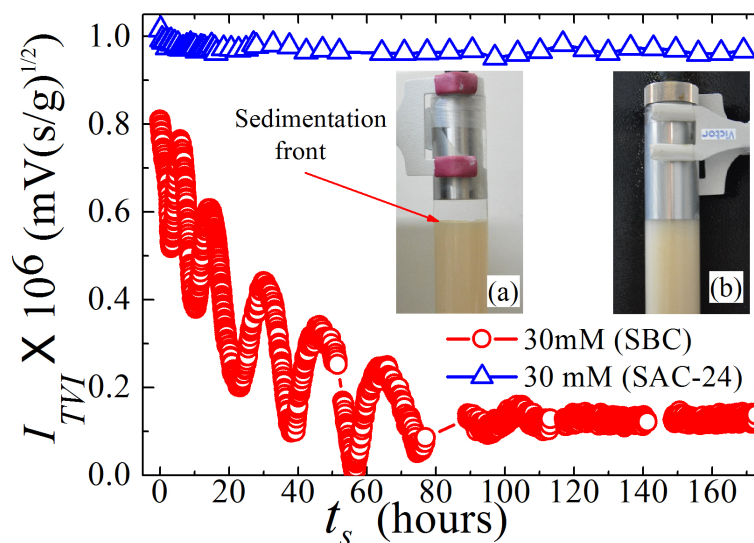


FIGURE 4.12: Evolution of total vibration current (I_{TVI}) normalized by ultrasound pressure gradient in an electroacoustic setup (Fig. 2.4 of Chapter 2) with observation time t_s since stirring of the suspensions is stopped. The samples are prepared by adding Na-montmorillonite to a 30 mM brine solution (SBC; \circ) and by adding 30 mM salt at $t_w = 24$ hours after dispersing Na-montmorillonite in water (SAC-24; \triangle). The Na-montmorillonite concentrations in both cases are 3% w/v. Insets (a) and (b) images of the SBC and SAC-24 samples respectively in the electroacoustic setup at $t_w = 171$ hours.

sample have higher exfoliation at $t_w = 252$ hours than at $t_w = 24$ hours (\square in Fig. 4.11). As a result, the SAC-252 sample has lower α_v and d_1 compared to that in the SAC-24 sample. However, the tactoid reformation process does not lead to identical PSDs for the SAC-24 and SAC-252 within the experimental time. This is presumably due to the irreversibility that arises due to kinetic arrest of the exfoliated layers with age [33].

The observations concerning the exfoliation behavior of the tactoids in the presence of counterions reported above are further verified by monitoring the gravitational stability of the Na-montmorillonite suspensions using an electroacoustic setup (Fig. 2.4 of Chapter 2). The total vibration current (I_{TVI}), which arises from ultrasound induced dipole moments in both the clay particles and salt molecules in these suspensions [34], is measured by keeping the flat surface of the electroacoustic probe in contact with the top surface of clay suspension (insets of Fig. 4.12). The magnitude of I_{TVI} is very sensitive to the particle concentration near the probe surface kept in contact with the top surface of the sample column. The evolution of the magnitude of I_{TVI} as a function

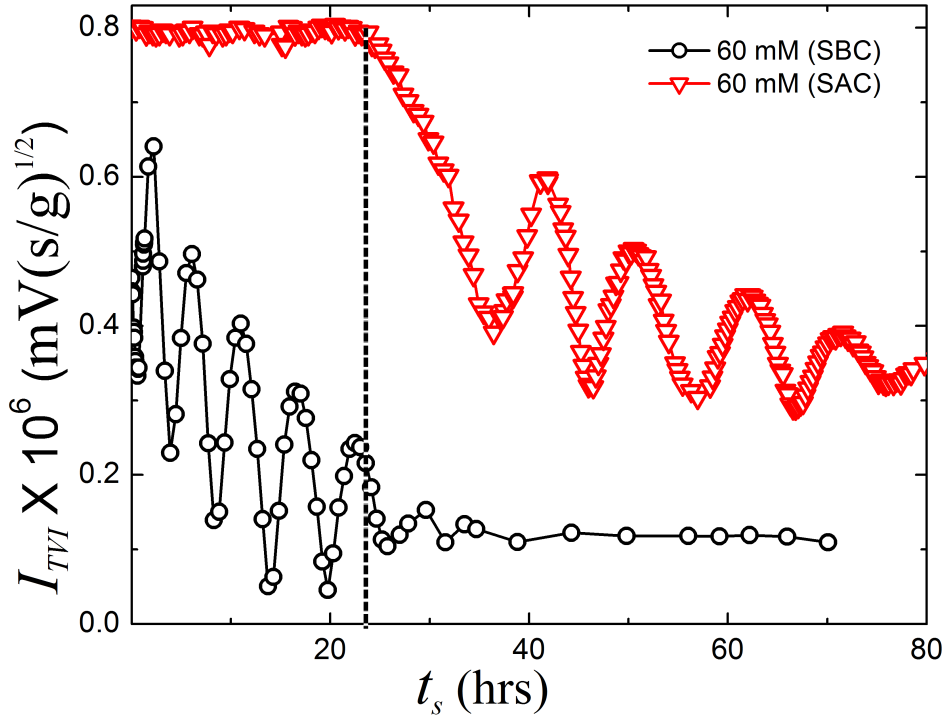


FIGURE 4.13: Evolution of total vibration current (I_{TVI}), normalized by ultrasound pressure gradient, in an electroacoustic setup (Fig. 2.4 of Chapter 2) with observation time t_s for 3% w/v Na-montmorillonite suspensions with $C_s = 60$ mM prepared in SBC (\circ) and SAC (∇) conditions. The vertical dashed line shows the position of the delay time $\tau_d = 23$ hours for the SAC sample.

of observation time t_s is plotted in Fig. 4.12 for the samples with added salt. It can be seen from this figure that the value of I_{TVI} for the SBC sample (\circ) is less compared to the SAC-24 sample (Δ) at $t_s = 0$ when the stirring of the sample is stopped inside the electroacoustic setup after adding salt. As the bulk solutions have identical salt concentrations, this result can be explained if the number of smaller tactoids, and hence the layer-water interfacial area, in the SAC-24 sample is higher than in the SBC sample. With increasing t_s , a sedimentation front appears (inset (a) of Fig. 4.12) for the SBC sample. Since the electroacoustic probe sets up a stable oscillatory pressure gradient along the vertical direction of the sample chamber, the sedimentation front passes through consecutive half wavelength regions having alternating directions of the pressure gradient during its downward movement under gravity. As a result, the sedimenting particles have opposite orientations of induced dipole moments, leading

to the observed oscillation in I_{TVI} with t_s for the SBC sample (\circ in Fig. 4.12). The presence of a sedimentation front in the SBC sample therefore indicates the formation of an unstable gel structure. It has already been verified here that the degree of exfoliation of tactoids in the SBC sample is less due to the prior presence of counterions (Fig. 4.11(b) and inset of Fig. 4.9). As a result, the strands of the network structure in this sample are heavy and the local yield stresses can be easily exceeded, leading to the eventual collapse of the network structure. In contrast, no change in the I_{TVI} value is observed with time t_s in the SAC-24 sample (Δ in Fig. 4.12), indicating the absence of migration of the Na-montmorillonite particles under gravity. Since the 3% w/v sample does not show a glass transition at sample age $t_w = 24$ hours (\square in Fig. 4.5), the most likely reason for kinetic arrest for this low concentration sample is the formation of stable system-spanning network structures due to the aggregation of the tactoids. As discussed earlier, the SAC-24 sample (Δ in Fig. 4.12) has a higher number of exfoliated entities and smaller tactoids than the SBC sample (\circ in Fig. 4.12). This gives rise to an enhanced network density in the SAC sample, resulting in the high dispersion-stability observed under gravity (inset (b) of Fig. 4.12). The gravitational stability test of 3% w/v Na-montmorillonite suspensions is repeated for 60 mM added salt (Fig. 4.13). Two samples are prepared by adding Na-montmorillonite to a 60 mM brine solution (SBC sample) and by adding 60 mM salt at $t_w = 24$ hours after dispersing Na-montmorillonite in water (SAC sample). It can be seen here that the SAC sample (∇ in Fig. 4.13) exhibits higher stability with higher I_{TVI} values than the SBC sample (\circ in Fig. 4.13). The SAC sample with 60 mM added salt shows transient gel collapse in which the suspension remains stable for a delay time $\tau_d = 23$ hours before collapse, with the collapse phenomenon being associated with the oscillations of I_{TVI} . On the contrary, the SBC sample with 60 mM salt shows negligible gravitational stability and exhibits oscillations in the measured I_{TVI} values immediately after stirring is stopped in the measuring cell. This data obtained here again confirms that the SAC sample is more likely to form a stable gel.

The state of exfoliation of tactoids has a strong effect on the viscoelasticity of the

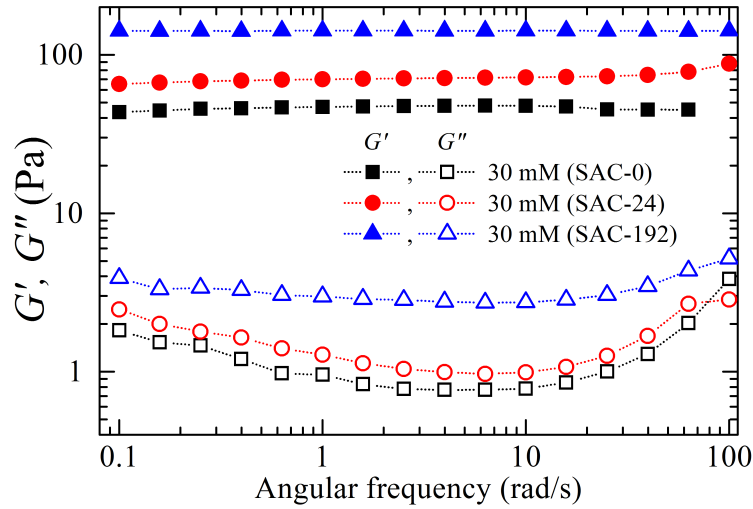


FIGURE 4.14: Frequency sweep rheological measurements of gel samples when gelation is induced by adding 30 mM salt at ages 0 hour (\square), 24 hours (\circ) and 192 hours (\triangle) to 3% w/v Na-montmorillonite suspension. G' and G'' are the elastic and viscous moduli respectively.

Na-montmorillonite gels studied here. To illustrate this, gelation is induced in 3% w/v Na-montmorillonite suspensions by adding 30 mM salt at different t_w values. It can be seen from Fig. 4.14 that all three samples prepared in this way and denoted as SAC-0, SAC-24 and SAC-192 show soft solid behavior, with $G' > G''$, a frequency independent G' and a weakly frequency dependent G'' . It is further observed that the values of both moduli increase when gelation is induced by adding salts to samples of higher ages t_w . It has already been established that the number of smaller tactoids increases with t_w due to exfoliation in 3% w/v sample (\circ in Fig. 4.4). The addition of salt in the 3% w/v sample at higher t_w therefore gives rise to an enhanced network density for the gels (\triangle in Fig. 4.12). This results in the larger values of the mechanical moduli observed for gels prepared at higher t_w . This observation further supports the data reported for samples SAC-24 (\triangle) and SAC-252 (\diamond) in Fig. 4.11(b), where it is seen that adding salt later to a Na-montmorillonite sample of higher t_w values results in smaller values of d_1 due to the growing irreversibility of tactoid reformation with age.

4.4 Conclusions

This chapter presents a study of the exfoliation state (the dispersibility) of aqueous suspensions of the natural clay Na-montmorillonite at different clay concentrations and ionic conditions using ultrasound attenuation and electroacoustic methods. It is shown here that below the sample jamming transition concentration of 4% w/v, the tactoids undergo an exfoliation process, with the tactoid thickness decreasing with increasing age of the sample (\square , \circ and \triangle in Fig. 4.4). Above the jamming concentration (∇ and \diamond in Fig. 4.4), the exfoliation process becomes extremely slow due to the strong repulsive interactions that exist between the tactoids. This hinders further exfoliation of the tactoids into single layers in the suspension, resulting in a substantial number of tactoids that are composed of more than one layer. Interestingly, incomplete exfoliation of tactoids is also clearly observed below the jamming concentration. This indicates that repulsive interactions may not be the sole factor responsible for the existence of tactoids. As the Na^+ counterions dissociate from the intra-tactoid space during exfoliation, the osmotic pressure difference between the bulk and the intra-tactoid spaces decreases as the hydrated counterion concentration increases. This can have a reverse effect on the exfoliation kinetics, with exfoliation becoming less likely at higher ages and clay mineral concentrations. To verify this, Na-montmorillonite powder is dispersed in brine water. It is found that the presence of counterions in the medium hinders the exfoliation process (\circ in Fig. 4.9 and Fig. 4.11). These results support previous X-ray diffraction observations of the restricted crystalline swelling of Na-montmorillonite in concentrated NaCl solutions [35]. The counterion concentration is also increased by adding salt to the bulk medium after dispersing Na-montmorillonite powder. It is noted that the median sizes of the particles in these suspensions increase before eventual saturation (\triangle and \diamond in Fig. 4.11). This indicates that the exfoliated layers aggregate to form tactoids initially due to the reverse osmotic pressure that is generated by the addition of counterions after the clay mineral exfoliation. Such a tactoid reformation process in Na-montmorillonite suspensions due to the addition of

CaCl_2 after dispersing the clay mineral powder has been seen earlier in X-ray scattering measurements [36]. However, the tactoid reformation process observed here is not fully reversible since the addition of identical amounts of salt at different time intervals after dispersing Na-montmorillonite does not lead to identical size distributions of tactoids (Δ and \diamond in Fig. 4.11). This result is indirectly confirmed by measuring the elastic and viscous moduli of Na-montmorillonite gel networks that are formed by adding salt to the samples at various ages after the clay mineral powder is dispersed in deionized water. The magnitudes of both the moduli are seen to increase for the samples in which salt is added later.

The effects of counterions on the exfoliation process are further verified using electroacoustics by monitoring the gravitational stability of Na-montmorillonite suspensions characterized by different counterion conditions. When the clay mineral powder is dispersed in brine water, the suspension becomes very unstable under gravity (\circ in Fig. 4.12). On the other hand, when an identical amount of salt is added well after dispersing the clay mineral powder in water (Δ in Fig. 4.12), the suspension is found to be highly stable. These results are interpreted in terms of the formation of stable system-percolating network structures or gels due to the presence of the smaller tactoids in the second sample. These data clearly indicate that the presence of counterions in the dispersing water medium slows down the tactoid exfoliation process. Hence, in addition to the important contribution of the interparticle repulsive interactions, the results reported in this article show that the osmotic pressure difference of hydrated counterions between the bulk aqueous medium and the intra-tactoid spaces plays a very important role in the tactoid exfoliation and reformation process.

References

- [1] R. Anderson, I. Ratcliffe, H. Greenwell, P. Williams, S. Cliffe and P. Coveney, *Earth-Science Reviews*, 2010, **98**, 201 – 216.
- [2] K. Norrish, *Discussions of the Faraday society*, 1954, **18**, 120–134.
- [3] S. L. Swartzen-Allen and E. Matijevic, *Chemical Reviews*, 1974, **74**, 385–400.
- [4] P. M. Amarasinghe and A. Anandarajah, *Environmental & Engineering Geoscience*, 2013, **19**, 173–183.
- [5] E. L. Hansen, H. Hemmen, D. M. Fonseca, C. Coutant, K. D. Knudsen, T. S. Plivelic, D. Bonn and J. O. Fossum, *Scientific Reports*, 2012, **2**, 618(1)–618(2).
- [6] W. B. Kleijn and J. D. Oster, *Clays and Clay Minerals*, 1982, **30**, 383.
- [7] L. Liu, *Colloids and Surfaces A: Physicochemical and Engineering Aspects*, 2013, **434**, 303 – 318.
- [8] L. Liu, L. Moreno and I. Neretnieks, *Langmuir*, 2009, **25**, 679–687.
- [9] J. D. F. Ramsay, S. W. Swanton and J. Bunce, *J. Chem. Soc., Faraday Trans.*, 1990, **86**, 3919–3926.
- [10] M. Segad, B. Jonsson, T. kesson and B. Cabane, *Langmuir*, 2010, **26**, 5782–5790.

- [11] M. V. Smalley, *Langmuir*, 1994, **10**, 2884–2891.
- [12] D. E. Smith, Y. Wang and H. D. Whitley, *Fluid Phase Equilibria*, 2004, **222-223**, 189 – 194.
- [13] T. J. Tambach, E. J. M. Hensen and B. Smit, *The Journal of Physical Chemistry B*, 2004, **108**, 7586–7596.
- [14] D. A. Young and D. E. Smith, *The Journal of Physical Chemistry B*, 2000, **104**, 9163–9170.
- [15] J. F. Lambert and F. Bergaya, in *Handbook of Clay Science*, ed. F. Bergaya and G. Lagaly, Elsevier, 2013, vol. 5, pp. 679 – 706.
- [16] S. Pavlidou and C. Papaspyrides, *Progress in Polymer Science*, 2008, **33**, 1119 – 1198.
- [17] S. S. Ray and M. Okamoto, *Progress in Polymer Science*, 2003, **28**, 1539 – 1641.
- [18] O. Abollino, M. Aceto, M. Malandrino, C. Sarzanini and E. Mentasti, *Water Research*, 2003, **37**, 1619 – 1627.
- [19] M. Boufatit, H. Ait-Amar and W. McWhinnie, *Desalination*, 2007, **206**, 394 – 406.
- [20] H. B. Bradl, *Journal of Colloid and Interface Science*, 2004, **277**, 1 – 18.
- [21] H. H. Murray, *Applied Clay Science*, 2000, **17**, 207 – 221.
- [22] S. Abend, S. and G. Lagaly, G, *Clay Minerals*, 2001, **36**, 557–570.
- [23] M. Franchi, J. Ferris and E. Gallori, *Origins of life and evolution of the biosphere*, 2003, **33**, 1–16.
- [24] A. Taki, B. John, S. Arakawa and M. Okamoto, *European Polymer Journal*, 2013, **49**, 923–931.

-
- [25] C. H. Zhou, *Applied Clay Science*, 2011, **53**, 87 – 96.
- [26] X. Chen, N. Hu, Y. Zeng, J. F. Rusling and J. Yang, *Langmuir*, 1999, **15**, 7022–7030.
- [27] C. Mousty, *Analytical and Bioanalytical Chemistry*, 2010, **396**, 315–325.
- [28] A. S. Dukhin and P. J. Goetz, *Characterization of Liquids, Nano- and Microparticulates, and Porous Bodies using Ultrasound*, Elsevier: New York, 2010.
- [29] S. Ali and R. Bandyopadhyay, *Langmuir*, 2013, **29**, 12663–12669.
- [30] P. Sollich, F. Lequeux, P. Hébraud and M. E. Cates, *Physical Review Letters*, 1997, **78**, 2020–2023.
- [31] B. R. Jennings and K. Parslow, *Proceedings of the Royal Society of London. A. Mathematical and Physical Sciences*, 1988, **419**, 137–149.
- [32] H. V. Olphen, *Journal of Colloid Science*, 1962, **17**, 660 – 667.
- [33] S. Abend and G. Lagaly, *Applied Clay Science*, 2000, **16**, 201 – 227.
- [34] B. J. Marlow, D. Fairhurst and H. P. Pendse, *Langmuir*, 1988, **4**, 611–626.
- [35] P. Slade, J. Quirk and K. Norrish, *Clays and Clay Minerals*, 1991, **39**, 234–238.
- [36] M. Segad, B. Jonsson and B. Cabane, *The Journal of Physical Chemistry C*, 2012, **116**, 25425–25433.

5

Effect of electrolyte on the microstructure and yielding of aqueous suspensions of colloidal clay

5.1 Introduction

Various bulk properties such as viscoelasticity [1], yielding and thixotropy [2, 3], stability and aging dynamics [4–8] of clay suspensions originate from the complex self organization of charged anisotropic clay platelets driven by DLVO interactions [9, 10]. Depending on the clay and salt concentrations, and age of suspensions, these interactions lead to various phases such as gels, glasses and nematic liquid crystals

[11, 12]. In the glassy phase, the interactions between platelets are dominated by screened Coulomb repulsions and the viscoelasticity and yielding behaviors originate from the caging of each platelet by its neighbors [13]. The gel phase, on the other hand, is a volume spanning network structure in which two platelets are connected by an attractive bond, with the strengths of the bonds determining their viscoelasticity and yielding behavior.

The nature of platelet association for attractive bond formation, and therefore the origin of the observed rheological behavior of Na-montmorillonite gels, has been widely debated in the literature [14–18]. Based on the DLVO theory and rheological measurements in suspensions of low platelet concentrations, it was predicted that at a low salt concentration and in a dispersing medium of $\text{pH} < 7$, attractive bond formation occurs through the association of the negative faces of the platelets with their positive edges. On the other hand, bond formation through edge-face, face-face and edge-edge interactions are predicted at varying salt concentrations in a dispersing medium of $\text{pH} > 7$ [9, 19]. The coagulation process becomes more complicated with increasing platelet concentration in the presence of salt and a house of cards (HoC) structure is frequently invoked to explain the nature of gel networks [20–25]. Surprisingly, the experimental evidence of such predicted microstructures is very limited. There have been some studies to visualize the underlying microscopic structures using scanning electron microscopy (SEM) [26] and transmission X-ray microscopy (TXM) [18, 27] for different conditions of sample preparation. These studies confirm the existence of either edge-edge or face-face microscopic configurations of platelets in the presence of salt. However, these studies do not systematically investigate the variation of the microscopic structures, and their influence on the strength and stability of clay gels, with changing salt concentration.

In this chapter, we address this issue by studying the rheology, stability properties and microstructures of 5% w/v Na-montmorillonite suspensions at their natural pH values after systematically varying the externally added salt concentration from 10 mM to 800 mM. The clay concentration chosen here is above the glass transition concentration

(4% w/v) for Na-montmorillonite as reported in Chapter 4. Clay particles therefore do not sediment under gravity in the salt-free 5% w/v suspension of Na-montmorillonite studied here. In the presence of salt, we find that the viscoelastic moduli and the yield stress of arrested phases (gels) in this suspension increase upto a peak value at a critical salt concentration and subsequently decrease due to the progressive increase in salt induced interparticle attractive interactions. The microscopic association of the platelets in gels with varying salt concentration is directly visualized using cryogenic scanning electron microscope (cryo-SEM). This shows a transition of the gel morphology, dominated by overlapping coin (OC) and house of cards (HoC) associations of clay particles to a new network structure dominated by face-face coagulation of platelets, across the critical salt concentration. The variation of the strength of the gels estimated from the rheological measurements is then interpreted in terms of the observed microstructures and changes in gel morphology. The influence of the morphology on the stability of the gels under gravity is further assessed using electroacoustics.

5.2 Sample preparation and experimental methods

We use Na-montmorillonite of Nanomer PGV grade with CEC value of $145 \pm 10\%$ meq/100g procured from Nanocor Inc [28]. Details of the clay structure can be found in Chapter 1 (Section 1.6). The clay mineral is hygroscopic in nature. The Na-montmorillonite powder is therefore baked for 24 hours in an oven kept at a temperature of 120°C to remove moisture. A stock suspension of 8% w/v is then prepared by dispersing the dry powder in highly deionized Milli-Q water under vigorous stirring conditions using a magnetic stirrer. The suspension is homogenized by stirring it for three hours and then stored in a sealed polypropylene bottle for seven days. The stock suspension is next used to prepare 5% w/v clay suspensions with different ionic strengths by adding predetermined quantities of NaCl solutions. The mixture of clay and salt solution is next stirred for three hours using a magnetic stirrer. The resultant suspensions are kept in vacuum for two minutes to remove air bubbles trapped in

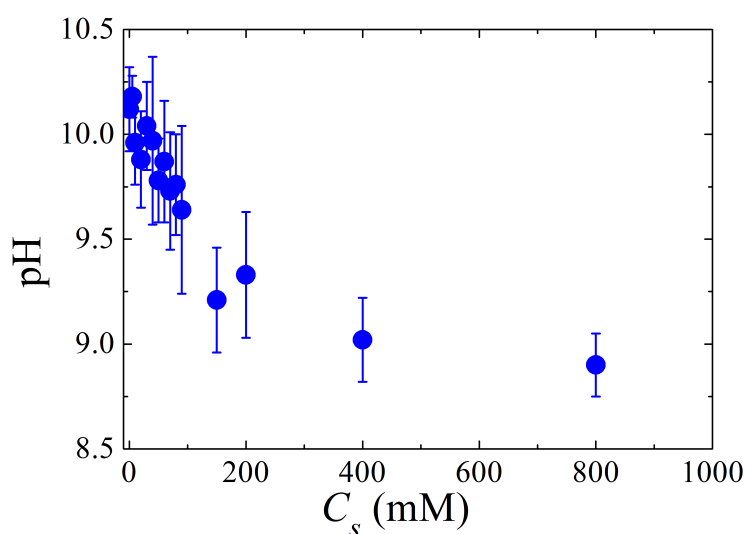


FIGURE 5.1: Change of natural pH with added salt concentration C_s in a freshly prepared 5% w/v Na-montmorillonite suspension.

the viscous medium. Samples with different salt concentrations, C_s , are then stored for four days in sealed glass vials before using them for rheological measurements, cryo-SEM imaging and electroacoustic measurements. The pH of these suspensions are maintained at their natural values that arise due to addition of Na-montmorillonite clay in water. The pH measurements are done using a CyberScan Eutech electrode (Model-ECFG7252001B) at a temperature of 25°C. The addition of salt leads to a slight decrease in the pH value of the suspension and has been shown in Fig. 5.1. It is seen that the pH of the suspension always remains above 8.8 in the salt concentration range investigated here.

Rheological measurements are performed in an Anton Paar MCR 501 rheometer working in a stress-controlled oscillatory mode. Details of the instrument can be found in Chapter 2 (Section 2.2.5). For each rheological experiment, a Couette geometry is filled carefully with 4.7 ml of sample using a syringe. The filling process partially rejuvenates the sample. The free surface of the sample is covered with a thin layer of silicone oil of viscosity 5 cSt to prevent evaporation of water. A well defined experimental protocol, as shown in the inset of Fig. 5.2, is used for all the measurements.

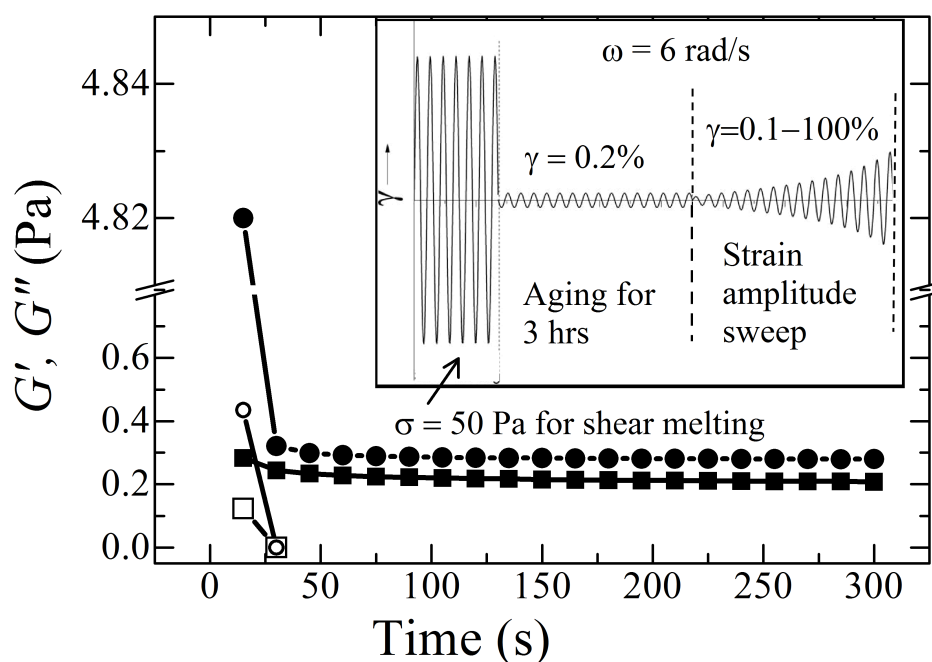


FIGURE 5.2: Variation of the elastic modulus G' (empty symbols) and viscous modulus G'' (solid symbols) with time during the shear melting process performed by applying a stress of 50 Pa at an angular frequency of 6 rad/s for 5 mins to 5% w/v Na-montmorillonite suspensions with 20 mM (\blacksquare and \square) and 300 mM (\bullet and \circ) salt concentrations. It is seen that elastic moduli of both the samples reach zero after 30 s of starting the shear melting process. Inset shows the experimental protocol used for strain amplitude sweep rheological measurements.

After filling the measurement geometry, the samples are shear rejuvenated by applying a large oscillatory stress of amplitude 50 Pa with an angular frequency of 6 rad/s. The application of this high shear stress liquifies the samples, leading to a zero elastic modulus G' and very small values of the viscous modulus G'' (Fig. 5.2). The samples are left to evolve for three hours after the cessation of the shear melting process at age $t_w = 0$. During this period, the suspensions undergo a spontaneous phase transition from a liquid-like state ($G' < G''$) to a kinetically arrested state ($G' > G''$), with the viscoelastic moduli evolving continuously with age t_w as shown for 5% w/v Na-montmorillonite samples with two typical salt concentrations 10 mM (\blacktriangle and \triangle) and 20 mM (\blacksquare and \square) in Fig. 5.3. Increasing the amount of salt results in faster approach to the kinetically arrested state. After $t_w = 3$ hours, a strain amplitude sweep test is carried out by varying strain amplitude, γ , in the range of 0.1 – 100% at a constant angular

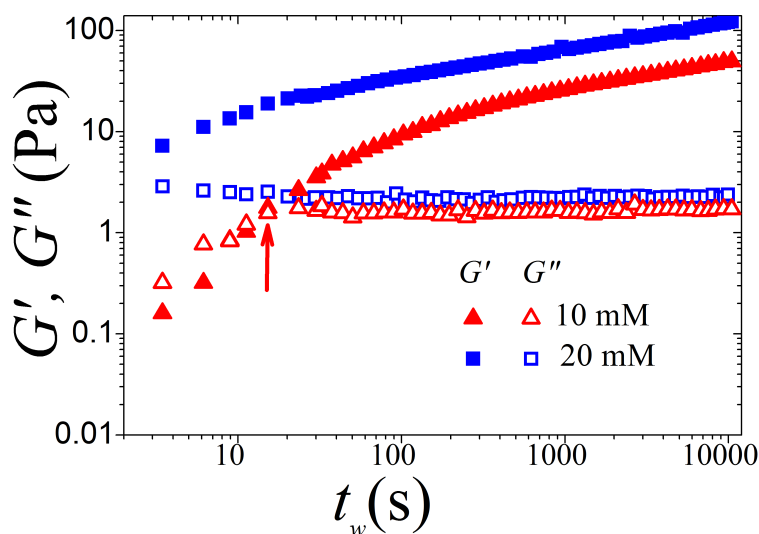


FIGURE 5.3: Evolution of the elastic modulus G' (filled symbols) and viscous modulus G'' (empty symbols) as a function of the aging time t_w of 5% w/v Na-montmorillonite suspensions with salt concentrations 10 mM (\blacktriangle and \triangle) and 20 mM (\blacksquare and \square). The arrow shows the cross-over position between G' and G'' for the sample with 10 mM salt. To monitor the aging of the suspensions, a small oscillatory strain of amplitude $\gamma = 0.2\%$ at an angular frequency of 6 rad/s is applied and the t_w dependence of G' and G'' of the samples is measured. The applied strain γ , which is very weak and much smaller than the yield strain, is not expected to interfere with the spontaneous aging process.

frequency of 6 rad/s (inset of Fig. 5.2). To determine the static yield stresses of gels, controlled shear stress flow curve measurements are performed by varying shear stress in the range 0.1 – 100 Pa at sample age of $t_w = 3$ hours. Flow curve data are obtained with a fixed time setting by allowing 5 s for each data measurement. All experiments reported here are carried out at a temperature of 25°C.

Cryo-SEM characterization of clay samples are performed using a field effect scanning electron microscope (FESEM) from Carl Zeiss at an electron beam strength of 2 KeV. Details of this setup and sample preparation method for cryogenic characterization are described in Chapter 2 (Sections 2.2.6 and 2.2.8).

Stability characterization of clay suspensions in the presence of salt is performed using an electroacoustic setup described in Chapter 2 (Section 2.2.2). The setup simultaneously measures the I_{CVI} induced by clay particles and I_{IVI} induced by salt ions. The total electroacoustic signal is a vector sum of I_{CVI} and I_{IVI} and measured as the

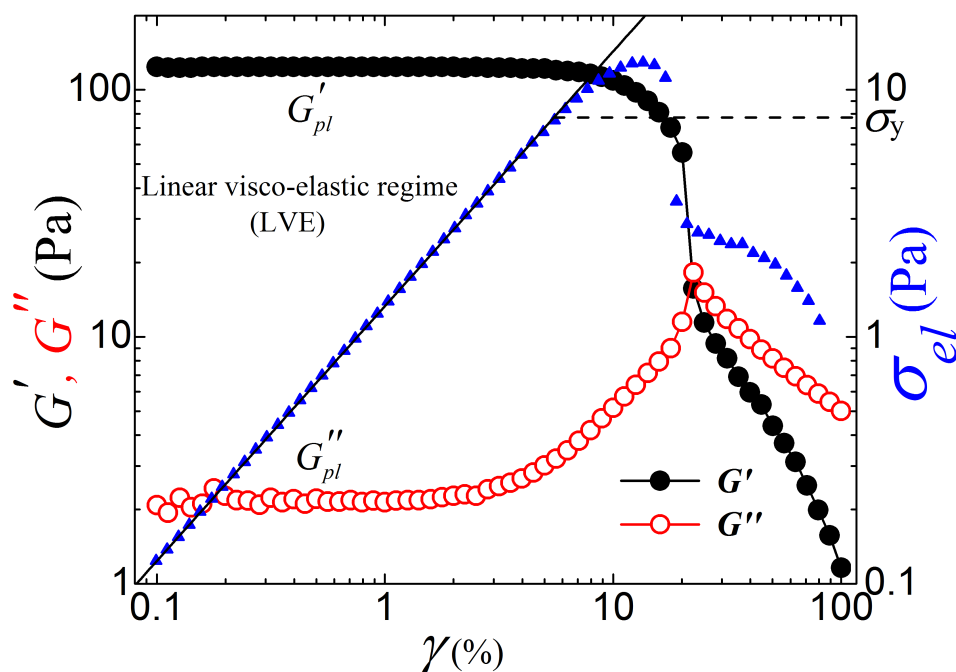


FIGURE 5.4: Variation of elastic modulus G' (\bullet), viscous modulus G'' (\circ) and elastic stress, $\sigma_{el} = G'\gamma$ (\blacktriangle) with strain amplitude, γ , for 5% w/v Na-montmorillonite with 20 mM added salt at $t_w = 3$ hours. The solid line is a linear fit to the σ_{el} vs γ data. The value of σ_y is shown by the horizontal dashed line.

total vibration current (I_{IV}) [29].

5.3 Results and discussion

The bulk mechanical behavior of Na-montmorillonite suspensions, with varying salt concentration C_s , is measured by performing strain amplitude sweep tests. Fig. 5.4 shows representative data of a strain amplitude sweep experiment at an angular frequency of 6 rad/s for a 5% w/v clay suspension with $C_s = 20$ mM at $t_w = 3$ hours. At small values of applied strain (γ), i.e., in the linear viscoelastic (LVE) regime, $G' > G''$, with both the moduli being independent of strain amplitudes. The plateau values of G' and G'' are designated by G'_{pl} and G''_{pl} respectively. On further increase in γ , the sample starts yielding due to the irreversible rearrangement of Na-montmorillonite platelets. In this nonlinear regime, G' decreases monotonically while G'' reaches a peak at the

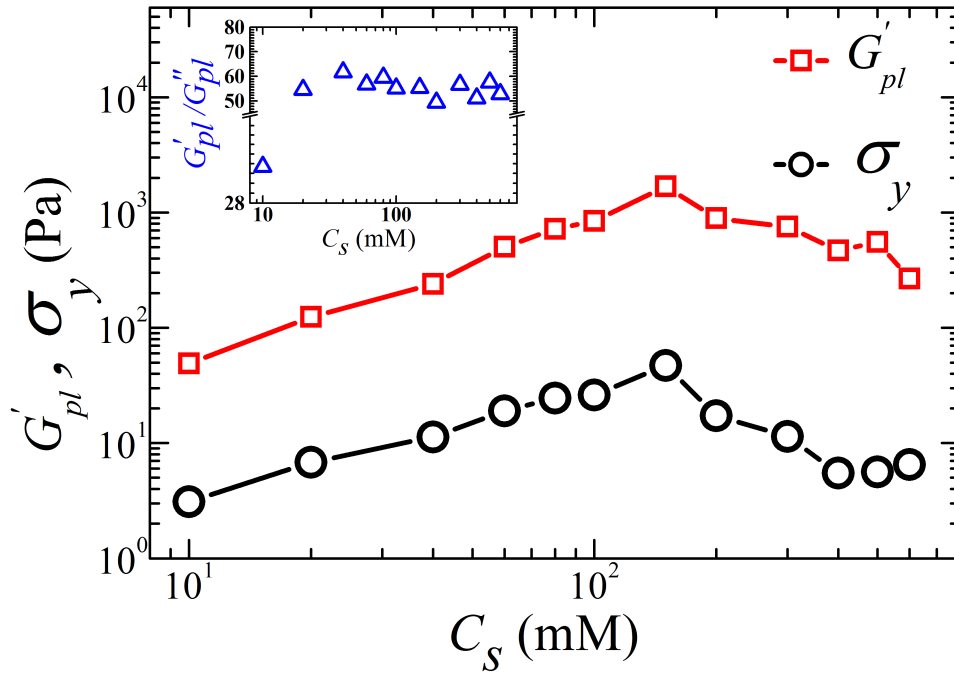


FIGURE 5.5: Variation of plateau value of elastic modulus G'_{pl} (\square) and yield stress σ_y (\circ) with increasing salt concentration C_s . The inset shows the change in ratio of the viscoelastic moduli G'_{pl}/G''_{pl} (\triangle), measured in the linear viscoelastic regime, versus C_s .

point of crossover between G' and G'' . Finally, at very high strains, the sample exhibits fluid-like behavior which is indicated by $G'' > G'$. Similar behavior of the stress moduli under high applied strains in the nonlinear regime was also observed previously in simulation and experimental studies [30, 31]. The yield stress, σ_y (indicated by horizontal dashed line in Fig. 5.4), is calculated from the strain amplitude sweep data following the method described by Laurati *et al.* [31]. In this method, the elastic stress $\sigma_{el} = G'\gamma$ (\blacktriangle in Fig. 5.4) is plotted versus γ , which helps to separate the contribution of the viscous stress from the total stress. At low γ values, the elastic stress vs strain data is fitted to $\sigma_{el} = G'\gamma$. The value of σ_y is defined as the magnitude of σ_{el} at which the measured value of σ_{el} starts deviating more than 3% from the theoretically calculated value. For the sample in Fig. 5.4, a yield stress $\sigma_y = 6.8$ Pa is calculated.

The variations of G'_{pl} and σ_y with varying salt concentration C_s are shown in Fig. 5.5. Both the quantities increase monotonically with C_s upto $C_s \approx 150$ mM, before decreasing with further addition of salt. The inset of Fig. 5.5 shows that G'_{pl} is

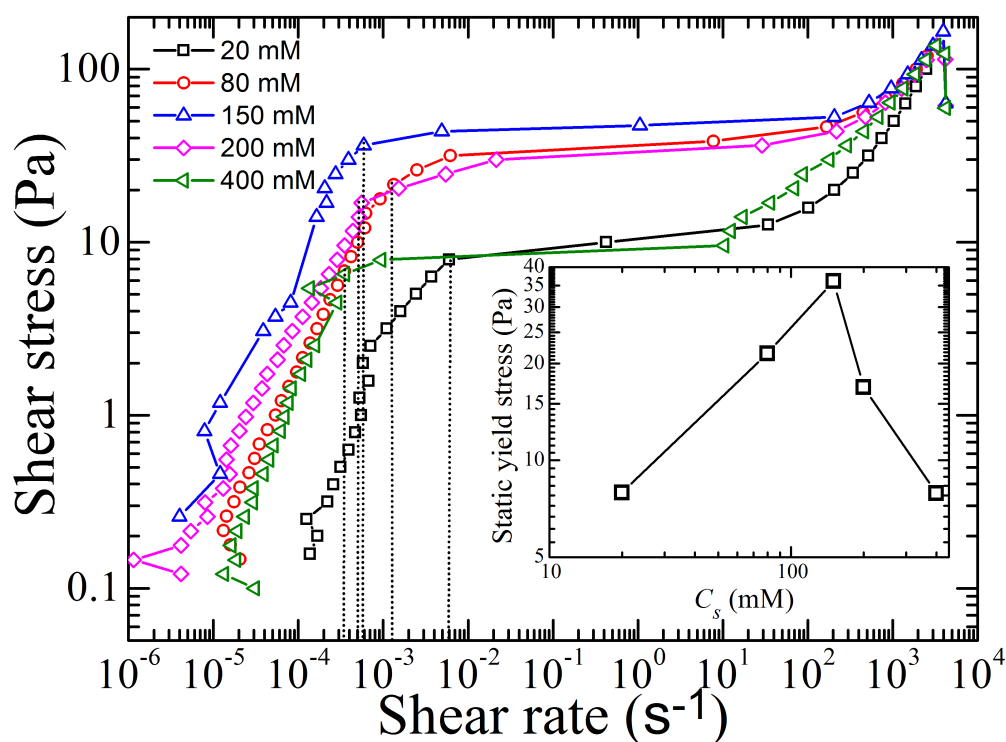


FIGURE 5.6: Shear stress vs shear rate profile measured in controlled shear stress (CSS) mode for 5% w/v Na-montmorillonite suspensions with salt concentrations 20 mM (\square), 80 mM (\circ), 150 mM (\triangle), 200 mM (\diamond) and 400 mM (\blacktriangle). The vertical dotted lines show the positions of the yielding points for the samples. The inset shows the variation of static yield stress with the salt concentrations, C_s .

approximately sixty times higher than G''_{pl} for samples with $C_s > 10$ mM. This indicates that the suspensions are essentially elastic in the linear viscoelastic regime, even though the strength of the underlying microstructures of the suspensions, which is estimated from the σ_y and G''_{pl} values, decreases for $C_s > 150$ mM. The observation in Fig. 5.5 therefore indicates a transition in the sample morphology at $C_s = 150$ mM.

To compare the data obtained in the strain sweep experiments reported above, we determine the static yield stresses of gels at different salt concentrations by performing flow curve measurements in controlled shear stress (CSS) mode. The data are shown in Fig. 5.6 for 5% w/v Na-montmorillonite gels with C_s varying in the range 20-400 mM. At low shear rate values, the shear stress varies almost linearly with shear rate (or effectively with strain) for all gel samples. This indicates solid-like response of the gels. The point where the stress value deviates from the linear regime can be defined

as the static yield stress which is indicated by vertical dotted lines in Fig. 5.6 for the different samples investigated here. The static yield stress thus measured increases with C_s , upto a peak value at $C_s = 150$ mM, and then decreases at higher C_s (inset of Fig. 5.6). A very similar trend for the yield stress was seen in the strain sweep measurements reported in Fig. 5.5.

We next investigate the salt induced morphological changes of Na-montmorillonite gels using cryo-SEM. Fig. 5.7 shows representative cryo-SEM micrographs of 5% w/v Na-montmorillonite gels with C_s varying in the range 10-500 mM. Honeycomb-like three dimensional network structures, with a systematic change in morphology and sizes of the polydisperse pores (voids left after sublimating the water molecules during the cryo-SEM sample preparation step), can be observed in all these samples. The branches of the gel networks observed here are thicker than the thickness of a single platelet (~ 1 nm) due to the presence of vitrified water on their surfaces. A close inspection of the honeycomb structures formed by 5% w/v Na-montmorillonite at 20 mM salt (Fig. 5.7 (b)) reveals that the average length of the branches is larger than the average lateral size of 425 nm (Chapter 3) of the Na-montmorillonite platelets. A magnified image of this sample is provided in Fig. 5.8 (a) which clearly shows that many of the branches have holes on their surfaces. This indicates that the platelets on each branch are connected in overlapping coin (OC) configurations, as predicted by Jonsson *et. al.* using Monte Carlo simulations in a system of clay platelets at low salt concentrations [32, 33]. In the OC configuration, the positive edge of a platelet attaches to the negative basal surface near the edge of another platelet in a parallel fashion, thereby forming longer sheets (branches of the network) through attractive bonds (Fig. 5.8(b)). The positive edges of two such sheets (the branches) attach to the negative faces of a third sheet comprising platelets which are also in OC configurations. Such attachments lead to the formation of an attractive network-junction of three branches as indicated in Fig. 5.8. We note here that such honeycomb-like network formation is not very dominant in the case of the sample with 10 mM salt (a magnified image is shown in Fig. 5.9) due to the presence of high face-face repulsions.

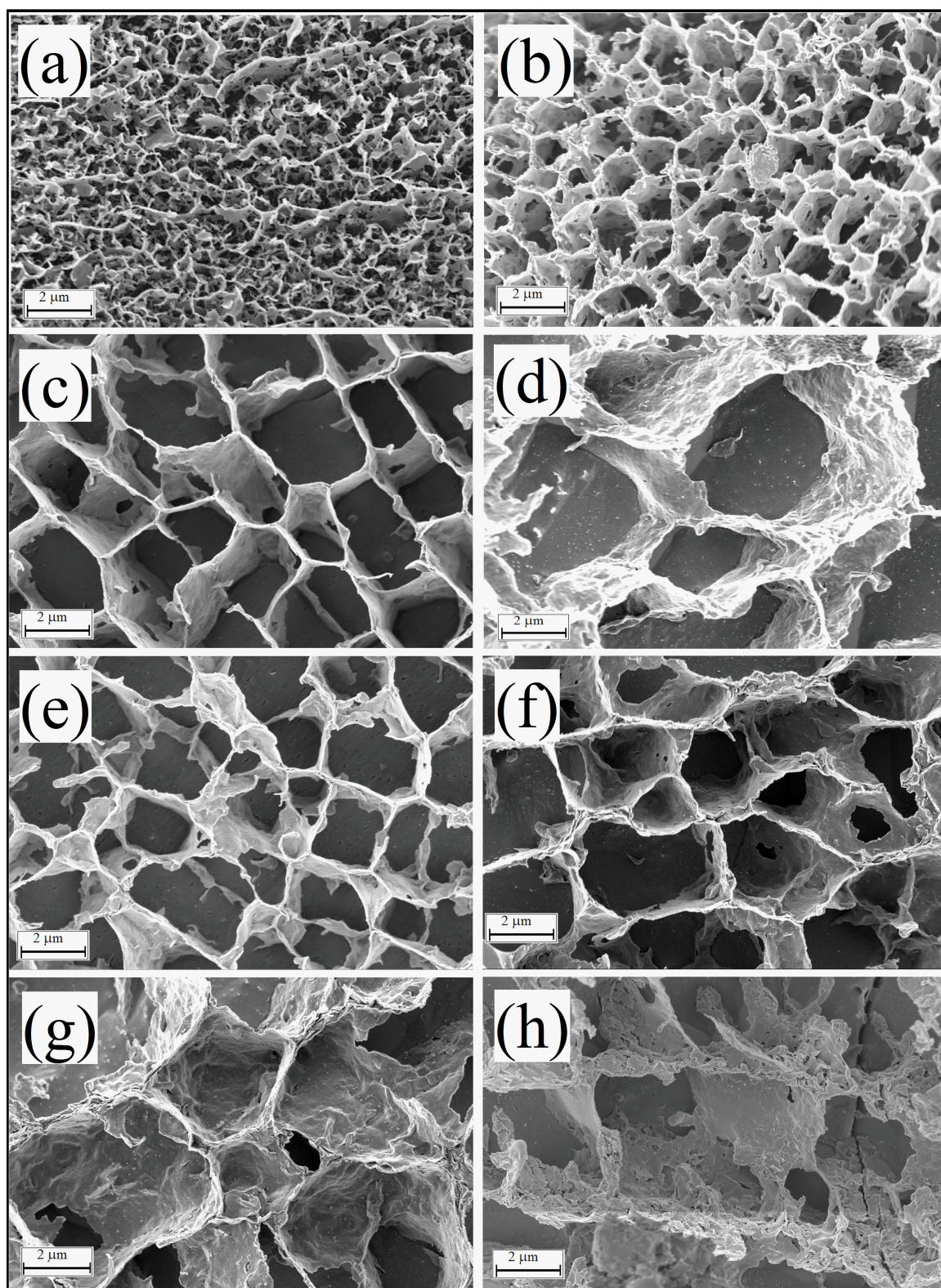


FIGURE 5.7: Representative micrographs obtained using cryo-SEM for 5% w/v Na-montmorillonite suspensions with $C_s = 10$ mM (a), 20 mM (b), 50 mM (c), 100 mM (d), 150 mM (e), 200 mM (f), 300 mM (g) and 500 mM (h). The scale bars represent $2 \mu\text{m}$.

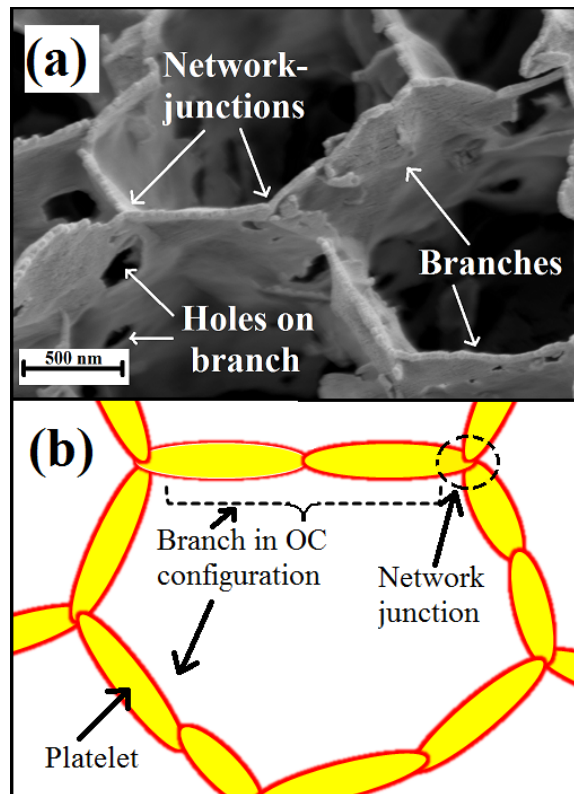


FIGURE 5.8: (a) Magnified view of a representative micrograph obtained using cryo-SEM for 5% w/v Na-montmorillonite suspension with $C_s = 20$ mM. (b) Schematic depiction of the microscopic arrangement of platelets showing overlapping coins (OC) in suspension in the presence of salt. The red color on the edges indicates positive charges and the yellow color on the basal surface indicates screened negative charges.

We use the cryo-SEM micrographs to quantify the pore (void) size distributions, porosity and branch thicknesses of all the gels studied in this chapter. Porosity is defined as a ratio of the total void area to the total area of the 2D projection of the gel structure. The image analysis tools used here and the details of the calculation of the porosity and network branch thickness are at the end of this chapter (section 5.5). Representative distributions of pore sizes and branch thickness, w , are shown in Fig. 5.10 (a) and (b) respectively for 5% w/v Na-montmorillonite samples with $c_s = 50$ mM. It is to be noted that the pore sizes and thicknesses measured here are, respectively, smaller and larger than the actual sizes due to the presence of vitrified water on the network. However, since the sublimation time (12 min) after fracturing the vitrified samples is same for all the suspensions, an equal sublimation-depth is expected for all

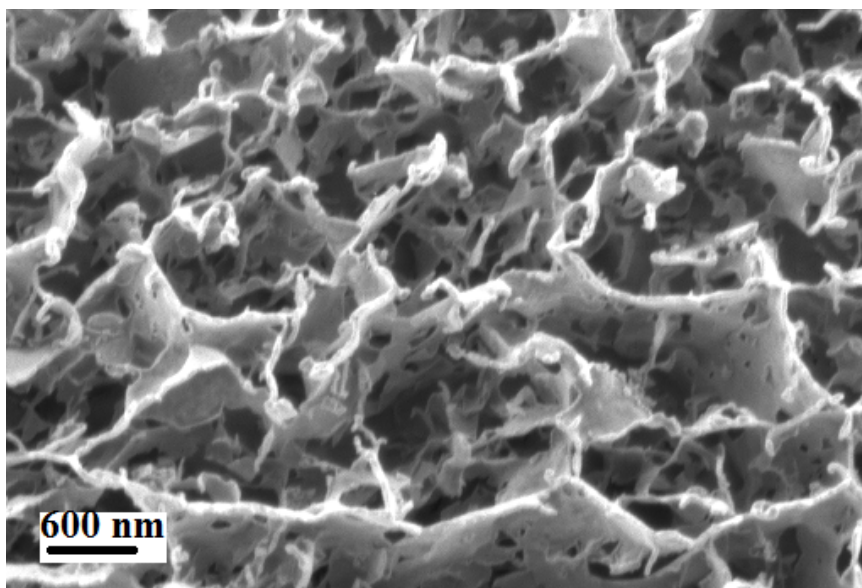


FIGURE 5.9: Magnified cryo-SEM micrograph showing gel structure in a vitrified sample of 5% w/v Na-montmorillonite with 10 mM added salt.

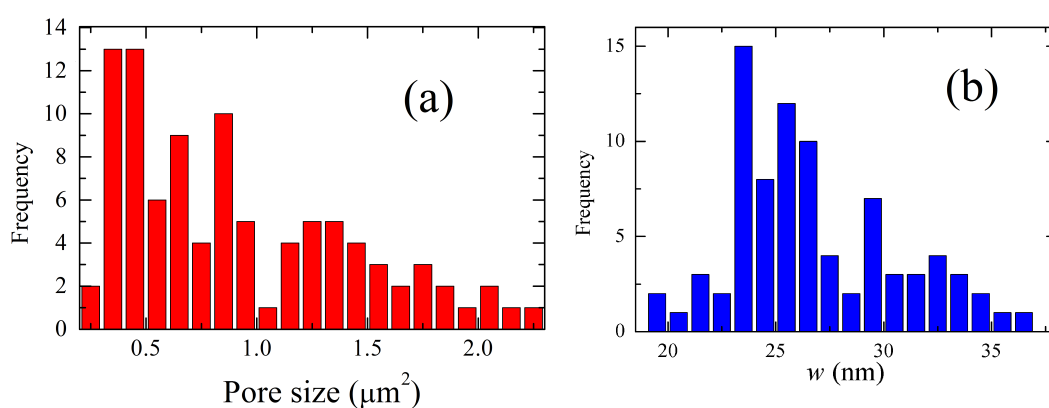


FIGURE 5.10: (a) Pore size distribution and (b) branch thickness w distribution calculated from eight SEM micrographs of a 5% w/v Na-montmorillonite sample with 50 mM salt mapped on a 2D plane using ImageJ.

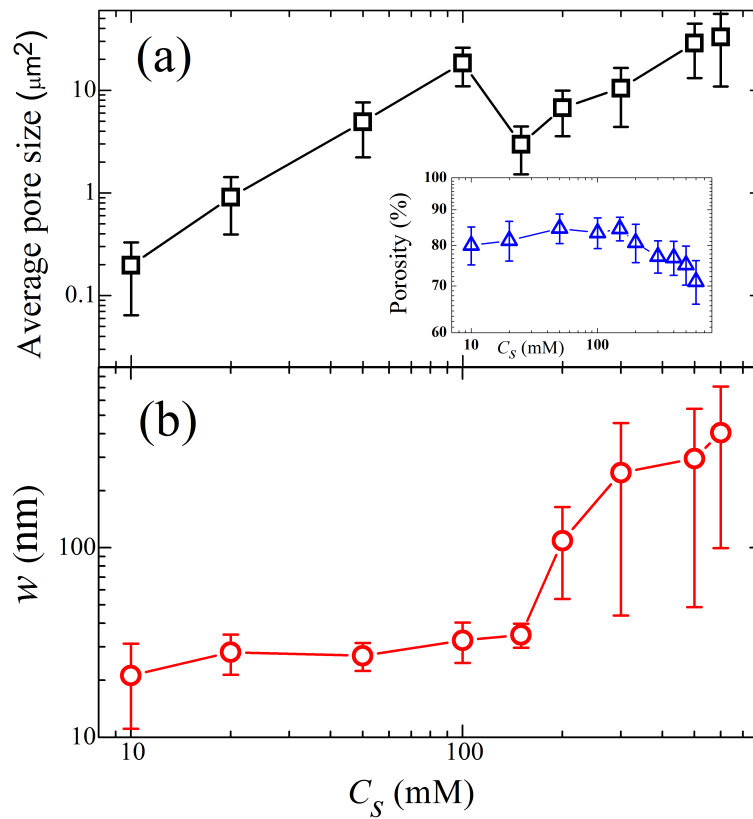


FIGURE 5.11: (a) Plot of average pore size (\square) of the gel network as a function of salt concentration C_s . Inset shows the variation of porosity (Δ) with C_s . (b) Plot of network-branch thickness, w , (\circ) as a function of C_s . The image analysis is performed using ImageJ.

the samples studied using cryo-SEM. When C_s is increased systematically upto 100 mM, the average pore size (\square in Fig. 5.11(a)) increases, while the porosity (Δ in the inset of Fig. 5.11(a)) and branch thickness w (\circ in Fig. 5.11(b)) of the gels remain almost unchanged. It can therefore be concluded that for $C_s \leq 100$ mM, the participation of platelets in the OC configurations increases. As C_s is increased to 100 mM, the number of network-junctions simultaneously decreases, while the lengths of the individual branches of the network increases with C_s . This was clearly observed in Fig. 5.7(a), (b), (c) and (d). Interestingly, at $C_s = 150$ mM, the average pore size (\square in Fig. 5.11(a)) decreases, while the porosity (Δ in inset of Fig. 5.11(a)) and w (\circ in Fig. 5.11(b)) remain unchanged. This reduction in pore size at $C_s = 150$ mM (cryo-SEM micrograph in Fig. 5.7 (e)) arises due to the participation of a substantial number of platelets in

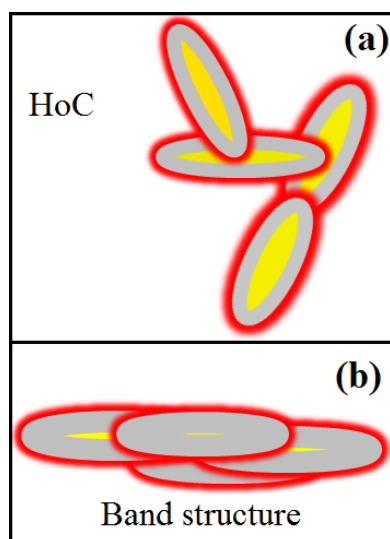


FIGURE 5.12: Schematic depiction of (a) house-of-card (HoC) arrangement of circular platelets and (b) face-face aggregation of platelets leading to band-type structures in the suspension in the presence of salt. The red color on the edges indicates positive charges and the yellow color on the basal surface indicates screened negative charges. The grey color indicates complete charge screening.

house-of-cards (HoC) configurations, apart from the OC configurations discussed earlier. In such HoC configurations, the positive edge of a platelet attaches attractively to the central negative part of the basal surface of another platelet (Fig. 5.12(a)). The coexistence of HoC and OC configurations can be seen in a magnified micrograph in Fig. 5.13 for a sample with $C_s = 150$ mM. Thus, at this salt concentration, the lengths of the network branches decrease and number of network junctions increases due to the participation of a substantial number of platelets in HoC configuration. This can be observed in Fig. 5.11(a). It is to be noted that the coexistence of such configurations was predicted earlier in simulations of clay suspensions at high salt concentrations [33].

Since the addition of salt in the dispersing medium leads to a decrease in the Debye screening length, the spillover of negative potential from the basal surface onto the positive edges of platelets decreases with increase in salt concentration [34–36]. The effective potentials on the edges of the platelets are expected to be positive at $C_s = 10$ mM. This leads to the formation of a gel network at this salt concentration as seen in Fig. 5.7(a). With increasing C_s , the magnitude of the effective positive potentials on

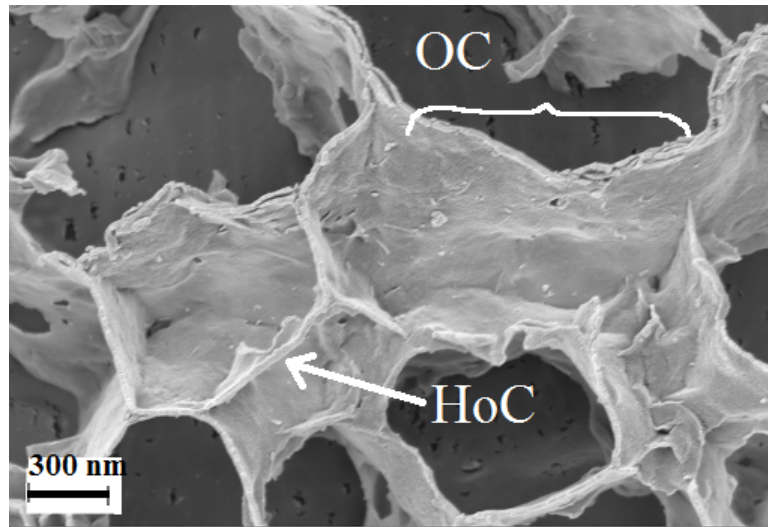


FIGURE 5.13: Magnified cryo-SEM micrograph showing gel structures comparing OC and HoC configurations in a vitrified sample of 5% w/v Na-montmorillonite with 150 mM added salt.

the platelet edges increases until the long-range effects of the negative charges of the basal surface becomes negligible due to screening. As a result, the number of attractive bonds and their strengths in OC and HoC configurations increase with C_s (Fig. 5.7(a), (b), (c), (d) and (e)). This contributes to the growing G'_{pl} and yield stresses of the gels upto $C_s = 150$ mM (Fig. 5.5 and inset of Fig. 5.6).

At $C_s > 150$ mM, the average pore size (\square in Fig. 5.11(a)) and w (\circ in Fig. 5.11(b)) increase with increasing C_s . The total void space simultaneously decreases slightly (Δ in the inset of Fig. 5.11(a)). These features, and a close inspection of the micrographs (a representative magnified image of the sample in Fig. 5.7 (g) is shown in Fig. 5.14), reveal that due to the considerable screening of negative charges on the basal surfaces, the face-face aggregation process due to van der Waals attractions becomes dominant at very high salt conditions [32]. Such parallel aggregation of platelets for low clay and high salt concentrations was also observed indirectly using ultrasound attenuation spectroscopy in our earlier study [37]. The face-face aggregation occurs very randomly and leads to elongated and thicker branches known as band structures (a schematic depiction in Fig. 5.12(b)) [38–40]. These band-type branches further connect at their ends and eventually form a kinetically arrested network characterized by a honeycomb

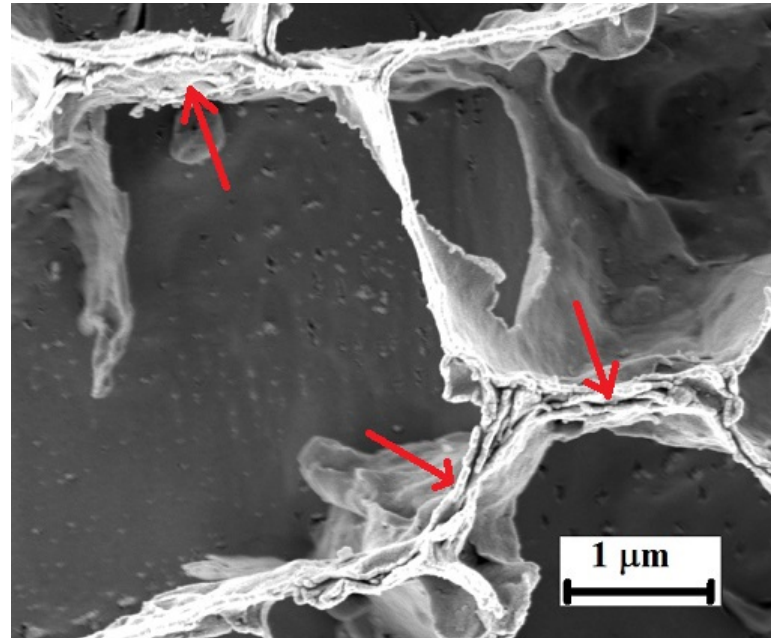


FIGURE 5.14: Magnified cryo-SEM micrograph showing gel structures in a vitrified sample of 5% w/v Na-montmorillonite with 300 mM added salt. The arrows shows the branches formed by random face-face stacking (band structure) of clay platelets.

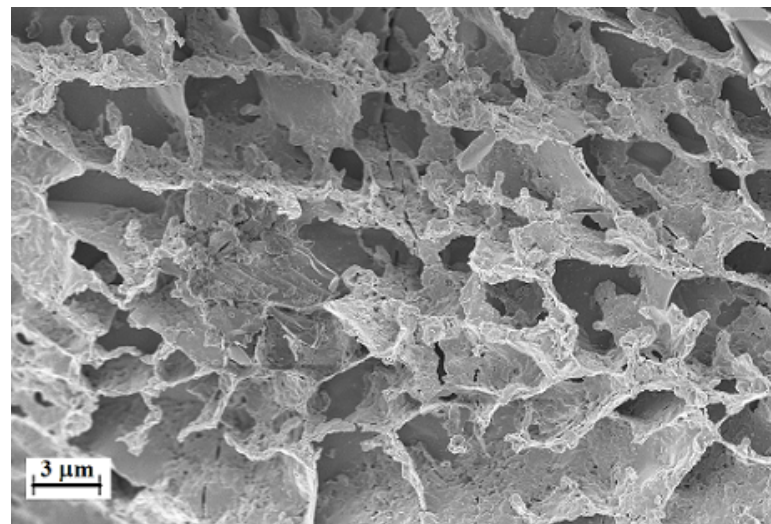


FIGURE 5.15: SEM micrograph showing incomplete network structures in a vitrified sample of 5% w/v Na-montmorillonite with 600 mM added salt.

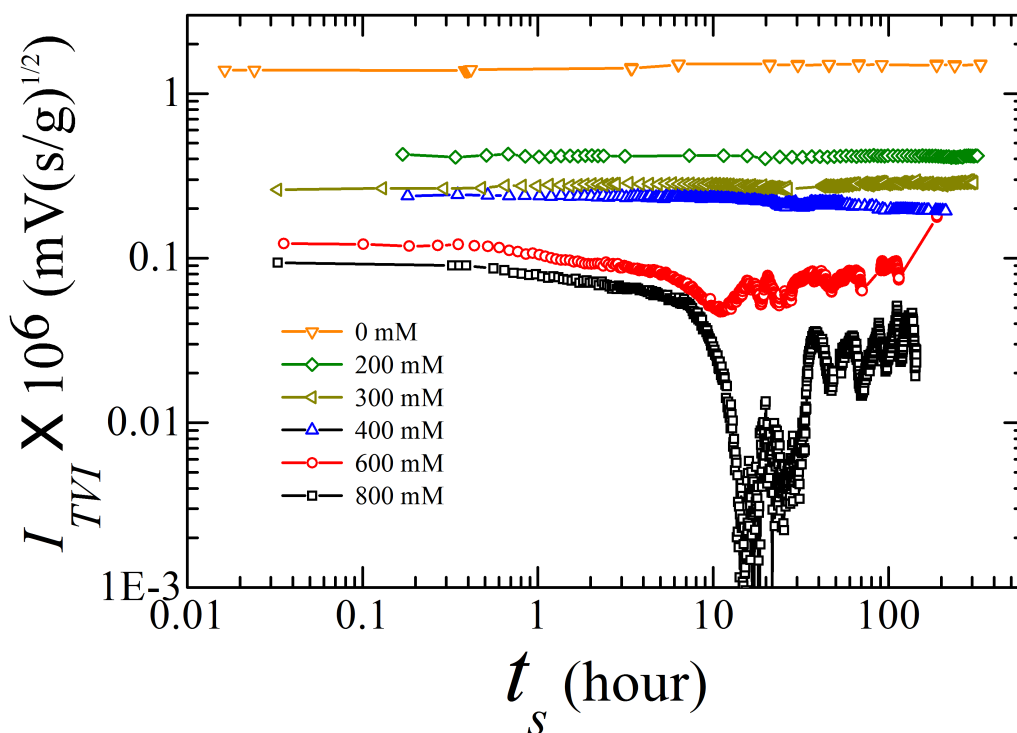


FIGURE 5.16: Evolution of total vibration current (I_{TVI}), normalized by the ultrasound pressure gradient in an electroacoustic setup versus observation time t_s . Here, $t_s = 0$ is defined as the time when the stirring of the sample is stopped inside the electroacoustic setup. The samples are 5% w/v Na-montmorillonite with $C_s = 0$ mM (∇), 200 mM (\diamond), 300 mM (\triangleleft), 400 mM (\triangle), 600 mM (\circ) and 800 mM (\square).

structure. This can be clearly observed in the cryo-SEM micrographs presented in Fig. 5.7(f),(g),(h). Incomplete network formation is also observed at very high salt concentrations, e.g. at $C_s = 500$ mM (Fig. 5.7(h)) and for a sample with 600 mM salt (Fig. 5.15) due to the strong face-face aggregation of a considerable fraction of clay platelets.

The observed decrease in G'_{pl} and yield stresses reported earlier (Fig. 5.5 and inset of Fig. 5.6) when C_s is increased beyond 150 mM can be attributed to the considerable increase in the pore sizes and thicknesses of the network branches which is observed in Fig. 5.11. In this salt concentration regime, the excluded volume due to the basal charge repulsions decreases substantially with increasing C_s . In addition, the strength of the attraction between the branches of the network also increases. As a result, applied strains promote irreversible aggregation of the thick branches. This process

leads to a higher pore size, larger branch thickness and decreasing network connectivity with increases C_s , leading to the observed decrease in G'_{pl} and σ_y . When these samples are subjected to small stresses, the coagulation of network branches under stress can lead to the collapse of the gel network, with the yielding happening at lower γ values as the network branches become increasingly thicker.

We verify the stability of the gels under gravity by measuring the total vibration current (I_{TVI}) using an electroacoustic setup described in Chapter 2 (Section 2.2.2). Fig. 5.16 shows the variation of I_{TVI} with observation time t_s , measured for 5% w/v Na-montmorillonite gels for a C_s range between 0 mM and 800 mM. The suspension with no added salt (∇ in Fig. 5.16) is highly stable under gravity due to the kinetic arrest of the constituent clay platelets. Surprisingly, we find no change in I_{TVI} values measured over two weeks for samples with $C_s \leq 300$ mM (\diamond and \triangleleft in Fig. 5.16). This confirms that the gels observed in Fig. 5.7(a)-Fig. 5.7(g) are highly stable under gravity. The sample with $C_s = 400$ mM (\triangle in Fig. 5.16) exhibits a small decrease in I_{TVI} after $t_s = 20$ hours. The suspensions with $C_s > 400$ mM (\circ and \square in Fig. 5.16) show irregular oscillations in I_{TVI} values with observation time t_s due to the intermittent collapse of the gel structures. When the sedimentation front collapses downward, it passes through consecutive half wavelength regions having alternating directions of the ultrasound pressure gradient set by the the electroacoustic probe along the sample height. As a result, the particles on the sedimenting front have opposite orientations of induced dipole moments at different t_s , leading to the observed oscillation in I_{TVI} with t_s . This behavior indirectly confirms that gels with $C_s = 600$ mM and 800 mM salt are not stable under gravity. Due to the large pore sizes and thick network branches of these samples (Fig. 5.7 (h) and Fig. 5.11), the weights of the branches exceed the local yield stresses of the network, resulting in the observed gel collapse.

5.4 Conclusions

In this chapter, we present our results on the influence of NaCl on the microstructures, viscoelasticity, yielding and stability of Na-montmorillonite gels at a clay concentration, 5% w/v, at which the suspension is expected to exhibit a glassy phase in the absence of salt [37]. Microscopic observations using cryogenic scanning electronic microscopy (cryo-SEM) reveal that at low salt concentrations, the clay platelets form long sheet structures (network branches) through attractive overlapping coin (OC) configurations predicted in a simulation study recently [32]. These sheets (branches) join at their ends to form crosslinked ribbons (network-junctions), giving rise to honeycomb-like network structures (Fig. 5.7 (a), (b), (c)). Interestingly, we find that platelet participation in the OC configurations in the network-branch increases with increase in salt concentration in the range of 10-100 mM. This leads to higher pore sizes without any change in the branch thickness w of the gels (Fig. 5.11). With further increase of C_s upto 150 mM, the thickness of the network branches remains unchanged but the pore size of the gels decreases with C_s due to the participation of a substantial number of clay platelets in the HoC configurations, besides the usual OC configurations (Fig. 5.7(d)). Such a coexistence of OC and HoC at higher salt concentration was also predicted in an earlier simulation study [33]. Our rheological measurements (Fig. 5.5 and inset of Fig. 5.6) further suggest that strength of the attractive bonds due to such platelet configurations increases with increasing C_s upto a value of 150 mM.

At $C_s > 150$ mM, the van der Waals attraction between platelets becomes dominant due to the high screening of the basal negative charges by the Na^+ ions. Under these conditions, the platelets coagulate in a face-to-face orientation randomly, leading to the formation of elongated structures known as ‘band-type structures’ that have been predicted in the literature ([38, 40]). These elongated bands further connect at their ends, with the emergence of kinetically arrested honeycomb structures (Fig. 5.7(e), (f), (g)). The pore sizes and branch thicknesses w of the gel networks increase with C_s due to the increase in the face-face bond formation of the platelets (Fig. 5.11). The strength of the gels decreases with C_s (Fig. 5.5 and inset of Fig. 5.6) in this salt concentration

regime due to a decrease in the repulsive excluded volume and a simultaneous increase in the attraction between the branches of gel network. This leads to the collapse of the gels under applied strains. It is also seen, using systematic electroacoustic measurements, that the gels exhibit considerable stability under gravity upto $C_s = 300$ mM (Fig. 5.16). At $C_s > 300$ mM, the gels become unstable due to irreversible branch coagulation, with the gel network eventually collapsing under gravity.

In conclusion, the present study elucidates the link between the bulk rheological and stability behaviors of natural Na-montmorillonite gels and their underlying microscopic structures. Apart from the significant importance of this study for various rheological applications of Na-montmorillonite, we believe that the results presented here will facilitate our understanding of the suspension behavior of other clays such as Laponite and Kaolinite in the presence of salt. Since soil is composed of many natural clay minerals, our results are also extremely useful in the understanding of many geophysical phenomena such as landslides, and the formation of quicksand and river deltas [41, 42].

5.5 Analysis of cryo-SEM images using ImageJ software

The cryo-SEM micrographs shown in Chapter 5 are analyzed using ImageJ (version: 1.49q) to calculate porosity, pore size distribution and thickness w of branches of the gel network. A cryo-SEM micrograph presents a three dimensional network structure in two dimensions with a range of pixel gray-values (intensity values). For a particular image, we manually adjust the threshold value of gray-scale using ImageJ in such a way that only the boundaries of the pores remain bright in the 2D plane. The image is then converted to binary form as shown in Fig. 5.17. In this figure, the dark pixels correspond to voids spaces. Thus, the total area of dark pixels gives the total area of void spaces in the binary image. The ratio of dark area to the total area of the

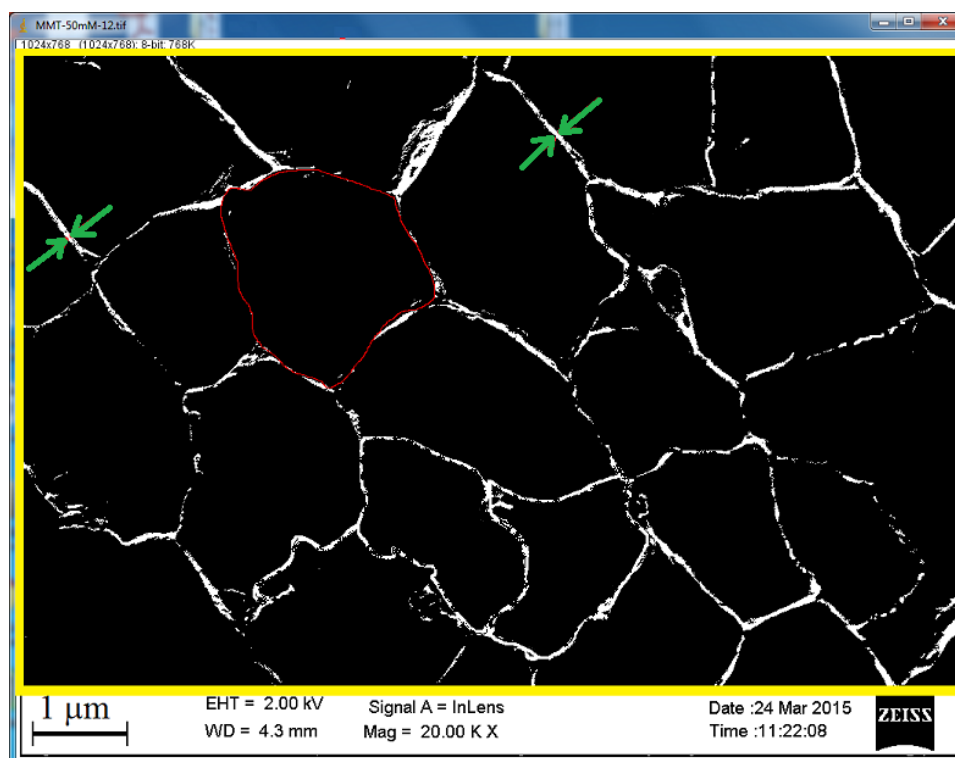


FIGURE 5.17: A 2D projected binary image obtained using ImageJ software for a 5% w/v Na-montmorillonite gel with $C_s = 50$ mM. The total area of the micrograph is shown by the yellow rectangle. The boundary of a pore is indicated by a closed red line. The distance between the tips of the green arrows gives the branch thickness w .

binary image gives the porosity value. To calculate sizes of the individual pores, each pore on the binary image is manually selected using the ImageJ pointer, as shown by a red boundary in Fig. 5.17. The total area within this red boundary gives the pore size. The thickness (shown by green arrows in Fig. 5.17) of a branch of the network is calculated manually using the ImageJ pointer. Such measurements are repeated over several micrographs of the same sample to get good statistical averages of porosity, pore sizes and branch thickness. Fig. 5.10 of Chapter 5 shows a representative plot of pore size and thickness distributions for a 5% w/v Na-montmorillonite gel with $C_s = 50$ mM.

References

- [1] A. Shahin and Y. M. Joshi, *Langmuir*, 2012, **28**, 15674–15686.
- [2] J. Fossum, *The European Physical Journal Special Topics*, 2012, **204**, 41–56.
- [3] L. Bailey, H. N. W. Lekkerkerker and G. C. Maitland, *Soft Matter*, 2015, **11**, 222–236.
- [4] R. Bandyopadhyay, D. Liang, H. Yardimci, D. A. Sessoms, M. A. Borthwick, S. G. J. Mochrie, J. L. Harden and R. L. Leheny, *Physical Review Letters*, 2004, **93**, 228302.
- [5] A. S. Negi and C. O. Osuji, *Journal of Rheology (1978-present)*, 2010, **54**, 943–958.
- [6] D. Saha, Y. M. Joshi and R. Bandyopadhyay, *Soft Matter*, 2014, **10**, 3292–3300.
- [7] V. Tudisca, M. A. Ricci, R. Angelini and B. Ruzicka, *RSC Advances*, 2012, **2**, 11111–11116.
- [8] D. Saha, R. Bandyopadhyay and Y. M. Joshi, *Langmuir*, 2015, **31**, 3012–3020.
- [9] J. Duran, M. Ramos-Tejada, F. Arroyo and F. Gonzalez-Caballero, *Journal of Colloid and Interface Science*, 2000, **229**, 107 – 117.

-
- [10] S. C. Glotzer and M. J. Solomon, *Nature Materials*, 2007, **6**, 557 – 562.
- [11] B. Ruzicka and E. Zaccarelli, *Soft Matter*, 2011, **7**, 1268–1286.
- [12] E. Paineau, A. Philippe, K. Antonova, I. Bihannic, P. Davidson, I. Dozov, J. Gabriel, M. Imperor-Clerc, P. Levitz, F. Meneau and L. Michot, *Liquid Crystals Reviews*, 2013, **1**, 110–126.
- [13] H. Tanaka, J. Meunier and D. Bonn, *Physical Review E*, 2004, **69**, 031404.
- [14] K. Norrish, *Discussions of the Faraday society*, 1954, **18**, 120–134.
- [15] F. A. Bowles, *Science*, 1968, **159**, 1236–1237.
- [16] S. Jabbari-Farouji, H. Tanaka, G. H. Wegdam and D. Bonn, *Physical Review E*, 2008, **78**, 061405.
- [17] H. van Olphen, *John Wiley and Sons Inc.: New York*, 1977, **53**, 230–230.
- [18] L. J. Michot, I. Bihannic, F. Thomas, B. S. Lartiges, Y. Waldvogel, C. Caillet, J. Thieme, S. S. Funari and P. Levitz, *Langmuir*, 2013, **29**, 3500–3510.
- [19] G. Lagaly and S. Ziesmer, *Advances in Colloid and Interface Science*, 2003, **100-102**, 105 – 128.
- [20] G. Broughton and L. Squires, *The Journal of Physical Chemistry*, 1935, **40**, 1041–1053.
- [21] H. van Olphen, *Journal of Colloid Science*, 1964, **19**, 313 – 322.
- [22] P.-I. Au and Y.-K. Leong, *Colloids and Surfaces A: Physicochemical and Engineering Aspects*, 2013, **436**, 530 – 541.
- [23] H. Kimura, M. Sakurai, T. Sugiyama, A. Tsuchida, T. Okubo and T. Masuko, *Rheologica Acta*, 2011, **50**, 159–168.
- [24] P. B. Laxton and J. C. Berg, *Journal of Colloid and Interface Science*, 2006, **296**, 749 – 755.

- [25] M. Dijkstra, J. P. Hansen and P. Madden, *Physical Review Letters*, 1995, **75**, 2236–2239.
- [26] J. Wierzechos, C. Ascaso, M. T. Garcia-Gonzalez and E. Kozak, *Clays and Clay Minerals*, 1992, **40**, 230–236.
- [27] M. S. Zbik, W. N. Martens, R. L. Frost, Y.-F. Song, Y.-M. Chen and J.-H. Chen, *Langmuir*, 2008, **24**, 8954–8958.
- [28] *Nanocor Inc. Technical data sheet*, Nanocor Inc. Technical data sheet G-105, (Last accessed on 22nd February 2015).
- [29] B. J. Marlow, D. Fairhurst and H. P. Pendse, *Langmuir*, 1988, **4**, 611–626.
- [30] K. Miyazaki, H. M. Wyss, D. A. Weitz and D. R. Reichman, *EPL (Europhysics Letters)*, 2006, **75**, 915–921.
- [31] M. Laurati, S. U. Egelhaaf and G. Petekidis, *Journal of Rheology (1978-present)*, 2011, **55**, 673–706.
- [32] B. Jonsson, C. Labbez and B. Cabane, *Langmuir*, 2008, **24**, 11406–11413.
- [33] M. Delhomme, B. Jonsson and C. Labbez, *Soft Matter*, 2012, **8**, 9691–9704.
- [34] R. Secor and C. Radke, *Journal of Colloid and Interface Science*, 1985, **103**, 237–244.
- [35] E. C. Y. Yan and K. B. Eisenthal, *The Journal of Physical Chemistry B*, 1999, **103**, 6056–6060.
- [36] D. Zhou, A. I. Abdel-Fattah and A. A. Keller, *Environmental Science & Technology*, 2012, **46**, 7520–7526.
- [37] S. Ali and R. Bandyopadhyay, *Applied Clay Science*, 2015, **114**, 85–92.
- [38] A. Weiss and R. Frank, *Naturforsch*, 1961, **16**, 141–142.

- [39] T. Permien and G. Lagaly, *Applied Clay Science*, 1994, **9**, 251 – 263.
- [40] P. F. Luckham and S. Rossi, *Advances in Colloid and Interface Science*, 1999, **82**, 43 – 92.
- [41] A. Thill, S. Moustier, J.-M. Garnier, C. Estournel, J.-J. Naudin and J.-Y. Bottero, *Continental Shelf Research*, 2001, **21**, 2127 – 2140.
- [42] A. Khaldoun, E. Eiser, G. Wegdam and D. Bonn, *Nature*, 2005, **437**, 635–635.

6

Sedimentation kinetics of weak clay gels

6.1 Introduction

All materials on earth are subject to gravitational forces which may affect the aggregation and stability behaviors of suspensions of particles with considerable density mismatch with the background medium [1–7]. Gravitational stability of various kinetically arrested phases such as clay colloidal glasses and gels [8–11] therefore depends on the competition between the strengths of their microstructures and their gravitational weights [12–16]. This is an important factor for the various technological applications of clay suspensions as thickeners and stabilizers [17–19], and also for many clay-related geophysical phenomena such as quicksands and river delta formation and landslides [20–22]. Influence of gravity becomes considerably important when kinetically arrested phases in clay suspensions have weak structures [23, 24]. Interestingly,

such competition between the gravity and mechanical strengths of clay suspensions can be controlled externally by changing salt and clay concentrations, and is the focus of discussion in this chapter.

In Chapter 4, we have shown that the stability of clay gels at high clay concentration can be enhanced by adding salt to a clay suspension that is prepared in deionized water, rather than by adding the clay mineral to a previously mixed salt solution. In this chapter, we report a detailed study of the stability behavior of Na-montmorillonite clay platelets and their aggregates in dilute aqueous suspensions under different ionic conditions using light transmission method and electroacoustics. It is observed that dilute salt-free suspensions, with clay concentration below the glass transition concentration, are not stable under gravity. Addition of salt to the suspensions leads to the formation of weak gels. Stability of these gels are studied by directly tracking the collapsing gel-interface. We find that adding salt after dispersing the clay mineral does indeed result in more stable gels even in very dilute suspensions. However, these weak gels are seen to exhibit transient collapse after a finite delay time. Furthermore, the velocity of the collapsing gel is seen to oscillate with increasing gel age, with the average magnitude of the velocity increasing upto a peak value before decreasing subsequently. With increasing salt concentration, the delay time for transient collapse decreases, while the peak value of the collapse velocity increases.

The phenomenon of transient collapse was first observed by Poon *et al.* in 1993 [25] and has been a subject of intense research since then. In the last two decades, the transient collapse phenomenon of colloidal gels has been studied in depletion gels [23, 26–28] and in colloidal gels flocculated at their secondary minima [29, 30]. However, a complete understanding of the microscopic origin of transient collapse remains elusive. Our study, using a combination of rheological measurements, ultrasound attenuation spectroscopy and cryogenic scanning electronic microscopy, reveals that the continuous restructuring and association of the clay platelets in overlapping coin configurations lead to increase in the widths and lengths of the gel network strands. We argue that a competition between the gravitational stresses on these network strands

and the local yield stresses plays an important role in determining the stability of gels formed from charged colloidal clay particles.

6.2 Sample preparation

Na-montmorillonite of Nanomer PGV grade with CEC value of $145 \pm 10\%$ meq/100g procured from Nanocor Inc [31] is used for this work. Details of the structure of this clay particle can be found in Chapter 1 (Section 1.6). The clay mineral is hygroscopic in nature. The clay powder is therefore baked for 24 hours in an oven at 120°C to remove absorbed moisture for good reproducibility of data. The powder is next dispersed in water using a magnetic stirrer under vigorous stirring conditions. Three batches of samples are prepared at different ionic conditions as noted below:

Samples without salt: Clay powder is dispersed in highly deionized Milli-Q water of resistivity $18.2 \text{ M}\Omega\cdot\text{cm}$. The suspension is stirred for seven days before using it for experiments.

SBC sample: Clay powder is dispersed in brine solution. The brine solution is prepared by adding a predetermined amount of NaCl in Milli-Q water. The mixture is kept under stirring conditions for seven days before experiments. We designate such a sample as SBC (Salt added Before Clay).

SAC sample: A predetermined amount of salt is added after seven days to a clay suspension prepared in a salt-free condition. The mixture is further stirred for three hours before experiments. We designate such a sample as SAC (Salt added After Clay).

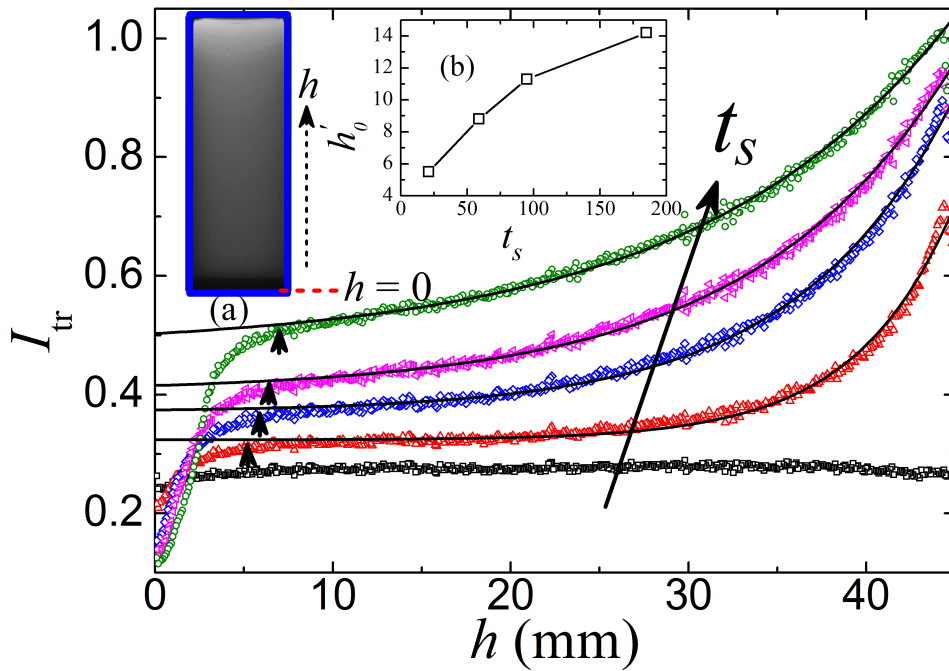


FIGURE 6.1: Variation of the transmitted intensity (I_{tr}) along the height h of the cuvette for a 0.8% w/v Na-montmorillonite suspension at ages $t_s = 0, 21, 59, 95$ and 185 hours (bottom to top). Here, $h = 0$ is at the bottom of the sample column and $t_s = 0$ is defined as the time when the stirring of the sample in the cuvette is stopped. The arrow heads indicate the positions of the top surfaces of the sediment at different t_s . The solid lines are the exponential fits [$I_{tr}(h) = I_0 + I' \exp(h/h'_0)$] to the data. Here, h'_0 is a length scale characterizing the particle concentration gradient. The inset (a) shows an image of the sample acquired at $t_s = 59$ hours using the CCD camera. The variation of h'_0 with t_s is shown in the inset (b).

6.3 Results and Discussion

6.3.1 Optical and rheological studies of sedimentation of dilute clay gels prepared at different ionic conditions

We first monitor the stability of clay platelets in dilute aqueous salt-free suspensions using the light transmission method at $25 \pm 0.1^\circ\text{C}$. Details of the setup and experimental procedure are given in Chapter 2 (Section 2.2.2). The clay samples are loaded inside a sedimentation cell (rectangular glass cuvette) immediately after preparation. The sample age $t_s = 0$ is measured from the moment at which the loading process of a sample is completed. Fig. 6.1 shows the variation of the transmitted intensity (I_{tr}) along the

height, h , of the cuvette for a 0.8% w/v aqueous suspension of Na-montmorillonite clay at several ages, t_s . Here, $h = 0$ is at the bottom of the sample cuvette. At age $t_s = 0$, I_{tr} remains almost constant with varying h . This indicates that the clay platelets are distributed uniformly in the suspension. For $t_s > 0$, I_{tr} increases with h . A representative CCD image of the sample acquired at $t_s = 59$ hours is shown in the inset (a) of Fig. 6.1. The I_{tr} vs h data can be fit to $I_{tr}(h) = I_0 + I' \exp(h/h'_0)$, where I_0 , I' and h'_0 are the fitting parameters. h'_0 is a length scale characterizing the intensity gradient, and therefore is a measure of the particle concentration gradient, along the sample height. At low h , a sharp change in I_{tr} can be observed due to the deposition of the clay platelets at the bottom of the sample cuvette. The positions where the I_{tr} data deviate from the exponential fits correspond approximately to the clay sediment heights and are indicated by arrow heads in Fig. 6.1. At larger h , the exponential variation of I_{tr} with h indicates a continuously varying concentration of platelets along the height of the sample. As a result of the wide size distribution of the clay platelets (Fig. 3.8 of Chapter 3), the bigger platelets settle faster than the smaller ones. The smaller particles diffuse out over larger length scales with increasing t_s , giving rise to a gradual increase in h'_0 with age as observed in the inset (b) of Fig. 6.1. The absence of any distinct interface between the supernatant and the clay rich region [inset (a) of Fig. 6.1] confirms the absence of a gel phase [32, 33].

Due to the high concentration of negative charges on the basal surfaces and the wide lateral sizes of Na-montmorillonite platelets, there is a small spillover of negative potential onto the positive edges of the platelets in suspensions of $\text{pH} > 7$ [34–36]. As a result, the effective potential on the edges are also negative. Hence, the Na-montmorillonite platelets in dilute suspensions, such as the ones reported in Fig. 6.1, do not show any aggregation and sediment under gravity. However, a salt-free aqueous suspension of Na-montmorillonite clay platelets exhibits strong stability above the glass transition concentration (4% w/v). This is probed by measuring colloidal vibration current I_{CVI} with age, t_s , at the top surface of the sample in an electroacoustic setup (Section 2.2.2 of Chapter 2). The data are shown in Fig. 6.2. For samples with

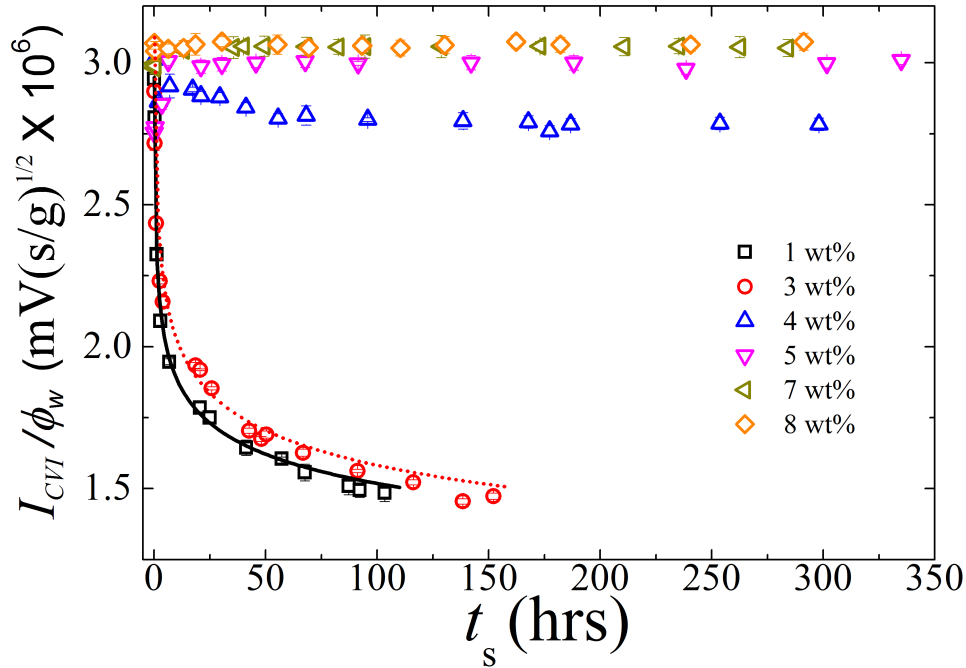


FIGURE 6.2: Evolution of the colloidal vibration current (I_{CVI}) measured in the electroacoustic setup (Fig. 2.4) versus the age t_s of Na-montmorillonite suspensions with clay concentrations of 1% w/v (\square), 3% w/v (\circ), 4% w/v (\triangle), 5% w/v (∇), 7% w/v (\triangleleft) and 8% w/v (\diamond).

clay concentrations below 4% w/v, the clay particles sediment under gravity. This can be seen from the exponentially decreasing I_{CVI} values with increasing t_s (\square and \circ in Fig. 6.2). For concentrations $\geq 4\%$ w/v, the clay suspensions are stabilized by long range repulsive interactions and form kinetically constrained, structurally disordered soft glasses [37, 38], which renders the particles increasingly stable under gravity. This can be seen from the values of the I_{CVI} which remain almost constant with changing t_s (\triangle , ∇ , \triangleleft and \diamond in Fig. 6.2).

We next investigate the aggregation and stability behaviors of dilute clay suspensions in the presence of added salt. Attractive interactions between the clay platelets in a 0.8% w/v Na-montmorillonite suspension are induced by the addition of salt to the medium which results in the reduction of the Debye screening lengths characterizing the Na-montmorillonite platelets in the suspensions. CCD images captured at different ages (t_s) of a 0.8% w/v Na-montmorillonite suspension (SAC) with 60 mM salt, prepared by adding the salt to the suspensions after dispersing clay powder in deionized

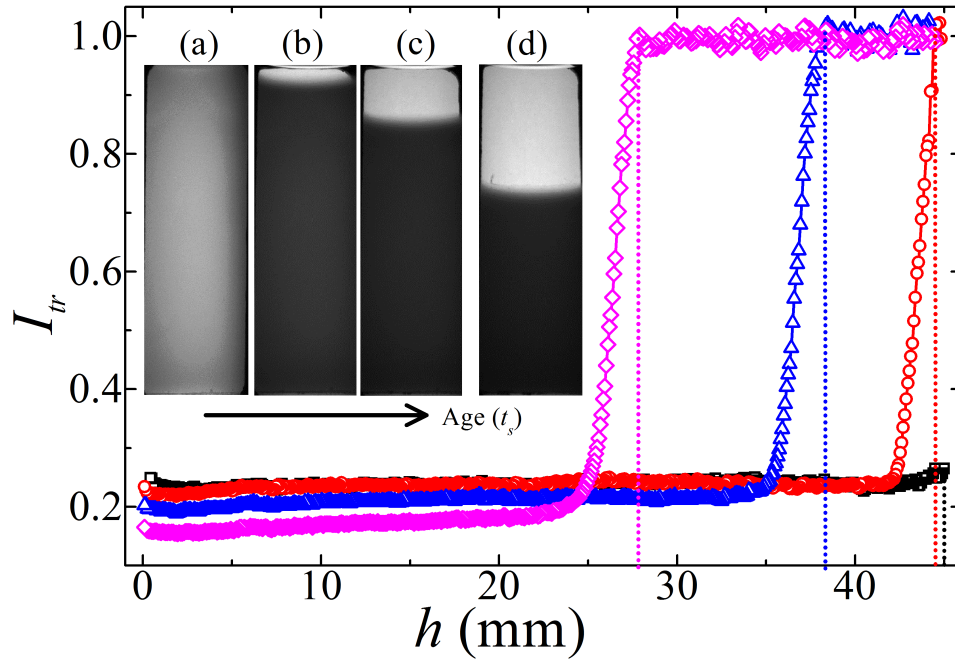


FIGURE 6.3: Variation of the transmitted intensity (I_{tr}) with sample column height, h , of a 0.8% w/v Na-montmorillonite suspension (SAC) with 60 mM salt at ages $t_s = 0.5$ hours (\square), 3 hours (\circ), 10 hours (\triangle) and 95 hours (\diamond). The corresponding CCD images of the gel at different t_s are shown in the insets (a), (b), (c) and (d). The vertical dotted lines in the main figure indicate the positions of the interface between the supernatant and the collapsing gel at different t_s .

water, are shown in the insets of Fig. 6.3. At $t_s = 0.5$ hours, the transmitted intensity, I_{tr} , remains constant with varying h (\square in Fig. 6.3), indicating that the clay particles are uniformly distributed along the sample height. At higher t_s , a distinct interface between the clear supernatant and the clay rich phase appears in the suspension, with the transmitted intensity through the supernatant reaching 100% at decreasing values of h with increasing sample age. The positions of the interface at different ages are shown by dotted lines in Fig. 6.3.

Representative time evolution data of the normalized positions h/h_0 of the interfaces in 0.8% clay suspensions with 40 mM salt, prepared at two different ionic conditions (SBC and SAC), are shown in Fig. 6.4. Here, h_0 is the total sample height. It is seen in this figure that the sample designated as SBC (\square), prepared by dispersing

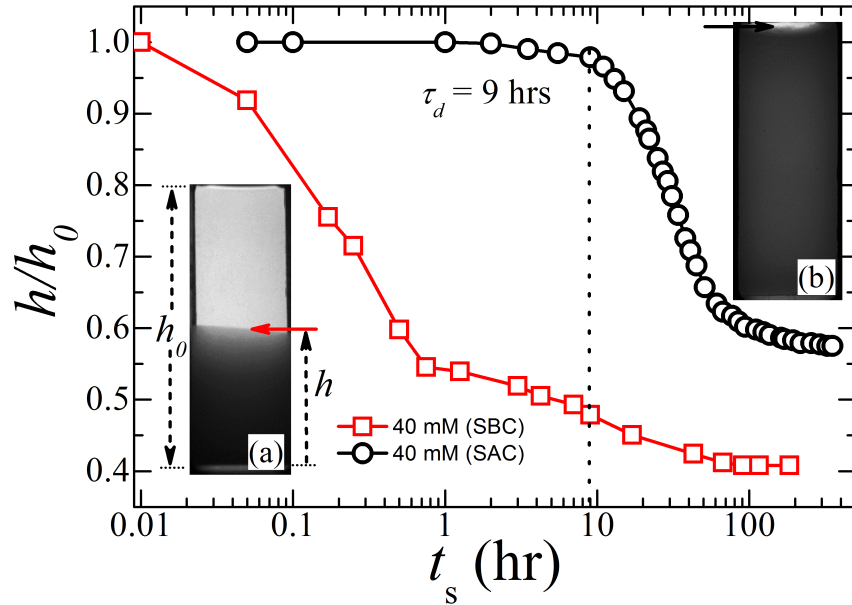


FIGURE 6.4: Variation of the normalized height, h/h_0 , of the interface between the clear supernatant and the collapsing gel versus age, t_s , in a 0.8% w/v Na-montmorillonite suspension (SBC), prepared by adding clay powder in 40 mM brine (\square) and a 0.8% w/v Na-montmorillonite suspension (SAC), prepared by adding 40 mM salt after dispersing the clay powder (\circ). Here, $h = 0$ is at the bottom of the sample column and $t_s = 0$ is defined as the time when stirring of the sample is stopped in the cuvette. The delay time, $\tau_d = 9$ hours, for the onset of collapse of the SAC sample is indicated by the vertical dotted line. The insets (a) and (b) show the CCD images acquired at $t_s = 10$ hours of the SBC and SAC gels respectively.

clay powder at a concentration of 0.8% w/v in a 40 mM salt solution, is highly unstable under gravity, with the normalized interface height (h/h_0) decreasing continuously with t_s . On the other hand, the sample designated as SAC (\circ in Fig. 6.4), prepared by adding 40 mM salt in a 0.8% w/v clay suspension, remains stable under gravity for a finite delay time, $\tau_d = 9$ hours, during which the interface remains in a quiescent state. At $t_s > \tau_d$, the interface height of the SAC sample decreases rapidly with t_s due to a transient collapse phenomenon and eventually saturates at longer times.

To understand the microstructures of these suspensions, we perform frequency sweep rheological experiments for samples at $t_s = 30$ min by varying the imposed oscillatory frequency in the range 0.1–50 rad/s at a strain amplitude of 0.1%. The frequency sweep measurement could not be extended to very low frequencies for the SBC gel due to the unstable nature of this sample. The SAC gel, in comparison, is

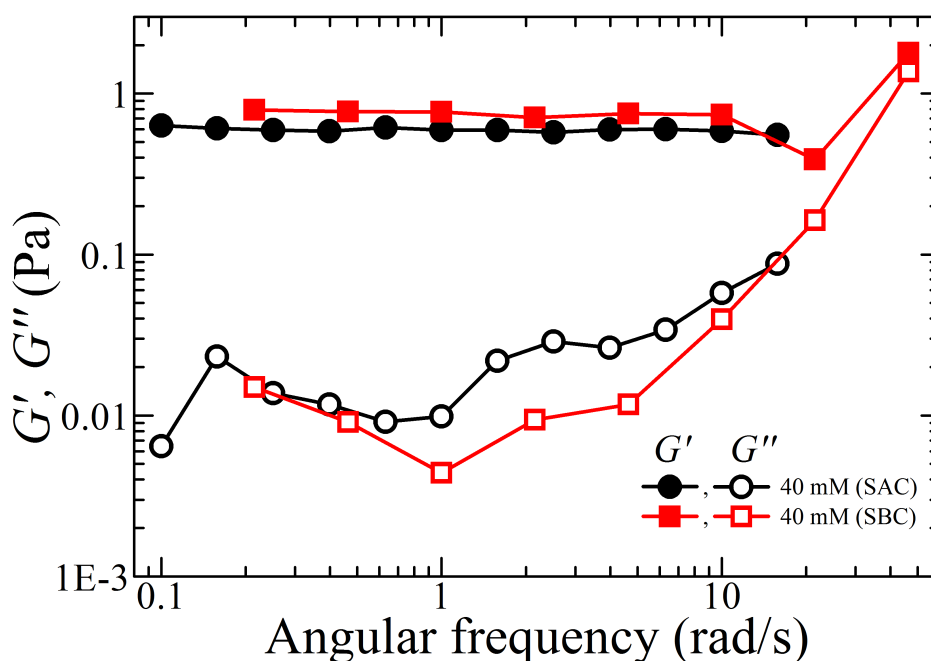


FIGURE 6.5: Frequency dependence of the storage modulus G' (solid symbols) and the loss modulus G'' (empty symbols) of the SBC sample (\circ), prepared by dispersing 0.8% w/v Na-montmorillonite clay powder in 40 mM salt solution and the SAC sample (\square), prepared by adding 40 mM salt to a 0.8% w/v Na-montmorillonite suspension. An oscillatory shear strain of amplitude 0.1% was applied in these experiments.

stable for a very long duration, allowing data collection even for very small oscillatory frequencies. It is seen from Fig. 6.5 that the elastic modulus G' is much higher than the viscous modulus G'' for both the samples. Furthermore, G' is almost independent of the applied oscillatory frequency, whereas G'' is weakly dependent on frequency for frequency values less than 10 rad/s. These are typical rheological signatures exhibited by kinetically arrested colloidal particles in suspension [39]. Since the clay concentration (0.8% w/v) investigated here is well below the glass transition concentration (4% w/v) (Fig. 6.2) [37], the observed kinetic arrest clearly arises from the formation of gel network structures that are facilitated by attractions between the clay platelets induced by the added salt. Indeed, the formation of clay gels has been verified by us using direct visualization methods and will be discussed in detail later.

To understand the observed stability behavior of these gels prepared at identical clay and salt concentrations, we estimate the particle size distributions (PSDs) of the

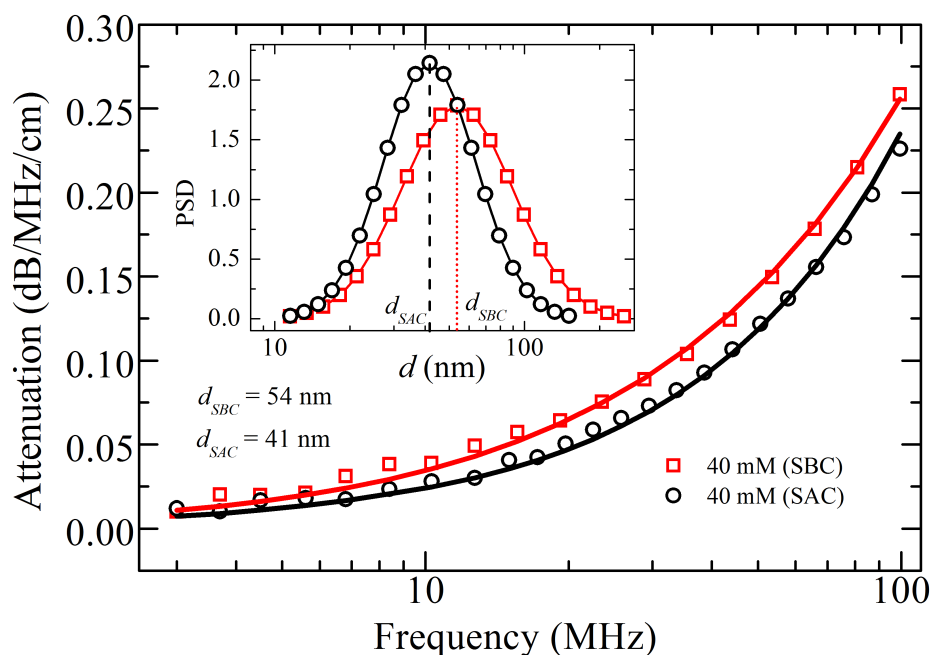


FIGURE 6.6: Ultrasound attenuation spectra measured in the frequency range of 3–99.5 MHz at $t_s = 0$ for a 0.8% w/v Na-montmorillonite suspension (SBC sample), prepared by adding the clay powder in 40 mM brine (\square), and for a 0.8% w/v Na-montmorillonite suspension (SAC sample), prepared by adding 40 mM salt after dispersing the clay powder in water (\circ). Solid lines are theoretical fits to the attenuation spectrum using Eqns. 2.1 – 2.6 (Chapter 2) for a unimodal size distribution of the clay particles. The inset shows the corresponding particle size distributions of the two samples. It is seen that $d_{SBC} = 54$ nm and $d_{SAC} = 41$ nm are the median values for the equivalent spherical sizes of the particles in the suspensions prepared in SBC (\square) and SAC conditions (\circ) respectively.

clay particles in their suspensions using the ultrasound attenuation method described in Chapter 2 (Section 2.2.1). The size measurements are performed while stirring the suspensions using a magnetic stirrer to avoid sedimentation of the particles. Fig. 6.6 shows the measured attenuation spectra in the ultrasound frequency range 3–99.5 MHz for 0.8% w/v Na-montmorillonite suspensions with 40 mM salt concentration prepared for the two different ionic conditions (SBC and SAC) described earlier. The attenuation spectra are fitted to the theoretical estimates for the attenuation spectra (solid lines in Fig. 6.6) considering a unimodal size distribution (Eqns. 2.1 – 2.6 of Chapter 2). The particle size distributions thus estimated from these spectra are plotted in the inset of Fig. 6.6. It is seen that the equivalent spherical median sizes are $d_{SBC} = 54$ nm for the

SBC sample (\square in Fig. 6.6) and $d_{SAC} = 41$ nm for the SAC sample (\circ in Fig. 6.6). The average thickness of tactoids in the SBC sample is therefore higher than in the SAC sample. The lower degree of exfoliation of tactoids in the SBC sample arises due to the presence of salt in the dispersing medium during the preparation stage. The salt present in the water reduces the osmotic pressure difference of the hydrated Na^+ counterions between the intratactoid spaces and the bulk medium. This inhibits the diffusion of the native Na^+ counterions from the intertactoid spaces into bulk water, thereby reducing the rate of exfoliation of the clay tactoids and leading to larger particle sizes in the SBC sample [37]. Owing to large d_{SBC} values, the gravitational stress on the SBC gel network dominates over the local yield stress and eventually leads to the rapid gravitational collapse of the gel immediately after stirring is stopped. In contrast, the degree of exfoliation in the SAC sample (\circ in Fig. 6.6) is higher, resulting in a larger number of exfoliated particles in this suspension compared to the SBC sample. Hence, the network connectivity in the SAC sample is expected to be higher. At the same time, the gravitational stress on the gel network in the SAC sample is comparatively weaker due to the smaller sizes of the constituent particles. In contrast to the SBC gel, a quiescent or steady state of the SAC sample can therefore be observed upto a delay time $\tau_d = 9$ hours (\circ Fig. 6.4).

The sedimentation data for 0.8% w/v Na-montmorillonite suspensions prepared under SAC conditions with varying salt concentrations C_s are shown in Fig. 6.7. All samples here exhibit quiescent regimes followed by collapse regimes. When C_s is increased, the delay time τ_d decreases (inset of Fig. 6.7), indicating faster collapse of the gels. To better describe the collapse process, we calculate the velocity, v_{int} , of the collapsing interface (Fig. 6.8) from the I_{tr} versus t_s data (Fig. 6.7) for different C_s . The value of v_{int} at any t_s value is estimated by calculating slope between two consecutive h/h_0 values in Fig. 6.7. Irregular oscillations in the values of v_{int} with t_s can be seen during collapse. It is seen that the average magnitude of v_{int} increases with t_s and shows a peak before decreasing at higher t_s . It is also observed that the peak shifts to lower t_s for higher salt concentrations. This observation will be discussed later.

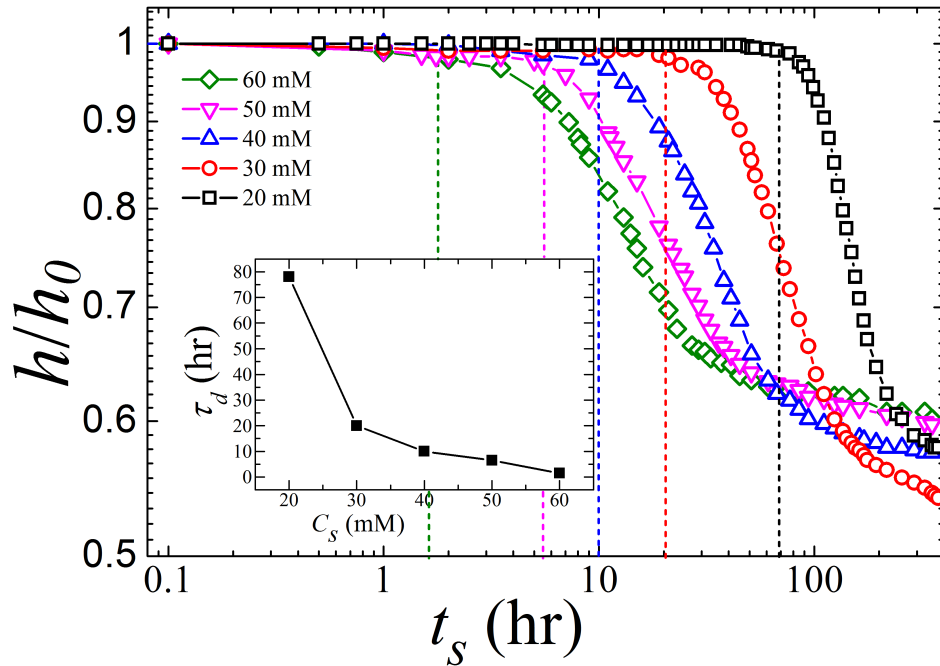


FIGURE 6.7: Evolution of the normalized heights, h/h_0 , of the interface between the clear supernatant and the collapsing gel versus age, t_s , of 0.8% w/v Na-montmorillonite suspensions (SAC) with salt concentrations of 20 mM (\square), 30 mM (\circ), 40 mM (\triangle), 50 mM (∇) and 60 mM (\diamond). Gelation is induced in these samples by dispersing clay powder in deionized water and then adding salt. The inset shows the variation of the delay time, τ_d , with varying salt concentrations. The vertical dashed lines indicate the positions of the delay time, τ_d , for the different salt concentrations.

To monitor the evolution of the mechanical strengths during the sedimentation of the gels with age, we performed rheological measurements with a cylindrical measuring head of length 25 mm and diameter 16.6 mm. The sample is kept in a cylindrical container of inner diameter 27.6 mm and length 42 mm. The measuring head is inserted into the sample upto 25 mm from the top surface of the sample so that the flat surface of the measuring head remains outside the sample. This avoids deposition of clay particles on the flat surface of the measuring head during the sedimentation process. The details of the rheometer used can be found in Chapter 2. After loading the sample, an oscillatory strain of amplitude 1000% and angular frequency 10 rad/s is applied for two minutes to shear-melt the sample. The variation of the elastic modulus G' with t_s is next measured by applying a small oscillatory strain of amplitude 0.1% and angular frequency 10 rad/s to samples prepared under SAC conditions with salt concentrations

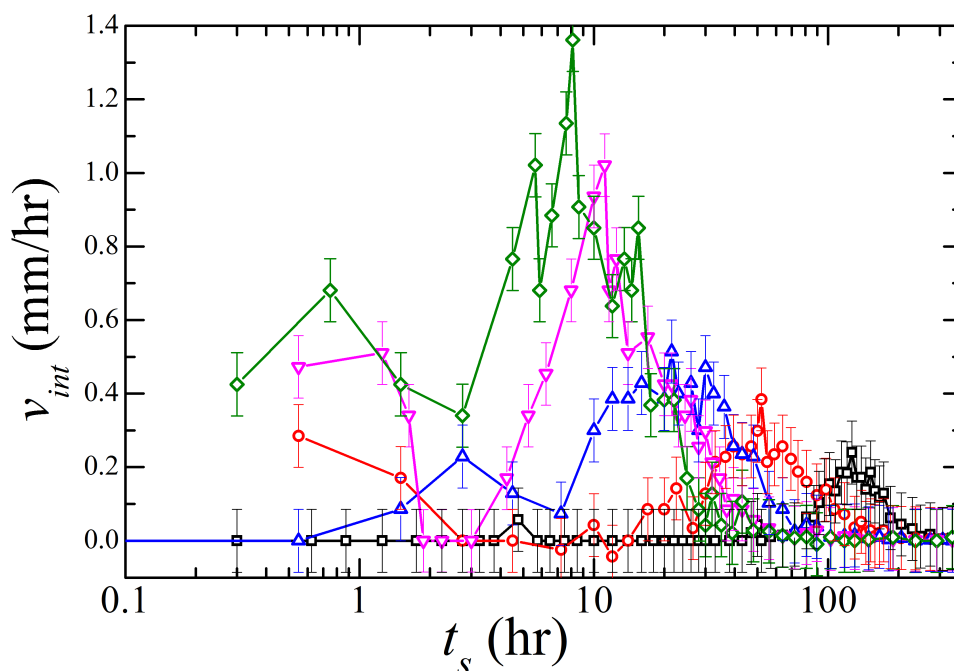


FIGURE 6.8: Plot of the collapse velocity, v_{int} , of the interface with age t_s for 0.8% w/v Na-montmorillonite suspensions (SAC) at salt concentrations 20 mM (\square), 30 mM (\circ), 40 mM (\triangle), 50 mM (∇) and 60 mM (\diamond). The error bars quantify the systematic errors that arise from the detection of the interface using the optical method described earlier.

20 mM, 30 mM, 40 mM and 60 mM. These data are shown in Fig. 6.9. It is seen that G' increases monotonically upto age $t_s = t_r$ (indicated by arrows in Fig. 6.9 for different salt concentrations). This is followed by a slight decrease in G' , with the data showing oscillations as t_s is increased further. However, the average magnitude of G' increases with t_s . The variations of t_r (time at which the first oscillation in G' is observed) and the delay time, τ_d , measured from the interface collapse profile (Fig. 6.7) are plotted in the inset of Fig. 6.9. These two characteristic times show very good agreement for all C_s values. This suggests that during the quiescent period ($t_s < \tau_d$), G' , and hence the yield stress of the gel, both increase. However, a mechanical failure of the gel network occurs at $t_s = t_r \sim \tau_d$, leading to transient collapse.

When C_s is increased, the platelets constituting the gels are expected to aggregate faster through the formation of stronger attractive bonds [40]. The weights of the gel strands increase substantially as a result, accelerating the transient collapse of the gels

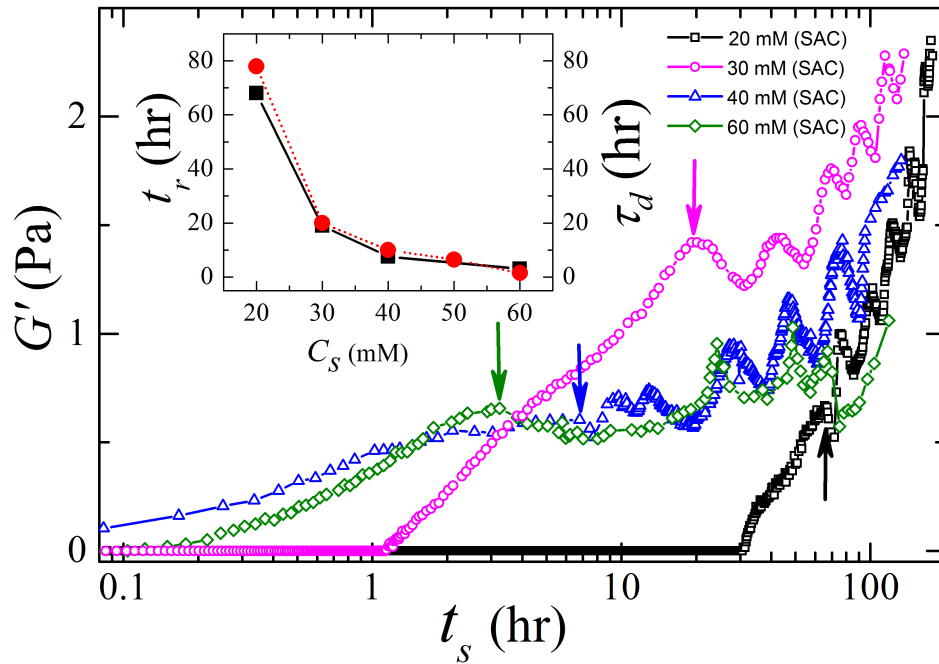


FIGURE 6.9: Evolution of the elastic modulus, G' , with age, t_s , of 0.8% w/v Na-montmorillonite (SAC) suspensions at salt concentrations 20 mM (\square), 30 mM (\circ), 40 mM (\triangle) and 60 mM (\diamond). Here, $t_s = 0$ is defined as the time at which the shear melting of the sample is stopped in the measuring cell. The moduli are measured by applying an oscillatory strain of amplitude 0.1% and angular frequency of 10 rad/s. The arrows indicate the positions of the delay times, t_r , at which G' s start exhibiting oscillations for all four salt concentrations. The inset shows the plot of t_r (\blacksquare) and τ_d (\bullet) with varying salt concentration.

(inset of Fig. 6.9). Once the transient collapse is initiated, the gel strands approach each other. This gives rise to even faster platelet aggregation. This, in turn, leads to an increase in the gravitational stress on the gel network, with the velocity of the collapsing interface increasing sharply with t_s as observed in Fig. 6.8. However, due to gel compaction and the formation of progressively stronger bonds between the particles in the network, the yield stress also increases simultaneously during the sedimentation process and eventually overcomes the gravitational stress. This results in a decreasing interface velocity at large t_s values. The competition between the gravitational and yield stress on the gel gives rise to a repetitive process of mechanical failure and build up of the gel structure in the collapse regime and results in the observed oscillations of v_{int} and G' at $t_s > t_r \sim \tau_d$.

To understand the mechanical failure of the gel network with age, we directly study

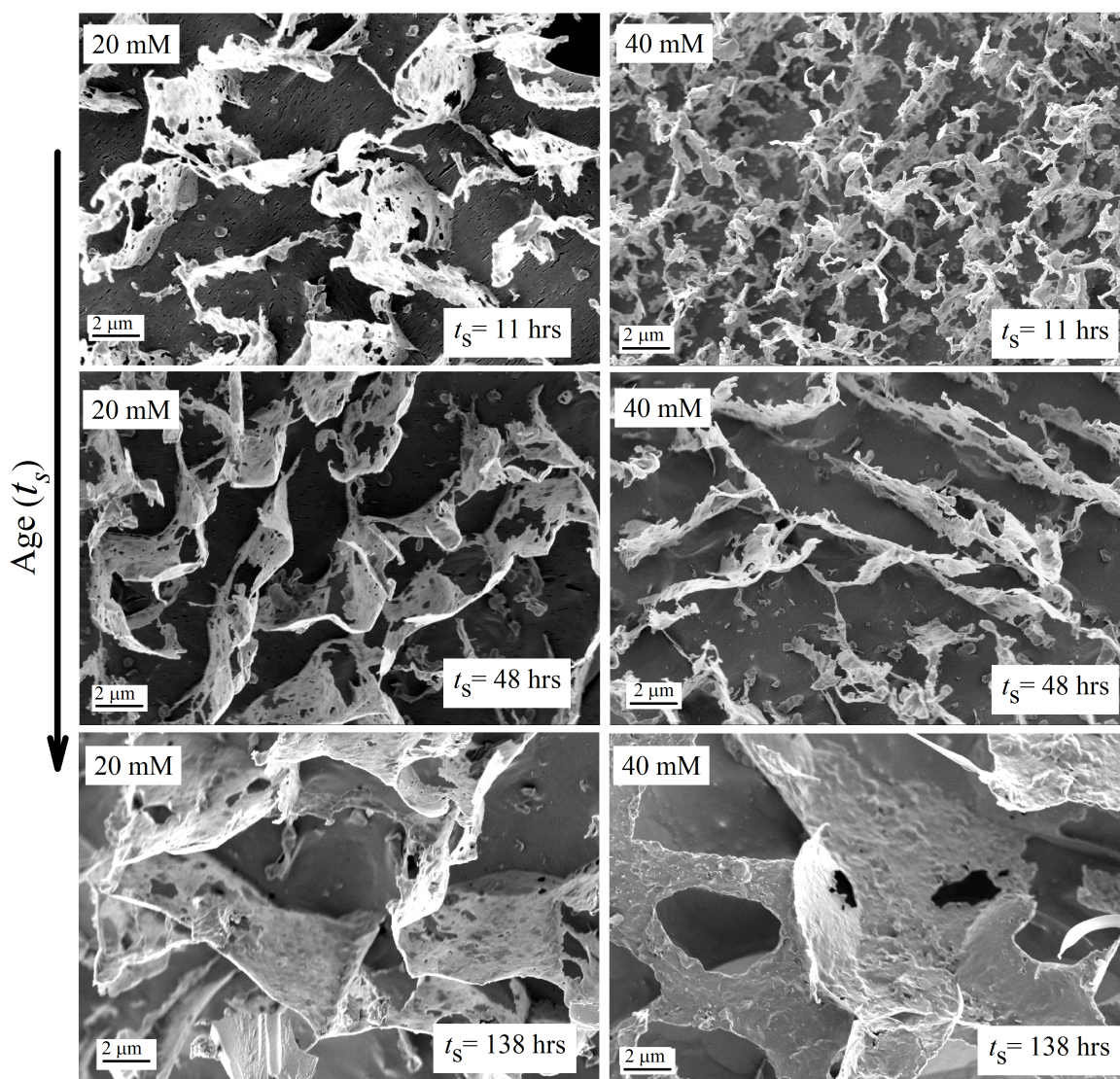


FIGURE 6.10: Representative micrographs obtained using cryo-SEM for 0.8% w/v Na-montmorillonite suspensions (SAC) with $C_s = 20$ mM (left panel) and 40 mM (right panel) at ages $t_s = 11$ hours, 48 hours and 138 hours (top to bottom). The scale bars represent 2 μm .

the variation of the microscopic structures of the aging gels using a cryogenic scanning electron microscope (cryo-SEM) described in Chapter 2 (Sections 2.2.6 and 2.2.8). Fig. 6.10 shows the cryo-SEM micrographs of the weak SAC gels formed with $C_s = 20\text{mM}$ and 40 mM at $t_s = 11$ hours, 48 hours and 138 hours. It is seen from these images that the clay platelets form highly disordered network structures. It is clearly observed that the average lengths and widths of the network strands are higher than the average lateral size of each clay platelet (425 nm reported in Chapter 2). This indicates that the platelets in the network structures are connected in overlapping coin (OC) configurations [41]. The gel structure formation dominated by OC association of platelets in the similar salt concentration range but at a higher clay concentration (5% w/v) is discussed in detail in Chapter 5. In an OC configuration, the positive edge of a platelet is attached to the negative basal surface near the edge of another platelet in a parallel fashion (Fig. 5.8 of Chapter 5). It is also clearly visible from the images in Fig. 6.10 that the widths and lengths of the network strands grow with age as an increasing number of platelets participate in network formation through OC configurations. This suggests that the gels restructure continuously due to thermal fluctuations and reorient in a way that eventually leads to the formation of stronger attractive bonds [42]. As a result, the elastic modulus, and hence the yield stress, increase continuously with age upto a time $t_r \sim \tau_d$ as observed in the rheological measurements earlier (Fig. 6.9). On the other hand, due to the increase in the dimensions of the network strands as observed in Fig. 6.10, the gravitational stresses on the network strands increase simultaneously with t_s . At $t_s = \tau_d$, the gravitational stresses overcome the local yield stresses of the gels leading to mechanical failure and the subsequent collapse of the gels as presented in Fig. 6.7 and Fig. 6.9. In the SBC gel samples, on the other hand, the network strands are thicker and longer, and the gravitational stresses typically always exceed the local yield stress, resulting in accelerated gel collapse (Fig. 6.4).

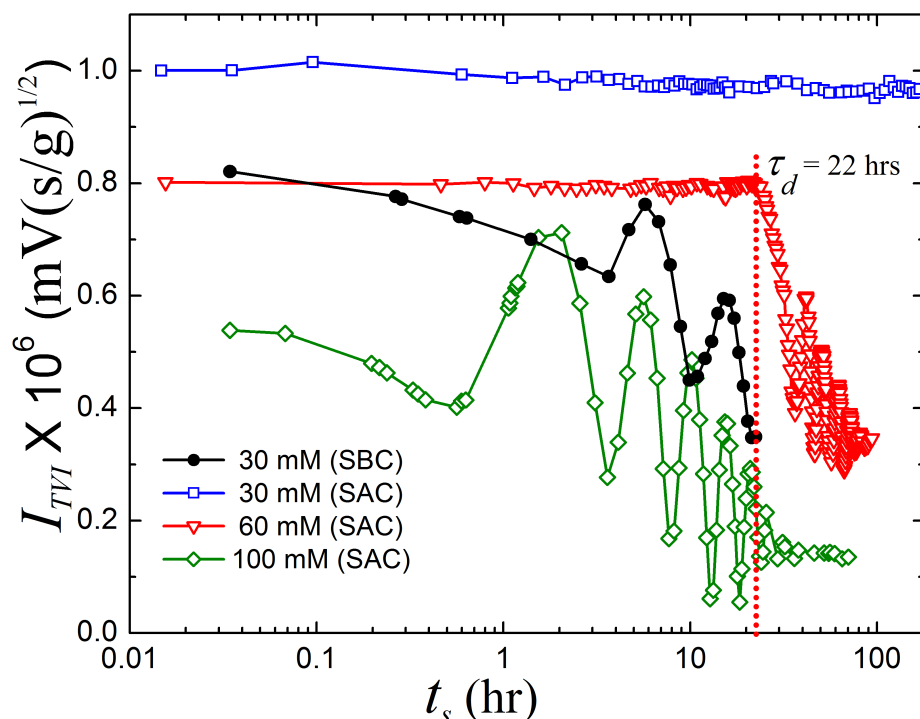


FIGURE 6.11: Evolution of the total vibration current (I_{TVI}) measured in the electroacoustic setup with increasing t_s for 3% w/v Na-montmorillonite suspension with salt concentration of 30 mM prepared in SBC condition (●) and for 3% w/v Na-montmorillonite suspensions (SAC) with salt concentrations of 30 mM (□), 60 mM (▽) and 100 mM (◇). The vertical dotted line shows the position of the delay time $\tau_d = 22$ hours for the sample with 60 mM salt.

6.3.2 Electroacoustic studies of stability of concentrated clay gels prepared at different ionic conditions

For comparison purpose, the stability of clay gels with higher particle concentrations is studied using an electroacoustic method that is suitable for monitoring the small collapse heights in gels of higher clay concentrations. Fig. 6.11 shows the variation of the total vibration current I_{TVI} measured in the electroacoustic setup (Section 2.2.2 of Chapter 2) for 3% w/v Na-montmorillonite suspensions with varying C_s prepared in different ionic conditions (SBC and SAC). It is seen that I_{TVI} for the SAC gel with $C_s = 30$ mM (□ in Fig. 6.11) remains almost unchanged with t_s . This indicates that the gel is highly stable in the experimental time window. For the SAC gel with $C_s = 60$ mM (▽ in Fig. 6.11), I_{TVI} remains constant upto a delay time $\tau_d = 22$ hours. The

subsequent decrease in I_{TVI} with increasing t_s is accompanied by oscillations. Such oscillations in I_{TVI} is due to the downward movement of the collapsing gel interface through consecutive half wavelength regions having alternating directions of the ultrasound pressure gradient which is set up by the electroacoustic probe along height h . The SAC gel with $C_s = 60$ mM therefore exhibits transient collapse after a delay time $\tau_d = 22$ hours. For an SAC gel with $C_s = 100$ mM (\diamond in Fig. 6.11), oscillations in I_{TVI} start immediately due to the very unstable nature of this gel. In contrast to the 3% w/v Na-montmorillonite SAC gel with $C_s = 30$ mM (\square in Fig. 6.11), the 3% w/v Na-montmorillonite SBC gel with $C_s = 30$ mM (\bullet in Fig. 6.11) collapses rapidly after preparation, leading to oscillations in I_{TVI} at very low t_s . Similar stability behaviors of SAC and SBC gels prepared with identical salt concentrations were already observed in Fig. 6.4 for 0.8% w/v Na-montmorillonite gels with 40 mM salt in light transmission experiments. Moreover, it can be seen in Fig. 6.11 and Fig. 6.7 by comparing data for samples prepared with identical salt concentrations (60 mM) that the 3% w/v Na-montmorillonite SAC gels exhibit better stability ($\tau_d > 178$ hours for 30 mM salt and $\tau_d = 20$ hours for 60 mM salt, Fig. 6.11) when compared to the 0.8% w/v Na-montmorillonite SAC gels ($\tau_d = 22$ hours for 30 mM salt and $\tau_d = 1.5$ hours for 60 mM salt, Fig. 6.4).

6.4 Conclusions

In this chapter, we present the aggregation and stability behaviors of highly polydisperse and charge-anisotropic clay particles of Na-montmorillonite in aqueous suspensions at a concentration (0.8% w/v) well below that required to achieve the glass transition. We show that these platelets are not stable in salt-free aqueous suspensions in the dilute concentration regime and sediment under gravity with a particle concentration gradient along the sample height that gets more pronounced with sample age (Fig. 6.1).

We next investigate the stability of gels formed by inducing attractive interactions between the clay platelets in a dilute concentration regime by directly monitoring the

gel interface in optical transmission experiments. Attraction is induced by screening the negative charges on the basal surfaces of the platelets by adding salt in the medium. The gels prepared by dispersing clay powder in NaCl solutions are not stable under gravity and collapse immediately with a distinct interface between the clear supernatant and a clay-rich sediment (the SBC gel indicated by \square in Fig. 6.4). In contrast, we report remarkable enhancement of the stability of the suspensions if identical amounts of salt are added to the clay suspensions after adding the clay powder to water (the SAC gel indicated by \circ in Fig. 6.4). We further observe that the SAC gel is stable for a finite delay time and eventually exhibits transient collapse under gravity with a sharp interface height that decreases with increasing ages (Fig. 6.4).

In the collapse regime, the velocity of the collapsing interface exhibits oscillations with sample age (Fig. 6.8). The average velocity of the interface increases with age upto a peak value before decreasing at higher ages. With a systematic increase in the salt concentration, the delay time for transient collapse decreases (Fig. 6.7), while the average collapse velocity increases (Fig. 6.8). The microscopic mechanism involved in the observed transient collapse is investigated using rheological measurements and with direct visualization of the gel microstructures using cryogenic scanning electron microscopy. It is seen that the elastic modulus G' of the gel increases with sample age upto a time t_r (Fig. 6.9), indicating the growing attractive strength of the gel network. The G' data shows oscillations at ages higher than t_r for all salt concentrations investigated here. The times, t_r , at which the oscillations in G' start are found to be in good agreement with the delay times τ_d for transient collapse (inset of Fig. 6.9).

The direct visualization of the microscopic structures at different salt concentrations and ages of the gels confirms that the gels undergo microscopic restructuring with time (Fig. 6.10), thereby attaining higher elastic moduli and, therefore, higher yield stresses with age since preparation. During the restructuring process, an increasing number of platelets is seen to participate in network formation through overlapping coin (OC) configurations. This leads to increase in the lengths and widths of the network strands. The gravitational stress on the gel strands increases as a result

and eventually overcomes the local yield stress after a delay period. This leads to the mechanical failure of the network strands and the subsequent transient collapse of the gels. During the collapse, the gravitational stresses on the gel network increase further due to the coarsening of the gel strands as they approach each other. This results in a further increase in the velocity of collapse. The processes of gradual gel compaction during sedimentation and the continuous restructuring lead to a substantial increase in the local yield stresses of the gel network. A condition eventually arises in which the yield stresses characterizing the network strands overcome the gravitational stresses, resulting in a decrease in collapse velocity at higher ages (Fig. 6.8). Such competition between the local yield stresses and the gravitational stresses on the gel network strands during gel collapse leads to oscillations in the interface collapse velocity (Fig. 6.8), and in the elastic modulus (Fig. 6.9).

It is important to conclude by noting that our study of the stability behavior of clay suspensions at a higher clay concentration (3% w/v) in the presence of added salt using electroacoustic methods (Section 2.2.2 of Chapter 2) shows similar stability behaviors for both SBC and SAC gels (Fig. 6.2) as observed in the dilute concentration regime studied here. However, it is seen for the 3% w/v gel that its yield stress dominates over the gravitational stress for relatively longer time durations due to the higher network connectivity and the slower rearrangement processes at higher clay concentrations.

In conclusion, the present study elucidates the influence of the salt concentration and preparation conditions on the stability of weak gels of Na-montmorillonite. The results obtained in case of weak gels are also compared with data obtained for concentrated gels. Our observations of the collapse behavior in salt-stabilized colloidal clay particle suspensions demonstrate the ubiquity of the transient collapse phenomenon previously only observed in depletion gels [23, 26–28] and in colloidal gels flocculated at their secondary minima [29, 30].

References

- [1] P. N. Segrè, F. Liu, P. Umbanhowar and D. A. Weitz, *Nature*, 2001, **409**, 594–597.
- [2] M. L. Kilfoil, E. E. Pashkovski, J. A. Masters and D. A. Weitz, *Philosophical Transactions of the Royal Society of London A: Mathematical, Physical and Engineering Sciences*, 2003, **361**, 753–766.
- [3] C. P. Royall, J. Dzubiella, M. Schmidt and A. van Blaaderen, *Phys. Rev. Lett.*, 2007, **98**, 188304.
- [4] S. Vesaratchanon, A. Nikolov and D. T. Wasan, *Advances in Colloid and Interface Science*, 2007, **134-135**, 268 – 278.
- [5] J. Russo, A. C. Maggs, D. Bonn and H. Tanaka, *Soft Matter*, 2013, **9**, 7369–7383.
- [6] D. J. Beltran-Villegas, B. A. Schultz, N. H. P. Nguyen, S. C. Glotzer and R. G. Larson, *Soft Matter*, 2014, **10**, 4593–4602.
- [7] M. Kohl and M. Schmiedeberg, *Soft matter*, 2014, **10**, 4340–4347.
- [8] S. Abend and G. Lagaly, *Applied Clay Science*, 2000, **16**, 201 – 227.
- [9] R. Bandyopadhyay, D. Liang, H. Yardimci, D. A. Sessoms, M. A. Borthwick, S. G. J. Mochrie, J. L. Harden and R. L. Leheny, *Physical Review Letters*, 2004, **93**, 228302.

-
- [10] D. Saha, Y. M. Joshi and R. Bandyopadhyay, *Soft Matter*, 2014, **10**, 3292–3300.
- [11] E. Paineau, L. J. Michot, I. Bihannic and C. Baravian, *Langmuir*, 2011, **27**, 7806–7819.
- [12] H. Emady, M. Caggioni and P. Spicer, *Journal of Rheology (1978-present)*, 2013, **57**, 1761–1772.
- [13] S. W. Kamp and M. L. Kilfoil, *Soft Matter*, 2009, **5**, 2438–2447.
- [14] G. Ovarlez, F. Bertrand, P. Coussot and X. Chateau, *Journal of Non-Newtonian Fluid Mechanics*, 2012, **177-178**, 19 – 28.
- [15] V. Savenko, L. Bulavin, M. Rawiso, M. Loginov, E. Vorobiev and N. I. Lebovka, *Physical Review E*, 2013, **88**, 052301.
- [16] A. Pototsky, U. Thiele and A. J. Archer, *Physical Review E*, 2014, **89**, 032144.
- [17] F. Uddin, *Metallurgical and Materials Transactions A*, 2008, **39**, 2804–2814.
- [18] H. H. Murray, *Applied Clay Science*, 2000, **17**, 207 – 221.
- [19] Y. Liu, M. Zhu, X. Liu, W. Zhang, B. Sun, Y. Chen and H.-J. P. Adler, *Polymer*, 2006, **47**, 1 – 5.
- [20] A. Thill, S. Moustier, J.-M. Garnier, C. Estournel, J.-J. Naudin and J.-Y. Bottero, *Continental Shelf Research*, 2001, **21**, 2127 – 2140.
- [21] A. Khaldoun, E. Eiser, G. Wegdam and D. Bonn, *Nature*, 2005, **437**, 635–635.
- [22] T. Pähz, J. F. Kok, E. J. R. Parteli and H. J. Herrmann, *Physical Review Letters*, 2013, **111**, 218002.
- [23] S. Manley, J. M. Skotheim, L. Mahadevan and D. A. Weitz, *Physical Review Letters*, 2005, **94**, 218302.
- [24] C.-N. Yuan, Y.-J. Sheng and H.-K. Tsao, *Applied Physics Letters*, 2009, **95**, –.

-
- [25] W. Poon, J. Selfe, M. Robertson, S. Ilett, A. Pirie and P. Pusey, *Journal de Physique II*, 1993, **3**, 1075–1086.
- [26] R. Buscall, T. H. Choudhury, M. A. Faers, J. W. Goodwin, P. A. Luckham and S. J. Partridge., *Soft Matter*, 2009, **5**, 1345–1349.
- [27] P. Bartlett, L. J. Teece and M. A. Faers, *Physical Review E*, 2012, **85**, 021404.
- [28] E. Secchi, S. Buzzaccaro and R. Piazza, *Soft Matter*, 2014, **10**, 5296–5310.
- [29] L. Bergstrom, *J. Chem. Soc., Faraday Trans.*, 1992, **88**, 3201–3211.
- [30] A. A. Potanin and W. B. Russel, *Physical Review E*, 1996, **53**, 3702–3709.
- [31] *Nanocor Inc. Technical data sheet*, Nanocor Inc. Technical data sheet G-105, (Last accessed on 22nd February 2015).
- [32] P. Snabre and B. Pouligny, *Langmuir*, 2008, **24**, 13338–13347.
- [33] É. Guazzelli and J. Hinch, *Annual Review of Fluid Mechanics*, 2011, **43**, 97–116.
- [34] R. Secor and C. Radke, *Journal of Colloid and Interface Science*, 1985, **103**, 237–244.
- [35] E. C. Y. Yan and K. B. Eisenthal, *The Journal of Physical Chemistry B*, 1999, **103**, 6056–6060.
- [36] D. Zhou, A. I. Abdel-Fattah and A. A. Keller, *Environmental Science & Technology*, 2012, **46**, 7520–7526.
- [37] S. Ali and R. Bandyopadhyay, *Applied Clay Science*, 2015, **114**, 85–92.
- [38] S. Ali and R. Bandyopadhyay, *Langmuir*, 2013, **29**, 12663–12669.
- [39] P. Sollich, F. Lequeux, P. Hébraud and M. E. Cates, *Physical Review Letters*, 1997, **78**, 2020–2023.
- [40] S. Ali and R. Bandyopadhyay, *Soft Matter*, 2015, DOI:10.1039/c5sm01700a.

- [41] M. Delhorme, B. Jonsson and C. Labbez, *Soft Matter*, 2012, **8**, 9691–9704.
- [42] E. Zaccarelli, *Journal of Physics: Condensed Matter*, 2007, **19**, 323101.

7

Stress relaxation in clay suspensions in linear and nonlinear viscoelastic regimes

7.1 Introduction

When a step strain is applied to a purely viscous liquid, the induced stress relaxes immediately, whereas a purely elastic solid stores the induced stress as elastic energy [1]. In viscoelastic materials, the induced stress dissipates slowly, over a time scale that depends on the underlying microstructures and the applied shear [1, 2]. In case of aging materials such as aqueous clay suspensions, the stress relaxation process also depends on the competition between the deformation field and the structural recovery due to the inherent aging process [3, 4]. Therefore, the stress relaxation in these systems usually

follows nonexponential decays, a study of which can provide important information about the underlying microscopic structures and dynamics of the constituent particles [5, 6].

There have been few studies on the stress relaxation behavior of aging clay suspensions. Bandyopadhyay *et al.* showed that the induced stress relaxes following two-step decays in 3.5% w/v Laponite suspensions at pH=10 (adjusted using NaOH) when nonlinear step strains are applied [7]. The slow mode of the relaxation process exhibits stretched exponential decay which can be modeled using the Kohlrausch-Williams-Watt (KWW) function [8]. Recent studies by Joshi *et al.* showed that the stress relaxation process of Laponite clay suspensions does not follow the Boltzmann superposition principle in real time domain due to the spontaneous aging process [9, 10]. However, relaxation behavior of these materials can be superposed when the real time domain is translated to the an effective time domain [3].

As discussed in Chapter 1, the aqueous suspensions of Laponite exhibit different phases such as glasses and gels when the age of the suspensions, clay and salt concentrations are varied [11]. A recent study by Angelini *et al.*, which used a combination of dynamic light scattering (DLS), small angle X-ray scattering (SAXS), simulations and dilution experiments, reported that a 3 wt% Laponite suspensions exhibits a smooth transition from a repulsive glass to an attractive glass after a spontaneous aging time of 3-4 days [12]. In the attractive glass phase, particles are found to be in a disconnected house of cards arrangement due to the bonding between particles. The influence of the attractive interactions in a salt-free Laponite suspension was also demonstrated by Saha *et al.* by performing DLS and conductivity measurements for a wide range of clay and salt concentrations [13]. The influence of the interparticle interactions between the Laponite particles in suspensions on their stress relaxation process is still poorly understood.

In this chapter, we report studies on the stress relaxation behavior of aging Laponite suspensions in both the linear and nonlinear viscoelastic regimes for varying idle times

(time duration of sample storage after preparation) and aging times after shear rejuvenation. We find that the relaxation process follows a single-step decay under linear step strains. The KWW function is used to determine the average relaxation times at varying age and step strains in this regime. It is found that the relaxation time decreases with increasing magnitude of the step strain in the linear viscoelastic regime. On the contrary, under a nonlinear step strain, the stress relaxation follows a single-step decay below a critical age, t_{wc} , while above t_{wc} , the relaxation follows a two-step decay. The single-step decay below t_{wc} follows a power-law decay at short times, while the slower decay process above t_{wc} is modeled using a KWW function. Finally, we compare the relaxation processes that are seen in salt-free and predominantly repulsive Laponite suspensions with Laponite samples with predominantly attractive interactions between the constituent particles due to the presence of salt in the aqueous medium.

7.2 Sample preparation

Laponite of XLG grade, supplied by Southern Clay Products, is used for this work. The structural information of this clay mineral is provided in detail in Chapter 1 (Section 1.6). To change the counterion concentration in clay suspensions, NaCl, supplied by Labort Fine Chem. Pvt. Ltd, is used. To ensure identical sample compositions in every experiment, the clay mineral powder is heated in an oven at a temperature of 120°C for 24 hours to remove absorbed moisture before it is dispersed in highly deionized Milli-Q water under vigorous stirring conditions. The mixture is stirred for three hours using a magnetic stirrer to ensure a homogeneous distribution of the aggregates. The samples are next stored in polypropylene syringes in air tight conditions. All rheological experiments are performed using the Anton Paar MCR 501 rheometer. Details of this setup can be found in Chapter-2.

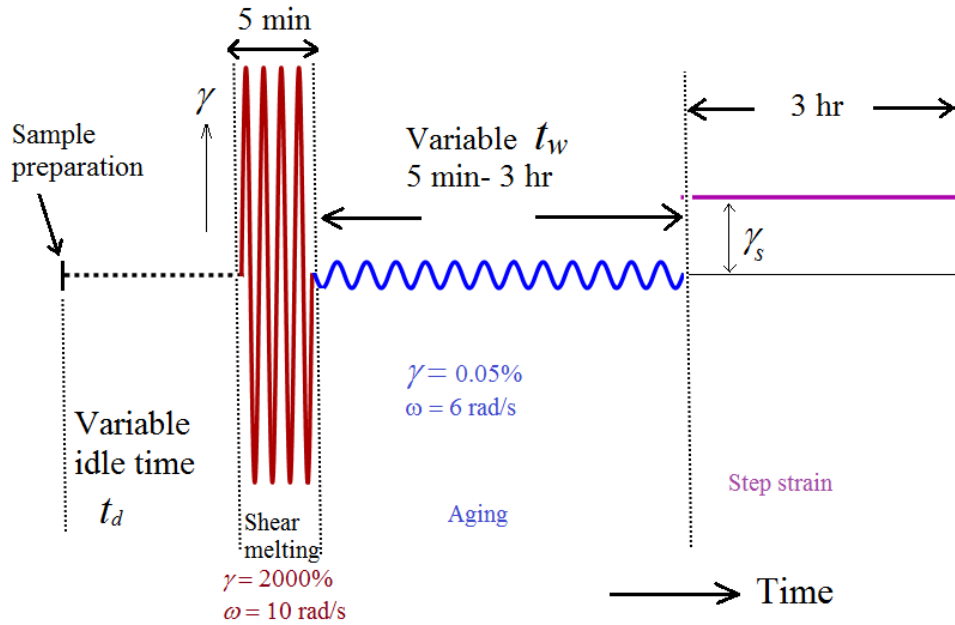


FIGURE 7.1: Schematic diagram of the experimental protocol used for stress relaxation studies.

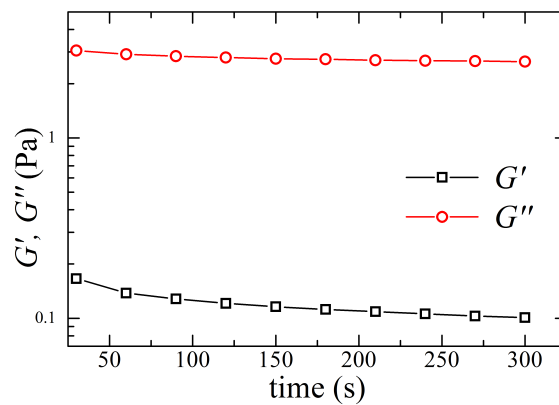


FIGURE 7.2: Variation of the elastic modulus G' (\square) and viscous modulus G'' (\circ) with time during the shear melting process performed by applying a strain amplitude of 2000 % at an angular frequency of 10 rad/s for 5 mins to 3% w/v Laponite suspension of idle time $t_d = 60$ days.

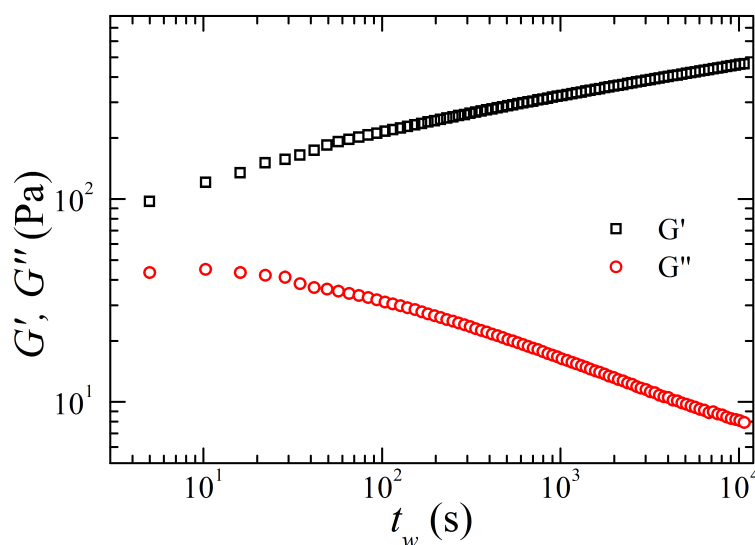


FIGURE 7.3: Typical data showing the evolution of elastic modulus G' and viscous modulus G'' with age t_w in a 3% w/v Laponite suspension of idle time $t_d = 60$ days.

7.3 Experimental results and discussion

The experimental protocol used for all stress relaxation experiments is shown in Fig. 7.1. After preparation, samples are stored in an undisturbed condition for different time durations, defined as idle time t_d , before loading the sample in the measuring cell of the rheometer. Here, $t_d = 0$ is defined as the time at which stirring of sample is stopped. The process of loading the sample into the measuring cell partially shear rejuvenates the sample. To avoid any shear history dependence on the rheological behavior, all samples are shear melted inside the measuring cell by applying an oscillatory strain of amplitude 2000% for five minutes at an angular frequency $\omega = 10$ rad/s. The application of this high strain liquifies the samples, leading to a substantial decrease in the viscoelastic moduli with $G'' > G'$ as can be seen in Fig. 7.2.

When the shear melting strain is removed, the particles in suspension start rearranging to achieve their minimum interparticle interaction potential. This is manifested as an evolution of the viscoelastic moduli with age t_w as shown in Fig. 7.3 for a 3% w/v Laponite suspensions. Here, $t_w = 0$ is defined as the time at which shear melting of sample is stopped inside the measuring cell. The evolution of the elastic modulus G'

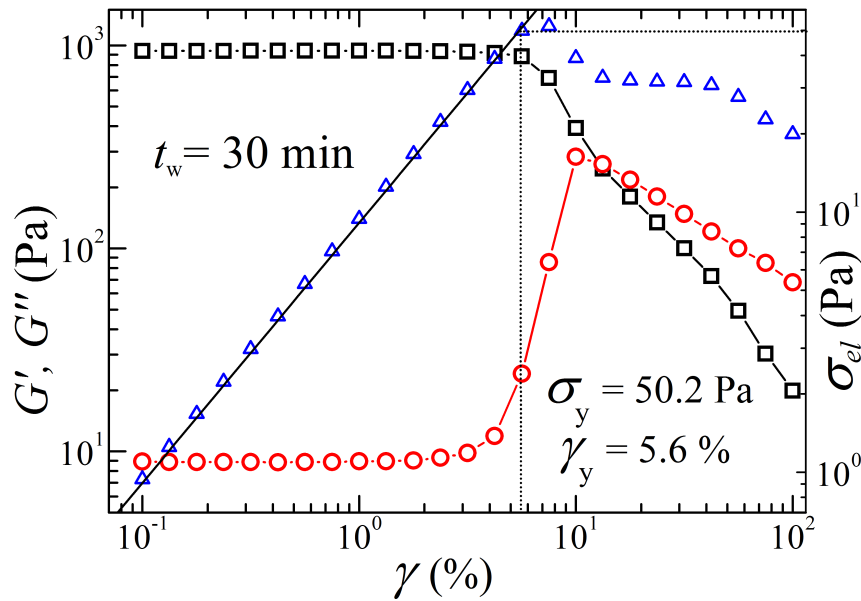


FIGURE 7.4: Variation of elastic modulus G' (\square), viscous modulus G'' (\circ) and elastic stress, $\sigma_{el} = G'\gamma$ (Δ) with strain amplitude, γ , measured at an angular frequency of 6 rad/s in a salt-free 3% w/v Laponite suspension of $t_d = 60$ days and $t_w = 30$ min. The solid line is a linear fit to the σ_{el} vs γ data. Vertical and horizontal dotted lines indicate the position of yield strain $\gamma_y = 5.6\%$ and yield stress $\sigma_y = 50.2$ Pa respectively. The details of the method for determining the yield values from the amplitude sweep experiment is discussed in Chapter 2 and can also be found in the literature [16].

and viscous modulus G'' are monitored by applying an oscillatory strain of strain amplitude 0.05% at a constant angular frequency $\omega = 6$ rad/s. The applied strain amplitude is extremely small, well within the linear viscoelastic regime and is not expected to destroy sample microstructures [14, 15]. It is seen in Fig. 7.3 that immediately after the shear melting process, the suspensions approach kinetic arrest with elastic modulus G' substantially higher than the viscous modulus G'' for the time range investigated. It is also noted that the crossover of G' and G'' lies outside the experimental time window. Subsequently, G' increases with age t_w , while G'' decreases with t_w , indicating that the suspension evolves to form a strong elastic material.

To estimate the linear viscoelastic (LVE) regime of the samples used in this study, we have performed oscillatory strain amplitude sweep experiments by sweeping strain amplitude, γ , in the range 0.1% – 100% at a constant angular frequency $\omega = 6$ rad/s. Representative data for a salt-free 3% w/v Laponite suspension of $t_d = 60$ days and

$t_w = 30$ min are plotted in Fig. 7.4, which shows the variation of G' (\square), G'' (\circ) and $\sigma_{el} = G'\gamma$ (Δ) as a function of strain amplitude γ . At small values of applied strain amplitude γ , $G' > G''$, with both the moduli being independent of γ , thereby indicating the LVE regime of the sample. On further increase in γ , the sample starts yielding due to the irreversible rearrangement of Laponite particles. In this nonlinear regime, G' decreases monotonically while G'' reaches a peak at the point of crossover between G' and G'' . Finally, at very high strains, the sample exhibits fluid-like behavior which is indicated by $G'' > G'$. The yield strain, γ_y , and yield stress, σ_y of this sample are calculated from the strain amplitude sweep data following the method described in section 2.2.5(b) of Chapter 2. The method can also be found in the literature [16]. At low γ values, the elastic stress vs strain data is fitted to $\sigma_{el} = G'\gamma$ (solid line in Fig. 7.4). The value of γ_y is defined at which the measured value of σ_{el} starts deviating more than 3% from the theoretically calculated value. The values of $\gamma_y = 5.6\%$ and $\sigma_y = 50.2$ Pa are indicated by the vertical and horizontal dotted lines in Fig. 7.4. The linear viscoelastic regime for this sample therefore lies upto $\gamma_y = 5.6\%$.

Figs. 7.5 (a) and (b) show the stress relaxation behavior in 3% w/v Laponite suspensions of idle time $t_d = 60$ days on the application of step strains $\gamma_s = 2\%$ and 5% respectively, at varying waiting times t_w . Both the γ_s values used here are within the linear viscoelastic regime (Fig. 7.4). Stress relaxes following a single-step decay at all t_w values. For $t_w \leq 15$ min, it is seen that the stress values approach plateaus. However, for all $t_w \geq 30$ min, the stress plateau remains outside the experimental time window.

We use Kohlrausch-Williams-Watt (KWW) function to model the stress relaxation behavior shown in Fig. 7.5. This function has a stretched exponential form and is suitable for describing time dependent relaxation processes in glassy materials which exhibit a wide distribution of relaxation time scales [8]. The KWW function, which was also used previously to model the slower mode of stress relaxation in 3.5% w/v Laponite suspensions [7] is given below:

$$\sigma = Ce^{-(t/t_1)^b} \quad (7.1)$$

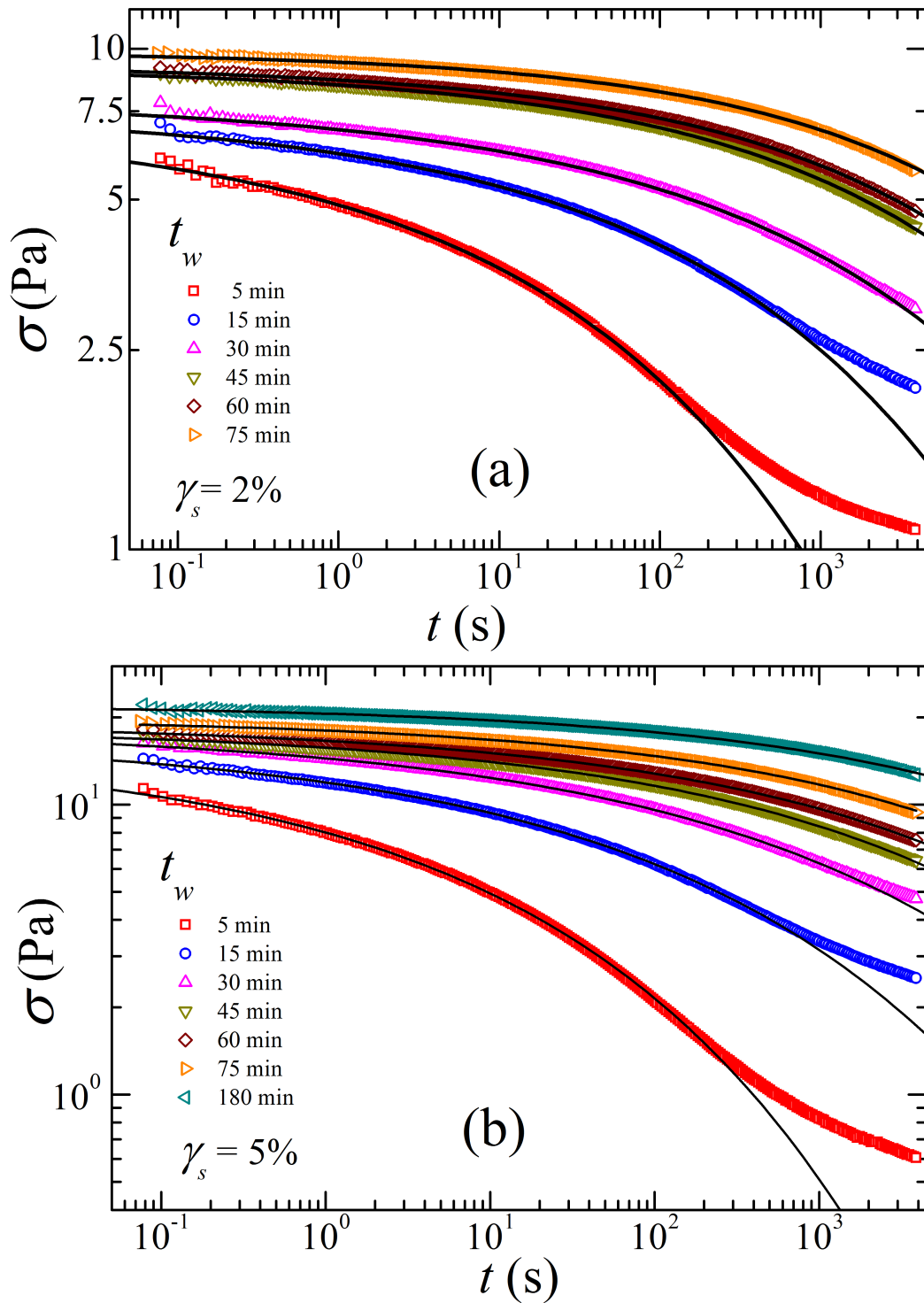


FIGURE 7.5: Decay of shear stresses σ in a salt-free 3% w/v Laponite suspensions of $t_d = 60$ days when linear step strains (a) $\gamma_s = 2\%$ and (b) $\gamma_s = 5\%$ are applied at $t_w = 5$ min (\square), 15 min (\circ), 30 min (\triangle), 45 min (∇), 60 min (\diamond), 75 min (\triangleright) and 180 min (\triangleleft). Solid lines are fits to KWW function (Eqn. 7.1).

where C is the intercept at $t = 0$ and can be interpreted as the induced stress upon application of step strain in case of single-step decay, t_1 is the average time scale of the relaxation process and b is a stretching exponent with a value between 0 and 1. The KWW function also describes the second decay of the intensity autocorrelation function in dynamic light scattering (DLS) experiments very well [13, 17, 18].

We fit the stress relaxation curves to Eqn. 7.1 [solid lines in Figs 7.5 (a) and (b)] for several t_w and γ_s values. It is seen that data for samples of $t_w \leq 30$ min could be fitted to a stretched exponential function (Eqn. 7.1) over several decades in time, t . At higher t (for example, above 200 s for sample of age $t_w = 5$ min), the stress data deviates from KWW behavior. This is due to a competition between the stress relaxation and buildup mechanism through the aging process, with the latter becoming quite important at high sample ages. When stress induced at the microscopic level (at the dimension of a cage for glass microstructure) becomes smaller than the microscopic yield stresses of cages, the aging process takes over with particles exploring deeper potential wells in the potential landscape [4, 19]. As a result, the relaxation process becomes extremely slow at higher t . This can be seen in our data for $t_w < 30$ min (Fig. 7.5 (a) and (b)).

Fig. 7.6 present the variation of average relaxation time t_1 with t_w for $\gamma_s=2\%$ (\square), 3% (\circ) and 5% (\triangle). The values of t_1 show a power law increase with t_w , which can be described by the relation $t_1 \sim t_w^\alpha$ where $\alpha = 2.34 \pm 0.06$, 2.48 ± 0.07 and 2.5 ± 0.06 for step strains 2% , 3% and 5% respectively. With increase in t_w , particles in a suspension occupy lower potential wells by a cooperative rearrangement process, which results in an increase in the elastic modulus of the sample (Fig. 7.3). This results in slower rearrangement process, thereby increasing the relaxation time, t_1 , with t_w (Fig. 7.6). Application of higher step strains induce higher stresses, which can be seen from the plot of intercept, C , as function of t_s (inset (a) of Fig. 7.6). However, the induced stress relaxes faster at higher step strains, which is seen in the plot of relaxation time t_1 as a function of γ_s in the inset (c) of Fig. 7.6. This indicates that the application higher strains makes the particle rearrangement process faster, even though initially, the induced stress is higher. The stretching exponents for all samples remain within

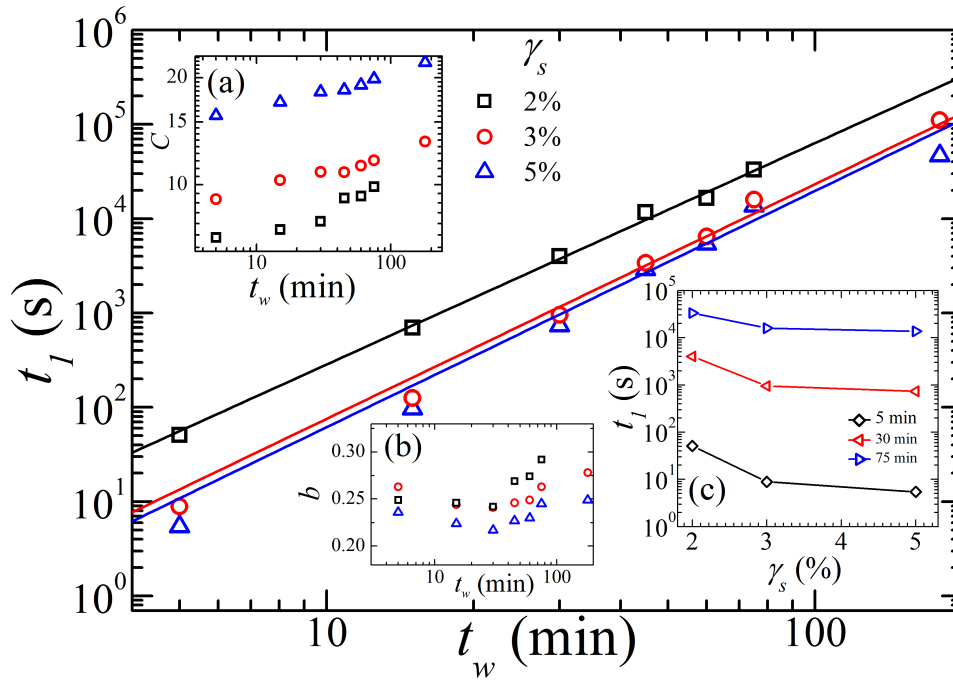


FIGURE 7.6: Plot of average relaxation time t_1 , intercept C [inset (a)] and exponent b [inset (b)] versus t_w obtained by fitting the KWW function (Eqn. 7.1) to stress relaxation data acquired experimentally for step strains $\gamma_s = 2\%$ (\square), 3% (\circ) and 5% (\triangle) applied to 3% w/v Laponite suspensions of $t_d = 60$ days. Solid lines are power law fits to the t_1 vs t_w data. Variation of t_1 with step strain, γ_s , is plotted in the inset (c) for $t_w = 5$ min (\diamond), 30 min (\triangleleft) and 75 min (\triangleright).

the range $0.21 - 0.29$ [inset (b) of Fig. 7.6].

$t_w(\text{min})$	ν ($\gamma_s = 10\%$)	ν ($\gamma_s = 20\%$)
5	0.18	0.20
10	-	0.18
15	0.13	0.16
30	0.11	0.15

Table 7.1: Values of exponents ν obtained from the power law fits to the stress versus time data for $\gamma_s = 10\%$ and 20% in Figs. 7.7 (a) and (b).

Figs. 7.7 (a) and (b) show the stress relaxation behavior in 3% w/v Laponite suspensions of idle time $t_d = 60$ days on the application of step strains $\gamma_s = 10\%$ and 20% respectively, at varying waiting times t_w . These step strains lie in the nonlinear viscoelastic regime of the sample (Fig. 7.4). Single-step decay of induced stresses can

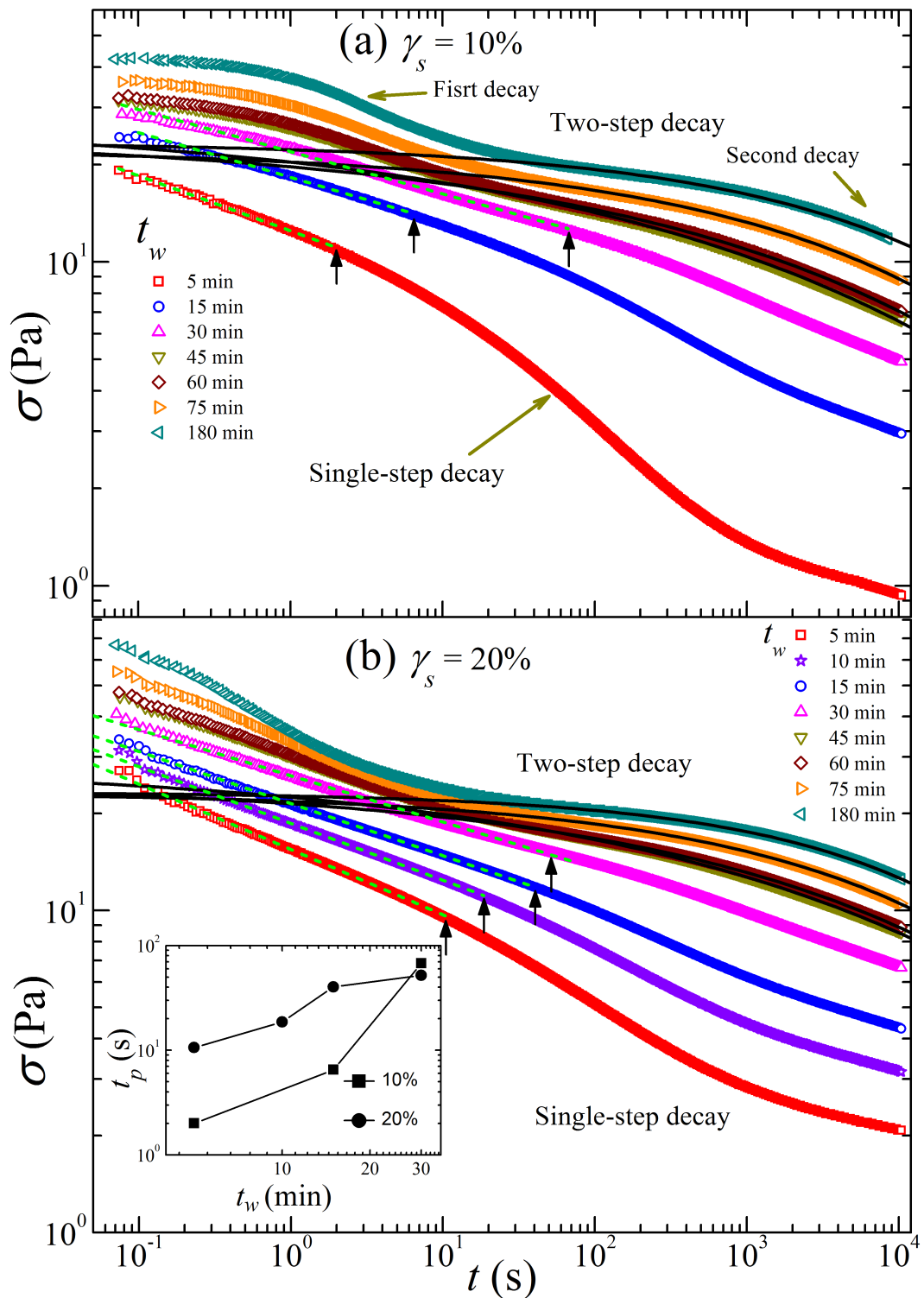


FIGURE 7.7: Decays of shear stresses σ in salt-free 3% w/v Laponite suspensions of $t_d = 60$ days when step strains (a) $\gamma_s = 10\%$ and (b) $\gamma_s = 20\%$ are applied at $t_w = 5$ min (\square), 10 min (\star), 15 min (\circ), 30 min (\triangle), 45 min (∇), 60 min (\diamond), 75 min (\triangleright) and 180 min (\triangleleft). Dashed lines are power law fits to the σ vs t data at low t values. Solid lines are fits to the KWW function (Eqn. 7.1). The vertical arrows indicates the extent (t_p) of the power law behavior of stress relaxation for different γ_s and t_w values. The inset shows the plot of t_p as a function of t_w for step strains $\gamma_s = 10\%$ (\blacksquare) and $\gamma_s = 20\%$ (\bullet).

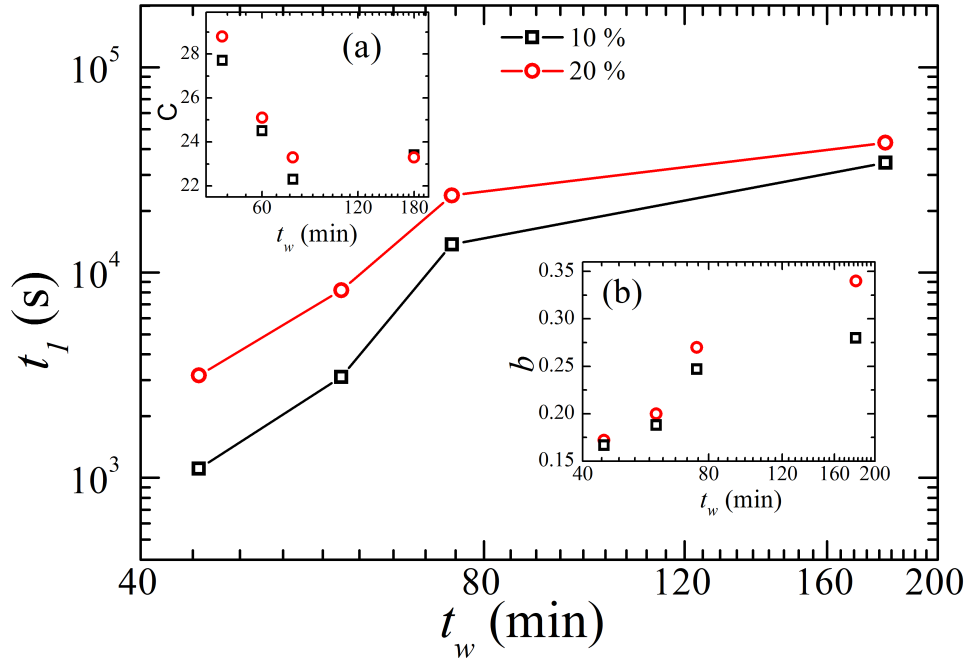


FIGURE 7.8: Plot of average relaxation time t_1 , intercept C [inset (a)] and exponent b [inset (b)] versus t_w obtained by fitting the KWW function (Eqn. 7.1) to stress relaxation data for step strains $\gamma_s = 10\%$ (\square) and 20% (\circ) applied to 3% w/v Laponite suspensions of $t_d = 60$ days. Solid lines are guides to the eyes.

be observed upto $t_w \leq 30$ min for both the step strains $\gamma_s = 10\%$ (Fig. 7.7 (a)) and $\gamma_s = 20\%$ (Fig. 7.7 (b)). Complete decay of stresses for these samples cannot be seen within the experimental time window. However, it can be seen that stress approaches a plateau for the $t_w = 5$ min data (\square in Figs. 7.7 (a) and (b)). On the other hand, at $t_w \geq 45$ min, the samples exhibit two-step stress decays with well separated relaxation regimes in the experimental time window. For the $t_w \leq 30$ min data reported here, it is seen that stress decays following a power law ($\sigma = At^{-\gamma}$) at short times for at least two decades in time (shown by dotted lines in Figs. 7.7 (a) and (b)). The time (t_p) upto which stresses decay following a power law is indicated by the vertical arrows in Figs. 7.7 (a) and (b) for varying γ_s and t_w values. The variation of t_p as a function of t_w is plotted in the inset of Fig. 7.7 (b). It can be seen from this figure that the extent of power-law decay increases with sample age upto $t_w = 30$ min for both the step strains. The fast mode of the two-step decay cannot be modeled using any standard function.

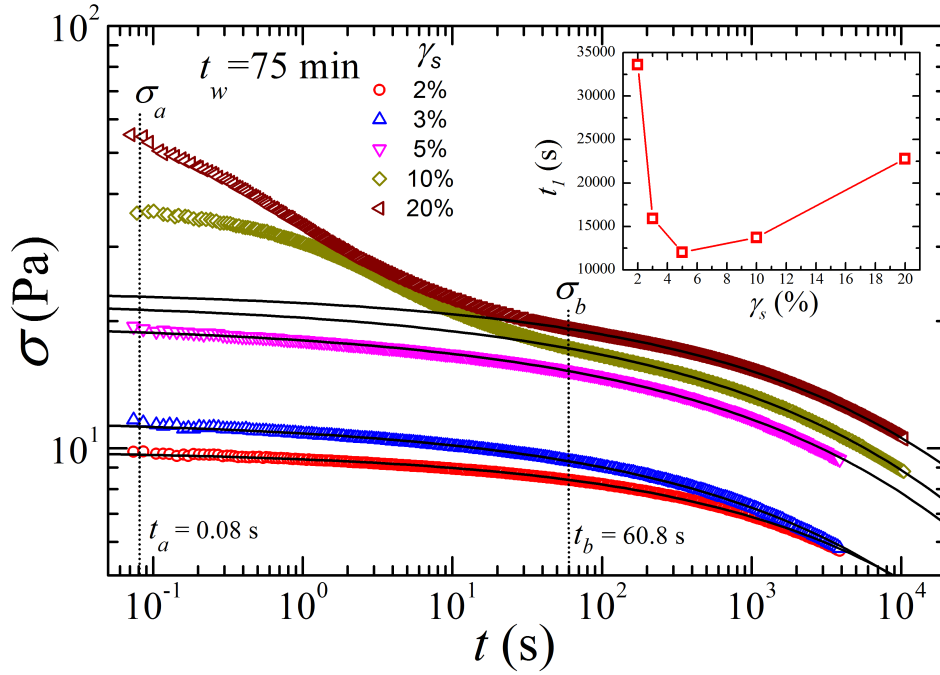


FIGURE 7.9: Decay of stresses σ in 3% w/v Laponite suspensions of $t_d = 60$ days when step strains $\gamma_s = 2\%$ (\circ), 3% (\triangle), 5% (∇), 10% (\diamond) and 20% (\triangleleft) are applied at $t_w = 75$ min. σ_a and σ_b are the stress values at times t_a and t_b respectively. Solid lines are fits to the KWW function (Eqn. 7.1). The inset shows the variation of average relaxation time t_1 with step strains γ_s .

However, the slower mode of the stress relaxation curves of samples of $t_w \geq 45$ min can be modeled by the KWW function (Eqn. 7.1) as shown by solid lines in Figs. 7.7 (a) and (b). The average relaxation time t_1 , the intercept C and the exponent b obtained from the KWW fits are plotted as the functions of t_w in Fig. 7.8. It is seen that the average relaxation times increase with t_w for both the nonlinear strains applied. The C values show weak decrease with increase in t_w (inset (a) of Fig. 7.8). On the other hand, exponents b increase weakly with increasing t_w (inset (b) of Fig. 7.8).

To compare the stress relaxation behaviors of 3% w/v Laponite suspensions under different step strains, we have replotted the stress relaxation data in Fig. 7.9 for varying γ_s at a fixed age $t_w = 75$ min. As discussed earlier, a clear transition from a single-step decay to a two-step decay of stresses can be observed with increasing γ_s . Moreover, induced stresses exhibit monotonic increase with the increasing magnitude of γ_s as can be seen by comparing stress data at $t_a = 0.08$ s indicated by a dotted line in Fig. 7.9. To

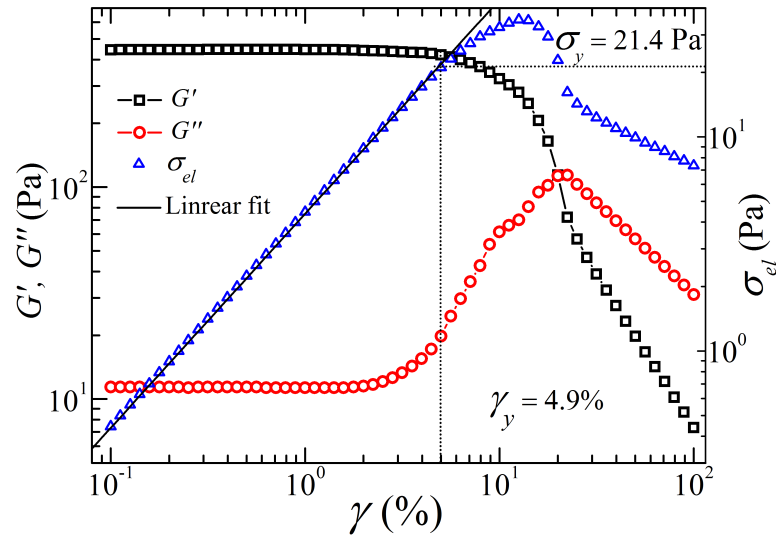


FIGURE 7.10: Variation of elastic modulus G' (\square), viscous modulus G'' (\circ) and elastic stress, $\sigma_{el} = G'\gamma$ (Δ) with strain amplitude, γ , measured at an angular frequency of 6 rad/s in a salt-free 3% w/v Laponite suspension of $t_d = 3$ days and $t_w = 30$ min. The solid line is a linear fit to the σ_{el} vs γ data. Vertical and horizontal dotted lines indicate the position of yield strain $\gamma_y = 4.9\%$ and yield stress $\sigma_y = 21.4$ Pa respectively. The details of the method for determining the yield values from the amplitude sweep experiment is discussed in Chapter 2.

estimate the average decay rate of the fast modes for step strains $\gamma_s = 10\%$ and 20% , we calculated the quantity, $\xi = (\sigma_b - \sigma_a)/(t_b - t_a)$ where σ_a and σ_b are the stresses at times t_a and t_b respectively. We find, $\xi(10\%) = 0.32$ Pa/s and $\xi(20\%) = 0.62$ Pa/s when the ξ is calculated for $t_a=0.08$ s and $t_b = 60.8$ s (vertical dotted lines Fig. 7.9). The rate of stress decay of the first mode is therefore higher at larger step strains in the nonlinear regime, indicating a faster yielding of the microstructures under higher strains. The inset of Fig. 7.9 shows the variation of t_1 obtained from the KWW fits to the stress relaxation data for different strain values. It is clearly seen in this figure that the relaxation time, t_1 , decreases monotonically with γ_s in the linear regime ($\gamma_s \leq 5\%$), while it increases with the increase in γ_s in the nonlinear regime ($\gamma_s \geq 10\%$). Such an increase in the relaxation times with increasing nonlinear step strains was also observed in a previous study in 3.5% w/v Laponite suspensions [7].

We have performed stress relaxation experiments in the nonlinear regime of salt-free 3% w/v Laponite suspensions of lower idle time $t_d = 3$ days at a step strain $\gamma_s = 40\%$ and for varying t_w values. The applied step strain value ($\gamma_s = 40\%$) is much

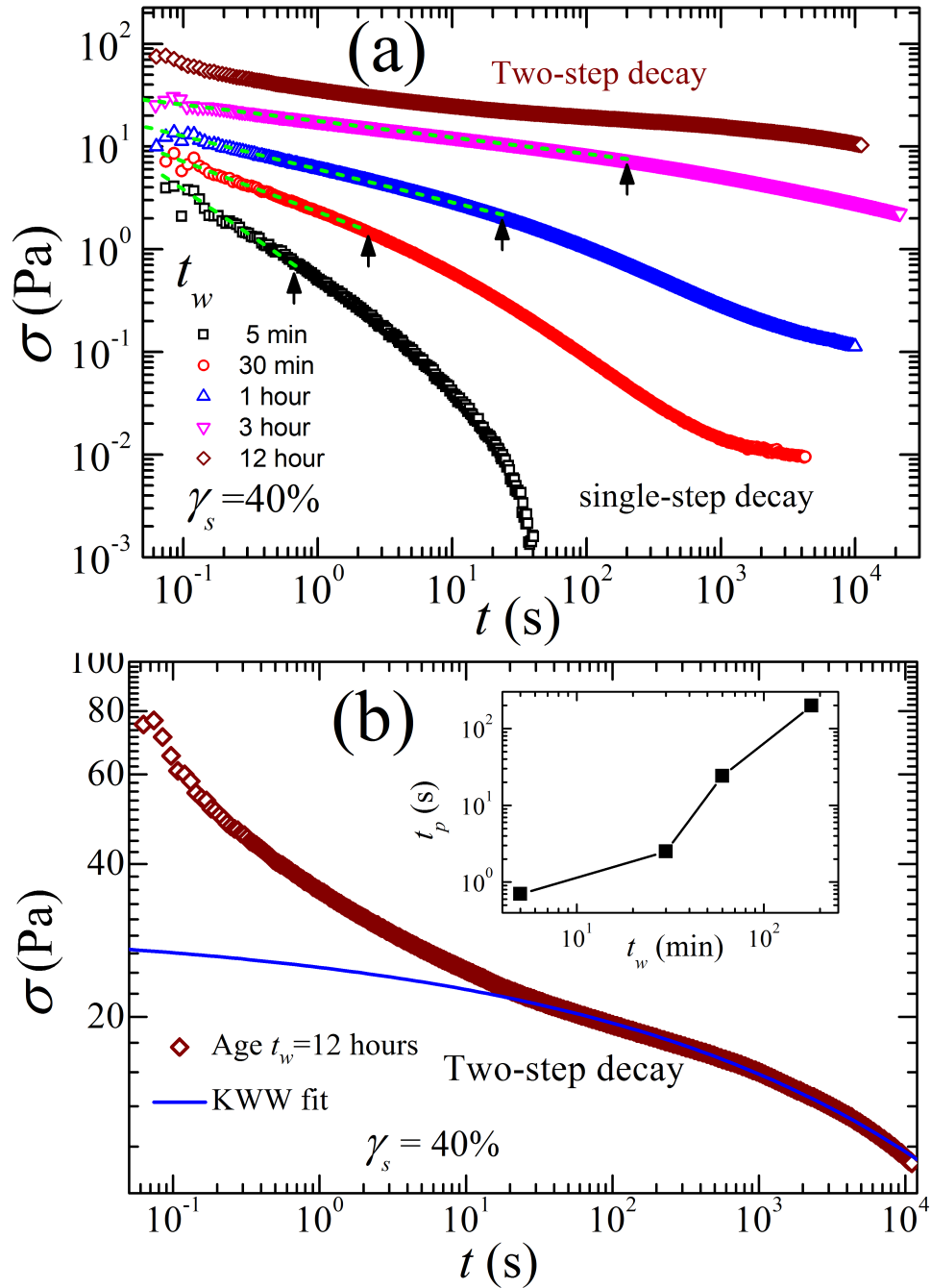


FIGURE 7.11: (a) Decay of shear stresses σ in salt-free 3% w/v Laponite suspensions of $t_d = 3$ days when a nonlinear step strain $\gamma_s = 40\%$ is applied at $t_w = 5$ min (\square), 30 min (\circ), 1 hour (\triangle), 3 hours (∇) and 12 hours (\diamond). Dashed lines are power law fits to the σ vs t data at low t values. The vertical arrows indicates the time (t_p) upto which the power law holds for different t_w values. (b) The data for $t_w = 12$ hours is replotted. The solid line is a fit of the slower mode of the decay to the KWW function (Eqn. 7.1) with a stretching exponent $b = 0.182 \pm 0.003$ and relaxation time $t_1 = 8582$ s. The inset shows the plot of t_p as a function of t_w .

larger than the yield strain $\gamma_y = 4.9\%$ and can be seen from the strain amplitude sweep data presented in Fig. 7.10. Fig. 7.11 (a) shows that the relaxing stress follows a single-step decay with power law behaviors at lower t for samples of age $t_w \leq 3$ hours (\square , \circ , \triangle , ∇). The times t_p upto which the power law behavior holds for different t_w values are indicated by the vertical arrows in Fig. 7.11 (a). For the sample idle time $t_d = 3$ days, we see that the extent of the power law decay regime increases with sample age, t_w , for the younger samples (inset of Fig. 7.11 (b)) and absent for $t_w = 12$ hours. A similar behavior of t_p was also observed in salt-free 3% w/v Laponite suspensions of idle time $t_d = 60$ days upto sample age $t_w = t_{wc} = 30$ min (inset of Fig. 7.7 (b)). It is to be noted that the critical age ($t_{wc} = 3$ hours) upto which the samples of lower idle time $t_d = 3$ days exhibit power law decay of stress is higher than that for the samples of higher idle time $t_d = 60$ days. For a sample of $t_w = 12$ hours, a two-step decay of stress can be observed (\diamond in Figs. 7.11 (a) and (b)). The transition from a single-step decay to a two-step decay regime therefore shifts to higher t_w value for samples with lower idle time t_d . The slower mode of the stress relaxation curve for the sample of $t_w = 12$ hours can be modeled by the KWW function with a stretching exponent $b = 0.182 \pm 0.003$ and relaxation time $t_1 = 8582$ s (Fig. 7.11 (b)).

We next investigate the stress relaxation behavior of 3% w/v Laponite suspensions in the presence of 5 mM NaCl under linear and nonlinear step strains. The sample used here is of idle time $t_d = 3$ days and age $t_w = 15$ min. The sample exhibits kinetic arrest with $G' > G''$ immediately after the shear melting process. The underlying microstructure in this sample is expected to be attraction dominated due to the presence of 5 mM salt [11, 20]. A yield strain of $\gamma_y = 8.8\%$ of this sample at $t_w = 15$ min is estimated using strain amplitude sweep experiment as shown in Fig. 7.12. Fig. 7.13 shows stress relaxation behavior of the 3% w/v Laponite gel with 5 mM salt at $t_w = 15$ min. The suspension shows a single-step decay under a step strain $\gamma_s = 1\%$ (\square in Fig. 7.13), which lies within the linear viscoelastic regime (Fig. 7.12). The decay curve can be fitted to the KWW function (Eqn. 7.1) with a stretching exponent $b = 0.362 \pm 0.001$.

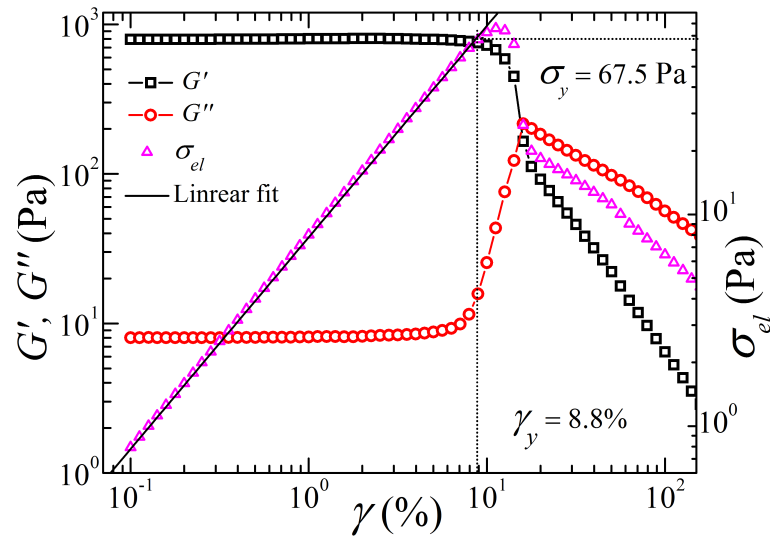


FIGURE 7.12: Variation of elastic modulus G' (\square), viscous modulus G'' (\circ) and elastic stress, $\sigma_{el} = G'\gamma$ (Δ) with strain amplitude, γ , measured at an angular frequency of 6 rad/s in a 3% w/v Laponite suspension with 5 mM salt of $t_d = 3$ days and $t_w = 15$ min. The solid line is a linear fit to the σ_{el} vs γ data. Vertical and horizontal dotted lines indicate the position of yield strain $\gamma_y = 8.8\%$ and yield stress $\sigma_y = 67.5$ Pa respectively. The details of the method for determining the yield values from the amplitude sweep experiment is discussed in Chapter 2.

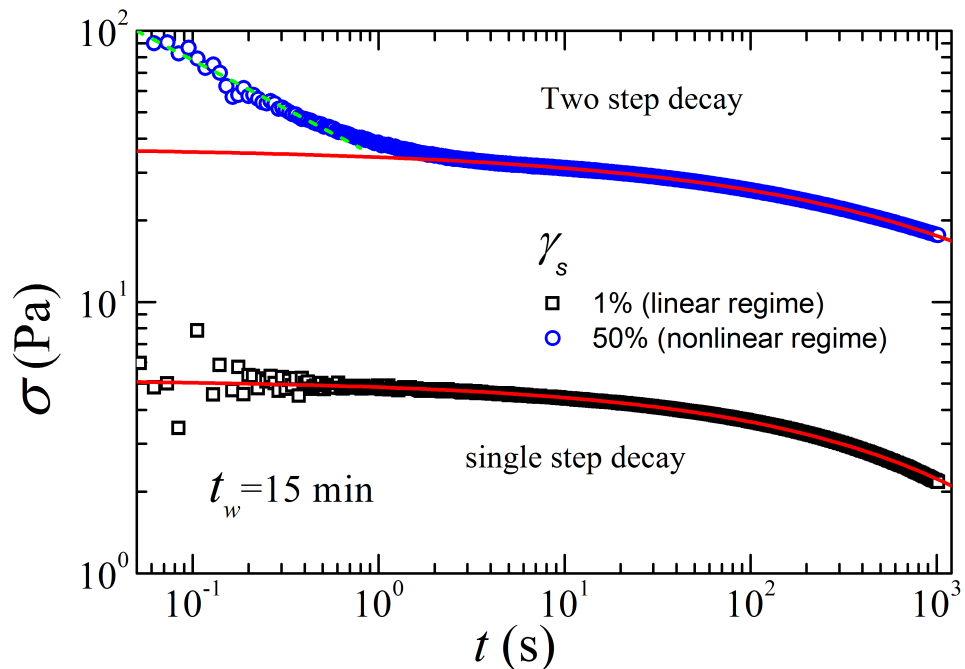


FIGURE 7.13: Decay of shear stresses σ in 3% w/v Laponite suspensions with 5 mM salt of $t_d = 3$ days when step strains $\gamma_s = 1\%$ (\square) and 50% (\circ) are applied at $t_w = 15$ min. The solid lines are fits to the KWW function (Eqn. 7.1).

Addition of 5 mM salt to a 3% w/v clay suspension produces a volume spanning gel network in which clay platelets are linked by attractive bonds [11, 21]. Stress relaxation in the linear regime of the gel suspension occurs via rearrangements of the particles of the gel network facilitated by thermal fluctuations [22]. Since the relaxation behavior in the linear regime can be modeled using the KWW function (\square in Fig. 7.13), it indicates that the process of particle rearrangement of the gel network has a wide distribution of time scales. The suspension exhibits a two-step decay upon application of a nonlinear step strain $\gamma_s = 50\%$ (\circ in Fig. 7.13). The short-time relaxation behavior of the sample could not be modeled satisfactorily with any theoretical prediction. However, the slow mode can be fitted to the KWW function with a stretching exponent $b = 0.301 \pm 0.002$. The fast decay in the stress relaxation is expected to arise from bond breaking in the gel network. This results in the formation of glass-like random structures reminiscent of attractive glasses under high strains [11, 23]. The subsequent second decay of stress happens through the slow rearrangement of the clay platelets.

We next measure the stress relaxation behavior in 10 months old ($t_d = 10$ months) salt-free suspensions of 1.5% w/v Laponite at $t_w = 15$ min. For this clay concentration, the process of kinetic arrest in a freshly prepared sample is much slower than in the samples of high concentrations [18]. It has been shown in a previous study that a salt-free Laponite suspension at this concentration undergoes an equilibrium gel transition over a time scale of a few months [11]. However, the present sample undergoes kinetic arrest ($G' > G''$) immediately after the cessation of the shear melting process as can be seen from the time evolution data shown in the inset of Fig. 7.14. The fast process of kinetic arrest indicates that the microstructures of this sample are dominated by attractive interparticle interactions. The yield strain measured using oscillatory strain sweep experiment for this sample is $\gamma_y = 10.2\%$ (Fig. 7.14). Fig. 7.15 shows the stress relaxation behavior of these suspensions at $t_w = 15$ min under varying step strains. Single-step decay can be observed for $\gamma_s = 1\%$ and 10% , while the suspensions exhibit two-step decay under nonlinear step strains of $\gamma_s = 20\%$ and 50% . However,

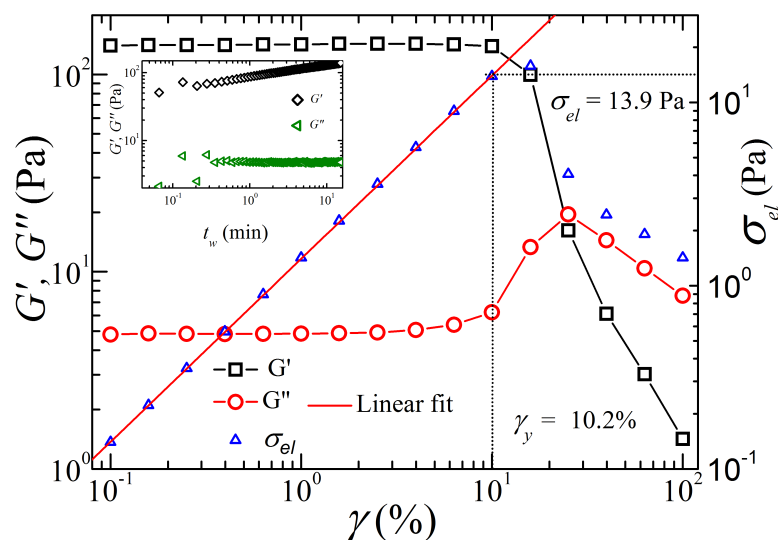


FIGURE 7.14: Variation of elastic modulus G' (\square), viscous modulus G'' (\circ) and elastic stress, $\sigma_{el} = G'\gamma$ (Δ) with strain amplitude, γ , measured at an angular frequency of 6 rad/s in a salt-free 1.5% w/v Laponite suspension of $t_d = 10$ months and $t_w = 15$ min. The solid line is a linear fit to the σ_{el} vs γ data. Vertical and horizontal dotted lines indicate the position of yield strain $\gamma_y = 10.2\%$ and yield stress $\sigma_y = 13.9$ Pa respectively. The details of the method for determining the yield values from the amplitude sweep experiment is discussed in Chapter 2. The inset shows the evolution of G' and G'' with age t_w after the shear melting of the sample is stopped at $t_w = 0$.

the induced stress at $\gamma_s = 50\%$ (\diamond in Fig. 7.15) is lower than the value for $\gamma_s = 10\%$ (\circ in Fig. 7.15), indicating considerable shear melting of sample under very high strains. Relaxation data in the linear regime ($\gamma_s \leq 10\%$) and the slow relaxation mode for $\gamma_s = 50\%$ are fitted to the KWW function (Eqn. 7.1). The relaxation time t_1 estimated from the KWW fits decreases (inset (a) of Fig. 7.15), while the intercept C increases (inset (b) of Fig. 7.15) with the increase in γ_s in the linear regime. A similar relaxation behavior under linear step strains is also observed in case of salt-free 3% w/v Laponite suspensions of $t_d = 60$ days (Fig. 7.9) earlier. It is to be noted that the shape of the slower mode of relaxation for $\gamma_s = 20\%$ changes and cannot be fitted to KWW function. Clearly, the complex dynamics of the gel sample under this step strain value needs further systematic investigations.

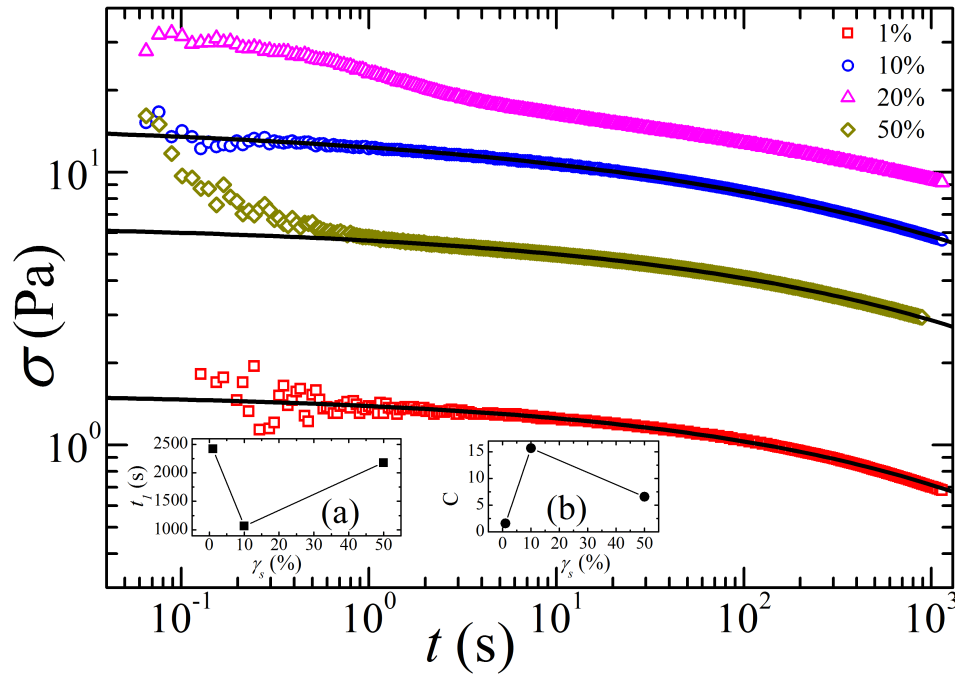


FIGURE 7.15: Decay of shear stresses σ in salt-free 1.5% w/v Laponite suspensions of $t_d = 10$ months when step strains $\gamma_s = 1\%$ (\square), 10% (\circ), 20% (\triangle) and 50% (\diamond) are applied at $t_w = 15$ min. The solid lines are fit to the KWW function (Eqn. 7.1). The insets (a) and (b) shows the variation of average relaxation time t_1 (\blacksquare) and inetrcept C (\bullet) as a function of step strains γ_s .

7.4 Conclusion

In this chapter, we explore the stress relaxation behavior of Laponite clay suspensions of different idle times t_d , ages t_w after shear melting, and for changes in clay and salt concentrations. Our data for stress relaxation behaviors of 3% w/v Laponite suspensions of $t_d = 60$ days (Fig. 7.5)(a), 3% w/v Laponite gel (salt concentration= 5 mM) of $t_d = 3$ days (Fig. 7.13) and 1.5% w/v Laponite suspensions of $t_d = 10$ months (Fig. 7.15) in linear viscoelastic regime show that the stress relaxation process always follows a single step decay which can be modeled using the KWW function (Eqn. 7.1). The relaxation time, t_1 in the salt-free Laponite suspensions exhibits a power law increase with increase in the sample ages, t_w (Fig. 7.6). No distinction between the stress relaxation behaviors of glassy samples and gel samples could be made from our data. It is believed that the slow rearrangement of particles correlated over large spatial extents contributes to the stress relaxation behavior of glassy materials in their linear

viscoelastic regime. Application of step strain within the linear regime facilitates particle hopping between particles [24]. On the other hand, relaxation in gel samples can occur due to the rearrangement of particles in the gel network.

On application of nonlinear step strains, the salt-free 3% w/v Laponite suspension exhibits single-step stress relaxation process upto $t_{wc} = t_w = 30$ min for a sample with idle time $t_d = 60$ days (Fig. 7.7) and upto $t_{wc} = t_w = 3$ hours for sample with idle time $t_d = 3$ days (Fig. 7.11), before showing two-step stress relaxation at higher t_w values. The relaxation curves follow a power law at the initial stages of the decay. Moreover, the extent of the the power law decay is seen to increase with the t_w upto t_{wc} in the single-step relaxation regime (inset of Fig. 7.7(b)). The power law-like initial decays of the stresses reported here are reminiscent of the stress relaxation behavior previously observed in critical gels [25–28], strong silica gels in the nonlinear regime [22] and during entanglement to disentanglement transition under nonlinear strains in solutions of block copolymers [29]. The relaxation times of the slower mode of the stress relaxation under nonlinear step strains are estimated using the KWW function (Figs. 7.7 (a) and (b)). Our further analysis of the t_1 obtained from the KWW fits at varying step strains shows that the relaxation time decreases with the increase step strains in the linear regime. On the contrary, the relaxation time increases with the applied step strains in the nonlinear viscoelastic regime (inset of Fig. 7.9). Such a strain induced sluggishness of the relaxation behavior under high step strains in the nonlinear regime was also observed in a previous study [7].

Recent studies by Angelini *et al.* showed that the microstructures of a salt-free 3 wt% Laponite suspensions becomes strongly attraction-dominated over a time scale of 3 days due to the gradual cooperative rearrangement of the clay platelets [12]. Further study in our group by Saha *et al.* on Laponite suspensions of varying clay and salt concentrations demonstrated that the role of attractive force between edges and basal surfaces of platelets could not be ignored even in a salt-free 3% w/v Laponite suspension when it approaches the glass transition [13]. In our case, the experiments are performed with shear melted samples. However, the kinetic arrest process is very

fast in shear melted suspensions as they evolve to achieve their lowest free energies characterized by edge-face alignment of particles in an incomplete shear rejuvenation process [30–32]. The power law-like stress relaxation in the single-step relaxation regime upto t_{wc} (inset of Fig. 7.7(b)) could presumably arise due to growing attractive interactions between particles in these samples. The fast mode of the relaxation process in the two-step regime could be due to the attractive bond breaking of underlying microstructures. The subsequent relaxation of stress can be attributed to the slow re-arrangement of particles [23]. Our further study shows that induced stress follows a two-step decay under nonlinear step strains in 3 days old 3% w/v Laponite gel with 5 mM salt and in 10 months old 1.5% w/v Laponite suspensions, both of which are expected to have structures that are attraction dominated.

References

- [1] C. W. Macosko and R. G. Larson, *Rheology: principles, measurements, and applications*, VCH New York, 1994.
- [2] R. G. Larson, *The structure and rheology of complex fluids*, Oxford University Press, Oxford, 1999.
- [3] A. Shahin and Y. M. Joshi, *Physical Review Letters*, 2011, **106**, 038302.
- [4] A. S. Negi and C. O. Osuji, *Physical Review E*, 2009, **80**, 010404.
- [5] R. Bohmer, K. L. Ngai, C. A. Angell and D. J. Plazek, *The Journal of Chemical Physics*, 1993, **99**, 4201–4209.
- [6] L. Ramos and L. Cipelletti, *Physical Review Letters*, 2001, **87**, 245503.
- [7] R. Bandyopadhyay, P. H. Mohan and Y. M. Joshi, *Soft Matter*, 2010, **6**, 1462–1466.
- [8] P. G. Debenedetti and F. H. Stillinger, *Nature*, 2001, **410**, 259–267.
- [9] R. Gupta, B. Baldewa and Y. M. Joshi, *Soft Matter*, 2012, **8**, 4171–4176.
- [10] M. Kaushal and Y. M. Joshi, *Soft matter*, 2014, **10**, 1891–1894.

-
- [11] B. Ruzicka and E. Zaccarelli, *Soft Matter*, 2011, **7**, 1268–1286.
- [12] R. Angelini, E. Zaccarelli, F. A. de Melo Marques, M. Sztucki, A. Fluerasu, G. Ruocco and B. Ruzicka, *Nature communications*, 2014, **5**, 1–7.
- [13] D. Saha, R. Bandyopadhyay and Y. M. Joshi, *Langmuir*, 2015, **31**, 3012–3020.
- [14] A. Shahin and Y. M. Joshi, *Langmuir*, 2012, **28**, 15674–15686.
- [15] Y. M. Joshi, *Annual review of chemical and biomolecular engineering*, 2014, **5**, 181–202.
- [16] M. Laurati, S. U. Egelhaaf and G. Petekidis, *Journal of Rheology (1978-present)*, 2011, **55**, 673–706.
- [17] B. Ruzicka, L. Zulian and G. Ruocco, *Physical Review Letters*, 2004, **93**, 258301.
- [18] D. Saha, Y. M. Joshi and R. Bandyopadhyay, *Soft Matter*, 2014, **10**, 3292–3300.
- [19] A. Negi and C. Osuji, *EPL (Europhysics Letters)*, 2010, **90**, 28003.
- [20] A. Mourchid, E. Lecolier, H. Van Damme and P. Levitz, *Langmuir*, 1998, **14**, 4718–4723.
- [21] D. Bonn, H. Kellay, H. Tanaka, G. Wegdam and J. Meunier, *Langmuir*, 1999, **15**, 7534–7536.
- [22] G. Yin and M. J. Solomon, *Journal of Rheology (1978-present)*, 2008, **52**, 785–800.
- [23] N. Koumakis and G. Petekidis, *Soft Matter*, 2011, **7**, 2456–2470.
- [24] P. Sollich, *Physical Review E*, 1998, **58**, 738–759.
- [25] D. Curtis, N. Badiiei, A. Holder, J. Claypole, D. Deganello, M. Brown, M. Lawrence, P. Evans, P. Williams and K. Hawkins, *Journal of Non-Newtonian Fluid Mechanics*, 2015, **222**, 227 – 233.

- [26] K. Broderix, T. Aspelmeier, A. K. Hartmann and A. Zippelius, *Physical Review E*, 2001, **64**, 021404.
- [27] M. De Rosa and H. Winter, *Rheologica Acta*, 1994, **33**, 220–237.
- [28] H. Winter, *Polymer Engineering and Science*, 1987, **27**, 1698–1702.
- [29] M. Rubinstein and S. Obukhov, *Macromolecules*, 1993, **26**, 1740–1750.
- [30] T. Gibaud, C. Barentin and S. Manneville, *Physical Review Letters*, 2008, **101**, 258302.
- [31] T. Gibaud, C. Barentin, N. Taberlet and S. Manneville, *Soft Matter*, 2009, **5**, 3026–3037.
- [32] A. Shahin and Y. M. Joshi, *Langmuir*, 2010, **26**, 4219–4225.

8

Influence of aggregate sizes on the aging behavior and viscoelasticity of clay suspensions

8.1 Introduction

A freshly prepared clay suspension undergoes spontaneous aging dynamics which is manifested in the increasing viscoelastic moduli and relaxation times with sample age [1, 2]. When a high shear stress above the yield value is applied to the sample, it reverses the aging process resulting in a decrease in the relaxation time of the particles [3, 4]. However, the influence of the shear on the exact nature of yielding and the subsequent aging after shear melting process is still poorly understood. Virgile *et al.* reported using diffusing wave spectroscopy that an application of a very high

shear rejuvenates the soft glassy samples, however, a moderate amount of shear leads to the over-aging of samples [5]. When the shear melting stress is removed, the colloidal suspension again exhibits spontaneous aging. The subsequent aging dynamics in a shear rejuvenated sample was seen to depend strongly on the critical time for kinetic arrest [6]. When the shear melting stress is applied before the critical time, the sample follows the same standard dynamics observed in a freshly prepared sample. However, when the shear melting stress is applied to the sample after the critical time, the shear rejuvenated sample exhibits faster aging dynamics. This fact is further investigated in detail by Shahin *et al.* using rheological measurements in samples of different storage times (idle time) [7, 8]. It is shown in this study that clay suspensions exhibit faster approach to kinetic arrest at higher idle times, which is attributed to the incomplete rejuvenation of the sample at higher idle times. Furthermore, the incomplete shear rejuvenation is interpreted in terms of the caging potential which increases due to particle rearrangement with increase in the idle time. This makes it more difficult to completely shear melt a sample with increasing sample idle time at a constant shear melting stress. As a result, the subsequent evolution of viscoelastic moduli after the shear melting process is faster with increasing idle time. A recent study by Angelini *et al.* using dynamic light scattering and X-ray photon spectroscopy shows that the intensity autocorrelation function of a freshly prepared 3 wt% Laponite suspension follows a stretched exponential decay [9]. On the contrary, the autocorrelation function exhibits compressed exponential behavior when the sample is shear rejuvenated after 3.5 days. Under application of a high shear melting stress, a coexistence of the liquid-like and solid-like regimes is observed in a two days old 3 wt% Laponite suspension by Gibaud *et al.* in recent studies using a combination of rheological, ultrasound velocimetry and direct visualization methods [10, 11]. The dimension of the solid-like aggregates decreases with increasing shear rates and with duration of shear. However, the microscopic structure of these aggregates is not completely known. Partial shear rejuvenation under step strains is also reported in the literature [12]. Another recent study by Angelini *et al.* showed that a clay suspension exhibits a transition from a

glassy phase stabilized by interparticle repulsions to an attractive glass with increasing sample age [13]. The microstructures of this attractive glass is dominated by a disconnected house of cards structure. Therefore, the possibility of the presence of edge-face attractive bonds in the microscopic structure of the aggregates that arise from the shear rejuvenation process cannot be neglected. We further note that influence of the varying initial aggregate size distributions on the aging and subsequent yielding behaviors has never been reported in the literature.

In this chapter, we present a preliminary work on the aging and yielding behaviors of Laponite suspensions when the samples are shear melted by a filtration method using cellulose membranes of submicrometer pore sizes. The filtration of Laponite suspensions having soft solid behavior through the membrane with varying flow rates and pore sizes is expected to produce different aggregate size distributions. The aging behaviors of these samples are monitored by the time evolution of the viscoelastic moduli, while the linear viscoelasticity and yielding are characterized using oscillatory strain sweep experiments. We observe that with increasing flow rates of filtration and decreasing membrane pore sizes, that is, with increasing shear rates on the samples, the shear melted samples undergo a faster aging process that results in higher viscoelastic moduli and yield values.

8.2 Sample preparation

Laponite of XLG grade, supplied by Southern Clay Products, is used for this work. The structural information of this clay mineral is given in Chapter 1 (Section 1.6). To maintain an identical sample composition for each experiment, the clay mineral powder is heated in an oven at a temperature of 120°C for 24 hours to remove absorbed moisture before it is dispersed in highly deionized Milli-Q water under vigorous stirring conditions. The mixture is stirred for three hours using a magnetic stirrer to ensure a homogeneous distribution of the aggregates. The samples are next stored in polypropylene syringes in air tight conditions at room temperature. The sample-filled syringes

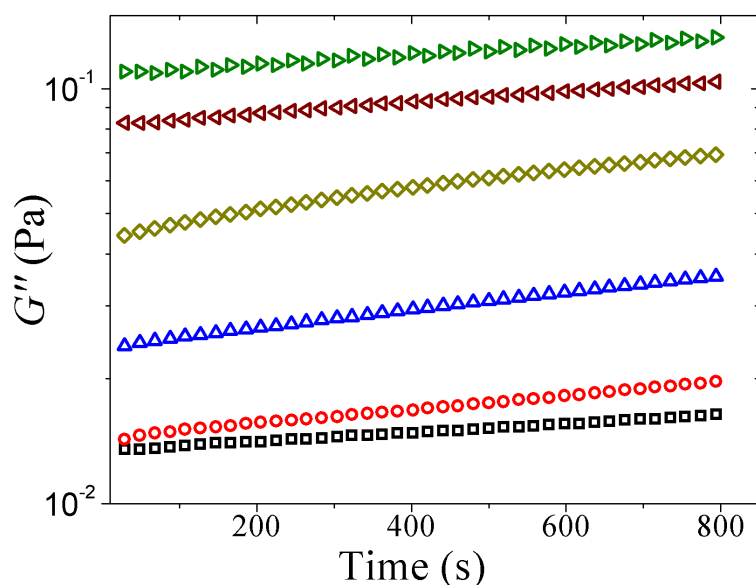


FIGURE 8.1: Variation of the viscous modulus G'' with time when an oscillatory stress of amplitude 50 Pa at an angular frequency of 1 rad/s is applied to samples filtered with flow rates of (bottom to top) 0.05, 0.2, 0.3, 1, 2 and 3 ml/min. The samples show zero elastic moduli G' under this oscillatory stress.

are then left in an undisturbed condition for different time durations, denoted as idle time, before shear melting the samples at varying flow rates using filtration membranes of different pore sizes. For the filtration of samples, Millipore Millex-HV syringe-driven filters are used. The filtration flow rate is precisely controlled using a syringe pump procured from Chemyx Inc. The sample is directly collected in the rheological measurement cell during the filtration process. The filtered sample is then immediately transferred to the rheometer unit for further experiments. A clay concentration of 3.5% w/v is used for all experiments reported here. The rheological experiments are performed using the Anton Paar MCR 501 rheometer. Details of this setup can be found in Chapter-2.

8.3 Experimental results and discussion

The time duration of the filtration process varies with the filtration flow rates. The filtered samples undergo an aging process before the completion of the filtration step. To minimize the aging effect during filtration, all samples are further subjected to high shear oscillatory stress of amplitude 50 Pa for 15 minutes at an angular frequency $\omega = 1$ rad/s inside the measuring cell of the rheometer. During this step all samples remain in liquid like states with zero elastic modulus, G' , and finite viscous modulus, G'' , as can be seen in Fig. 8.1. The viscous modulus under the high stress exhibits weak increase with time, possibly due to the aging effect. It is also seen in this figure that the samples filtered with lower flow rates exhibit lower values of G'' under the high shear stress. Since the filtration of the sample at a higher flow rate is expected to produce lower aggregate sizes, the results in Fig. 8.1 indicate that the viscosity of samples in the liquid state increases with decreasing aggregate sizes.

On the cessation of the oscillatory shear melting stress, the particle aggregates in suspension start rearranging to achieve their minimum interparticle interaction potential. This is manifested as an evolution of the viscoelastic moduli (G' and G'') with age t_w as shown in Fig. 8.2 for 3.5% w/v Laponite suspensions filtered with flow rates in the range of 0.05 – 3 ml/min. Here, $t_w = 0$ is defined as the time at which shear melting of sample is stopped inside the measuring cell. The evolution of the elastic modulus G' and viscous modulus G'' are monitored by applying an oscillatory strain of amplitude 0.5% at a constant angular frequency $\omega = 0.6$ rad/s. The applied strain amplitude is extremely small, well within the linear viscoelastic regime and is not expected to destroy sample microstructures [14, 15]. It is seen in Fig. 8.2 that G' and G'' initially exhibit strong dependence on the age t_w . Such dependence becomes weak with the age of the suspensions. It is also seen in that all samples exhibit clear transition from a liquid-like state ($G' < G''$) to a kinetically arrested state ($G' > G''$) with sample age at $t_w = t_c$. The crossover time, $t_c = 1601$ s, for a representative flow rate of 0.05 ml/min (squares in Fig. 8.2) is denoted by a vertical dotted line in Fig. 8.2. For the flow rate values ≥ 0.3 ml/min, a broad peak in G'' appears with age at $t_w = t_p$ (shown by arrow heads in

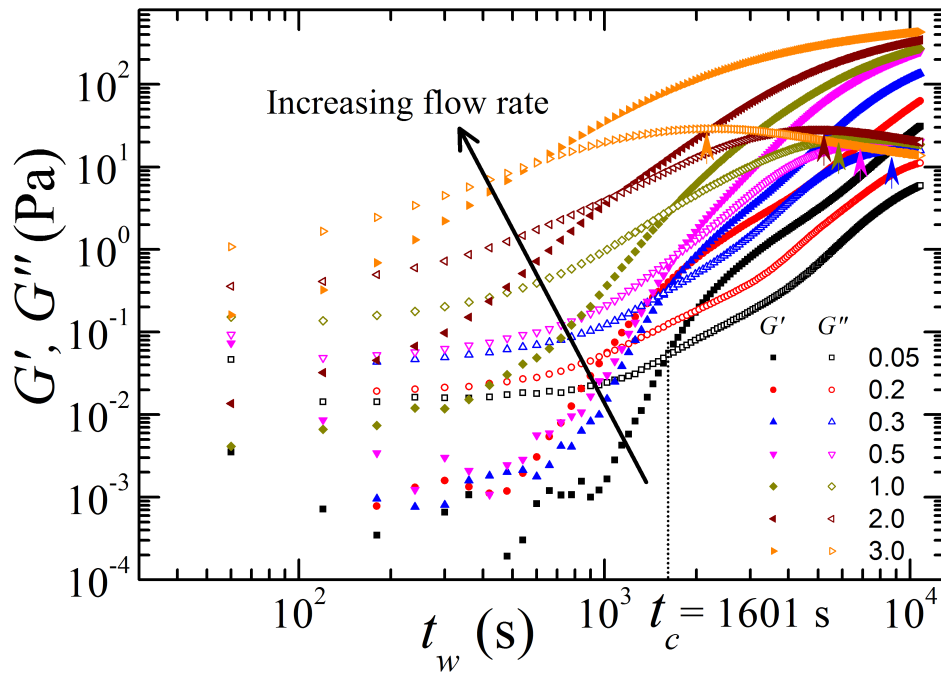


FIGURE 8.2: Evolution of elastic modulus G' (filled symbols) and viscous modulus G'' (empty symbols) with age, t_w , of 3.5% w/v Laponite suspensions of idle time 9 days filtered through a membrane of pore size of $0.45 \mu\text{m}$ with varying flow rates in the range 0.05 – 3 ml/min. The vertical dotted line shows the position of the crossover time, $t_{tr} = 1061$ s, between G' and G'' of the sample filtered at flow rate of 0.05 ml/min (squares). The arrow heads shows the position t_p of the peaks in G'' for samples filtered with flow rates ≥ 0.3 ml/min.

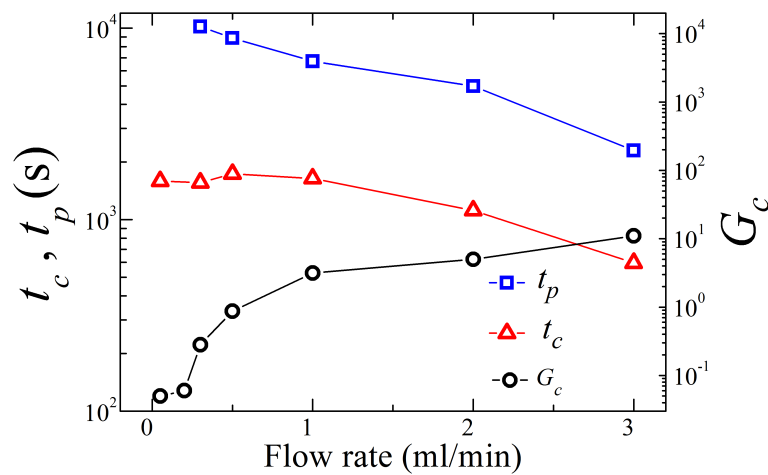


FIGURE 8.3: Plot of the crossover time, t_{tr} , as a function of flow rate during filtration of 3.5% w/v Laponite suspensions though memebrane of pore size of $0.45 \mu\text{m}$.

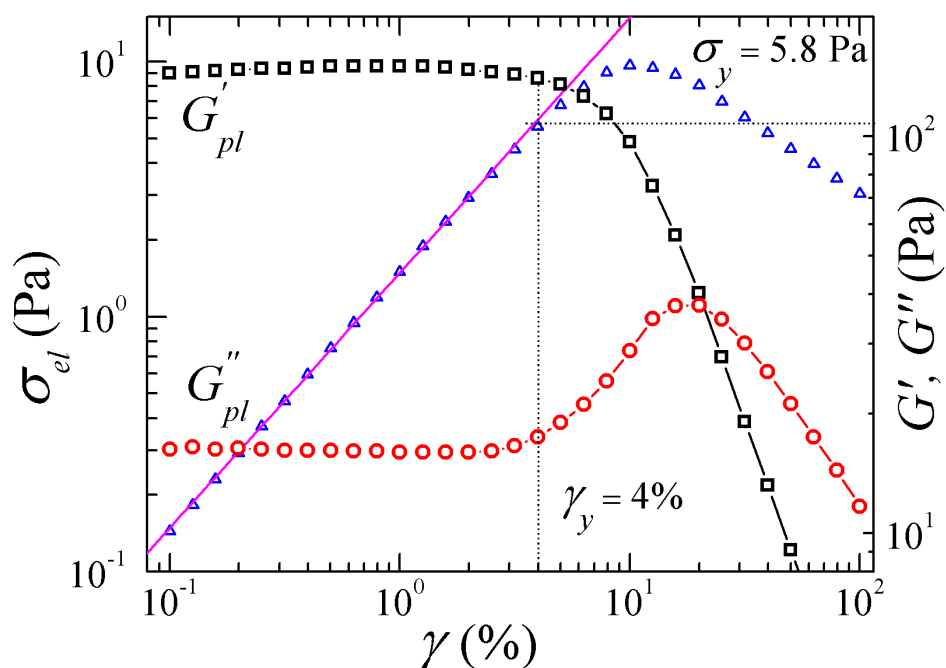


FIGURE 8.4: Variation of elastic modulus G' (\square), viscous modulus G'' (\circ) and elastic stress $\sigma_{el} = G'\gamma$ (Δ) with strain amplitude, γ , measured at an angular frequency of 6 rad/s for a 3.5% w/v Laponite suspension of idle time of 9 days filtered through a membrane of pore size of 0.45 μm with flow rate of 0.3 ml/min and evolved for $t_w = 3$ hours. The solid line is a linear fit to the σ_{el} vs γ data. Vertical and horizontal dotted lines indicate the position of yield strain $\gamma_y = 4\%$ and yield stress $\sigma_y = 5.8$ Pa respectively. The details of the method for determining the yield values from the amplitude sweep experiment is discussed in Section 2.2.5(b) of Chapter 2.

Fig. 8.2). The variation of the t_c , the value of the moduli $G_c = G' = G''$ at $t_w = t_c$ and t_p are plotted in Fig. 8.3. It is seen in this figure that the positions of the t_c and t_p shift to lower ages with increase in the flow rates used for sample filtration. Moreover, the critical value of the moduli (G_c) at the transition point increases with the increase in flow rate values. This behavior indicates that the rearrangement process which drives the systems to kinetically arrested states is faster in suspensions with lower aggregate sizes which are obtained by filtering the samples at higher flow rates.

We next perform oscillatory strain amplitude sweep experiments to find the influence of the filtration rate on the linear viscoelasticity and yielding behavior of the shear melted samples. A representative strain amplitude sweep data is shown in Fig. 8.4 for a 3.5% w/v sample of idle time 9 days filtered using a membrane of pore size 0.45 μm at a flow rate of 0.3 ml/min and subsequently evolved for $t_w = 3$ hours. At small values

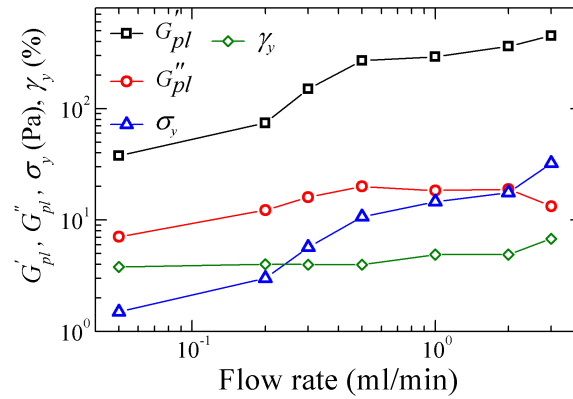


FIGURE 8.5: Plot of the plateau values of the elastic modulus, G'_{pl} (□) and viscous modulus, G''_{pl} (○), yield stress, γ_y (◇) and σ_y (△) vs flow rate of filtration of 3.5% w/v Laponite suspensions of idle time of 9 days and evolved for $t_w = 3$ hours.

of applied strain (γ), both the moduli G' (□ in Fig. 8.4) and G'' (○ in Fig. 8.4) remain independent of the strain amplitudes, while the plateau value G'_{pl} of elastic modulus is much larger than the plateau value G''_{pl} of the viscous modulus. On further increase in γ , the sample starts yielding due to the irreversible rearrangement of particles in the suspension under high strains. In this nonlinear regime, G' decreases monotonically while G'' reaches a peak at the point of crossover between G' and G'' . Finally, at very high strains, the sample exhibits fluid-like behavior which is indicated by $G'' > G'$. The yield strain, γ_y , and yield stress, σ_y of this sample are determined from the linear fit (solid line in Fig. 8.4) to the elastic stress, G'_{el} (△ in Fig. 8.4) vs strain data. The details of the method for determining the yield values from this fit are discussed in Section 2.2.5(b) of Chapter 2. The values of $\gamma_y = 4\%$ and $\sigma_y = 5.8$ Pa are indicated by the vertical and horizontal dotted lines for the representative data plotted in Fig. 8.4. The plots of the G'_{pl} , G''_{pl} , σ_y and γ_y as functions of flow rates are shown in Fig. 8.5. Monotonic increases in G'_{pl} , γ_y and σ_y are observed with increasing flow rate. This again confirms that suspensions of lower aggregate sizes give rise to stronger soft solid materials.

We next monitor the evolution of the viscoelastic moduli for samples filtered with varying pore sizes at constant flow rates. The shear rate on samples passing through the membrane pores increases when the pore sizes of membrane is decreased, keeping

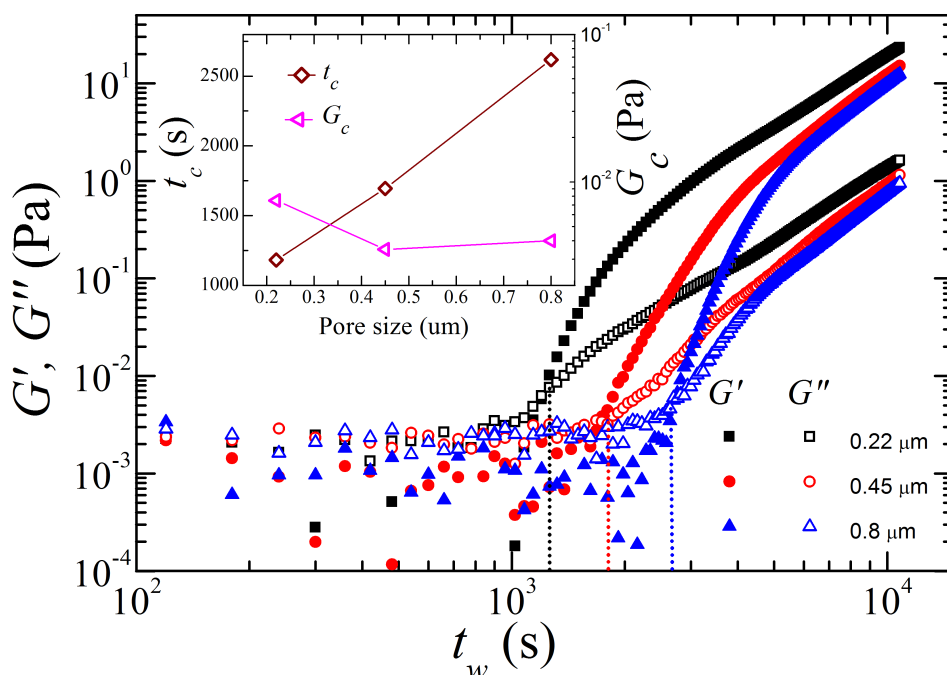


FIGURE 8.6: Evolution of elastic modulus G' (filled symbols) and viscous modulus G'' (empty symbols) with age, t_w , of 3.5% w/v Laponite suspensions of idle time of 1 hour filtered through membranes of pore sizes 0.22 μm (squares), 0.45 μm (circles) and 0.8 μm (triangles) at a constant flow rate of 3 ml/min. The vertical dotted lines indicate the positions of t_c for different flow rates. The inset shows the variation of crossover time, t_c (\diamond) and values of moduli at the crossover point, G_c (\triangleleft) with pore sizes.

the overall flow rate constant. It is therefore expected that suspensions filtered with the smaller pore size will have smaller aggregate size distribution due to the higher shear rates on the aggregates [11]. The evolutions of the elastic modulus G' and viscous modulus G'' with age t_w are shown in Fig. 8.6 for shear melted 3.5% Laponite suspensions of idle time of 1 hour filtered with membranes of pore sizes 0.22 μm (squares), 0.45 μm (circles) and 0.8 μm (triangles) at a flow rate of 3 ml/min. A clear transition from a liquid-like ($G' < G''$) regime to the solid-like ($G' > G''$) regime can be observed for all the samples. Unlike the samples filtered at higher idle times, samples filtered at lower idle times do not exhibit peaks in G'' with age. This can be seen by comparing data (\triangleright in Fig. 8.2 and \circ in Fig. 8.6) for samples of different idle times filtered with a membrane pore size of 0.45 μm with a flow rate of 3 ml/min. The variations of the crossover time (t_c) and the values of the moduli at the crossover point (G_c) with the

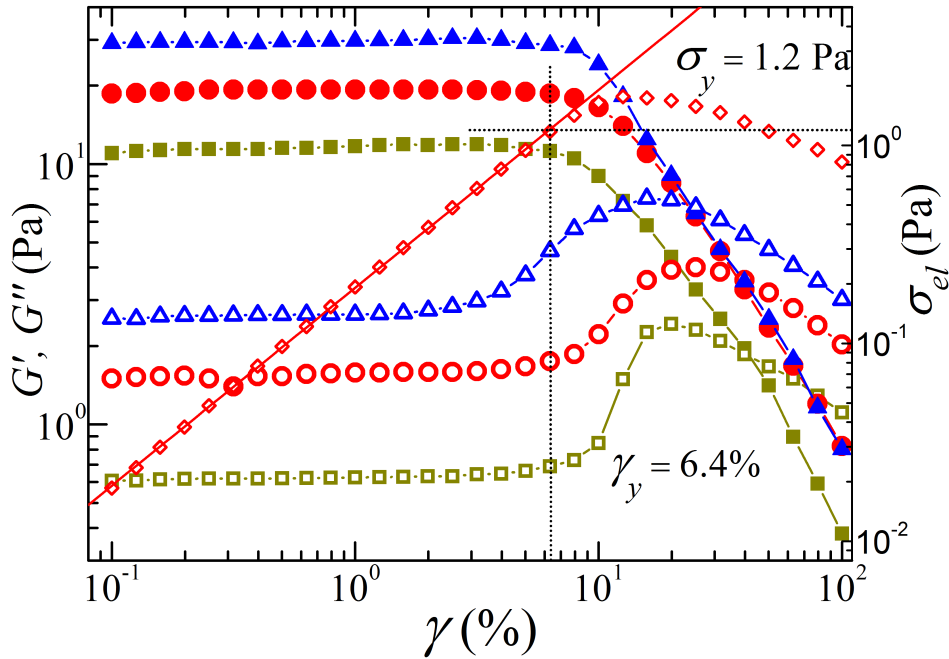


FIGURE 8.7: Variation of elastic modulus G' (filled symbols), viscous modulus G'' (empty symbols) with strain amplitude, γ , measured at an angular frequency of 6 rad/s for a 3.5% w/v Laponite suspension of idle time of 1 hour filtered through a membrane of pore size of $0.22 \mu\text{m}$ (triangles), $0.45 \mu\text{m}$ (circles) and $0.8 \mu\text{m}$ (squares) with flow rate of 3 ml/min and evolved for $t_w = 3$ hours. The plot of elastic stress, $\sigma_{el} = G' \gamma$ (\diamond) as a function of γ is shown only for the pore size of $0.45 \mu\text{m}$ for clarity. The solid line is a linear fit to the σ_{el} vs γ data. Vertical and horizontal dotted lines indicate the position of yield strain $\gamma_y = 6.4\%$ and yield stress $\sigma_y = 1.2$ Pa respectively for this experiment.

varying pore sizes are shown in the inset of Fig. 8.6. It is seen in this figure that G_c exhibits weak dependence on the pore sizes, while t_c shifts to higher ages with increasing pore sizes. These results again confirm that the suspensions filtered with higher shear rates undergo a faster aging process due to the smaller initial aggregate sizes.

The viscoelasticity and yielding behavior of the samples filtered with varying pore sizes are next characterized using oscillatory strain amplitude sweep experiments (Fig. 8.7). For all the samples, the elastic modulus G' and viscous modulus G'' , measured at $t_w = 3$ hours, show qualitatively similar behaviors such as reported in Fig. 8.4 for samples filtered with varying flow rates. The yield strains and the yield stresses of these samples are determined using the method described above. Fig. 8.8 shows the G'_{pl} , G''_{pl} , σ_y and

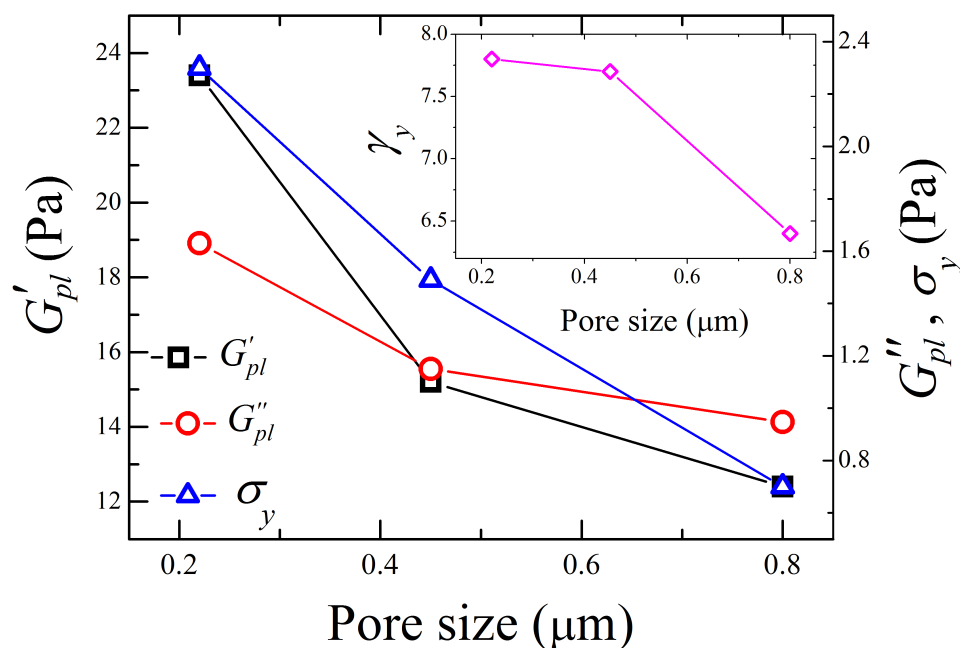


FIGURE 8.8: Plot of the plateau values of the elastic modulus, G'_{pl} (□) and viscous modulus, G''_{pl} (○), yield stress, and σ_y (Δ) and γ_y (◇ in the inset) vs membrane pore sizes. These values are determined from the strain amplitude sweep experiments shown in Fig. 8.7.

γ_y determined from the strain amplitude sweep data (Fig. 8.7), decrease with the increase in the pore sizes. This behavior again confirms that samples with lower initial aggregate sizes exhibit higher viscoelasticities and yield stresses.

8.4 Conclusion

In this chapter, we report the influence of the initial aggregate sizes on the aging kinetics, viscoelasticity and yielding behavior of shear melted 3.5% w/v Laponite suspensions at different idle times. The different initial aggregate sizes are obtained by filtration of the kinetically arrested samples using filtration membranes with varying pore sizes and flow rates. When the flow rate of filtration is systematically increased (Fig. 8.3) and membrane pore size is decreased (inset of Fig. 8.6), it is seen that the evolutions of the viscoelastic moduli (G' and G'') with age after the filtration of samples become faster and the transition time to change from liquid-like behavior to solid-like

behavior shifts to lower ages. The plateau values of the viscoelastic moduli, yield strains and yield stresses determined from oscillatory experiments exhibit monotonic increase with increase in the filtration rate (Fig. 8.5) and with the decrease in the membrane pore sizes (Fig. 8.8).

The imposed shear rate on the samples increases with the increasing flow rates of filtration and decreasing pore sizes of membranes. It is shown in the literature that increasing the shear rate beyond the linear viscoelastic regime of the sample results in smaller aggregate sizes in the suspension [11]. Our results therefore indicate a suspension with smaller aggregate sizes undergo faster rearrangement processes facilitated by thermal fluctuations, which results in enhanced aging dynamics in these suspensions. However, the nature of the resulting microstructures due to the rearrangement process in the filtered samples at different idle times is not clear from our data. In summary, this work demonstrates the enhancement of the aging process and the sample viscoelasticity when a kinetically arrested clay suspension is subjected to progressively higher shear melting stresses that are above the yield value. However, for a complete understanding of such behavior, further dynamical studies using light scattering must be performed systematically for samples with varying clay concentrations, ages and idle times.

References

- [1] B. Abou, D. Bonn and J. Meunier, *Physical Review E*, 2001, **64**, 021510.
- [2] D. Saha, Y. M. Joshi and R. Bandyopadhyay, *Soft Matter*, 2014, **10**, 3292–3300.
- [3] D. Bonn, S. Tanase, B. Abou, H. Tanaka and J. Meunier, *Physical Review Letters*, 2002, **89**, 015701.
- [4] F. Ozon, T. Narita, A. Knaebel, G. Debrégeas, P. Hébraud and J.-P. Munch, *Physical Review E*, 2003, **68**, 032401.
- [5] V. Viasnoff and F. Lequeux, *Physical Review Letters*, 2002, **89**, 065701.
- [6] F. Ianni, R. Di Leonardo, S. Gentilini and G. Ruocco, *Physical Review E*, 2007, **75**, 011408.
- [7] A. Shahin and Y. M. Joshi, *Langmuir*, 2010, **26**, 4219–4225.
- [8] A. Shahin and Y. M. Joshi, *Langmuir*, 2012, **28**, 5826–5833.
- [9] R. Angelini, L. Zulian, A. Fluerasu, A. Madsen, G. Ruocco and B. Ruzicka, *Soft Matter*, 2013, **9**, 10955–10959.
- [10] T. Gibaud, C. Barentin and S. Manneville, *Physical Review Letters*, 2008, **101**, 258302.

- [11] T. Gibaud, C. Barentin, N. Taberlet and S. Manneville, *Soft Matter*, 2009, **5**, 3026–3037.
- [12] R. Bandyopadhyay, P. H. Mohan and Y. M. Joshi, *Soft Matter*, 2010, **6**, 1462–1466.
- [13] R. Angelini, E. Zaccarelli, F. A. de Melo Marques, M. Sztucki, A. Fluerasu, G. Ruocco and B. Ruzicka, *Nature communications*, 2014, **5**, 1–7.
- [14] A. Negi and C. Osuji, *EPL (Europhysics Letters)*, 2010, **90**, 28003.
- [15] A. Shahin and Y. M. Joshi, *Langmuir*, 2012, **28**, 15674–15686.

9

Summary and future directions

This thesis presents experimental studies of the dispersibility of clay tactoids in various nonequilibrium phases, such as glasses and gels, of aqueous clay suspensions, and their rheological and stability properties using the synthetic clay mineral Laponite and the natural clay mineral Na-montmorillonite as model charge-anisotropic particles. The focus of this thesis has been to link the bulk properties of clay suspensions to the time and composition dependent dynamical processes and microscopic structures of clay suspensions. Various bulk properties such as aging, viscoelasticity, yielding, stress relaxation are studied using a rheometer, while stability under gravity is studied using table top experimental setups developed based on a light transmission method and electroacoustics. On the other hand, some microscopic processes, such as clay tactoid exfoliation and clay particle transport under gravity, are indirectly monitored using ultrasound attenuation spectroscopy and electroacoustics, while the microscopic structures of clay suspensions are studied directly using scanning electron microscopy and atomic force microscopy.

Chapter 1 contains a brief description of the background information required for understanding the experimental results presented in this thesis. Colloidal particles and the interactions between them in suspension are discussed in the context of hard

spheres and charged colloidal particles. Some common features such as glass and gel transitions exhibited by typical colloidal suspensions and their viscoelastic and stability behaviors are discussed. Significance of colloidal suspensions as model systems to understand the molecular glass transition process and some similarities between jammed colloidal suspensions and supercooled liquids are further highlighted. The soft glassy rheology (SGR) model for soft solid materials and the sedimentation stability of colloidal gels are further discussed. This is followed by the structural description of the clay minerals Laponite and Na-montmorillonite which are used in this thesis work. Clay tactoid exfoliation processes at dilute concentrations and the formation of electric double layers on the charged and shape anisotropic clay particles are discussed. Equilibrium conformations between two clay platelets at varying degrees of charge screening proposed in the literature are also presented. We next discuss the phase behavior of clay suspensions reported in the literature at varying clay and salt concentrations, and ages of suspensions. This is accompanied by a discussion on the rheological behaviors of soft glassy materials and various models proposed in the literature.

A detailed description of the experimental methods used in this thesis work is presented in Chapter 2. This includes the technique and relevant theory for ultrasound attenuation spectroscopy which is used in this thesis for estimating particle size distributions of clay particles in suspensions, two complementary tabletop experimental setups based on light transmission and electroacoustics, rheological measurement methods, high frequency conductivity measurement, atomic force microscopy and scanning electron microscopy that were used to visualize the microstructures of dried and vitrified samples.

The time-dependent exfoliation process of clay in aqueous suspensions has a direct influence on the jamming transition, rheological and stability behavior and aging dynamics of clay suspensions. Moreover, having a good degree of exfoliation of clay tactoids is very important for their potential technological applications in clay-polymer nanocomposites, ion exchange and rheological thickeners. In Chapter 3, we have used non-destructive ultrasound attenuation spectroscopy (UAS) to monitor the degree of

exfoliation of tactoids by estimating the size distributions of clay particles. We have used atomic force microscopy to measure the lateral sizes of platelets. Ultrasound attenuation spectra (plot of ultrasound attenuation coefficients as a function of ultrasound frequency) are measured at varying clay concentrations and ages of Laponite suspensions. The particle size distributions in these samples are further determined by fitting the experimental attenuation spectrum to the theoretical attenuation spectrum calculated based on the theory of viscous attenuation of ultrasound. We next develop a methodology using Jennings-Parslow relation for estimating the average number of platelets in clay tactoids from the spherical equivalent sizes obtained in the ultrasound attenuation measurements. We find that a substantial fraction of the aggregates in suspension are actually tactoids that are composed of more than one platelet. This is in contrast to the general belief that clay disperses into individual platelets in the concentration range where their suspensions exhibit glassy behavior. We conclude that the incomplete fragmentation of the clay tactoids arises from the rapid enhancement of the intertactoid screened Coulombic repulsion. Our further measurements of viscoelastic moduli of clay suspensions during the aging process show a good correlation between the tactoid exfoliation and kinetic arrest processes.

More ultrasound experiments are reported in Chapter 4 for salt-free suspensions of the natural clay Na-montmorillonite. We have shown here that the complete exfoliation of tactoids is not achieved even below the jamming concentration of these suspensions. This observation is next verified indirectly by measuring the conductivity of suspensions of varying clay concentrations. These measurements indicate that besides the intertactoid repulsive interactions, osmotic pressure of the hydrated Na^+ counterions in the intertactoid space (bulk medium) has a crucial influence on the incomplete exfoliation process. This is verified by monitoring the exfoliation process in various ionic conditions using UAS. It is seen that when the clay mineral is dispersed in a premixed salt solution, the tactoid exfoliation process becomes extremely slow and the tactoids show a substantially lower degree of exfoliation compared to the tactoids in a salt-free suspension. We also observe a signature of an irreversible process

of tactoid reformation when counterion concentration is increased in the suspension by adding salt. Finally, electroacoustic and rheological measurements are performed to assess the influence of tactoid exfoliation on the stability and viscoelasticity of the arrested phases formed under different ionic conditions.

The influence of the osmotic pressure of the counterions on the exfoliation process has been established by us for Na-montmorillonite clay which is a superior attenuator of ultrasound compared to the smaller Laponite platelets. Since Laponite is structurally similar to the Na-montmorillonite, it is expected that exfoliation kinetics of Laponite tactoids in suspension will exhibit identical behavior. However, it is worth performing similar experiments in Laponite suspensions to find the time scale of the exfoliation process at different ionic conditions. This information would be very important for their use as model gels as well as for their technological applications. A complementary measurement can be performed using synchrotron based SAXS to monitor the tactoid exfoliation process with age of clay suspensions prepared with the identical protocol described here. The rate of diffusion of hydrated Na^+ counterions into the bulk water from the intratactoid space depends on the lateral sizes of the tactoids. This leads to a slower exfoliation process for tactoids of higher lateral sizes. This can be seen in Chapters 1 and 2 by comparing data for Laponite and Na-montmorillonite. However, a systematic study has not been undertaken here. It would be interesting to investigate the exact nature of the lateral size dependence of the exfoliation rate by using samples of carefully size-segregated tactoids from a highly polydisperse clay such as Na-montmorillonite.

In Chapter 5, we have elucidated the link between the bulk rheological and stability behaviors of natural Na-montmorillonite gels and their underlying microscopic structures. The rheological behavior of clay gels at varying NaCl salt concentrations is measured using oscillatory strain amplitude sweep and controlled shear stress flow measurements. When the salt concentration in the dispersing medium is increased systematically, viscoelasticity and yield stress of the suspension increases upto a peak value at a critical salt concentration and decreases monotonically for further increase

in the salt concentrations. This monotonic rheological behavior with varying salt concentration signifies a morphological change in the suspension microstructures. We directly visualize the microscopic structures of these kinetically arrested phases using cryogenic scanning electron microscopy (cryo-SEM). We observe the existence of honeycomb-like network morphologies over a wide range of salt concentrations. The association of clay platelets in the form of overlapping coins (OC), house of cards (HoC) and face-face aggregations on the gel network are identified by calculating the pore sizes and network-branch thicknesses using ImageJ and also by direct inspection of the microstructures in the cryo-SEM micrographs. This analysis shows a transition of gel morphology, dominated by overlapping coin (OC) and house of cards (HoC) associations of clay particles at low salt concentrations to a new network structure dominated by face-face coagulation of platelets, across the critical salt concentration. The influence of the network morphology on the stability of these gels under gravity is further assessed using electroacoustics. It is seen that the gels remain stable for a wide salt concentration range above the critical concentration where particles undergo face-face aggregation due to the van der Waals attraction. However, further increase in the salt concentration leads to large pore sizes and very thick network-branches which collapse under gravity.

The observation of morphological transitions by varying salt concentrations reported here must be complemented using synchrotron source X-ray scattering in future studies. This will help in accurate estimation of the network branch thicknesses at various salt concentrations. The microscopic process of the yielding of clay glasses and gels is still poorly understood. Simultaneous rheological and scattering measurements can be undertaken to elucidate the nature of the yielding process. It is believed that the effective potential on the edges of Na-montmorillonite platelets is negative due to the spillover effect of basal negative potential. Such spillover strongly depends on the lateral sizes of the platelets. The rheological and phase behaviors of Na-montmorillonite platelets of sizes for which such spillover effect is negligible must be performed. This

will help in the understanding of several novel phases reported for Laponite suspensions such as empty liquids and equilibrium gels [Ruzicka *et al.*, *Nature Materials*, 2011, **10**, 56 – 60]. A transition of a repulsive glass to an attractive glass in a salt-free Laponite clay suspensions has been reported in the literature [Angelini *et al.*, *Nature communication*, 2014, **5**, 4049(1) – 4049(7)]. However, a direct evidence of such a proposal is still lacking. Experiments must be performed to find signatures of such transitions in Laponite and Na-montmorillonite suspensions following an approach similar to the one described in Chapter 5.

Chapter 6 presents the aggregation and stability behaviors of highly polydisperse Na-montmorillonite platelets in aqueous suspensions at a dilute concentration well below that required to achieve the glass transition. It is seen that these platelets are not stable in salt-free aqueous suspensions in the dilute concentration regime and sediment under gravity with a particle concentration gradient along the sample height. We next investigate the stability of weak gels formed by inducing attractive interactions between the clay platelets in the dilute concentration regime by directly monitoring the gel interface in optical transmission experiments. We observe that the gels prepared by dispersing clay powder in NaCl solutions are not stable under gravity and collapse immediately with a distinct interface between the clear supernatant and a clay-rich sediment. In contrast, we find remarkable enhancement of the stability of the suspensions if identical amounts of salt are added to the clay suspensions after adding the clay powder to water. These gels remain stable for a finite delay time and eventually exhibit transient collapse under gravity with a sharp interface height that decreases with increasing sample ages. In the collapse regime, the velocity of the collapsing interface exhibits oscillations with sample age. Moreover, the average velocity of the interface increases with age upto a peak value before decreasing at higher ages. When the salt concentration is increased systematically, the delay time for transient collapse decreases, while the average collapse velocity increases. Our rheological measurements show that the elastic moduli of the gels increase with sample age upto the delay

time before exhibiting oscillations at higher ages. The microscopic mechanism involved in the observed transient collapse is studied with direct visualization of the gel microstructures using cryogenic scanning electron microscopy. It is seen that the gel network undergo microscopic restructuring with time, thereby attaining higher elastic moduli and, therefore, higher yield stresses with age since preparation. During the restructuring process, an increasing number of platelets is seen to participate in network formation through overlapping coin configurations. This leads to increase in the lengths and widths of the network strands. On the other hand, the gravitational stresses on the gel strands increase with the increase in the dimensions of the network strands. From the rheological and direct microscopy observations, we conclude that the transient collapse of weak gels and the subsequent oscillations in the collapse velocity arise due to the competition between the local yield stresses and the gravitational stresses on the gel network strands. Our further study using electroacoustic shows that the delay time for transient collapse increases significantly with the increase in the particle concentration in the gels.

The interaction between the gels and the walls of sedimentation cell is very important for the stability of gels. In future, it would be worth understanding the effect of such interactions by varying hydrophilicity and roughness of the walls of the sedimentation cell. Furthermore, it is also important to understand the influence of the initial heights and diameters of the samples on gel stability. An effort could also be made to model the platelet aggregation and restructuring rates during collapse. This could be combined with the existing poroelastic models of collapsing gels to quantitatively understand the stability of clay gels.

Chapter 7 presents the stress relaxation behavior of shear melted Laponite suspensions for varying particle and salt concentrations, sample idle times (time since preparation), suspension ages and applied step strains. When the step strain values lie in the linear viscoelastic regime, both the salt-free and gel samples exhibit stress relaxation with a single-step decay which can be modeled using the Kohlrausch-Williams-Watt (KWW) function. The average relaxation times estimated from the KWW fits are seen

to follow a power law increase with the age of the suspension in this regime. On the other hand, for step strain values in the nonlinear regime, a transition from a single-step to a two-step decay of stress is observed with sample age in the salt-free clay suspensions. The single-step decay of the relaxation could not be modeled using a single function in this regime. However, initial decay of the relaxation could be fitted to a power law. The extent of the power law fits is seen to increase with sample age upto a critical age above which the relaxation exhibit two-step decays. When the relaxation process is repeated for a salt-free Laponite suspension of lower idle time, it is found that the extent of the power law fits shift to higher ages of the sample. Such a power law decay of the induced stress was previous reported in the literature for critical gels [Broderix *et al.*, *Physical Review E*, 2001, **64**, 021404]. It is also observed in this study that the relaxation time decreases with increase in the step strain in the linear viscoelastic regime. On the contrary, the relaxation time increases with increase in step strain in the nonlinear viscoelastic regime. Such an increase in the relaxation time for higher applied strains is counter intuitive and is assumed to be due to the strain-induced hardening process. Interestingly, we find similar two-step decay process of stress in gels samples under nonlinear step strains. The influence of the interparticle attractive interactions on the age-dependent phase behavior of freshly prepared clay suspensions in salt-free condition was previously reported in the literature [Angelini *et al.*, *Nature communication*, 2014, **5**, 4049(1) – 4049(7) and Saha *et al.*, *Langmuir*, 2015, **31**, 3012 – 3020]. The stress relaxation behavior reported in this chapter indicates that the influence of attractive interaction cannot be ignored in shear melted salt-free Laponite suspension at very large idle times. However, a systematic study of the relaxation time at varying clay and salt concentrations should be performed both in freshly prepared and shear melted samples using a combination of rheological and scattering measurements to verify these results over a larger range of physicochemical parameters that influence the rheology of Laponite suspensions.

Chapter 8 presents a preliminary study showing the influence of the initial aggregate size distribution on the aging dynamics and rheology of glassy colloidal clay suspensions. In this work, we have varied the initial size distribution of clay particles in a concentrated suspension by shear melting the aging samples of different idle times with varying flow rates of filtration using porous membranes of different pore sizes. The aging dynamics and jamming phase transitions of the resulting suspensions are studied using oscillatory rheological measurements. It is observed that the evolutions of the viscoelastic moduli with age after filtration of the samples become faster, with the time required to achieve kinetic arrest shifting to lower ages when the flow rate of filtration is increased and the membrane pore size is decreased systematically. The viscoelastic moduli in the linear viscoelastic regime, the yield strains and yield stresses determined from oscillatory rheology experiments exhibit monotonic increases with increase in the filtration rate and with decrease in the membrane pore sizes. These results indicate that a suspension with smaller aggregate sizes undergoes faster rearrangement processes facilitated by thermal fluctuations, which results in enhanced aging dynamics in the suspensions.

The exact nature of the microstructure that arises from the shear melting process is not completely understood from the present study. A detailed study by varying the clay concentrations, sample ages and idle times is required to determine the dependence of the aging dynamics on these parameters. Moreover, experiments should also be performed in suspensions in the presence of salt. This will elucidate the role of interparticle attractions on the observed behavior. Quantification of the aggregate sizes in suspensions filtered with varying pore sizes and filtration rates can be performed using scanning electron microscopy. The aging dynamics of the suspensions following the shear melting process can be studied using dynamic light scattering. Moreover, simultaneous rheological and scattering experiments using X-rays would be very helpful in uncovering the underlying mechanisms and aggregate microstructures.